Synthesis and Characterisation of Novel Molecular Indacenodithiophene Semiconductors for Transistor Applications

Imperial College London

Thomas Hodsden

Supervisor - Professor Martin Heeney

Submitted in partial fulfilment of the requirements for the degree of Doctor of Philosophy in Chemistry

Imperial College London

April 2020

Declaration

The work described in this thesis was carried out in the Department of Chemistry at Imperial College London between October 2016 and January 2020, under the supervision of Professor Martin Heeney. The content is the author's original work, unless stated otherwise.

Thomas Hodsden, April 2020

Contributions

The field of Plastic Electronics is hugely interdisciplinary, meaning much of this work has been carried out in collaboration with others from Chemistry, Materials and Physics departments. I would particularly like to thank the following people for their contributions:

Organic field-effect transistors (OFETs) were fabricated and tested by Julianna Panidi (Chapter 2) and Dr. Luxi Tan (Chapter 3) at Imperial College London, and Dr. Aniruddha Basu (Chapters 2 – 6) at KAUST.

Single crystal analysis (Chapters 2 – 5) was performed by Dr. Andrew J. P. White at the Chemical Crystallography Laboratory, Imperial College London.

Transfer integral and intermolecular interaction analysis (Chapters 2 – 5) was carried out by Dr. Karl J. Thorley at the University of Kentucky.

Thermal gravimetric analysis (TGA) (Chapters 2 – 6) was performed by Dr. Lisa Haigh at Imperial College London.

Preparation of dimethyldioxirane (DMDO) (Chapter 5) was carried out by Martina Rimmele at Imperial College London. Development of the synthesis of **IDT-difluorenone** and **IDT-difluorenylidene-di(C(CN)$_2$)** (Chapter 6) was carried out in partnership with Woyuan Luo at Imperial College London.

Copyright

The copyright of this thesis rests with the author and is made available under a Creative Commons Attribution Non-Commercial No Derivatives licence. Researchers are free to copy, distribute or transmit the thesis on the condition that they attribute it, that they do not use it for commercial purposes and that they do not alter, transform or build upon it. For any reuse or redistribution, researchers must make clear to others the licence terms of this work.

Acknowledgements

The past 4 years or so at Imperial have been a hugely rewarding time. The experiences gained and people met leave a lot to be thankful for.

I would like to begin by thanking the Engineering and Physical Science Research Council and Merck Chemicals Ltd for providing the funding for this project.

Thank you unreservedly to Prof. Martin Heeney in the first instance for giving me the opportunity to do a PhD. I could not have imagined this as being possible when I think back to some challenging school days. You have always made yourself available for consultation despite your busy schedule and go out of your way to make sure each of your students feels valued and supported. Also, to my industrial supervisors, Dr. Changsheng Wang and Dr. William Mitchell, for your vital support and discussions.

Thank you to all the members of the Heeney and McCulloch groups, past and present, who made for a stimulating and joyful laboratory environment. This includes Fei, Simeng, Marsh, Brett, Iain, Tingmang, Shengyu, Charlotte, Notina, Florian, Matthias, Martina, Simon, Filip, Petr, Qiao, Ilknur, Haojie, Bowen, Tao, Yang and Luxi from the Heeney group, and Alex, Mark, James, Karl, Max, Cameron, Helen, Petruta, Matt and Ada from the McCulloch group. I apologise for inevitably missing some people off this list.

Joining the Plastic Electronics CDT has been a highly fulfilling experience, not the least owing to the members of my cohort; Adam, Alice, Andreea, Djamshid, Jaspreet, Julianna, Luiz, Max, Ross, Ryley, Saurav, Shengyang, Tian.

Thank you to my oldest friends, Sam and Katherine, for putting up with me since school and always being there for a much needed escape. Also, to my tudderenderweg companion James for the regular catch up sessions over pool and Belgian beer.

Thank you to my parents, whose unquestioning support has been invaluable. You have always supported Dan and I in whatever pursuits we have chosen and instilled in us the work ethic and humility to succeed. To Dan and Amy, particularly for helping me settle in when I first moved to London. Dan – I will start a 'real job' now.

Finally, thank you to Emily. We met during the tough early stages of my PhD and you changed my life. I know I would not have gotten here without your wonderful support. Thank you for being the perfect balance to my often stressed and pessimistic outlook, all whilst going through your own challenges as a proper Doctor. I honestly do not know how you do it.

Abstract

The use of organic semiconductors (OSCs) for electronic applications is of interest due to their myriad desirable properties, including being lightweight, flexible and low-cost. This work focuses primarily on the synthesis and characterisation of novel molecular OSCs for field-effect transistor (OFET) applications. While the majority of high-performing OFETs are comprised of p-type OSCs, the performance of n-type OSCs still lags behind. New n-type OSCs are eagerly sought for use in complementary circuits and organic photovoltaics (OPVs), where balanced charge transport between the n-type and p-type components is crucial.

In Chapter 2, core fluorination is used as a tool to modify the n-type characteristics and device performance of an indacenodithiophene (IDT)-based molecular OSC – **2,7-dihexyl-IDT-di(C(CN)$_2$)**. Fluorination is shown to effectively depress the lowest-unoccupied molecular orbital (LUMO) energy level as well as cause a surprising improvement in solubility. OFET devices fabricated via solution-processing of the OSC thin-film display high mobility in the absence of non-idealities, in addition to good retention of performance in ambient conditions.

The following chapters (Chapters 3 – 5) then seek to modify this fluorinated core and investigate the effects on electronic, physical and device performance. In Chapter 3 we perform alkyl side-chain engineering, including modifications to the side-chain length, branching and regiochemistry. The nature and position of the alkyl side-chains are shown to have a significant impact on the physical properties – particularly processability and charge transfer characteristics – as well as device performance. In Chapter 4, the use of an alternative electron-withdrawing group (EWG) – *N*-cyanoimine – is explored in an attempt to avoid several issues associated with dicyanomethylene. Chapter 5 focuses on further modifications to the

fluorinated core, including i) end-functionalisation via direct heteroarylation coupling and ii) substitution of the fluorine groups via nucleophilic aromatic substitution.

Finally, in Chapter 6 a route to a novel class of nonacyclic IDT-based ladder-type molecular is outlined. Electronic and physical properties are explored to examine the applicability of these materials as OSCs for OFETs.

Contents

Declaration 1

Contributions 2

Copyright 3

Acknowledgements 4

Abstract 6

Contents 8

Publications 12

Abbreviations 13

1. Introduction 19

1.1 Organic Electronics 19

1.2 Organic Field-Effect Transistors 20

1.3 Charge Transport in OSCs 28

1.4 Designing OSCs for OFETs 29

1.5 Use of IDT in Organic Electronic Devices 33

1.6 Thesis Aims and Overview 36

2. Core Fluorination of 2,7-dihexyl-IDT-di($C(CN)_2$) 40

2.1 Introduction 40

2.2 Synthesis 43

2.3 Optoelectronic and Electrochemical Properties 45

2.4 Crystal Structures 48

2.5 Thermal Properties 56

2.6 OFET Performance 58

2.7 Conclusion 62

2.8 Experimental 63

3. Effect of alkyl side-chain on properties and performance of dialkyl-diFIDT-di($C(CN)_2$) 68

3.1 Introduction 68

3.2 Synthesis 71

3.2.1 Synthesis of 2,7-didodecyl-diFIDT-di(O) and 2,7-didodecyl-diFIDT-di($C(CN)_2$) 71

3.2.2 Synthesis of 2,7-bis(2-ethylhexyl)-diFIDT-di(O) and 2,7-bis(2-ethylhexyl-diFIDT-di($C(CN)_2$) 73

3.2.3 Synthesis of 3,8-dihexyl-diFIDT-di(O) and 3,8-dihexyl-diFIDT-di($C(CN)_2$) 74

3.3 Optoelectronic and Electrochemical Properties 77

3.4 Crystal Structures 81

3.5 Thermal Properties 87

3.6 OFET Performance 91

3.7 Conclusion 93

3.8 Experimental 94

4. *N*-Cyanoimine as an alternative electron-withdrawing group to dicyanomethylene 105

4.1 Introduction 105

4.2 Synthesis 109

4.3 Optoelectronic and Electrochemical Properties 112

4.4 Crystal Structures 115

4.1 Thermal Properties 121

4.2 OFET Performance 124

4.3 Conclusion 126

4.4 Experimental 127

5. Further modifications of 2,7-dialkyl-diFIDT-di(O) 130

5.1 End-functionalisation via Direct (Hetero)arylation 130

5.1.1 Introduction 130

5.1.2 Synthesis 134

5.1.3 Optoelectronic and Electrochemical Properties 135

5.1.4 Crystal Structure 137

5.1.5 Thermal Properties 140

5.1.6 Conclusion 141

5.1.7 Experimental 142

5.2 Nucleophilic Aromatic Substitution (S_NAr) of the Fluorine Group 144

5.2.1 Introduction 144

5.2.2 Synthesis 148

5.2.3 Optoelectronic and Electrochemical Properties 149

5.2.4 Thermal Properties 153

5.2.5 Conclusion 155

5.2.6 Experimental 157

6. Novel nonacyclic IDT-based OSCs 159

6.1 Introduction 159

6.2 Synthesis 161

6.3 Optoelectronic and Electrochemical Properties 163

6.4 Thermal Properties 166

6.5 Conclusion 169

6.6 Experimental 170

7. General Conclusion 177

8. General Experimental 180

9. References 183

10. Appendix 200

10.1 Chapter 2 200

10.2 Chapter 3 216

10.3 Chapter 4 241

10.4 Chapter 5 252

10.4.1 End-functionalisation via Direct (Hetero)arylation 252

10.4.2 Nucleophilic Aromatic Substitution (S_NAr) of the Fluorine Group 255

10.5 Chapter 6 258

11. Permissions 267

Publications

Publications relating to the work carried out in this thesis:

- F. Paterson, S. Singh, K. J. Fallon, **T. Hodsden**, Y. Han, B. C. Schroeder, H. Bronstein, M. Heeney, I. McCulloch, and T. D. Anthopoulos, *Adv. Mater.* **2018**, 30, 1801079 [doi.org/10.1002/adma.201801079] (**All Chapters**)
- **T. Hodsden**, K. J. Thorley, J. Panidi, A. Basu, A. V. Marsh, H. Dai, A. J. P. White, C. Wang, W. Mitchell, F. Glöcklhofer, T. D. Anthopoulos, and M. Heeney, *Adv. Funct. Mater.* **2020**, 2000325 [doi.org/10.1002/adfm.20200032] (**Chapter 2**)
- C. Wang, W. Mitchell, **T. Hodsden**, M. Heeney, J. Panidi, (Merck KGaA) *WO2020011831A1*, **2020** (**Chapter 2** – **4**)

Other publications (not discussed in this thesis):

- Z. Fei, Y. Han, E. Gann, **T. Hodsden**, A. S. R. Chesman, C. R. McNeill, T. D Anthopoulos, and M. Heeney, *J. Am. Chem. Soc.* **2017**, 139, 8552−8561 [doi.org/10.1021/jacs.7b03099]
- R. Lu, Y. Han, W. Zhang, X. Zhu, Z. Fei, **T. Hodsden**, T. D. Anthopoulos, and M. Heeney, *J. Mater. Chem. C*, **2018**, 6, 2004-2009 [doi.org/10.1039/c7tc05162j]
- Q. He, M. Shahid, J. Wu, X. Jiao, F. D. Eisner, **T. Hodsden**, Z. Fei, T. D. Anthopoulos, C. R. McNeill, J. R. Durrant, and M. Heeney, *Adv. Funct. Mater.* **2019**, 29, 1904956 [doi.org/10.1002/adfm.201904956]

Abbreviations

$°C$	Degrees Celsius
δ	Chemical Shift
ΔH_m	Enthalpy Change of Melting
ε	Dielectric Permittivity and Molar Absorption Coefficient
λ	Wavelength
λ_{max}	Maximum Absorption Wavelength
μ	Mobility
μ_{lin}	Linear Mobility
μ_{sat}	Saturated Mobility
A	Channel Area
$Å$	Ångström
$A-D-A$	Acceptor-Donor-Acceptor
$AlCl_3$	Aluminium Chloride
$APCI$	Atmospheric Pressure Chemical Ionisation
$Ar\text{-}B(OR)_2$	Aromatic Boronic Ester
$Ar\text{-}SnR_3$	Aromatic Trialkyltin
$B3LYP$	Becke, 3-parameter, Lee–Yang–Parr Functional
$BG-BC$	Bottom Gate-Bottom Contact
$BG-TC$	Bottom Gate-Top Contact
BT	2,1,3-Benzothiadiazole
BTz	Benzotriazole
Bu_4NPF_6	Tetrabutylammonium Hexafluorophosphate

$C(CN)_2$	Dicyanomethylene/Malononitrile
$CDCl_3$	Deuterated Chloroform
C_g	Capacitance
CI	Chemical Ionisation
$ClCO_2Et$	Ethyl Chloroformate
CV	Cyclic Voltammetry
DCM	Dichloromethane
DFT	Density Functional Theory
DHAP	Direct (Hetero)arylation Polymerisation
DMDO	Dimethyldioxirane
DMF	*N*,*N*-dimethylformamide
DMSO	Dimethylsulfoxide
DPP	Diketopyrrolopyrrole
DSC	Differential Scanning Calorimetry
$E^{1/2}$	Half-cell Potential
EDG	Electron-donating Group
E^e	Edge Potential
E_{ES}	Electrostatic Interaction Energy
E_g	Energy Gap
E^i	Inversion Point Potential
equiv	Equivalents
E_{SAPT}	Total Interaction
ES – TOF	Electrospray Time-of-Flight
Et	Ethyl
EtOH	Ethanol

eV	Electronvolts
EWG	Electron-withdrawing Groups
f	Oscillator Strength
Fc/Fc^{+}	Ferrocene/Ferrocenium Redox Couple
FET	Field-effect Transistor
HfO_2	Hafnium (IV) Dioxide
HOMO	Highest Occupied Molecular Orbital
Hz	Hertz
I	Current
I_{ds}	Drain Current
IDT	Indacenodithiophene
IDT-di(O)	Indacenodithiophene-4,9-dione
IDTT	Indacenodithienothiophene
IF	Indenofluorene
I_{on}/I_{off}	On/Off Current Ratio
IR	Infrared Spectroscopy
J	Coupling Constant or Joules
K_2CO_3	Potassium Carbonate
KF	Potassium Fluoride
$kcal\ mol^{-1}$	Kilocalories per Mole
KOH	Potassium Hydroxide
L	Channel Length
LC	Liquid Crystal
LUMO	Lowest Unoccupied Molecular Orbital
M	Molarity

m/z	Mass-to-charge Ratio
MALDI	Matrix-assisted Laser Desorption Ionisation
Me	Methyl
meV	Millielectronvolts
mg mL^{-1}	Milligram per Millilitre
$MgSO_4$	Magnesium Sulfate
MHz	Megahertz
mmol	Millimole
N(CN)	*N*-cyanoimine
NFA	Non-fullerene Acceptor
nm	Nanometre
NMR	Nuclear Magnetic Resonance
Nu	Nucleophile
OFET	Organic Field-effect Transistor
OLET	Organic Light-emitting Transistor
OPV	Organic Photovoltaic
OSC	Organic Semiconductor
PCE	Power Conversion Efficiency
$Pd_2(dba)_3.CF$	Tris(dibenzylideneacetone)dipalladium(0)-chloroform adduct
$Pd(PPh_3)_4$	Tetrakis(triphenylphosphine)palladium(0)
POM	Polarised Optical Microscopy
ppm	Parts per Million
PV	Photovoltaics
RSH	Alkyl Thiol

S/D	Source/Drain Electrodes
SAPT	Symmetry-adapted Perturbation Theory
SiO_2	Silicon Dioxide
S_N1	Unimolecular Nucleophilic Substitution
S_N2	Bimolecular Nucleophilic Substitution
S_NAr	Aromatic Nucleophilic Substitution
SO_2R	Sulfone
$SOCl_2$	Thionyl Chloride
t	Dielectric Thickness
^tBuOK	Potassium *tert*-Butoxide
$TCE\text{-}d_2$	Deuterated 1,1,2,2-tetrachloroethane
T_d	Thermal Decomposition Temperature
TD – DFT	Time-Dependent Density Functional Theory
TGA	Thermogravimetric Analysis
TG – BC	Top Gate-Bottom Contact
TG – TC	Top Gate-Top Contact
THF	Tetrahydrofuran
$TiCl_4$	Titanium (IV) Chloride
TLC	Thin-layer Chromatography
T_m	Melting Temperature
TMPMgCl.LiCl	2,2,6,6-Tetramethylpiperidinylmagnesium Chloride Lithium Chloride
UV – Vis	Ultraviolet-Visible
V	Volts
V_d	Drain Voltage

V_g	Gate Voltage
V_t	Threshold Voltage
W	Channel Width
XRD	X-ray Diffraction
ZrO_2	Zirconium (IV) Dioxide

1. Introduction

1.1 Organic Electronics

Semiconductors power the information age we now live in, most notably in the transistors, capacitors, resistors, diodes and miniaturised integrated circuits that comprise our mobile phones, TVs and laptops. Historically, silicon has been used as the semiconductor of choice. It was found that this inorganic, intrinsic semiconductor could be 'doped' into either the p-type or n-type state. By the substitution of some silicon atoms for more electron-deficient atoms (e.g. boron) or electron-rich atoms (e.g. phosphorus) an excess of holes or electrons respectively could be generated.[1] Optimisation of the large-scale manufacture of highly crystalline silicon wafers coupled with device fabrication has enabled silicon-based electronics to dominate the modern world.

Since the discovery that conjugated polymers, such as polyacetylene, also exhibit semiconducting properties, vast amounts of effort has been directed to applying these organic semiconductors (OSCs) to an array of electronic applications, spawning an area generally called 'organic electronics'.[2] OSCs have attracted much attention for use in optoelectronic applications owing to the potential for flexible, lightweight devices where performance can be fine-tuned by means of chemical and processing modifications. In particular, solution-processable OSCs could find use as organic field-effect transistors (OFETs) in applications such as flexible displays and wearable electronics, as well as in emerging fields that include organic thermoelectrics, electrochemical transistors, spintronics and energy storage systems, to name a few.[3,4] The main challenges involve improvements in performance and stability, and the optimisation of fabrication and manufacturing techniques, in conjunction with gaining

a better understanding of the fundamental properties and processes behind how these devices work. The modern field of organic electronics is highly multidisciplinary, with chemists, physicists, materials scientists and engineers all working together to gain a better understanding of charge transport processes, material design and device fabrication. These collaborations foster an interconnected feedback loop where all inform each other, serving to push this field forward.

That being said, it is important to note that organic semiconductors comprise only a subset of the non-silicon-based electronic materials currently in development. Many other inorganic and hybrid materials are competing in this area, including gallium nitride and perovskites, with the latter seeing substantial progress in the area of photovoltaics (PV).[5–8] Each class of materials possess their own advantages and disadvantages. In an increasingly 'smart' and connected world, several of the new technologies may find a place alongside silicon, as applications become ever more demanding and varied.

1.2 Organic Field-Effect Transistors

Transistors are remarkably simple electronic devices that can act as switches (rectifiers) and/or current amplifiers in electronic circuits. Transistors are able to transform a small current into a much larger current. The most intuitive applications of this property are in devices such as loudspeakers or hearing aids, where sounds can be changed into electrical current, which can then be amplified and converted back into much louder sounds. However, the simple application of transistors as electrical switches is the most powerful, providing the basic mechanism for storing and moving data.

The category of transistor popular in organic electronics is the field-effect transistor (FET). These devices exploit the use of an applied electric field to induce the switching behaviour.

FETs usually consist of four main electrical components, namely the gate electrode, the dielectric, the semiconductor and the source/drain electrodes, all deposited onto a substrate in layers. OFETs comprise a device where an organic semiconductor is utilised as the active layer. Commonly, metals such as aluminium, gold and silver are used as gate and/or source/drain electrode materials. Increasingly, one or more the components (electrodes, dielectric and/or substrate) are being replaced for organic equivalents. For example, insulating polymers such as the fluorinated polymer Cytop^{TM} are now routinely employed as dielectric layers.[9–12] Replacement of rigid glass substrates for plastic alternatives are also aiding the path towards flexible electronics.[13–16]

Figure 1 presents one possible transistor architecture, which can be used to outline the key operating principles of FETs. The gate electrode and source/drain electrodes are spatially separated by layers of dielectric (an electrical insulator) and semiconductor. Potential applied at the gate electrode ultimately controls if current will flow between source and drain electrodes, through the semiconductor. Crucially, the gate electrode and semiconductor are not connected directly, meaning that no current flows between the two. The potential at the gate electrode creates an electrical field that is felt by the semiconductor, which induces charge carriers to be accumulated in the semiconductor layer.[17] These charge carriers accumulate at the semiconductor-dielectric interface, providing a transport channel when a potential difference is applied between the source and drain electrodes.

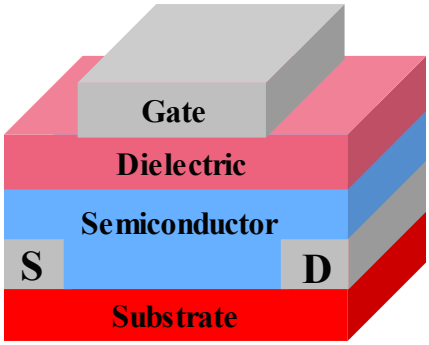


Figure 1: Possible FET Architecture (top-gate, bottom-contact, TG-BC).

To explain this further, take the case of a transistor using an n-type (electron transporting) semiconductor layer. The operating procedure would be as follows:

1. Positive bias is applied at the gate electrode
2. Electric field induced through the dielectric attracts electrons in the semiconductor layer
3. Electrons accumulate at the semiconductor – dielectric interface
4. Potential difference is applied across the source – drain electrode
5. Current flows across the semiconductor between source and drain electrodes
6. Removal of gate and/or source – drain biases
7. Current stops flowing across semiconductor

No current will flow, and the device be in an 'off' state, unless the appropriate gate and source/drain biases are applied (both positive for n-type).

Device performance is inferred by analysing transfer and output curves, which show the effect of gate bias (V_G) and drain bias (V_D) respectively on the source/drain current (I_{DS}). Transfer characteristics are generated by plotting the change in I_{DS} with V_G (while keeping V_D constant) (**Figure 2a**). Sweeping V_D (while keeping V_G constant) will give the output characteristics

(**Figure 2b**). These allow the extraction of the two key performance indicators, charge carrier mobility (μ) and threshold voltage (V_T), applying the gradual channel approximation.[18]

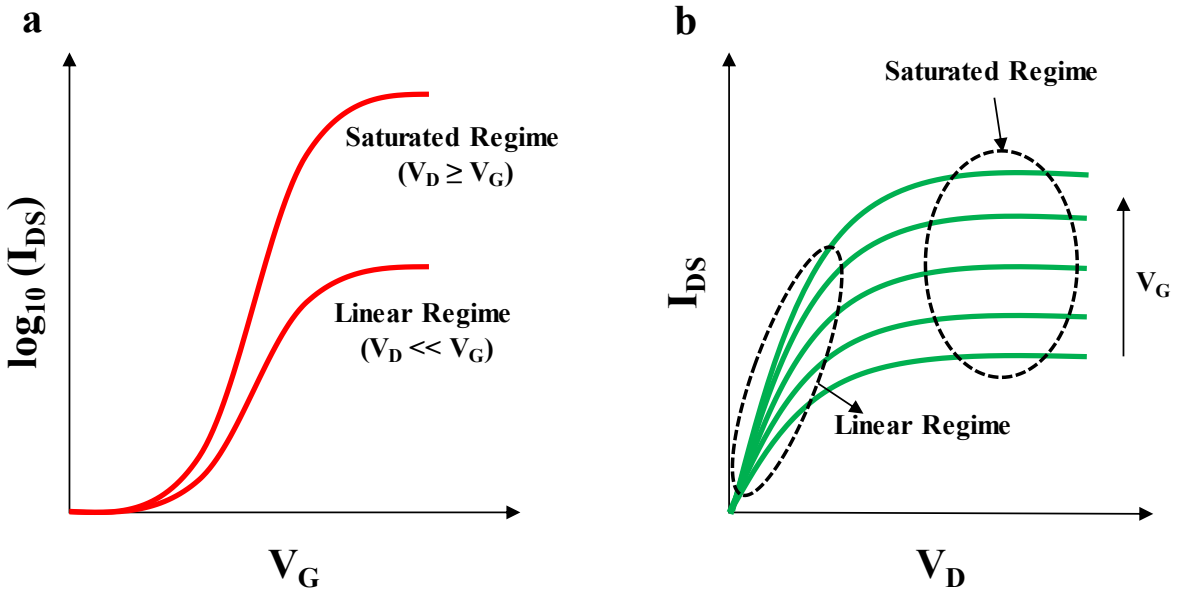


Figure 2: Typical a) Transfer curve and b) Output curve for an n-type OFET.

FET devices can operate in two distinct regions depending on the relative magnitude of V_G and V_D applied. When $V_D << V_G$, the devices are said to operate in the 'linear regime'. In this region I_{DS} increases linearly with increasing V_D (at a constant V_G) and can be expressed using **Equation 1**. The linear mobility (μ_{lin}) can be extracted from the first derivative of the transfer curve, using **Equation 2**.

$$I_{DS\,(saturated)} = \frac{WC_G\mu(V_G - V_T)V_D}{L} \qquad \textbf{Equation 1}$$

$$\mu_{sat} = \frac{L}{WC_GV_D}\frac{\partial I_{DS}}{\partial V_G} \qquad \textbf{Equation 2}$$

As V_D increases further and $V_D \geq V_G$, the device enters the saturated regime where I_{DS} becomes independent of V_D. This can be explained by a 'pinching off' of the channel due to a large potential drop across source/drain electrodes. These conditions are now better described by

Equation 3. In this case, the saturated mobility (μ_{sat}) can be extracted from the derivative of the $\sqrt{I_{DS}}$ vs V_G curve, using **Equation 4**.

$$I_{DS\,(saturated)} = \frac{W C_G \mu (V_G - V_T)^2}{2L} \quad \textbf{Equation 3}$$

$$\mu_{sat} = \frac{2L}{W C_G} \frac{\partial \sqrt{I_{DS}}}{\partial V_G} \quad \textbf{Equation 4}$$

In an ideal transistor, μ_{lin} and μ_{sat} should be equal. However, μ_{sat} is often found to be markedly larger than μ_{lin}, particularly in the case of transistors using polymeric semiconductors. In many cases, I_{DS} does not fully saturate with increasing V_G in the 'saturated' region but continues to gradually increase. This may be attributed to the filling of deeper-lying trap states (present due to conformational/energetic disorder of the thin-films) at the higher voltages.[19]

There are many factors that influence the performance of transistors – materials, device fabrication and architecture, and operating conditions. Optimal devices will allow a large current to be drawn with minimal applied voltage. Ideally, ohmic contacts between the source/drain electrodes and the semiconductor are desired to allow effective charge injection and transport. However, there is usually some contact resistance. This can be explained by differences in energy between the work function of the metal electrodes and the energy levels of the frontier molecular orbitals of the semiconductor, which cause a barrier to charge injection.

The function of the dielectric is to act as a capacitive surface where charge can accumulate when a voltage is applied at the gate electrode. Capacitance across the interface depends on the permittivity of the dielectric (ε) and the area of the channel ($A = L$ x W), while inversely on the thickness of the dielectric (t, separation between gate electrode and semiconductor).[20]

$$C_G = \frac{A\varepsilon}{t} \quad \textbf{Equation 5}$$

A larger capacitance means that a higher density of charge carriers will be generated for a given gate voltage, enabling a larger current to by drawn from the device. The easiest way to improve the capacitance is therefore to simply make the dielectric thinner, which can be achieved by optimisation of deposition techniques. Having said that, at a particular thickness, the dielectric will break down and charge will be able to tunnel between gate electrode and semiconductor. This is detrimental to the transistor performance since this current leakage will hinder the switching capabilities of the transistor. The minimum thickness is dictated by the permittivity of the dielectric. Historically, the chosen dielectric in silicon-based transistors is SiO_2 due to the ease of formation on top of the doped silicon gate electrode (by simple oxidation). This was a dominant factor in the use of silicon over other semiconductors. Modern methods have pushed SiO_2 dielectric layers to the limit in terms of thickness and acceptable current leakage. Hence, to achieve thinner devices while maintaining or improving capacitance has required materials with higher dielectric constants to be developed. Examples include simple analogues of SiO_2 such as ZrO_2 or HfO_2, as well as a variety of polymer-based dielectrics.[21]

Optimisation of the physical and electrical properties of the organic semiconductor are needed to improve the intrinsic carrier mobility capabilities of these materials. This is the area where chemists can have the most impact, and involve tuning the energy levels, coplanarity/rigidness, solubilities, thermal stabilities etc. See Section 1.4 for further discussion.

There are a variety of possible FET architectures (**Figure 3**). Each will influence the performance as well as posing different challenges to fabrication. The bottom-gate/top-contact architecture (BG – TC) is considered as offering lower contact resistance, suggested by a better penetration of the metal source/drain electrode layers into the semiconductor layer (improving interface morphology). This could be as a result of the need to thermally evaporate the electrodes onto the sensitive organic semiconductor layer. Bottom-gate/bottom-contact (BG –

BC) devices are easier to fabricate since the least-stable organic semiconductor can be solution deposited last. However, this can usually result in poor interface morphology between the source-drain electrodes and the OSC, resulting in poorer charge injection.[22]

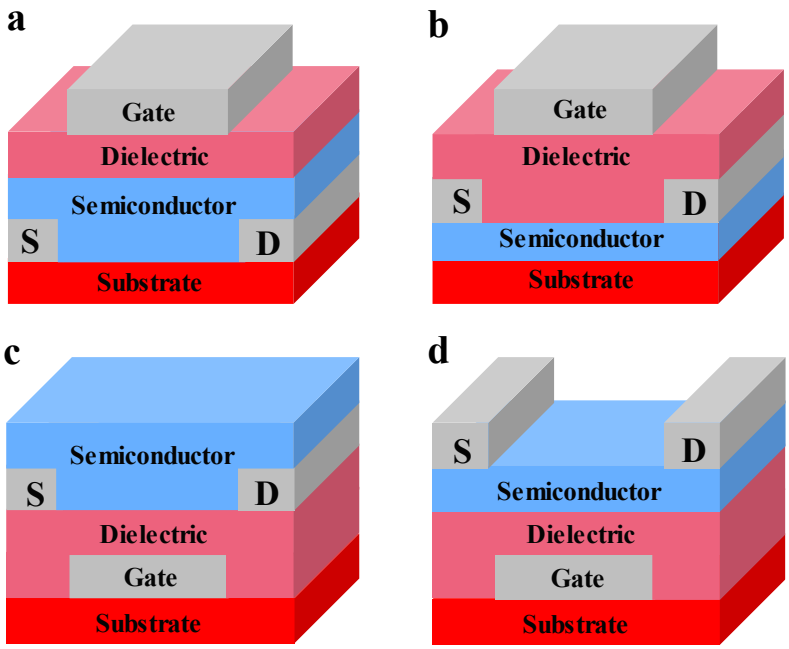


Figure 3: Common FET Architectures. a) top-gate/bottom-contact (TG-BC), b) top-gate/top-contact (TG-TC), c) bottom-gate/bottom-contact (BG-BC) and d) bottom-gate/top-contact (BG-TC).

Charge carriers are only accumulated at the semiconductor – dielectric interface, in the path between the source and drain electrodes. Consequently, the dimensions of this path area will also affect the performance of the transistor. The length between the source and drain electrodes (L) should ideally be as small as possible. This will mean that charge carriers generated in this region will have a shorter distance to move from source to drain electrodes, resulting in a higher possible current. Additionally, a minimisation of this length will improve the switching rate of the transistor, since this is inversely proportional to the time which it takes for the charges to move between electrodes. A physical limit on the minimum channel length is usually imposed by the ease of fabrication. At very short channel lengths it becomes difficult to deposit source and drain electrodes so close to each other with high precision. Short channel lengths can also

result in increased contact resistance. The channel width (W) on the other hand, will ideally be as large as possible. A wider channel provides a larger semiconductor-source/drain electrode contact area, normal to the direction of transport. This will allow injection of a higher density of charge carriers from the source electrode, as well as a generation of a higher density of charge carriers, via the application of a gate voltage, both resulting in a higher current. As seen in **Equation 5**, the path area also affects the capacitance. As a result, a trade-off between the W/L ratios need to be considered.

It has also been shown extensively that post-deposition thermal annealing of the semiconductor layer can lead to marked improvements in carrier mobilities. Common solution deposition techniques, such as spin coating or blade coating, lead to fast thin-film formation. This can result in disordered films with suboptimal morphology. Thermal annealing allows the OSC molecules to reorganise into more ordered, thermodynamically-favoured arrangements, which helps charge transfer.[23–25] As a result, this processing step is widely utilised to achieve optimised device performance. Having said that, high annealing temperatures are undesirable at an industrial level due to higher energy consumption.

Applying a higher gate voltage will create a higher density of charge carriers at the semiconductor – dielectric interface, allowing a larger current to be drawn. Equally, applying a larger potential difference across the source-drain electrodes will have the same effect. Ideally, power consumption is desired to be as low as possible while optimising performance. Therefore, both gate and source/drain voltages need to be as small as reasonably possible meaning performance improvements need to be achieved in other ways.

1.3 Charge Transport in OSCs

There are fundamental differences between the way in which inorganic (e.g. silicon) and organic semiconductors transport charge through the bulk material. This results primarily from the differences in disorder and dimensionality in the respective systems. Inorganic semiconductors form very highly crystalline, ordered structures, connected by strong covalent bonds. This long-range positional ordering leads to highly delocalised molecular states, allowing a band-type regime to be considered. As a result, charge carriers generated in these systems can be considered to be delocalised over the whole structure and are transported via this band regime. There is negligible coupling to the crystalline structure itself, and charge carriers can be considered as free charges.

In contrast, OSCs exist as molecular solids, where discrete covalently-bonded molecular or polymer units aggregate in the solid state via weaker intermolecular interactions (e.g. electrostatic, dispersion or induction). This results in increased disorder and reduced dimensionality, introducing significant anisotropy. The consequence of this are that electronic states are far more localised, and the coupling of the states to the molecular or polymer units needs to be considered. In this case, a band-type description is no longer appropriate. Placing charges on these units creates local distortions in the bond angles and bond lengths, creating phonons. Charges can no longer be considered free but instead exist as coupled charge – phonon quasiparticles known as polarons (e.g. negative polaron = negative charge + phonon). The charge carriers will move freely along the conjugated region of a single molecular or polymer unit but will have to hop between different units for longer range transport in the bulk. This hopping will be rate-limiting for the charge transport and is influenced by the relative order of the units and the relative interactions between units.[26] Such charge hopping requires thermal activation, meaning hopping efficiency increases with temperature.

Akin to the inorganic description, OSCs are commonly classified as p-type or n-type depending on their ability to transport holes or electrons respectively. This distinction is predicated on the relative energies of the frontier molecular orbitals – relative to the S/D electrode work functions and the HOMO/LUMO energy level gap – as well as the distribution of the orbitals across the molecular or polymer unit, with holes being injected into the HOMO and electrons into the LUMO. Unlike the inorganic description, these properties are somewhat more flexible, with many OSCs being intrinsically ambipolar.[27] Instead, dominant charge carriers in OSCs are usually device-dependent, where they are largely reliant on device properties such as the work functions of electrodes and interfacial properties.[28–30]

1.4 Designing OSCs for OFETs

The design of OSCs for all organic electronic applications is centred around control of the energies of the frontier molecular orbitals and the distribution of these orbitals in the π-conjugated system. These two features play decisive roles in intra- and intermolecular charge transport, light absorption/emission, charge injection/extraction/trapping and electrochemistry. The breadth of organic chemistry provides scope for materials chemists to tune these properties by careful manipulation of the chemical structures, dictated by the intended application.

For instance, the demands of an OSC for OPV applications are markedly different from that for OFET applications (the focus of this thesis) by account of the different working principles of each device. In the case of OPV, at least two OSCs comprise the active layer (usually termed the ‘donor’ unit and ‘acceptor’ unit), primarily in a bulk heterojunction arrangement. The donor and acceptor need to absorb light well in the visible region, ideally with good complementarity, to enable efficient photoexcitation to generate excitons. These bulk heterojunctions need to be designed to allow optimal charge transfer through the respective OSCs to the interface, which

also needs to be optimised to ensure efficient charge separation to generate free carriers (holes and electrons). Finally, good alignments of energy levels between frontier molecular orbitals and electrodes are required for efficient charge extraction. Charge generation, charge separation and charge extraction are all dictated by the intricate interplay between the frontier molecular orbitals and orbital distribution in the OSC layers.[31–33]

In comparison, the demands of an OSC for OFETs can be regarded as somewhat less complex. Firstly, the optical properties are usually not important, since charge carriers are instead injected from the electrodes. Exceptions to this include organic light-emitting transistors (OLETs) and optical transistors, where light emission and light absorption respectively do need to be considered.[34–38] Additionally, basic OFET devices comprise a single OSC active layer, meaning the complexities of bulk heterojunction design are absent. Again, there are exceptions, including with various polymer – small molecule blended OFETs, where high performance has been reported.[39–42]

Having said this, the charge mobility requirements for OFETs far exceed that for OPV, due to the necessity for high currents and fast switching. Resultingly, the sensitivity of charge mobility to the π-π interactions within the molecular solid means there are strict requirements regarding the crystallinity. High transfer integrals and low reorganisation energies favour rigid, highly ordered systems.[26,43,44] In addition to this, molecular orientation of the OSC at the OSC – dielectric interface in the active channel, as opposed to the bulk, is considered to dominate charge transport properties.[45–47] This ordering can be controlled by careful interface engineering.[48,49] Finally, as with all organic electronic applications, appropriate energy alignment between frontier molecular orbitals of the OSC and electrode work functions is needed for efficient charge injection by limiting contact resistance.

While the majority of high-performing OFETs are comprised of p-type OSCs, n-type OSCs are far less numerous.[50,51] New n-type OSCs are eagerly sought for use in devices such as complementary circuits and OPVs, where balanced charge transport between the n-type and p-type components is crucial.[52–55] OSCs for n-type applications are generally considered to require a deep LUMO energy level, often quoted as below - 4 eV, to enable good charge injection from the metal electrode and to impart ambient stability of the reduced species.[56–58] These strict demands illustrate why n-type performance appears to lack behind p-type. High mobilities of > 10 $cm^2 V^{-1} s^{-1}$ for OFETs using n-type molecular OSCs have been reported on a couple of occasions.[59,60] However, doubts surround the true validity of these values, due to issues with the rigorous, standardised extraction of mobilities that has plagued this field.[61–66] In reality, mobilities of ~ 1 $cm^2 V^{-1} s^{-1}$ appear more reliable.

Materials chemists can manipulate the frontier molecular orbital energies of OSCs via a variety of approaches. The first is by modification of the π-conjugated core itself. The relative energies of the frontier molecular orbitals can be modified by changing the number of π-electrons in the system and by the extent to which this π-system can be delocalised. For instance, the classic example of acenes illustrates how extending the π-system leads to modification of the HOMO and LUMO energy levels, proceeding from benzene to tetracene and pentacene, both of which have been shown to endow high performing OFETs. See Chapter 6 for further discussion on π-extension.

Beyond this, an array of heteroaromatic units can be used to further control the frontier molecular orbital energies, including 6- and 5-membered units such as pyridine, thiophene, furan and thiazole (**Figure 4**).[67–74] Pyridyl units can be viewed as electron-poor analogues of benzene due to the presence of the electronegative nitrogen in the ring, which can lower both the HOMO and LUMO energy levels by increasing the solid-state electron affinity.

Conversely, 6 π-electron/5 centre units such as thiophene and furan can be viewed as electron-rich variants, which can raise the HOMO by decreasing the solid-state ionisation potential. Furthermore, these 5-membered heteroaromatics exhibit lower aromatic stabilisation energies, allowing more effective delocalisation of the π-system.

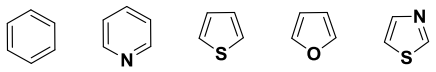


Figure 4: Commonly used (hetero)aromatic units.

Furthermore, electron-donating (EDG) or electron-withdrawing (EWG) functional groups can be incorporated onto the π-conjugated cores (**Table 1**). EDGs donate electron density into the π-system, which can raise the HOMO. This is achieved either mesomerically or inductively. Mesomerically donating groups are able to donate electron density into the π-system by either π-π or π-lone pair interactions. Examples include lone pair donation from N, O or S heteroatoms. Inductively donating groups influence the electron density in the π-system by means of electropositivity. An example is alkyl chains. Conversely, EWGs can act to lower both the HOMO and LUMO energy levels. Examples include F, C(O)R and C≡N groups. Mesomeric effects are usually larger than inductive effects owing to the direct interaction with the π-system. Many functional groups contribute a mix of mesomeric and inductive effects.

Table 1: Common electron-donating (EDG) and electron-withdrawing (EWG) groups.

EDG	*EWG*
-OR	**-F, -Cl, -Br**
-SR	**-C(O)R**
-NR_2	**-CO_2R**
-CR_3	**-CN**

As one can imagine, judicious selection of the type of (hetero)aromatic core as well as the nature, number and/or position of EDGs/EWGs will influence the solid-state packing. This is

due to changes in intermolecular interactions between π-conjugated units brought about by alterations to the frontier molecular orbital distributions and steric effects.[44,75] For example, introduction of favourable intermolecular interactions (e.g. O···H or N···H) can promote planarity by 'locking' torsion at single bonds, reducing reorganisation energy. Additionally, similar intermolecular interactions between different molecular or polymer units can promote close π-π interactions for improved charge transfer.[76–78] Inclusion of alkyl side-chains are common to promote organic solvent solubility for solution-processing. Such alkylation can have profound impacts on the way in which the molecular or polymer units aggregate, for example by introducing alkyl···alkyl dispersion interactions leading to interdigitation.[79,80] See Chapter 3 for further discussion.

The ability of material chemists to affect the smallest changes to the properties of OSCs is often lauded as one of the major advantages versus their inorganic counterparts. This is certainly the case; however, it is worth noting that this ability also introduces added complexity. Especially, accurate prediction of the impact of structural changes on the solid-state ordering is often still lacking. This is particularly the case as the chemical structures of new OSCs become ever more complex. Prediction of frontier molecular orbital energies and distribution by computational methods is now commonplace, though extension of this methodology to simulate the bulk properties is so far still problematic.[81]

1.5 Use of IDT in Organic Electronic Devices

OSCs designed for OFET applications require π-conjugated backbones as well as close intermolecular π-π stacking interactions to facilitate efficient charge transport, by maximisation of orbital overlap. One attractive approach towards such materials has been the fusion of aromatic moieties into rigid, ladder-type systems.[82] The high rigidity minimises

reorganisation energy by reduction of torsional disorder, as well improving intra- and intermolecular charge delocalisation. However, these modifications inherently reduce processability, meaning careful selection of the nature and position of suitable alkyl side-chains needs to be considered to improve solution-processability while maintaining favourable charge transport properties.[83]

Amongst the various reported ladder-type systems, OSCs incorporating IDT have demonstrated particular promise.[84–86] These units can be viewed as thiophene-containing analogues of the widely investigated indenofluorenes (IF) (**Figure 5**).[87,88] High performance has been related to the fused, highly rigid nature of the IDT and good processability by facile alkylation at the bridging points. When IDT is used as a building block for polymers, the terminal thienyl units help to reduce torsional twisting with adjacent comonomers, facilitating backbone planarisation.[89] Thienyl units provide the added benefit of exhibiting more quinoid-like character (due to a reduced aromaticity), which further promotes coplanarity and charge delocalisation, as well as improving solid-state packing by the introduction of sulfur-based intermolecular interactions.[90,91]

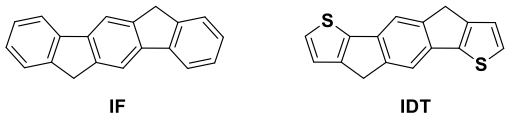


Figure 5: Structures of Indenofluorene (IF) and Indacenodithiophene (IDT).

The IDT core is naturally electron-rich, in part due to the presence of two fused thienyl units. This has led to wide applicability of IDT and its analogues for p-type applications. Specifically, donor – acceptor copolymers utilising IDT as the donor unit have been widely explored for use in OPV and OFET applications. Polymers obtained by coupling IDT with various 2,1,3-benzothiadiazole (BT) units have proven popular (**Figure 6**).[86,92] These polymers enabled power conversion efficiencies (PCEs) up to 7.5 %.[93,94] Recently, attention has moved away

from IDT-based donor polymers to the use of more elaborate structures to achieve higher PCEs (> 10 %).[95,96] IDT – BT copolymers incorporating linear alkyl side-chains have been reported with hole mobilities up to 3.6 cm^2 V^{-1} s^{-1}, while copolymers based on indacenodithienothiophene (IDTT)-BT exhibited hole mobilities up to 8.7 cm^2 V^{-1} s^{-1} in OFET devices.[84,97,98]

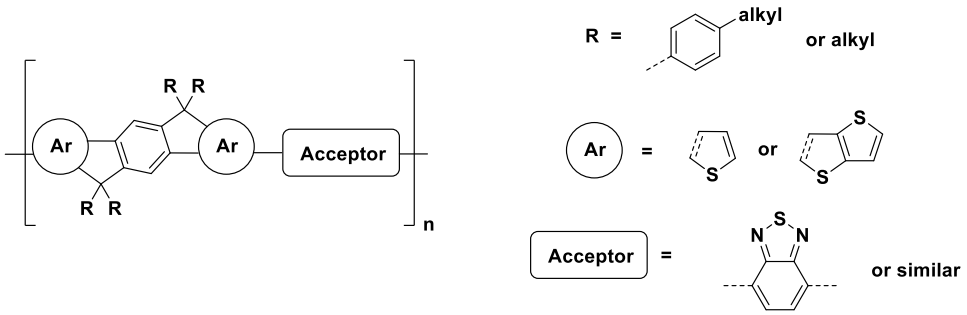


Figure 6: General structure of common IDT-based copolymers (dashed lines indicate where groups are connected to the general structure).

Research into non-fullerene acceptors (NFAs) for OPVs has boomed in the last 5 years or so. Much recent success has been seen using molecular units with an acceptor – donor – acceptor (A – D – A) arrangement. Such NFAs incorporating IDT and its analogues as the donor unit emerged as popular frameworks, enabling high efficiency devices to be fabricated. The general structure is shown in **Figure 7**. High performance is primarily thought to be driven by strong absorption, narrow bandgap and enhanced self-aggregation properties imparted by the IDT unit. NFAs incorporating IDTT as the donor unit were until very recently the highest-performing class, boasting PCEs above 10 %.[99–101] A number of review articles have been published giving an extensive overview of this area.[102–104] IDT-based A – D – A molecules have also recently been shown to display promising OFET performance.[105,106] See Chapter 2 for further discussion.

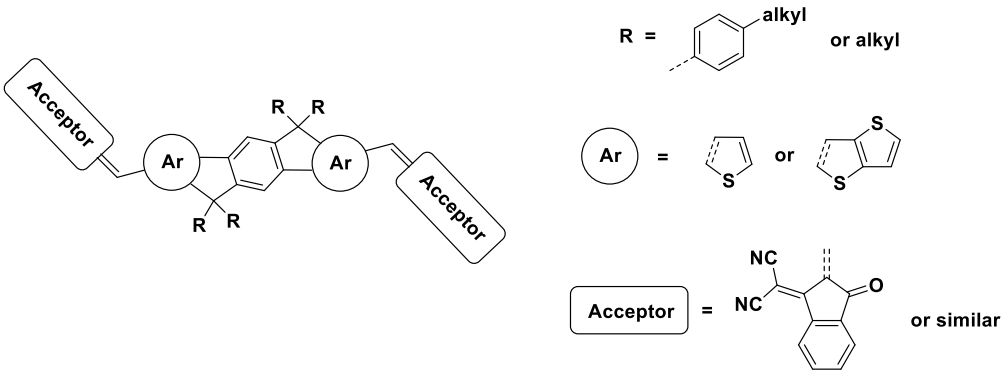


Figure 7: General structure of common IDT-based NFAs (dashed lines indicate where groups are connected to the general structure).

Up until very recently, IDT has been predominantly accessed through a multi-step ring-closure route (**Figure 8**).[107] In particular, the final step involves the reduction of indaceno[1,2-b:5,6-b']dithiophene-4,9-dione (**IDT-di(O)**). As research focus has shifted to the search for higher performing n-type OSCs, electron-deficient cores such as **IDT-di(O)** appear as promising candidates.

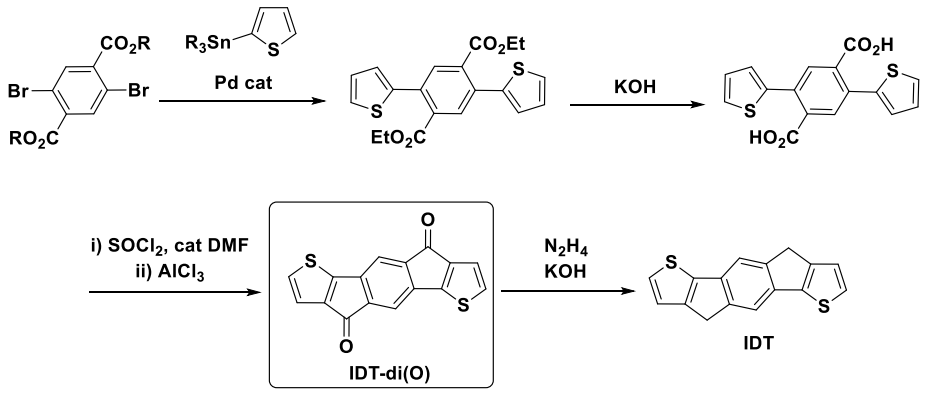


Figure 8: Common synthetic route to IDT.

1.6 Thesis Aims and Overview

This thesis will focus predominantly on modifications to **IDT-di(O)** in order to access novel n-type molecular semiconductors (Chapters 2 – 5). Detailed analyses of optoelectronic properties (UV-Vis), electrochemical properties (CV) and physical properties (TGA, DSC,

XRD, POM) as well as device performance (OFET) are performed so as to investigate the complex relationships between molecular structure, material properties and device performance.

In Chapter 2, fluorination is exploited as a tool to alter the electronic and physical properties of promising n-type OSCs, **2,7-dihexyl-IDT-di(O)** and **2,7-dihexyl-IDT-di(C(CN)$_2$)** (**Figure 9**). Fluorination is widely utilised in the literature to tune the LUMO energy levels of OSCs, due to the highly electronegative nature of fluorine, whilst also influencing crystal packing, due to the introduction of fluorine-based intermolecular interactions (e.g. S···F). Specifically, fluorination of the central phenyl unit is achieved by accessing a novel fluorinated precursor.

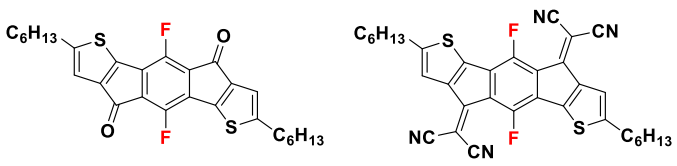


Figure 9: Chemical structures of 2,7-dihexyl-diFIDT-di(O) (left) and 2,7-dihexyl-diFIDT-di(C(CN)$_2$) (right).

Encouraged by the findings outlined in Chapter 2, Chapter 3 directs attention to the role of the alkyl side-chains in **dialkyl-diFIDT-di(O)** and **dialkyl-diFIDT-di(C(CN)$_2$)** (**Figure 10**). This is approached in three ways – chain extension, chain branching and chain regiochemistry – to provide a comprehensive investigation into the impact of the side-chains. The synthetic approach developed in Chapter 2 is adapted to generate 2,7-didodecyl-, 2,7-bis(2-ethylhexyl)- and 3,8-dihexyl- analogues. The primary motivation was a potential improvement to material processing, in an effort to advance the device performance.

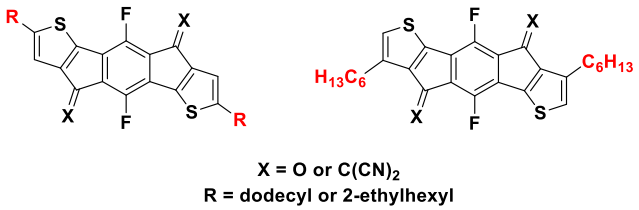


Figure 10: Chemical structures of dialkyl-diFIDT-di(O) and dialkyl-diFIDT-di(C(CN)$_2$) bearing different alkyl side-chains.

In Chapter 4 we explore the use of an alternative to dicyanomethylene as an electron-withdrawing group (EWG) at the 4,9-bridging positions, namely *N*-cyanoimine (**Figure 11**). The *N*-cyanoimine group was attractive as it has been shown to be effective at stabilising the LUMO energy level, whilst also being less sterically demanding, potentially enabling improved planarity. The synthesis of **dialkyl-diFIDT-di(N(CN))** analogues bearing 2,7-dihexyl-, 2,7-bis(2-ethylhexyl)- and 3,8-dihexyl- side-chains enabled the effect of fluorination as well as alkyl side-chains on electronic properties, physical properties and device performance to be investigated.

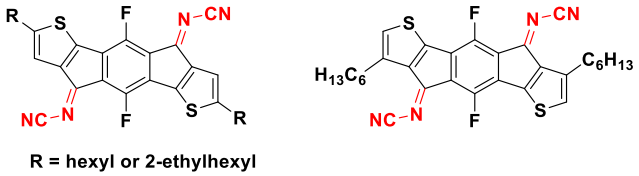


Figure 11: Chemical structures of dialkyl-diFIDT-di(N(CN)) bearing different alkyl side-chains.

Chapter 5 explores further modifications to the **dialkyl-diFIDT-di(O)** unit at two positions (**Figure 12**). Firstly, development of a methodology for end-functionalisation of **3,8-dihexyl-diFIDT-di(O)** by direct (hetero)arylation exploiting C-H activation is examined, yielding the novel **2,7-bis(4-benzonitrile)-3,8-dihexyl-diFIDT-di(O)**. Direct (hetero)arylation has become a popular alternative to classical cross-couplings (e.g. Stille and Suzuki), primarily due to avoidance of the need for pre-functionalisation. This allows a reduction in the number of synthetic steps as well as circumventing the use of toxic reagents. The second half of this

chapter focuses on functionalisation of the aromatic core by nucleophilic aromatic substitution. Substitution by thiol groups as well as subsequent thiol oxidation are achieved to modify the electronic and physical properties.

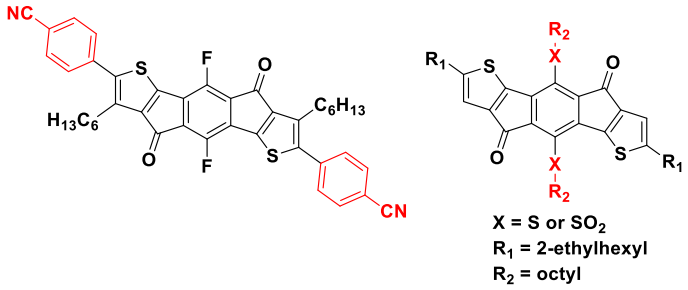


Figure 12: Chemical structures end-functionalised (left) and core-substituted (right) dialkyl-diFIDT-di(O) analogues.

Lastly, in Chapter 6 we focus on the synthesis and characterisation of a novel class of highly π-extended fused nonacycles based on IDT (**Figure 13**). Alkylation at the bridging points on the central IDT moiety permits wide scope for controlling material processability and functionalisation at the peripheral bridging points allows effective tuning of the energy levels.

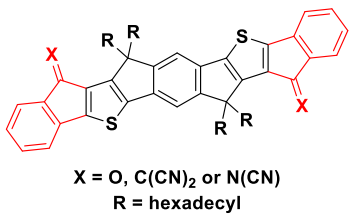


Figure 13: Chemical structure of the IDT-based nonacycle bearing different EWGs.

2. Core Fluorination of 2,7-dihexyl-IDT-di(C(CN)$_2$)

Figures and text in Chapter 2 are reproduced with permission from ['*Core Fluorination Enhances Solubility and Ambient Stability of an IDT-Based n-Type Semiconductor in Transistor Devices'* Thomas Hodsden, Karl J. Thorley, Julianna Panidi, Aniruddha Basu, Adam V. Marsh, Haojie Dai, Andrew J. P. White, Changsheng Wang, William Mitchell, Florian Glöcklhofer, Thomas D. Anthopoulos and Martin Heeney, *Adv. Funct. Mater.*, 2020, 2000325, doi.org/10.1002/adfm.20200032]

2.1 Introduction

Based on the high performance of IDT as a p-type OSC, there have been to attempts modify the core for use in n-type applications. The inherently electron-rich nature of IDT results in a high lying LUMO energy level making it a poor candidate for n-type transport. This can be improved however by the introduction of strong EWGs which act to depress the LUMO energy level. Introduction of EWGs at the terminal thienyl units have been explored in acceptor – donor – acceptor (A – D – A) NFAs for use in organic solar cells (**Figure 14a**).[92,103] Several reports have also shown that these IDT-based NFAs display promising performance in thin-film transistor applications.[105,106] Alternative attempts have focussed upon chemically modifying the core via the introduction of strong EWGs at the 4,9-bridging positions of the IDT backbone (**Figure 14b**). Work by Zhao et al., Tian et al. and more recently Peltier et al. has explored the use of carbonyl bridge IDTs (**IDT-di(O)**) in OFETs.[108–110] It has been shown that vacuum-processed devices of 2,7-dihexyl-s-indaceno[1,2-b5,6-b']dithiophene-4,9-dimalononitrile (**2,7-dihexyl-IDT-di(C(CN)$_2$)**) exhibited unipolar electron mobility up to 0.33

$cm^2V^{-1}s^{-1}$. With the bridging positions occupied by the EWGs, hexyl solubilising side-chains were placed at the terminal thienyl units. A low density of alkyl chains (2 alkyl chains per molecule) coupled with an in-plane configuration (owing to positioning of the alkyl chains at a sp^2 C) led to the material being poorly soluble in common organic solvents. This is in contrast to the highly soluble IDT materials with alkylation at the bridging point (4 alkyl chains per molecule, sp^3 C, out-of-plane). As a result, **2,7-dihexyl-IDT-di(C(CN)$_2$)** was unsuitable for device processing from solution. Solution processing is highly desirable due to the low processing temperatures and high scalability compared to vacuum processing. The devices were further noted to exhibit poor stability in ambient conditions before interface engineering.

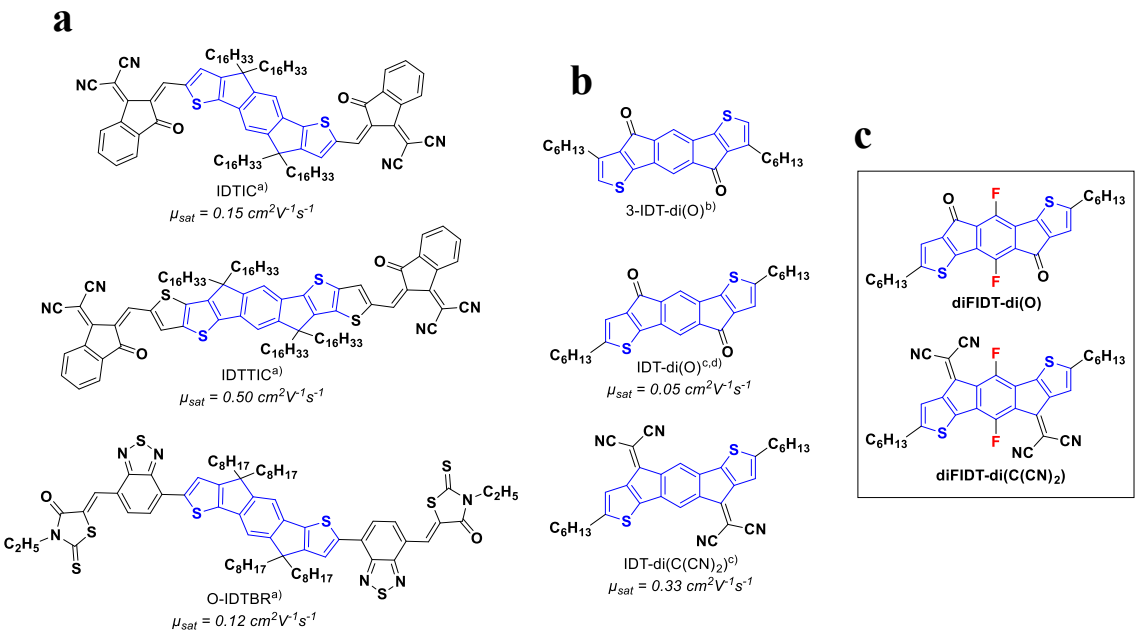


Figure 14: Chemical structures of previously reported n-type IDT-based small molecules for OFETs. a) end-modified IDT. b) bridge-modified IDT. This work: c) 2,7-dihexyl-diFIDT-di(O) and 2,7-dihexyl-diFIDT-di(C(CN)$_2$). [a)]solution-processed, [b)]mobility not reported, [c)]vacuum-processed, [d)]hole mobility.

Halogenation, in particular fluorination, has been widely explored in the literature as another tool to tune the properties of OSCs.[111,112] The introduction of strongly electronegative fluorine groups has been shown to be an effective strategy for stabilising the LUMO energy levels.[113–

[116] In addition, fluorination often helps to promote inter- and intramolecular interactions via a range of non-covalent interactions.[91,99,117,118] Owing to the small van der Waals radius, fluorination is highly attractive as these benefits can usually be achieved without the disruption to backbone planarity from the introduction of undesired steric clashes.

As such, the motivation of this project was to explore core fluorination as a route to improving the performance of **2,7-dihexyl-IDT-di(C(CN)$_2$)** (**Figure 14c**). Density functional theory (DFT) calculations using the B3LYP level of theory and 6-311+G(d,p) basis set were performed for **2,7-dialkyl-diFIDT-di(O)** and **2,7-dialkyl-diFIDT-di(C(CN)$_2$)** to probe the potential impact of fluorination on conformation and HOMO/LUMO energy levels. Optimisation and frequency calculations were carried out to ensure global minima were reached. The hexyl side-chains were replaced with methyl chains to reduce computational time. As shown in **Figure 15**, fluorination was shown to have little impact on the planarity of the IDT core which is important for maintaining good π-π stacking. The HOMO/LUMO energy levels were predicted to be - 6.07 eV/- 3.55 eV and - 6.40 eV/- 4.47 eV for **2,7-dialkyl-diFIDT-di(O)** and **2,7-dialkyl-diFIDT-di(C(CN)$_2$)** respectively compared to - 5.84 eV/- 3.26 eV and - 6.24 eV/- 4.24 eV for **2,7-dialkyl-IDT-di(O)** and **2,7-dialkyl-IDT-di(C(CN)$_2$)**. This indicated that core fluorination should also depress the LUMO energy level (~ 0.2 – 0.3 eV), helping to stabilise the reduced state in ambient conditions.

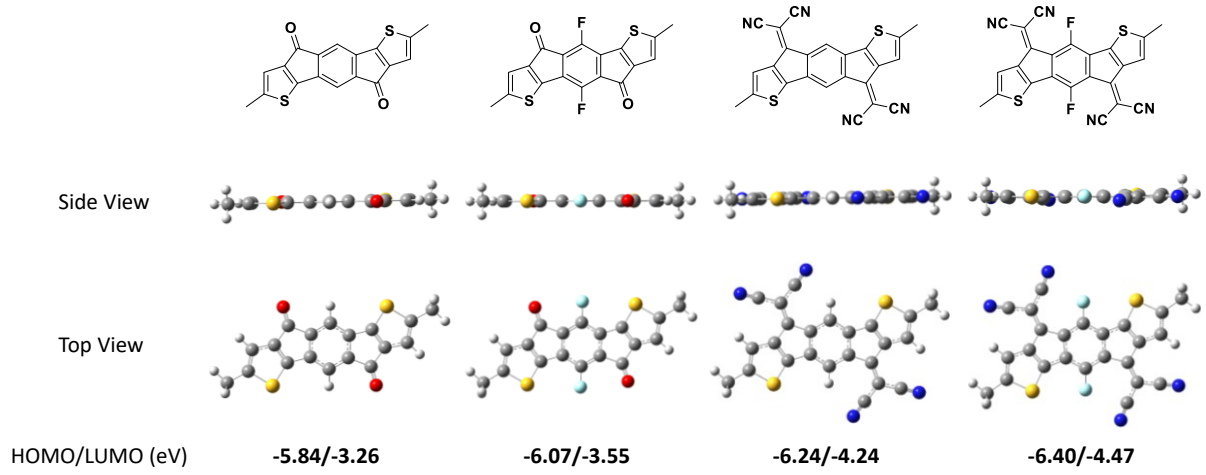


Figure 15: Optimised Structures for 2,7-dialkyl-diFIDT-di(O) and 2,7-dialkyl-diFIDT-di(C(CN)₂), along with the non-fluorinated analogues for comparison, calculated by DFT,

Two new fluorinated OSCs, namely **2,7-dihexyl-diFIDT-di(O)** and **2,7-dihexyl-diFIDT-di(C(CN)₂)** are synthesised. The effect of core fluorination is investigated by analysis of physiochemical properties and device performance.

2.2 Synthesis

2,7-Dihexyl-5,10-difluoro-s-indaceno[1,2-b5,6-b']dithiophene-4,9-dimalononitrile (**2,7-dihexyl-diFIDT-di(C(CN)₂)**) was synthesised following a route modified from the reported synthesis of the non-fluorinated analogue, **2,7-dihexyl-IDT-di(C(CN)₂)** (**Figure 16**).[109,110] The critical step was the formation of the hexa-substituted benzene derivative, diethyl 2,5-dibromo-3,6-difluoroterephthalate (**[2]**). After some experimentation it was found that 1,4-dibromo-2,5-difluorobenzene (**[1]**) could be doubly deprotonated by the Knochel-Hauser base, 2,2,6,6-tetramethylpiperidinylmagnesium chloride lithium chloride, at - 40 °C. Subsequent reaction with ethyl chloroformate afforded the desired product in 30 % yield.[119,120] The bromo substituents were subsequently utilised in a Stille cross-coupling with trimethyl(5-hexylthiophen-2-yl)stannane (**[3]**) using tetrakis(triphenylphosphine)palladium(0) to afford diethyl 2,5-difluoro-3,6-bis(5-hexylthiophen-2-yl)terephthalate in high yield (**[4]**) (83 %) after

purification by silica gel chromatography. Saponification with KOH in ethanol afforded a quantitative conversion to the diacid (**[5]**), which was converted to the acid chloride by treatment with $SOCl_2$ in DCM in the presence of a catalytic amount of DMF. After solvent removal, the resulting water-sensitive material was used directly without purification.

Ring closure was achieved by a Lewis acid-promoted intramolecular Friedel-Crafts acylation with $AlCl_3$ to afford the diketone, 2,7-dihexyl-5,10-difluoro-s-indaceno[1,2-b:5,6-b']dithiophene-4,9-dione (**2,7-dihexyl-diFIDT-di(O)**) (80 %). **2,7-Dihexyl-diFIDT-di(O)** was soluble in common organic solvents (such as chloroform, DCM and THF). Knoevenagel condensation of the diketone with malononitrile and pyridine at room temperature gave the title compound, 2,2'-(5,10-difluoro-2,7-dihexyl-s-indaceno[1,2-b:5,6-b']dithiophene-4,9-diylidene)dimalononitrile (**2,7-dihexyl-diFIDT-di(C(CN)$_2$)**) (80 %). Surprisingly it was found that **2,7-dihexyl-diFIDT-di(C(CN)$_2$)** displayed significantly improved solubility in organic solvents (such as chloroform and THF) compared to the previously reported non-fluorinated analogue, despite the higher molecular weight of the former. This is strikingly in contrast to most reports of fluorinated organic semiconductors, in which solubility and processability is significantly lower than their non-fluorinated analogues.[121–123] The improved solubility facilitated purification via liquid phase extraction and reprecipitation. Solubility tests revealed that **2,7-dihexyl-diFIDT-di(C(CN)$_2$)** (4 mg mL^{-1}) was more than 20 times as soluble as **2,7-dihexyl-IDT-di(C(CN)$_2$)** (< 0.2 mg mL^{-1}) in chlorobenzene at 25 °C (procedure outlined in the General Experimental section, Chapter 8). Notably, the solubility of **2,7-dihexyl-diFIDT-di(C(CN)$_2$)** increased to > 10 mg mL^{-1} in chlorobenzene with gentle heating (50 °C), indicating suitability of this OSC for solution-processing (*vide infra*).

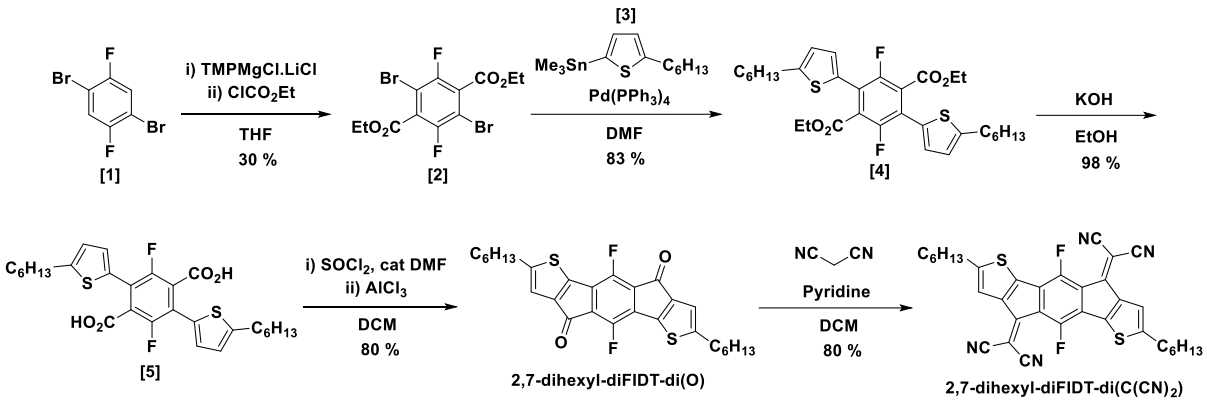


Figure 16: Synthesis of 2,7-dihexyl-diFIDT-di(O) and 2,7-dihexyl-diFIDT-di(C(CN)$_2$).

The chemical structures of **2,7-dihexyl-diFIDT-di(O)** and **2,7-dihexyl-diFIDT-di(C(CN)$_2$)** were verified by ^{1}H NMR, ^{19}F NMR, ^{13}C NMR, IR, HRMS and XRD. To enable a direct comparison of physical and electrochemical properties, the non-fluorinated analogues **2,7-dihexyl-IDT-di(O)** and **2,7-dihexyl-IDT-di(C(CN)$_2$)** were synthesised in accordance with the literature procedures.

2.3 Optoelectronic and Electrochemical Properties

The absorption spectra for **2,7-dihexyl-diFIDT-di(O)** and **2,7-dihexyl-diFIDT-di(C(CN)$_2$)** in solution (toluene and chloroform, 10^{-5} M) were recorded (**Figure 17**). As with the non-fluorinated analogues, both compounds displayed strong well-defined absorption bands at shorter wavelengths (250 – 450 nm) as well as broad weak absorption at longer wavelengths (450 – 750 nm and 550 – 1050 nm respectively). From the onset of absorption at the longer wavelengths, optical gaps of 1.65 eV and 1.21 eV are observed for **2,7-dihexyl-diFIDT-di(O)** and **2,7-dihexyl-diFIDT-di(C(CN)$_2$)** respectively. Time-dependent DFT (TD-DFT) indicated that the very weak oscillator strength of this transition (f = 0.074 and 0.048 respectively) arises due to the absence of significant overlap between the HOMO, located on the IDT core, and the LUMO, located on the cyclopentadienyl-dicyanomethylene bridging unit (**Figure A16** & **A17**).

Optical gaps were slightly reduced versus **2,7-dihexyl-IDT-di(O)** and **2,7-dihexyl-IDT-di(C(CN)$_2$)** (1.84 eV and 1.29 eV respectively).

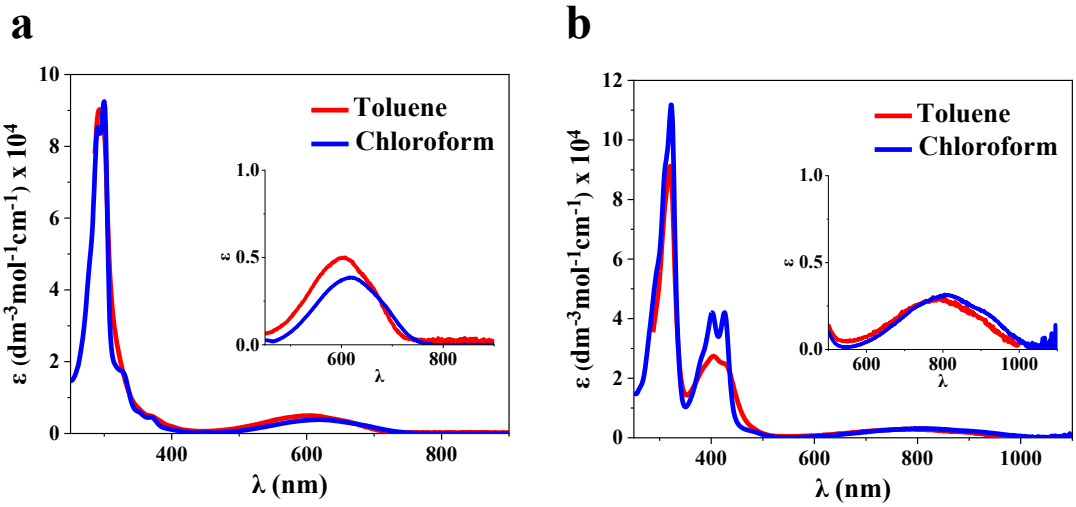


Figure 17: Solution absorption spectra for a) 2,7-dihexyl-diFIDT-di(O) and b) 2,7-dihexyl-diFIDT-di(C(CN)$_2$), in chloroform and toluene.

Electrochemical studies of **2,7-dihexyl-diFIDT-di(O)** and **2,7-dihexyl-diFIDT-di(C(CN)$_2$)** were performed by cyclic voltammetry (CV) using a 0.1 M solution of Bu_4NPF_6 in DCM solutions and a ferrocene (Fc/Fc^+) internal standard. Potentials were swept from 0 V to a positive maximum, then swept back to a negative maximum before returning to 0 V. In line with best practice, energy levels were estimated from $E^{1/2}$ (when reversibility is observed) or E^i (when irreversibility is observed), where $E^{1/2}$ is the half-wave potential, E^i is the inflection-point potential.[124] HOMO = - ($E^{1/2\ or\ i}$ + 4.8) eV and LUMO = - ($E^{1/2\ or\ i}$ + 4.8) eV for oxidation and reduction respectively, with the ferrocene/ferrocenium reference redox system at 4.8 eV below the vacuum level. Electrochemical data for **2,7-dihexyl-IDT-di(O)**, was reanalysed by the method above to ensure a reliable comparison. $E^{1/2}$ and E^i values for **2,7-dihexyl-IDT-di(C(CN)$_2$)** were estimated from the literature data due to poor solubility. Oxidation and reduction potentials are summarised in **Table 2**.

Both **2,7-dihexyl-diFIDT-di(O)** and **2,7-dihexyl-diFIDT-di(C(CN)$_2$)** exhibit multiple chemically reversible reductions with $E^{1/2}$ located at - 1.04 V/- 1.53 V and - 0.56 V/- 0.95 V/- 2.19 V respectively (**Figure 18**). This corresponds to estimated LUMO levels of - 3.76 eV and - 4.24 eV respectively. For comparison, use of E^e (edge potential) instead of $E^{1/2}$ estimated LUMO levels ~ 0.1 eV lower (- 3.85 eV and - 4.35 eV). This systematic overestimation of LUMO level for small molecule OSCs is an important factor to consider for n-type applications, where energy alignment with the electrodes and thermodynamic stability (LUMO < - 4 eV) are crucial. A large depression in the LUMO level (0.48 eV) of **2,7-dihexyl-diFIDT-di(C(CN)$_2$)** versus **2,7-dihexyl-diFIDT-di(O)** reflects how the introduction of the strongly electron-withdrawing dicyanomethylene group can act to effectively stabilise the reduced state. A LUMO level < - 4 eV indicated potential ambient stability for **2,7-dihexyl-diFIDT-di(C(CN)$_2$)** as well as good energy alignment with electrodes for charge injection in OFET devices. As predicted by DFT, the introduction of highly electronegative F groups caused a stabilisation of the LUMO level by 0.2 – 0.3 eV versus the non-fluorinated analogues (- 3.43 eV and - 4.02 eV respectively).

Unlike the reductions, **2,7-dihexyl-diFIDT-di(O)** and **2,7-dihexyl-diFIDT-di(C(CN)$_2$)** showed weakly chemically reversible/irreversible oxidations with E^i located at 1.14 V and 1.20 V respectively, corresponding to estimated HOMO levels - 5.94 eV and - 6.00 eV. A significant depression of LUMO without a corresponding effect on HOMO results in a large decrease in electrochemical gap, from 2.20 eV to 1.76 eV. This effect is explained by the highly localised nature of the LUMO at the bridge point, allowing selective tuning of the LUMO level by choice of functionality at this position, as previously observed.[110] The introduction of F groups was seen to decrease the HOMO level by 0.1 eV and 0.36 eV versus **2,7-dihexyl-IDT-di(O)** and **2,7-dihexyl-IDT-di(C(CN)$_2$)** respectively (- 5.84 eV and - 5.64 eV).

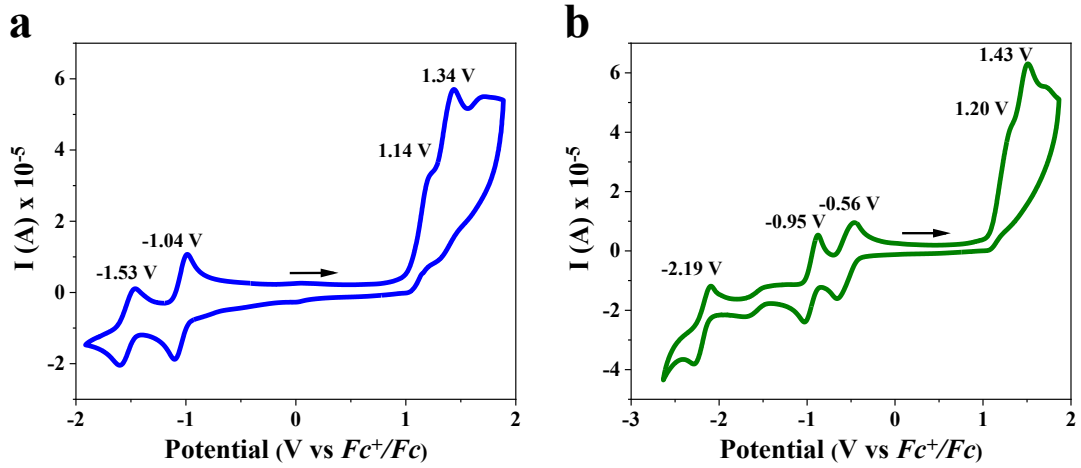


Figure 18: Cyclic voltammograms of a) 2,7-dihexyl-diFIDT-di(O) and b) 2,7-dihexyl-diFIDT-di(C(CN)₂), showing corresponding $E^{1/2}$ or i potentials.

Table 2: Summary of material properties of 2,7-dihexyl-diFIDT-di(O) and 2,7-dihexyl-diFIDT-di(C(CN)₂) compared to the non-fluorinated analogues.

OSC	*HOMO*[a]	*LUMO*[a]	λ_{max} *(solution)*
	[eV]	[eV]	[nm]
IDT-di(O)[b]	- 5.84	- 3.43	579, 296[c]
IDT-di(C(CN)₂)[b]	- 5.64	- 4.02	743, 332[d]
diFIDT-di(O)	- 5.94	- 3.76	598, 293[e]
diFIDT-di(C(CN)₂)	- 6.00	- 4.24	617, 300, 290[f] 779, 405, 320[f] 814, 426, 402, 322[f]

[a] extracted from CV measurements, [b] all data taken from Peltier et al.[110], [c] in cyclohexane, [d] in THF, [e] in toluene, [f] in chloroform.

2.4 Crystal Structures

Single crystals were grown via the solvent vapour exchange method using either chloroform/methanol (**2,7-dihexyl-diFIDT-di(O)**) or chlorobenzene/methanol (**2,7-dihexyl-diFIDT-di(C(CN)₂)**) mixtures. The crystal structures for **2,7-dihexyl-IDT-di(O)** and **2,7-**

dihexyl-IDT-di(C(CN)$_2$) were downloaded from the Cambridge Crystallographic Data Centre for comparison. **2,7-dihexyl-diFIDT-di(O)** crystallised in the triclinic *P*-1 space group (**Figure 19a**). The IDT core was completely coplanar, in agreement with the DFT calculation. The hexyl side-chains on the thienyl α-position lie outside the plane with a dihedral angle of 52 °. A planar slipped π-π stacking arrangement is formed along the *a* axis with partial alkyl chain interdigitation (**Figure 19c** & **d**). There is co-facial packing of the conjugated core within a stack, along the *a* axis, with an interplanar stacking distance of 3.49 Å and a slipping distance of 4.34 Å (angle 51.0 °) (**Figure A19b**). These values are larger than **2,7-dihexyl-IDT-di(O)** (interplanar stacking distance of 3.26 Å, slipping distance of 3.95 Å). Specific short contacts are observed between stacks, including F···F (2.91 Å), S···F (3.23 Å), S···O (3.24 Å) and O···H (2.54 Å) interactions as well as intramolecular C···F (3.08 Å) interactions (**Figure 19b, top**).

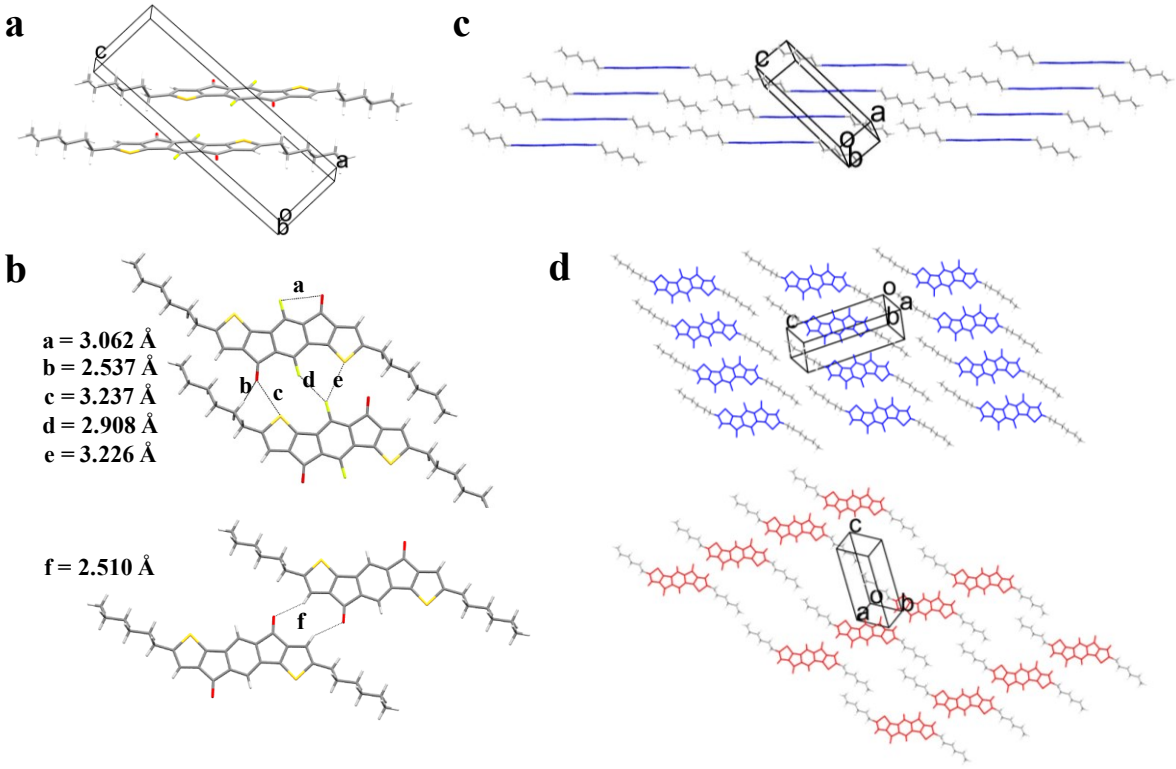


Figure 19: a) Unit cell of 2,7-dihexyl-diFIDT-di(O). b) Inter- and intramolecular short contacts for 2,7-dihexyl-diFIDT-di(O) (top) and 2,7-dihexyl-IDT-di(O) (bottom). c) 4 x 3 packing motif of 2,7-dihexyl-

diFIDT-di(O). d) Interchain registry and alkyl chain interdigitation of 2,7-dihexyl-diFIDT-di(O) (top) and 2,7-dihexyl-IDT-di(O) (bottom).

The presence of short contacts, particularly like the S···F and S···O interactions observed for **2,7-dihexyl-diFIDT-di(O),** is often assumed to be stabilising and therefore desirable for enabling efficient charge transport through the OSC. However, recent work has highlighted that the overall effect is highly dependent on the balance between repulsive (exchange) and attractive (induction, electrostatic and dispersion) interactions.[91,125] To gain insight into the intermolecular interaction energies, symmetry adapted perturbation theory (SAPT0) calculations were performed. SAPT0 analysis allows the total interaction energies between molecular pairs extracted from the crystal structures to be decomposed into the respective non-covalent interactions. Analysis was performed on molecular pairs of **2,7-dihexyl-IDT-di(O)** and **2,7-dihexyl-diFIDT-di(O)** from their respective crystal packing motifs. In addition, the **2,7-dihexyl-IDT-di(O)** molecules in their crystal packing were altered by substitution of the central protons for fluorine atoms, thus leading to the hypothetical **2,7-dihexyl-diFIDT-di(O)** molecules in the **2,7-dihexyl-IDT-di(O)** packing. Similarly, **2,7-dihexyl-IDT-di(O)** molecules were placed in the **2,7-dihexyl-diFIDT-di(O)** packing. This allowed the specific effect of F substitution to be isolated. The SAPT0 analysis shows that many of the intermolecular contacts in the **2,7-dihexyl-diFIDT-di(O)** crystal packing motif are similar, irrespective of H or F substitution (See Appendix for full SAPT0 analysis). Surprisingly, the interactions between close heteroatoms identified in **Figure 19b** gave little difference in total interaction energy, partly as the increase in stabilising dispersion and electrostatic energies are offset by increased steric exchange repulsion. One example of this is shown in **Figure 20a**, where the in-plane longitudinal interaction in the **2,7-dihexyl-diFIDT-di(O)** crystal packing is almost identical irrespective of H or F substitution. The largest stabilisation (2.4 kcal mol^{-1}) by introduction of fluorine appears in an edge π-stacked interaction (**Figure 20b**). This difference

is mostly down to an increase in electrostatic stabilisation by 2.8 kcal mol^{-1}. Another difference between these two molecular alignments is that the C···F bond dipoles directly oppose each other in the in-plane interaction, reducing the gain in electrostatic stabilisation from S···F interaction, while the vertical offset of the edge π-stacked pair means the dipoles can form an anti-parallel stacked stabilising alignment. These results highlight the caution needed in interpreting the impact of close intermolecular contacts.

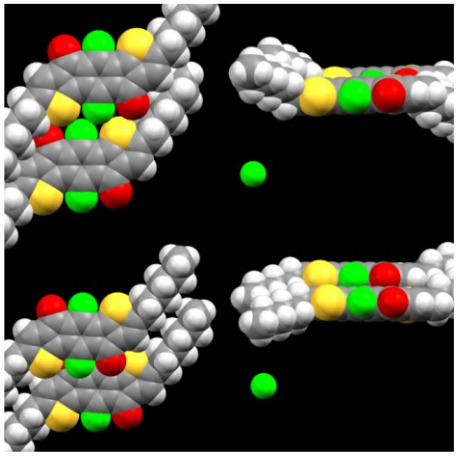


Figure 20: a) in-plane longitudinal interaction and b) edge pi stacked interaction in 2,7-dihexyl-diFIDT-di(O) crystal packing. Total SAPT energies (E_{SAPT}) and electrostatic energies (E_{ES}) are given for 2,7-dihexyl-diFIDT-di(O) and the hypothetical 2,7-dihexyl-IDT-di(O) molecules for the same molecular alignments. All energies in kcalmol^{-1}. Atom colours; yellow = sulfur, green = hydrogen or fluorine, red = oxygen.

2,7-dihexyl-diFIDT-di(C(CN)$_2$) crystallised in the monoclinic $P2_1/n$ space group, with a planar IDT core and the fluorine groups in this plane (**Figure 21a**). The hexyl side-chains on the thienyl α-position lie outside the plane, with a larger dihedral angle of 82 °, similar to that seen for the non-fluorinated analogue. Additionally, there is a slight bowing of the dicyanomethylene groups away from the IDT core plane (7.5 °), as predicted by DFT calculations, with the two dicyanomethylene groups being positioned on opposite sides of the IDT core plane in a 'trans'-like conformation (**Figure 21b**). This bowing is greater than that observed for the non-fluorinated analogue (1.5 °). This, in addition to a slightly increased **C=C-C≡N** angle (126.7 ° vs 124.5 °), indicates a weakly repulsive effect from the presence of a F

group, most likely due to its larger van der Waals radius compared to hydrogen (1.47 Å versus 1.09 Å). There also appears to be a F···CN non-covalent interaction (F···C (2.69 Å) and F···N (2.84 Å)) (**Figure 21c**).

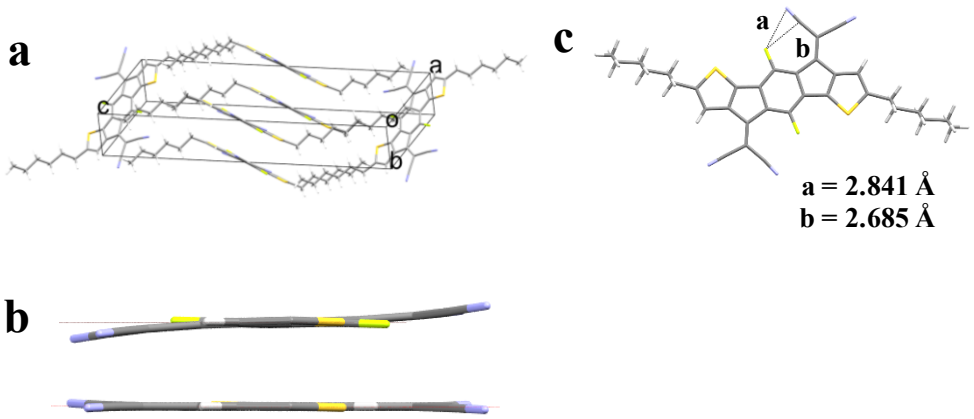


Figure 21: a) Unit cell of 2,7-dihexyl-diFIDT-di(C(CN)₂). b) Planarity of 2,7-dihexyl-diFIDT-di(C(CN)₂) (top) versus 2,7-dihexyl-IDT-di(C(CN)₂) (bottom), with alkyl chains removed for clarity (viewed along the long axis). c) Intramolecular short contacts.

More noticeably, a tilted slipped π-π stacking arrangement is shown for **2,7-dihexyl-diFIDT-di(C(CN)₂)**, as opposed to the planar slipped π-π stacking arrangement observed for **2,7-dihexyl-IDT-di(C(CN)₂)** (**Figure 22a** & **c** respectively). This indicates a dramatic change in solid state packing due to the introduction of the F groups. There are alternating aliphatic and conjugated core layers along the *c* axis and the alkyl chains are interdigitated with each other. There is good co-facial packing of the conjugated core within a stack, with interplanar stacking distance 3.43 Å and slipping distance 2.37 Å (angle 41.8 °) (**Figure A23**). A slight decrease in stacking distance versus **2,7-dihexyl-diFIDT-di(O)** (3.49 Å) and **2,7-dihexyl-IDT-diC(C(CN)₂)** (3.47 Å) is unexpected considering the slight bowing of the dicyanomethylene groups out of plane, however it may indicate more favourable intermolecular overlap from positioning of the δ- F groups directly above the δ+ **C=C**(CN)₂ on neighbouring units in the stack.

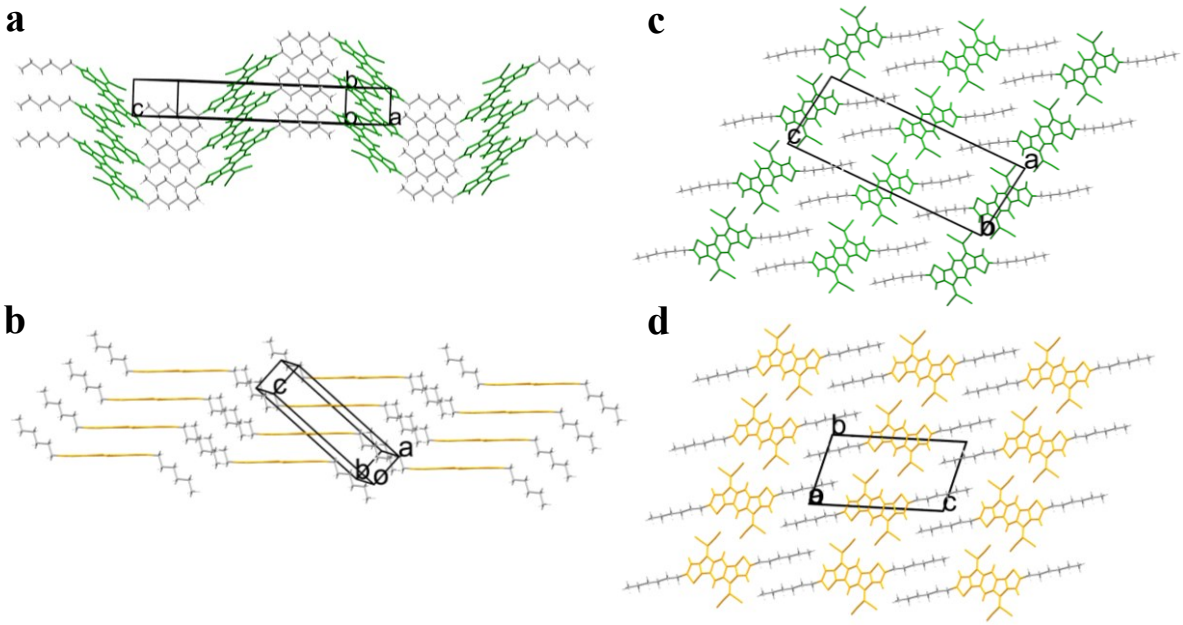
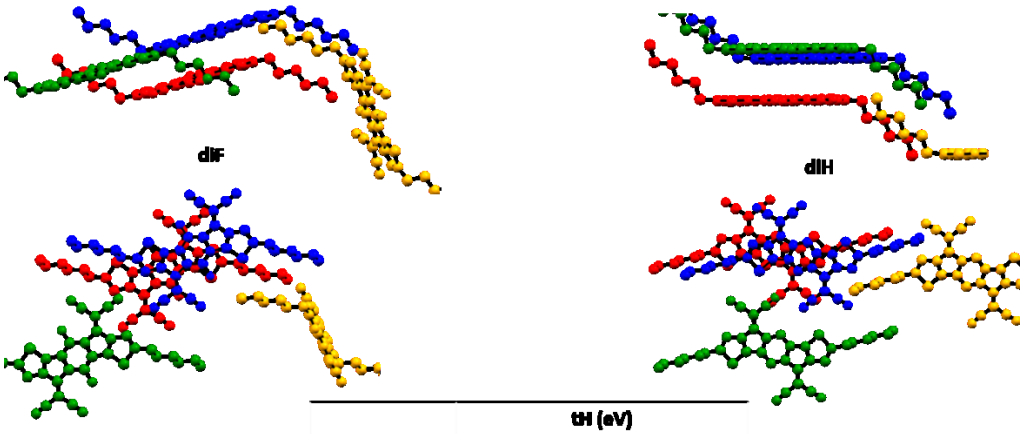


Figure 22: a) Tilted slipped stacking of 2,7-dihexyl-diFIDT-di(C(CN)₂) versus b) Planar slipped stacking of 2,7-dihexyl-IDT-di(C(CN)₂). c) Interchain registry and alkyl chain interdigitation of 2,7-dihexyl-diFIDT-di(C(CN)₂) and d) 2,7-dihexyl-IDT-di(C(CN)₂) .

A key factor affecting transport through organic crystals is the electronic coupling between neighbouring units, often called the transfer integral. A larger value indicates better overlap between frontier molecular orbitals on neighbouring units (LUMO – LUMO in the case of electron transport) and therefore the potential for more efficient charge transfer. Both **2,7-dihexyl-IDT-di(C(CN)₂)** and **2,7-dihexyl-diFIDT-di(C(CN)₂)** single crystals display one-dimensional (1D) charge transfer pathways, with calculated electron transfer integrals (B3LYP/6-31G(d)) of 96 meV and 129 meV respectively for the main π-stacks. Other close contacts resulted in low transfer integrals of < 10 meV (**Figure 23**). While 1D packing can result in lower charge mobility than multidimensional structures, the transfer integrals obtained here are amongst the highest for small molecule organic semiconductors and may help to explain the high transistor performance (*vide infra*).[126–128]



	tH (eV)	
	diF	diH
Blue -> Red	0.129	0.097
Blue -> Green	0.001	0.004
Red -> Green	0.007	0.003

Figure 23: Electron transfer integrals (LUMO:LUMO overlap, B3LYP/6-31G) for molecular pairs from crystal structures of 2,7-dihexyl-IDT-di(C(CN)$_2$) and 2,7-dihexyl-diFIDT-di(C(CN)$_2$), calculated using the approach of Valeev et al..*

Once again, SAPT0 analysis was used to distinguish between the packing configurations, placing both fluorinated and non-fluorinated molecules into each crystal structure. In the case of the **2,7-dihexyl-diFIDT-di(C(CN)$_2$)** packing, the substitution of F with H makes very little difference to pairwise interaction energies. This can be seen by the location of the fluorine substituent (**Figure 24a**), where it has no in-plane intermolecular short contacts and thus has little influence. The main difference in packing originates from the in-plane edge-to-edge interaction of the **2,7-dihexyl-IDT-di(C(CN)$_2$)** crystal, between adjacent molecules in **Figure 24b**. The non-fluorinated derivative results in an interaction stabilisation 11.8 kcal mol^{-1} stronger than the fluorinated one. This difference is the result of a large steric repulsion by the inclusion of fluorine, which is simply too large to fit into the close packing between the nitrile groups. Thus, **2,7-dihexyl-diFIDT-di(C(CN)$_2$)** prefers to adopt the crystal packing where intermolecular interactions involving the fluorine atom are minimised.

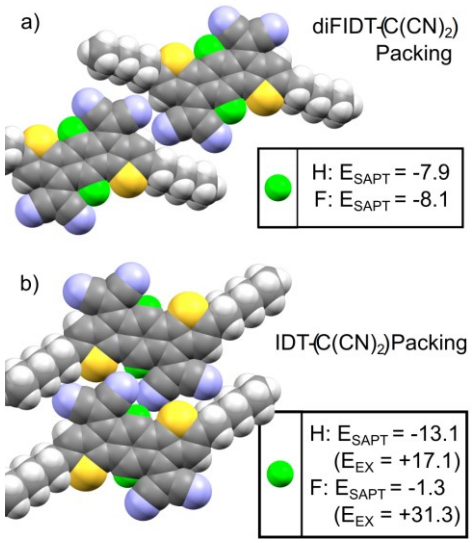


Figure 24: In-plane longitudinal interaction in a) 2,7-dihexyl-diFIDT-di(C(CN)$_2$) crystal packing and b) 2,7-dihexyl-IDT-di(C(CN)$_2$) crystal packing. Total SAPT energies (E_{SAPT}) and repulsive exchange energies (E_{EX}) are given for 2,7-dihexyl-IDT-di(C(CN)$_2$) and 2,7-dihexyl-diFIDT-di(C(CN)$_2$) molecules in each packing motif. All energies in kcal/mol. Atom colours: yellow = sulfur, green = hydrogen or fluorine, purple = nitrogen.

Introduction of EWGs to polycyclic aromatics usually reduces the exchange repulsion while keeping similar dispersion stabilisation, promoting π-stacking. A surprising finding from all the SAPT0 analysis is that the inclusion of fluorine does not strengthen the π-stacking interactions. The presence of strong electron-deficient carbonyl or nitrile groups in close proximity to the central phenyl could explain why the addition of fluorine does not significantly improve the π-stacking stabilisation. The other main conclusion is that inclusion of fluorine does not necessarily introduce more favourable non-covalent interactions with other heteroatoms (e.g. S) simply because the two atoms are close in space. The close contact is accompanied by increased steric repulsion such that the overall intermolecular interaction energy is no different to if there were just a hydrogen substituent, and in some cases making the interaction less stable.

2.5 Thermal Properties

The thermal behaviour of **2,7-dihexyl-diFIDT-di(O)** and **2,7-dihexyl-diFIDT-di(C(CN)$_2$)** was investigated by thermal gravimetric analysis (TGA) (**Figure 25**) and differential scanning calorimetry (DSC) (**Figure 26**). Key data are summarised in **Table 3**.

Both compounds exhibit high thermal stability, with the onset of decomposition occurring at > 310 °C, as with the non-fluorinated analogues. There is a large decrease in T_d (temperature at which 5% mass loss is reached) from **2,7-dihexyl-diFIDT-di(O)** to **2,7-dihexyl-diFIDT-di(C(CN)$_2$)** (T_d = 360 °C versus T_d = 319 °C). Moreover, while **2,7-dihexyl-diFIDT-di(O)** shows improved thermal stability compared to the non-fluorinated analogue (T_d = 331 °C), the opposite is observed for **2,7-dihexyl-diFIDT-di(C(CN)$_2$)** (T_d = 349 °C).

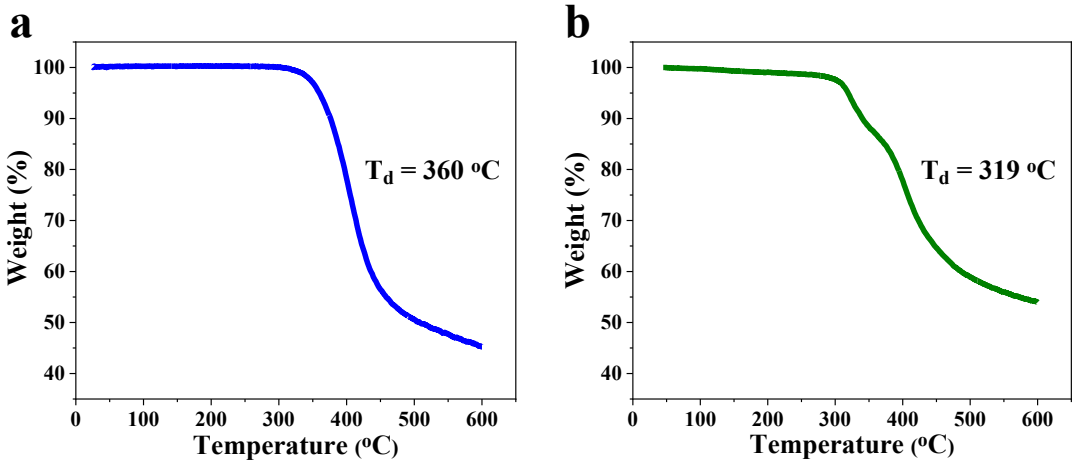


Figure 25: TGA plots of a) 2,7-dihexyl-diFIDT-di(O) and b) 2,7-dihexyl-diFIDT-di(C(CN)$_2$).

2,7-dihexyl-diFIDT-di(O) melts at 221 °C (ΔH_m = 83 J g^{-1}), which is more than 50 °C above that reported for **2,7-dihexyl-IDT-di(O)** (T_m = 172 °C). This compound is also stable in the liquid state up to the maximum temperature used in this experiment (250 °C), with no changes observed upon repeated thermal cycling (**Figure 26a**). In contrast, **2,7-dihexyl-diFIDT-di(C(CN)$_2$)** displays degradation upon melting at 248 °C (59 J g^{-1}), evidenced by a gradual

shift and reduction in melting/crystallising endo-/exotherms upon repeated thermal cycling (**Figure 26b**). An increase in melting temperature (T_m) from **2,7-dihexyl-diFIDT-di(O)** to **2,7-dihexyl-diFIDT-di(C(CN)$_2$)** is in line with that seen for the non-fluorinated analogues, highlighting stronger intermolecular π-π stacking interactions. However, it is surprising that the liquid state of **2,7-dihexyl-diFIDT-di(C(CN)$_2$)** is accessible as this is not the case for **2,7-dihexyl-IDT-di(C(CN)$_2$)**, where no melting endotherm is observed up to 300 °C.

Fluorination of the central phenyl ring is thus shown to have differing effects on the thermal properties, depending on the bridging electron-withdrawing group present. For **2,7-dihexyl-diFIDT-di(O)**, the relative increase in thermal stability and melting point suggests stronger intermolecular interactions in the solid state. For **2,7-dihexyl-diFIDT-di(C(CN)$_2$)** however, the presence of fluorine groups appears to disrupt aggregation, resulting in a lower thermal stability and melting point (and increased solubility). These observations correlate well with the XRD and DFT analysis, particularly for **2,7-dihexyl-diFIDT-di(C(CN)$_2$)** where the non-planarity imposed by steric repulsion from the fluorine groups appears to noticeably disrupt aggregation in the solid state.

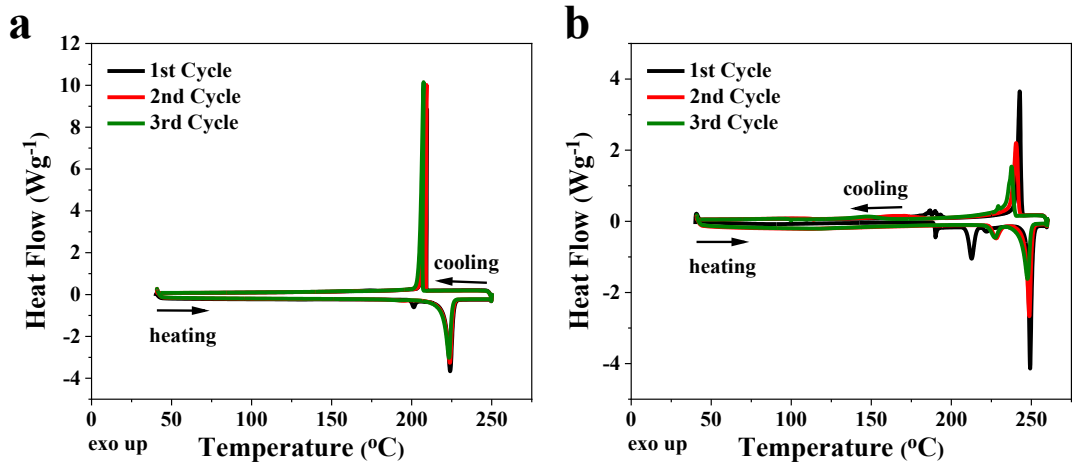


Figure 26: DSC plots of a) 2,7-dihexyl-diFIDT-di(O) and b) 2,7-dihexyl-diFIDT-di(C(CN)$_2$).

Table 3: Summary of TGA and DSC data for diFIDT-di(O) and diFIDT-di(C(CN)$_2$) with the non-fluorinated analogues for comparison.

OSC	T_d	T_m	ΔH_m
	[°C]	[°C]	[J g^{-1}]
2,7-dihexyl-IDT-di(O)[a)]	**331**	**172**	**66**
2,7-dihexyl-IDT-di(C(CN)$_2$)[a)]	**349**	**-**[b)]	**-**[b)]
2,7-dihexyl-diFIDT-di(O)	**360**	**221**	**83**
2,7-dihexyl-diFIDT-di(C(CN)$_2$)	**319**	**248**	**59**

[a)]data taken from Peltier et al.[110], [b)]sample degraded before melting.

2.6 OFET Performance

The solubility of **2,7-dihexyl-diFIDT-di(C(CN)$_2$)** was improved to such an extent as to allow device fabrication via solution-processing of the semiconductor layer. Previous reports using the non-fluorinated **2,7-dihexyl-IDT-di(C(CN)$_2$)** quote a distinct lack of solubility in common organic solvents at room temperature. Tian et al. report that the highest performance for **2,7-dihexyl-IDT-di(C(CN)$_2$)** devices using vacuum-deposition, with a saturated mobility up to 0.33 cm^2 V^{-1} s^{-1}, with extensive device structure engineering. Far inferior performance was achieved via drop-casting, which was only possible from hot 1,2-dichlorobenzene at low concentration (2 mg mL^{-1}), and gave mobilities on the order of 10^{-4} cm^2 V^{-1} s^{-1}.[109]

In the first instance, organic thin film transistors (OTFTs) for **2,7-dihexyl-diFIDT-di(C(CN)$_2$)** were fabricated in bottom-contact top-gate (BC – TG) configuration (**Figure 27a**) via spin-coating of the organic semiconductor. Gold source-drain electrodes of 40 nm were deposited via thermal evaporation in high vacuum, while the organic semiconductor small molecule was spin coated from hot chlorobenzene followed by deposition of Cytop^{TM} dielectric and thermal evaporation of the aluminum gate electrode. The primary parameters of devices performance, including mobility (μ), threshold voltage (V_T) and on-off ratio (I_{on}/I_{off}) were extracted from both

the linear and saturated regimes for devices annealed at 100 °C, 150 °C and 200 °C. All measurements were recorded in a glovebox under a nitrogen atmosphere. Both linear and saturated mobilities are reported (**Table 4**). Linear mobility is more susceptible to non-idealities associated with device operation such as high threshold voltages, contact resistance, etc. due to low voltages applied. These effects however tend to be minimised at the high voltage required to reach the saturation regime. Thus, saturation mobility is often considered to be closer to the intrinsic mobility of the material under test.

Devices with **2,7-dihexyl-diFIDT-di(C(CN)$_2$)** exhibit unipolar electron transport. This reflects the role of the deep LUMO level in allowing stable electron transport (**Figure 27b**). Also, a deep HOMO energy level (- 6.00 eV) imparts a large energy level offset with the S/D electrode helping to suppress competing hole injection and possible ambipolar behavior. The best performance was obtained for devices annealed at 100 °C, with a saturated electron mobility of 0.33 $cm^2\ V^{-1}\ s^{-1}$ with a V_T of 8.16 V and I_{on}/I_{off} of 10^2 across 7 devices (**Table 4**). This mobility is three orders of magnitude higher than that observed for solution-processed devices based on **2,7-dihexyl-IDT-di(C(CN)$_2$)** (10^{-4} $cm^2\ V^{-1}\ s^{-1}$) and comparable to the mobility reported when using vacuum-deposited films. A comparable device performance by solution-processing is highly promising. Impressively low V_T indicated the presence of minimal charge injection barriers between the S/D electrodes and OSC, suggesting good energy alignment for efficient charge injection as well as good interface morphology. Furthermore, extraction of similar mobility values in the linear and saturation regimes reflected minimisation of device non-idealities such as large V_T and/or contact resistance etc, as described above.

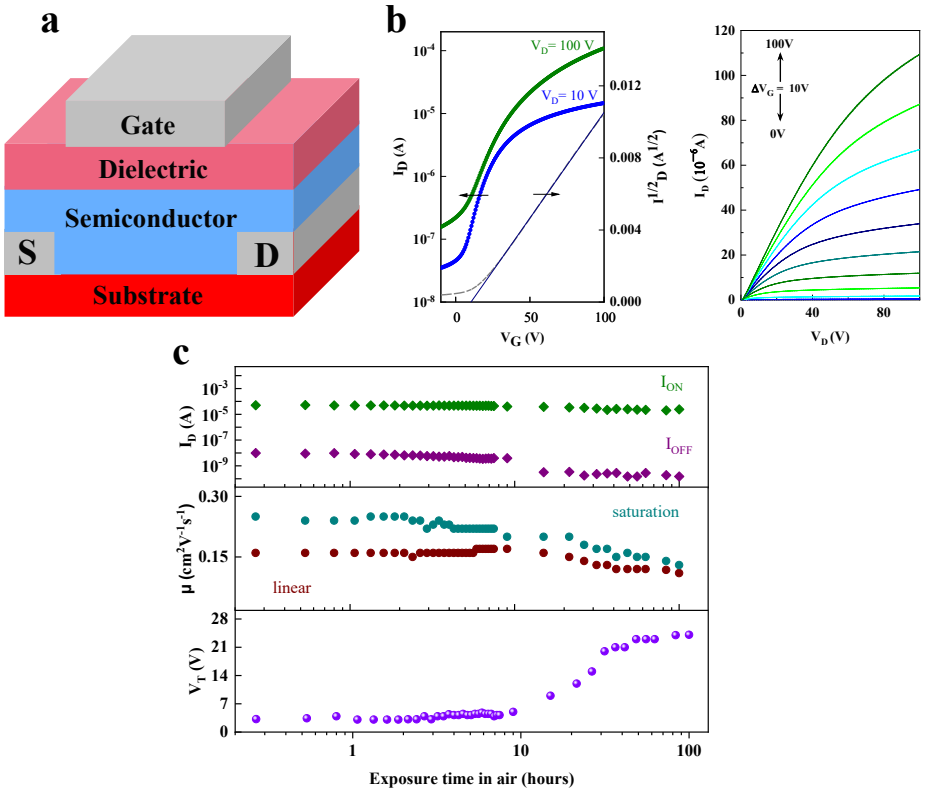


Figure 27: a) OFET device architecture, where S/D are source/drain electrodes b) Transfer (left) and Output (right) curves for BC-TG devices, post-annealed at 100 °C and tested in N_2. c) Stacked plot showing the OFET performance of 2,7-dihexyl-diFIDT-di(C(CN)$_2$) tested in air over 100 hours.

The promising performance observed with spin-coating prompted us to investigate the performance in blade-coated devices. Blade-coating is seen as an attractive solution-processing technique due to better scalability and potential for roll-to-roll processing for industrial production.[129] Al/Au source-drain electrodes (5 nm/35 nm) were deposited via thermal evaporation in high vacuum. The **2,7-dihexyl-diFIDT-di(C(CN)$_2$)** solution (5 mg mL^{-1} in chlorobenzene) was blade coated on the substrates at 100 °C with the blade speed of 50 mm s^{-1} and then the substrates were kept at 100 °C for 5 mins. This was followed by deposition of Cytop^{TM} dielectric and thermal evaporation of the aluminum gate electrode. **Figure A26** shows the transfer characteristics of OTFTs fabricated using identical processing conditions. **Figure A26a – c** displays representative curves for a transistor with low threshold voltage (- 0.91 V) and a reasonably high saturated electron mobility (0.39 cm^2 V^{-1} s^{-1}), while **Figure A26d – f**

shows representative curves for an OTFT with the highest saturated electron mobility (0.49 $cm^2\ V^{-1}\ s^{-1}$) both prepared via blade coating. **Figure A27** shows the statistical distribution of the electron mobility and threshold voltage extracted from 18 blade-coated OTFT devices fabricated simultaneously. The large variations in the threshold voltage suggests the presence of interfacial traps and a strong relation to the local processing conditions. Such non-idealities associated with the device operation can suppress the linear mobility, which is more vulnerable to such effects due to lower operating voltage. Hence, the blade coated device suffers from low linear mobility value. These adverse effects are greatly minimised in the saturation regime however, since higher voltages are applied. The saturated mobility is extracted from the linear part of the square root of the drain current. Absence of any double slope in the plot confirms the reliability of the data. Also, the saturated mobility value remains relatively constant with gate voltage above V_T and well within the value extracted by the above method (**Figure A26c & f**).

Tian et al. observed a rapid decrease in performance of vacuum-processed **2,7-dihexyl-IDT-di(C(CN)$_2$)** devices in air. However, improved thin film morphology via surface modification greatly improved stability. A series of spin-coated devices with **2,7-dihexyl-diFIDT-di(C(CN)$_2$)** were also exposed to air and device performance (in air) tested periodically over an extended period of time (100 hours) in order to probe ambient operating stability (**Figure 27c**). The performance is maintained during initial stages (up to 10 hours), but there is a reduction in mobility, by about half, after 100 hours (~ 0.28 $cm^2\ V^{-1}\ s^{-1}$ to ~ 0.14 $cm^2\ V^{-1}\ s^{-1}$). While I_{on} was maintained, there was a sharp increase in V_T and decrease in I_{off} after 10 hours. This potentially indicates the introduction of charge trapping states at the dielectric/OSC interface. The slight delay may reflect the time needed for O_2 to diffuse into the device and towards the interface. While the deep LUMO level (- 4.24 eV) indicates ambient thermodynamic stability of the reduced state, a fact supported by the retention of I_{on} throughout,

these observations highlight that device structure and thin film quality play a crucial part in truly air stable devices, as was observed by Tian et al..[36] These results indicate that similar optimisation of **2,7-dihexyl-diFIDT-di(C(CN)$_2$)** thin film morphology could enable access to truly air-stable devices.

Table 4: Summary of OFET device performance for 2,7-dihexyl-diFIDT-di(C(CN)$_2$) in bottom contact-top gate contact configuration, annealed at 100 °C (best values in brackets).

Deposition Technique	V_T	μ_{linear}	$\mu_{saturated}$	I_{on}/I_{off}
	[V]	[cm^2 V^{-1} s^{-1}]	[cm^2 V^{-1} s^{-1}]	
Spin-coated	8.16	0.12	0.33 (0.33)	10^2
Blade-coated	12.37	0.01	0.34 (0.49)	10^2 – 10^3

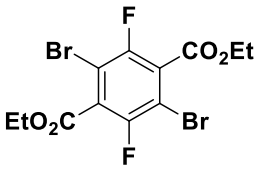
2.7 Conclusion

In summary, we report the synthesis of two new highly electron-deficient small molecules based on the IDT core incorporating backbone fluorination on the central phenyl ring, namely **2,7-dihexyl-diFIDT-di(O)** and **2,7-dihexyl-diFIDT-di(C(CN)$_2$)**. **2,7-dihexyl-diFIDT-di(O)** and **2,7-dihexyl-diFIDT-di(C(CN)$_2$)** exhibit LUMO/HOMO energy levels of - 3.76 eV/- 5.96 eV and - 4.24 eV/- 6.00 eV respectively, corresponding to a depression of 0.2 – 0.3 eV in the LUMO energy level by direct comparison with the non-fluorinated analogues, **2,7-dihexyl-IDT-di(O)** and **2,7-dihexyl-IDT-di(C(CN)$_2$)**. The deep LUMO and surprisingly superior solubility of **2,7-dihexyl-diFIDT-di(C(CN)$_2$)** compared to the non-fluorinated analogue enabled the fabrication of solution-processed OFET devices exhibiting high unipolar electron mobility (up to 0.49 cm^2 V^{-1} s^{-1}) via scalable blade-coating. Such devices exhibited highly promising stability under ambient conditions, with good performance maintained after 100 hrs.

As indicated by TGA and DSC analysis, fluorination of **2,7-dihexyl-IDT-di(O)** is shown to increase degradation and melting temperature (T_d = 360 °C vs 331 °C and T_m = 224 °C vs 172 °C) while a decrease is observed for fluorination of **2,7-dihexyl-IDT-di(C(CN)$_2$)** (T_d = 319 °C vs 349 °C and T_m = 249 °C vs > 300 °C). In addition, fluorination is shown to modify crystal packing considerably. **2,7-dihexyl-diFIDT-di(O)** retains a planar slipped stack motif with improved inter-stack registry, whereas **2,7-dihexyl-diFIDT-di(C(CN)$_2$)** adopts a tilted slipped stack motif. Interestingly, many of the observed differences in packing were for unexpected reasons, as investigated by computational analysis of intermolecular interactions involving fluorine. Such results demonstrate that core fluorination is a potential approach to improving processability in conjugated materials, as well as promoting stable n-type performance.

2.8 Experimental

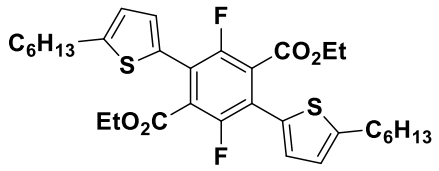
***Diethyl 2,5-dibromo-3,6-difluoroterephthalate ([2])**:*



To a 1.0 M solution (THF 1:1 toluene) of 2,2,6,6-Tetramethylpiperidinylmagnesium chloride lithium chloride complex (100 mL, 100 mmol) at - 40 °C under inert atmosphere was added drop-wise a solution of 1,4-dibromo-2,5-difluoro-benzene (11.82 g, 43.48 mmol) in anhydrous THF (150 mL) over 30 minutes via syringe pump. After addition, the reaction mixture was stirred at - 40 °C for 5 hours before ethyl chloroformate (9.98 mL, 104 mmol) was added in one go. The mixture was then allowed to warm to room temperature overnight. Aqueous hydrochloric acid (1.0 M, 200 mL) was added and the mixture stirred at room temperature for 30 minutes. The product was extracted with diethyl ether (3 x 50 mL). The combined organics

were dried over anhydrous magnesium sulphate, filtered and the solvent removed in vacuo. The crude product was triturated with n-pentane to form a suspension. The product was filtered and washed with cold n-pentane then cold acetone, collected and dried under vacuum to give 2,5-dibromo-3,6-difluoro-terephthalic acid diethyl ester (5.50 g, 30 %) as a cream solid. ^{1}H NMR (400 MHz, $CDCl_3$, δ): 4.47 (q, ^{3}J = 7.0 Hz, 4 H, CH_2), 1.41 (t, ^{3}J = 7.0 Hz, 6 H, CH_3). ^{13}C NMR (101 MHz, $CDCl_3$, δ): 161.62, 152.44 (dd, ^{1}J = 252 Hz, ^{4}J = 4.5 Hz, CF), 127.21 – 126.78 (m, CF), 107.79 – 107.49 (m, CF), 63.37, 14.19. ^{19}F NMR (377 MHz, $CDCl_3$, δ) -108.69 (s, CF). HRMS (ES-TOF) m/z: $[M+H]^+$ calcd. for $C_{12}H_{10}O_4F_2Br_2$, 413.8932; found, 413.8914.

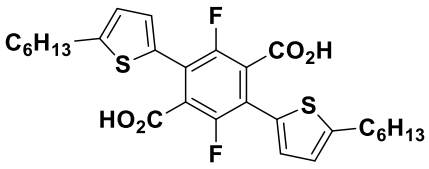
***Diethyl 2,5-difluoro-3,6-bis(5-hexylthiophen-2-yl)terephthalate ([4])**:*



A mixture of 2,5-Dibromo-3,6-difluoroterephthalic acid diethyl ester (2.2 g, 5.7 mmol), (5-hexylthiophen-2-yl)trimethylstannane ***([3])*** (5.5 g, 12.7 mmol) in anhydrous DMF (40 mL) were degassed for 45 mins. Tetrakis(triphenylphosphine)palladium(0) (306 mg, 0.26 mmol, 0.05 equiv) was added and the mixture degassed for a further 15 mins. The mixture was stirred at 100 °C for 17 hours. The mixture was diluted with DCM (100 mL) and the crude reaction mixture passed through a plug of 15 % KF in silica, eluting with DCM. The solvent was then concentrated in vacuo. DCM (100 mL) was added and the organic phase washed with water (4 x 50 mL) and brine (50 mL). The combined organics were dried over anhydrous magnesium sulfate, filtered and the solvent removed in vacuo. The crude product was purified by silica gel chromatography (petroleum ether 2:1 DCM). The product was collected and dried under vacuum to give diethyl 2,5-difluoro-3,6-bis(5-hexylthiophen-2-yl)terephthalate (2.60 g, 83 %)

as a pale orange solid. ^{1}H NMR (400 MHz, $CDCl_3$, δ): 7.00 (d, ^{3}J = 3.5 Hz, 2 H, ArH)), 6.76 (d, ^{3}J = 3.5 Hz, 2 H, ArH), 4.26 (q, ^{3}J = 7.2 Hz, 4 H, CH_2), 2.83 (t, ^{3}J = 7.5 Hz, 4 H, CH_2), 1.74 – 1.64 (m, 4 H, CH_2), 1.42 – 1.24 (m, 12 H, CH_2), 1.18 (t, ^{3}J = 7.2 Hz, 6 H, CH_3), 0.89 (t, ^{3}J = 6.8 Hz, 6 H, CH_3). ^{13}C NMR (101 MHz, $CDCl_3$, δ): 163.94, 152.06 (dd, ^{1}J = 252 Hz, ^{4}J = 4.5 Hz, CF), 149.40, 129.44, 128.43, 125.16 – 124.79 (m, CF), 124.47, 122.08 – 121.76 (m, CF), 62.42, 31.67, 30.21, 28.90, 22.70, 14.20, 13.95 (some overlapping carbons). ^{19}F NMR (377 MHz, $CDCl_3$, δ): - 119.94 (s, CF). HRMS (ES-TOF) m/z: $[M+H]^+$ calcd. for $C_{32}H_{41}O_4S_2F_2$, 591.2413; found, 591.2414.

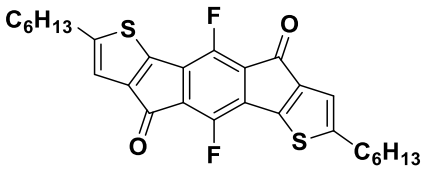
***2,5-Bis(5-hexylthiophen-2-yl)-3,6-difluoroterephthalic acid ([5])**:*



Diethyl 2,5-difluoro-3,6-bis(5-hexylthiophen-2-yl)terephthalate (1.5 g, 2.37 mmol) was suspended in ethanol (30 mL). KOH (1.06 g, 19.00 mmol) was added as a single portion. The suspension was heated to reflux overnight. Upon heating a solution followed by a suspension was observed. The reaction was cooled to room temperature and aqueous hydrochloric acid (2.0 M, 75 mL) was added with stirring for 5 mins. The resulting precipitate was filtered, washed with plenty of water and dried in an oven at 140 °C to give the product (1.32 g, 98 %) as a greenish solid. ^{1}H NMR (400 MHz, DMSO-d_6, δ): 7.13 (d, ^{3}J = 6.9 Hz, 2 H, ArH), 6.93 (d, ^{3}J = 6.9 Hz, 2 H, ArH), 2.83 (t, ^{3}J = 7.4 Hz, 4 H, CH_2), 1.69 – 1.58 (m, 4 H, CH_2), 1.41 – 1.21 (m, 12 H, CH_2), 0.8 (t, ^{3}J = 7.0 Hz, 6 H, CH_3). ^{13}C NMR (101 MHz, DMSO-d_6, δ): 164.39, 150.64 (dd, ^{1}J = 247 Hz, ^{4}J = 2.5 Hz, CF), 148.73, 129.58, 127.45, 125.63 – 125.17 (m, CF), 124.98, 120.21 – 119.78 (m, CF), 30.98, 30.90, 29.20, 28.14, 22.00, 13.90. ^{19}F NMR (377

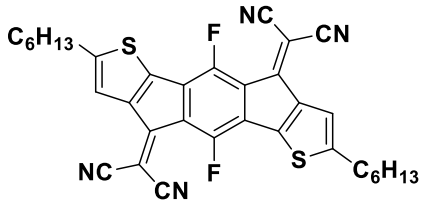
MHz, DMSO-d_6, δ): - 118.49 (s, CF). HRMS (CI) m/z: $[M+H]^+$ calcd. for $C_{28}H_{31}O_4S_2F_2$, 533.1626; found, 533.1639.

2,7-Dihexyl-5,10-difluoro-s-indaceno[1,2-b:5,6-b']dithiophene-4,9-dione (2,7-dihexyl-diFIDT-di(O)):



2,5-Difluoro-3,6-di-(5-hexylthiophen-2-yl-terephthalic acid (1.2 g, 2.24 mmol) was suspended in anhydrous DCM (25 mL) and catalytic anhydrous DMF (0.1 mL; 1.12 mmol). Thionyl chloride (0.98 mL, 13.47 mmol) was added dropwise over 15 minutes. The reaction heated reflux overnight. Solvent was removed to give an orange oil which was used in the next step without further purification. The acyl chloride was redissolved in anhydrous DCM (50 mL) and then added to a suspension of anhydrous $AlCl_3$ (1.52 g) in DCM (50 mL) at 0 °C. The resultant mixture was allowed to warm to room temperature and stirred overnight. The mixture was poured into cold aqueous hydrochloric acid (2.0 M, 100 mL), causing a deep blue precipitate to form which was collected by filtration. Washing with aqueous hydrochloric acid (2.0 M), water, and acetone followed by drying in vacuo afforded a cyan blue solid (0.89 g, 80 %). m.p. 221 °C. ^{1}H NMR (400 MHz, $CDCl_3$, δ): 6.83 (s, 2H, ArH), 2.80 (t, 4H, ^3J = 7.5 Hz, CH_2), 1.69 (m, 4H, CH_2), 1.33 (m, 12H, CH_2), 0.90 (t, 6H, ^3J = 6.9 Hz, CH_3). ^{13}C NMR (101 MHz, TCE-d_2, 120 °C, δ): 181.33, 154.16, 149.26, 146.14 (dd, ^1J = 265 Hz, ^4J = 2.9 Hz, CF), 140.56, 129.35 (m, CF), 127.19 (m, CF), 31.13, 30.88, 30.42, 28.31, 22.12, 13.51. ^{19}F NMR (377 MHz, $CDCl_3$, δ): - 129.99 (s, CF). IR (cm^{-1}) 1708 (C=O). HRMS (ES-TOF) m/z: $[M+H]^+$ calcd. for $C_{28}H_{27}F_2O_2S_2$, 497.1421; found, 497.1415.

2,2'-(5,10-Difluoro-2,7-dihexyl-s-indaceno[1,2-b:5,6-b']dithiophene-4,9-diylidene)dimalononitrile (2,7-dihexyl-diFIDT-di(C(CN)$_2$)):



2,7-Dihexyl-5,10-difluoro-s-indaceno[1,2-b:5,6-b']dithiophene-4,9-dione (250 mg, 0.50 mmol) and malononitrile (317 mg, 5.0 mmol) were dissolved in anhydrous DCM (40 mL). Pyridine (0.39 mL, 6.0 mmol) was added and the mixture stirred overnight at room temperature. Aqueous hydrochloric acid (2.0 M, 40 mL) was added and the crude product extracted with chloroform (2 x 50 mL). The combined organic extracts were rinsed with water (2 x 50 mL) and brine (50 mL), dried over anhydrous sodium sulfate, filtered and concentrated under reduced pressure. The residue was reprecipitated in the minimum amount of hot DCM with methanol, filtered, washed with methanol and dried to give a deep green solid (239 mg, 80 %). m.p. 248 °C. ^{1}H NMR (400 MHz, $CDCl_3$, δ): 7.34 (s, 2 H, ArH), 2.84 (t, ^{3}J = 7.0 Hz, 4 H, CH_2), 1.70 (m, 4 H, CH_2), 1.33 (m, 12 H, CH_2), 0.90 (t, ^{3}J = 7.0 Hz, 6 H, CH_3). ^{13}C NMR (101 MHz, $CDCl_3$, 50 °C, δ): 155.27, 152.64, 149.40 (dd, ^{1}J = 265 Hz, ^{4}J = 2.5 Hz, CF), 144.68, 139.65, 127.82 (m, CF), 127.18 (m, CF), 120.46, 113.53, 112.34, 82.07, 31.58, 31.40, 31.08, 28.77, 22.65, 14.10. ^{19}F NMR (377 MHz, $CDCl_3$, δ): - 108.18 (s, CF). IR (cm^{-1}) 2226 (C≡N). HRMS (ES-TOF) m/z: $[M-H]^-$ calcd. for $C_{34}H_{28}F_2N_4S_2$, 594.1723; found, 594.1711.

3. Effect of alkyl side-chain on properties and performance of dialkyl-diFIDT-di($C(CN)_2$)

Single crystal characterisation was carried out by Dr. Andrew J. P. White (Imperial College London). Analysis of transfer integrals and intermolecular interactions was performed by Dr. Karl J. Thorley (University of Kentucky). OFET device fabrication and testing was performed by Dr. Luxi Tan (Imperial College London) and Dr. Aniruddha Basu (KAUST).

3.1 Introduction

The complex structure-property relationships associated with OSC material performance means that a chemist must always consider potential secondary and/or undesired effects that could arise with any modification when designing new materials. This fact is no clearer than in the area of 'side-chain engineering'. As discussed in the introduction, the primary motivation for alkylation of OSCs is to impart processability. In many cases alkylation primarily acts to improve processability by limiting the natural propensity of the conjugated aromatic units to aggregate, in turn reducing the melting point. This can manifest also as improved solubility in the instance of solution-processing.[79,131] However, good π-π interactions are required to ensure efficient charge transport between molecules in the solid state. Therefore, a balance must be made such that processability is achieved while incurring minimal disruption to charge transport properties. This requirement has led to extensive investigations into the effect of alkyl side-chains on the physiochemical properties and device performance of OSCs. These investigations have enabled materials chemists to formulate some general design rules. That being said, the intricate relationship between side-chains, OSC core, morphology and

performance makes the procedure of 'side-chain engineering' commonplace for any new OSC material, in order to optimise performance.

This complexity is highlighted by a number of recent reports. For example, Welford et al. describe a detailed investigation into the influence of alkyl side-chain type and length on naphthalene diimide (NDI)-based small molecule performance (**Figure 28a**).[132] Both short (C_4H_9 and C_5H_{11}) and long (C_8H_{17} and $C_{12}H_{25}$) alkyl side-chains gave high mobilities, while the intermediate C_6H_{13} alkyl chain mobility was much lower. The authors attribute this to the competing influence of molecular packing and molecular order. Zhang et al. investigated the effect of branched versus linear alkyl chains on the transistor performance of two regioisomers of an electron-deficient quinoidal terthiophene small molecule (**Figure 28b**).[133] In this instance, the branched side-chain analogue was shown to give far superior performance (up to 5.2 $cm^2 V^{-1} s^{-1}$) versus the linear for one regioisomer, justified by a favourable 2D brickwork type face-to-face packing, but not the other. Subsequent work showed that extension of the branching point away from the backbone led to lower mobility, despite more favourable π-π stacking distance.[134] An undesired increase in the prevalence of face-on orientation in the film is explained as the contributing factor. Meanwhile, Lim et al. studied the use of a siloxane side-chains in place of alkyl side-chains in a donor-acceptor DPP-based small molecule (**Figure 28c**).[135] The siloxane-containing small molecule is shown to boost mobility by more than 3 times that of the alkyl-containing analogue. A combination of XRD, AFM and POM indicated that the improved mobility could be attributed to higher crystallinity and shorter intermolecular distance arising from stronger siloxane···siloxane interactions.

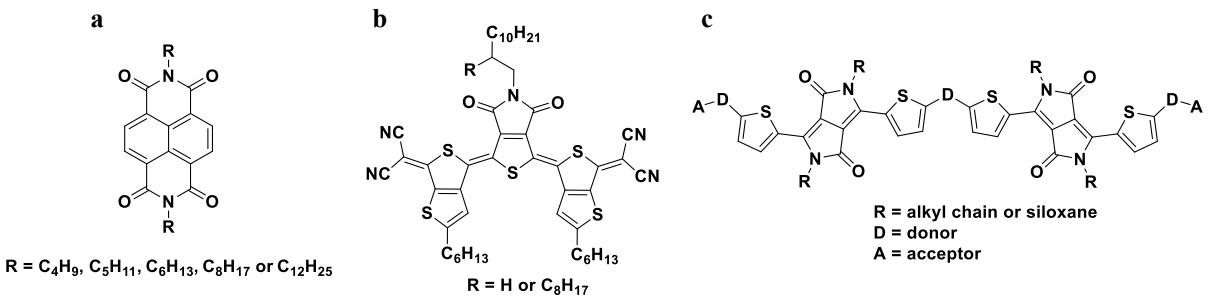


Figure 28: Examples of side-chain engineering from the literature.

To the best of our knowledge, there has been limited exploration of side-chain engineering for the already reported **dialkyl-IDT-di(O)** and **dialkyl-IDT-di(C(CN)$_2$)** OSCs. Hexyl side-chains are most prevalent, presumably due to the commercial availability of the 2-hexylthiophene precursor. Xu et al. studied the effect of linear chain length on the morphology and device performance three **2,7-dialkyl-IDT-di(O)** OSCs, including 2,7-diethyl, 2,7-dihexyl and 2,7-didodecyl chains.[136] It was shown that the nature of the alkyl side-chain could affect the polarity of resulting vacuum-processed devices, namely **2,7-diethyl-IDT-di(O)** and **2,7-didodecyl-IDT-di(O)** displayed ambipolar behaviour while **2,7-dihexyl-IDT-di(O)** displayed unipolar p-type behaviour. This was justified by changes in the thin film morphology leading to differences in electron and hole transfer integrals. The effect of alkyl side-chain length on the solubility was not explored.

In this work, a series of novel **dialkyl-diFIDT-di(O)** and **dialkyl-diFIDT-di(C(CN)$_2$)** materials bearing different alkyl side-chains were synthesised in order to probe the impact on the physiochemical properties and device performance. Various approaches to 'side-chain engineering' were explored; *linear chain extension*, affording **2,7-didodecyl-diFIDT-di(O)** and **2,7-didodecyl-diFIDT-di(C(CN)$_2$)**; *chain branching*, affording **2,7-bis(2-ethylhexyl)-diFIDT-di(O)** and **2,7-bis(2-ethylhexyl-diFIDT-di(C(CN)$_2$)**; *chain regiochemistry*, affording **3,8-dihexyl-diFIDT-di(O)** and **3,8-dihexyl-diFIDT-di(C(CN)$_2$)**. With these novel analogues

it was envisaged that the device performance of **dialkyl-diFIDT-di(C(CN)$_2$)** may be optimised beyond that reported for **2,7-dihexyl-diFIDT-di(C(CN)$_2$)** in Chapter 2.

3.2 Synthesis

Novel **dialkyl-diFIDT-di(O)** and **dialkyl-diFIDT-di(C(CN)$_2$)** molecular OSCs bearing different alkyl side-chains (2,7-didodecyl-, 2,7-bis(2-ethylhexyl)- and 3,8-dihexyl-) were synthesised, broadly following the synthetic route outlined in Section 2.2. Only minor modifications to the synthesis were necessitated, predominantly centred on the final Knoevenagel condensation step (*vide infra*). Access to the branched side-chain analogues required the synthesis of 2-(2-ethylhexyl)thiophene, which was prepared following a literature procedure (Section 3.2.2).[137]

3.2.1 Synthesis of 2,7-didodecyl-diFIDT-di(O) and 2,7-didodecyl-diFIDT-di(C(CN)$_2$)

2,7-didodecyl-diFIDT-di(C(CN)$_2$) was synthesised following the route outlined in **Figure 29**. Diethyl 2,5-dibromo-3,6-difluoroterephthalate (**[2]**) was utilised in a Stille cross-coupling with trimethyl(5-dodecylthiophen-2-yl)stannane (**[6]**) using tetrakis(triphenylphosphine)palladium(0) to afford diethyl 2,5-difluoro-3,6-bis(5-dodecylthiophen-2-yl)terephthalate (**[7]**) in moderate yield (64 %) after purification by silica gel chromatography. Saponification with KOH in ethanol afforded a quantitative conversion to the diacid (**[8]**), which was converted to the acid chloride by treatment with $SOCl_2$ in DCM in the presence of a catalytic amount of DMF. After solvent removal, the resulting water-sensitive material was used directly without purification. Ring closure was achieved by a Lewis acid-promoted intramolecular Friedel-Crafts acylation with $AlCl_3$ to afford the diketone, 2,7-

didodecyl-5,10-difluoro-s-indaceno[1,2-b:5,6-b']dithiophene-4,9-dione, **2,7-didodecyl-diFIDT-di(O)** (85 %). The solubility of **2,7-didodecyl-diFIDT-di(O)** common organic solvents (such as chloroform, DCM and THF) was greatly reduced compared to **2,7-dihexyl-diFIDT-di(O)**. Due to the poor solubility of **2,7-dihexyl-diFIDT-di(O)**, Knoevenagel condensation with malononitrile and pyridine was performed in toluene (as opposed to DCM) at elevated temperature (50 °C) to afford 2,2'-(5,10-difluoro-2,7-didodecyl-s-indaceno[1,2-b:5,6-b']dithiophene-4,9-diylidene)dimalononitrile, **2,7-didodecyl-diFIDT-di(C(CN)$_2$)** (66 %). These conditions ensured good dissolution of starting materials during the reaction. **2,7-didodecyl-diFIDT-di(C(CN)$_2$)** displayed significantly reduced solubility also. Solubility tests revealed that **2,7-didodecyl-diFIDT-di(C(CN)$_2$)** (0.3 – 0.5 mg mL^{-1}) was an order of magnitude less soluble than **2,7-dihexyl-diFIDT-di(C(CN)$_2$)** (4 mg mL^{-1}). It is noted that **2,7-dihexadecyl-diFIDT-di(O)** was also synthesised and was completely unprocessable. As such, its preparation is not reported in this thesis. While longer linear alkyl side-chains are often incorporated explicitly to improve solubility of OSCs, this is evidently not true for the class of OSCs reported here.

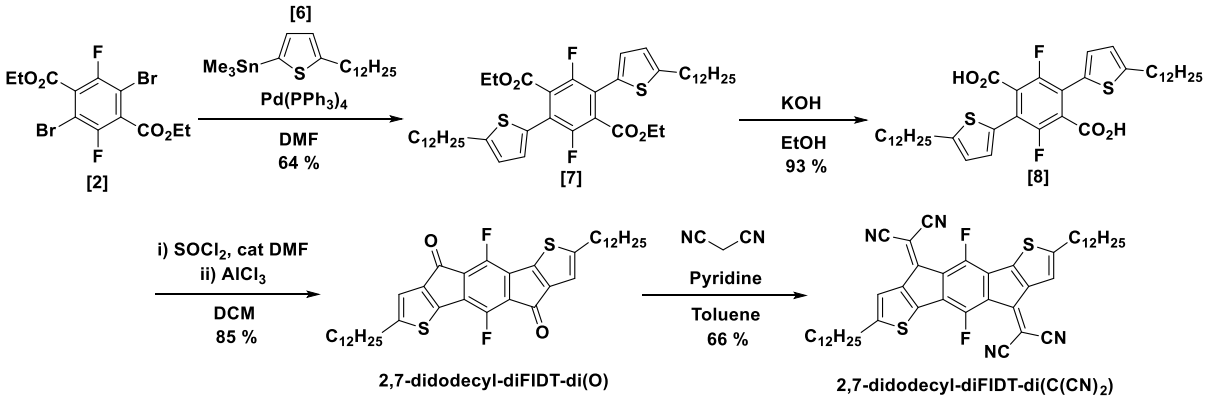


Figure 29: Synthesis of 2,7-didodecyl-diFIDT-di(O) and 2,7-didodecyl-diFIDT-di(C(CN)$_2$).

The chemical structures of **2,7-didodecyl-diFIDT-di(O)** and **2,7-didodecyl-diFIDT-di(C(CN)$_2$)** were verified by ^{1}H NMR, ^{19}F NMR, ^{13}C NMR, IR and HRMS. Unfortunately,

growth of crystals to the standard required for single crystal XRD analysis was not achieved for either compound.

3.2.2 Synthesis of 2,7-bis(2-ethylhexyl)-diFIDT-di(O) and 2,7-bis(2-ethylhexyl-diFIDT-di(C(CN)$_2$)

2,7-bis(2-ethylhexyl)-diFIDT-di(C(CN)$_2$) was synthesised following the route outlined in **Figure 30**. Diethyl 2,5-dibromo-3,6-difluoroterephthalate (**[2]**) was utilised in a Stille cross-coupling with trimethyl(5-(2-ethylhexyl))thiophen-2-yl)stannane (**[9]**) using tetrakis(triphenylphosphine)palladium(0) to afford diethyl 2,5-difluoro-3,6-bis(5-(2-ethylhexylthiophen-2-yl)terephthalate (**[10]**) in high yield (80 %) after purification by silica gel chromatography. Saponification with KOH in *tert*-butanol afforded a quantitative conversion to the diacid (**[11]**), which was converted to the acid chloride by treatment with $SOCl_2$ in DCM in the presence of a catalytic amount of DMF. After solvent removal, the resulting water-sensitive material was used directly without purification. Ring closure was achieved by a Lewis acid-promoted intramolecular Friedel-Crafts acylation with $AlCl_3$ to afford the diketone, 2,7-bis(2-ethylhexyl)-5,10-difluoro-s-indaceno[1,2-b:5,6-b']dithiophene-4,9-dione, **2,7-bis(2-ethylhexyl)-diFIDT-di(O)** (88 %). **2,7-bis(2-ethylhexyl)-diFIDT-di(O)** common organic solvents (such as chloroform, DCM and THF). Knoevenagel condensation with malononitrile and pyridine at room temperature afforded 2,2'-(5,10-difluoro-2,7-bis(2-ethylhexyl)-s-indaceno[1,2-b:5,6-b']dithiophene-4,9-diylidene)dimalononitrile, **2,7-bis(2-ethylhexyl)-diFIDT-di(C(CN)$_2$)** (77 %). **2,7-bis(2-ethylhexyl)-diFIDT-di(C(CN)$_2$)** was freely soluble in many common organic solvents (e.g. chloroform, DCM and THF) and displayed by far the highest solubility of all dicyanomethylene analogues synthesised (40 mg mL^{-1}) and an order of magnitude higher than **2,7-dihexyl-diFIDT-di(C(CN)$_2$)** (4 mg mL^{-1}). This result indicates that the addition of an ethyl branch close to the aromatic core is sufficient to suppress aggregation.

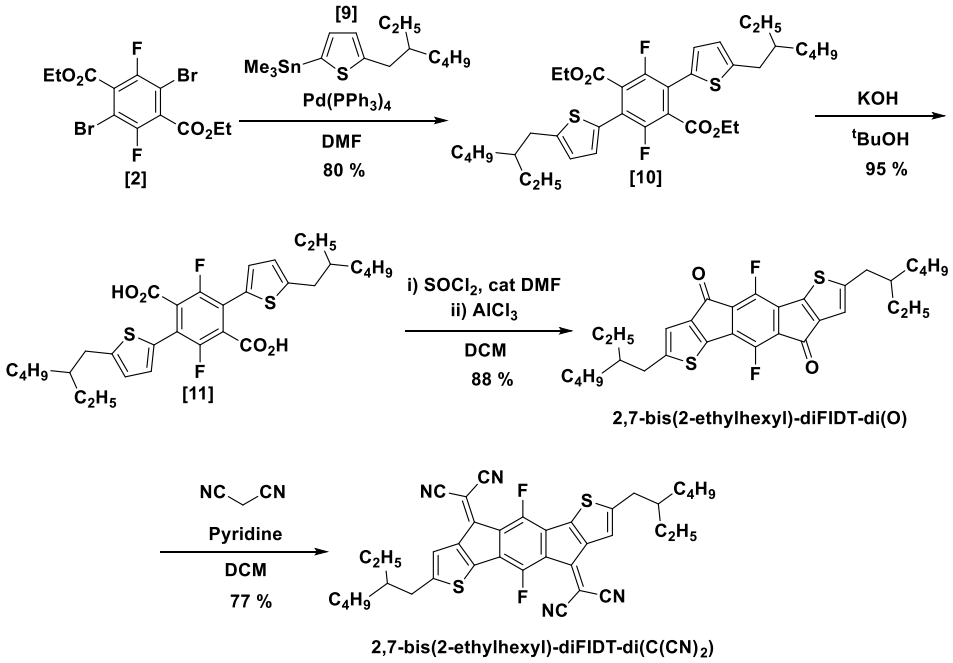


Figure 30: Synthesis of 2,7-bis(2-ethylhexyl)-diFIDT-di(O) and 2,7-bis(2-ethylhexyl-diFIDT-di(C(CN)₂).

The chemical structures of **2,7-bis(2-ethylhexyl)-diFIDT-di(O)** and **2,7-bis(2-ethylhexyl)-diFIDT-di(C(CN)₂)** were verified by ^{1}H NMR, ^{19}F NMR, ^{13}C NMR, IR and HRMS. Single crystal growth was achieved for **2,7-bis(2-ethylhexyl)-diFIDT-di(O)** but not **2,7-bis(2-ethylhexyl)-diFIDT-di(C(CN)₂)**, meaning XRD analysis was possible only on the former.

3.2.3 Synthesis of 3,8-dihexyl-diFIDT-di(O) and 3,8-dihexyl-diFIDT-di(C(CN)₂)

3,8-dihexyl-diFIDT-di(C(CN)₂) was synthesised following the route outlined in **Figure 31**. Diethyl 2,5-dibromo-3,6-difluoroterephthalate (**[2]**) was utilised in a Stille cross-coupling with trimethyl(4-hexylthiophen-2-yl)stannane (**[12]**) using tetrakis(triphenylphosphine)palladium(0) to afford diethyl 2,5-difluoro-3,6-bis(4-hexylthiophen-2-yl)terephthalate (**[13]**) in high yield (83 %) after purification by silica gel chromatography. Saponification with KOH in ethanol afforded a quantitative conversion to the diacid (**[14]**), which was converted to the acid chloride by treatment with $SOCl_2$ in DCM in the

presence of a catalytic amount of DMF. After solvent removal, the resulting water-sensitive material was used directly without purification. Ring closure was achieved by a Lewis acid-promoted intramolecular Friedel-Crafts acylation with $AlCl_3$ to afford the diketone, 3,8-dihexyl-5,10-difluoro-s-indaceno[1,2-b:5,6-b']dithiophene-4,9-dione, **3,8-dihexyl-diFIDT-di(O)** (78 %).

It is noted that limiting the reaction time of the Friedel-Crafts acylation to 4 hrs, as opposed to overnight, was crucial in avoiding the formation of unwanted side-products. NMR and MS analysis appears to indicate that the side-products were some kind of **dialkyl-diFIDT-di(O)**-like dimer/oligomer (**Figure A59** & **A60**). It is well-known that thiophene can polymerise in the presence of a strong Lewis acid (e.g. $AlCl_3$), hence it is feasible that these side-products arise due to the presence of a reactive α-position on the thienyl units.[138] This is supported by the fact that no side-products were observed for any **2,7-dialkyl-diFIDT-di(O)**, where the α-positions are occupied by alkyl chains.

Knoevenagel condensation with malononitrile, pyridine and $TiCl_4$ at room temperature afforded 2,2'-(5,10-difluoro-3,8-dihexyl-s-indaceno[1,2-b:5,6-b']dithiophene-4,9-diylidene)dimalononitrile, **3,8-dihexyl-diFIDT-di(C(CN)$_2$)** (52 %). No reaction was observed, including at elevated temperature, without the addition of $TiCl_4$. $TiCl_4$ is a strong Lewis acid and commonly employed to activate sterically hindered ketones towards nucleophilic attack.[139] The need for $TiCl_4$ indicated that repositioning of the alkyl chain closer to the bridging point induced sufficient steric crowding to hinder attack by the malononitrile anion. **3,8-dihexyl-diFIDT-di(C(CN)$_2$)** displayed unexpectedly high solubility (10 – 13 mg mL^{-1}) in chlorobenzene. This was roughly three times that of the regioisomer **2,7-dihexyl-diFIDT-di(C(CN)$_2$)** (4 mg mL^{-1}), indicating a significant disruption to aggregation.

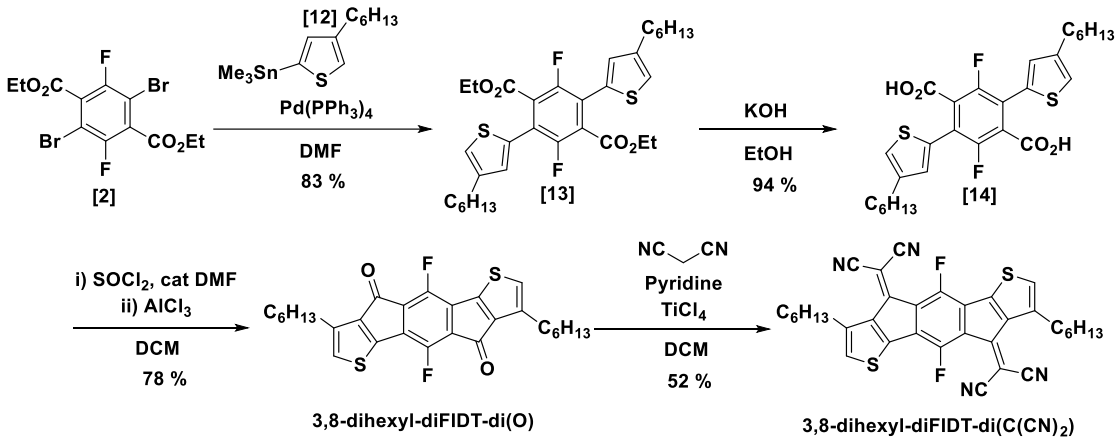


Figure 31: Synthesis of 3,8-dihexyl-diFIDT-di(O) and 3,8-dihexyl-diFIDT-di(C(CN)$_2$).

The chemical structures of **3,8-dihexyl-diFIDT-di(O)** and **3,8-dihexyl-diFIDT-di(C(CN)$_2$)** were verified by ^{1}H NMR, ^{19}F NMR, ^{13}C NMR, IR, HRMS and XRD.

To briefly summarise the discussion on solubility, it was found that the nature of the side-chains has a huge impact on the processability of **dialkyl-diFIDT-di(C(CN)$_2$)**. Linear chain extension from hexyl to dodecyl was shown to reduce solubility dramatically, while replacement with a branched chain, 2-ethylhexyl, had the opposite effect, enhancing solubility ten times versus hexyl. Additionally, repositioning of the hexyl chains from the 2,7-positions to 3,8-positions results in a significant boost to solubility. These observations point to substantial changes in solid state packing and aggregation properties, dependent on the nature of the side-chain. The results are summarised in **Table 5** (procedure outlined in the General Experimental section, Chapter 8).

Table 5: Solubility of dialkyl-diFIDT-di(C(CN)$_2$) analogues in chlorobenzene.

	Alkyl Side-Chain	*Solubility* [mg mL^{-1}, 25 °C]
Non-F	**2,7-dihexyl**	**< 0.2**
Fluorinated	**2,7-dihexyl**	**4.0**
	2,7-didodecyl	**0.3 – 0.5**
	2,7-bis(2-ethylhexyl)	**40**
	3,8-dihexyl	**10 – 13**

3.3 Optoelectronic and Electrochemical Properties

The absorption spectra for the **dialkyl-diFIDT-di(O)** and **dialkyl-diFIDT-di(C(CN)$_2$)** analogues were recorded in solution (10^{-5} M) (**Figure 32**). Spectra were recorded in toluene and chloroform in all cases except for **2,7-didodecyl-diFIDT-di(O)** and **2,7-didodecyl-diFIDT-di(C(CN)$_2$),** where spectra were recorded in chloroform solely due to limited solubility.

As with the 2,7-dihexyl analogues reported in Chapter 2, both **dialkyl-diFIDT-di(O)** and **dialkyl-diFIDT-di(C(CN)$_2$)** analogues displayed strong well-defined absorption bands at shorter wavelengths (250 – 450 nm) as well as broad weak absorption at longer wavelengths (450 – 750 nm and 550 – 1050 nm respectively). Specifically, absorption spectra for 2,7-didodecyl and 2,7-bis(2-ethylhexyl) analogues were very similar to the 2,7-dihexyl analogues, as well as each other. This was expected, owing to the negligible impact of the alkyl side-chains on the electronic properties. Additionally, potential differences due aggregation effects appear minimal, likely due to the low concentration used. Aggregation studies, by either changing the concentration or temperature, were not performed here. Repositioning of the alkyl side-chains

from the 2,7- to 3,8-positions similarly had little effect on the main spectral features yet did result in a more pronounced shoulder at 350 – 450 nm, particularly in **3,8-dihexyl-diFIDT-di(O)**. Time-dependent DFT (TD-DFT) indicated that the oscillator strength of this transition (f = 0.103) arises primarily from improved overlap between HOMO-2 and LUMO (**Figure A66**). **3,8-dihexyl-diFIDT-di(C(CN)$_2$)** also displays greatly reduced absorption intensity at shorter wavelengths than the **2,7-dialkyl-diFIDT-di(C(CN)$_2$)** analogues (**Figure 32f**).

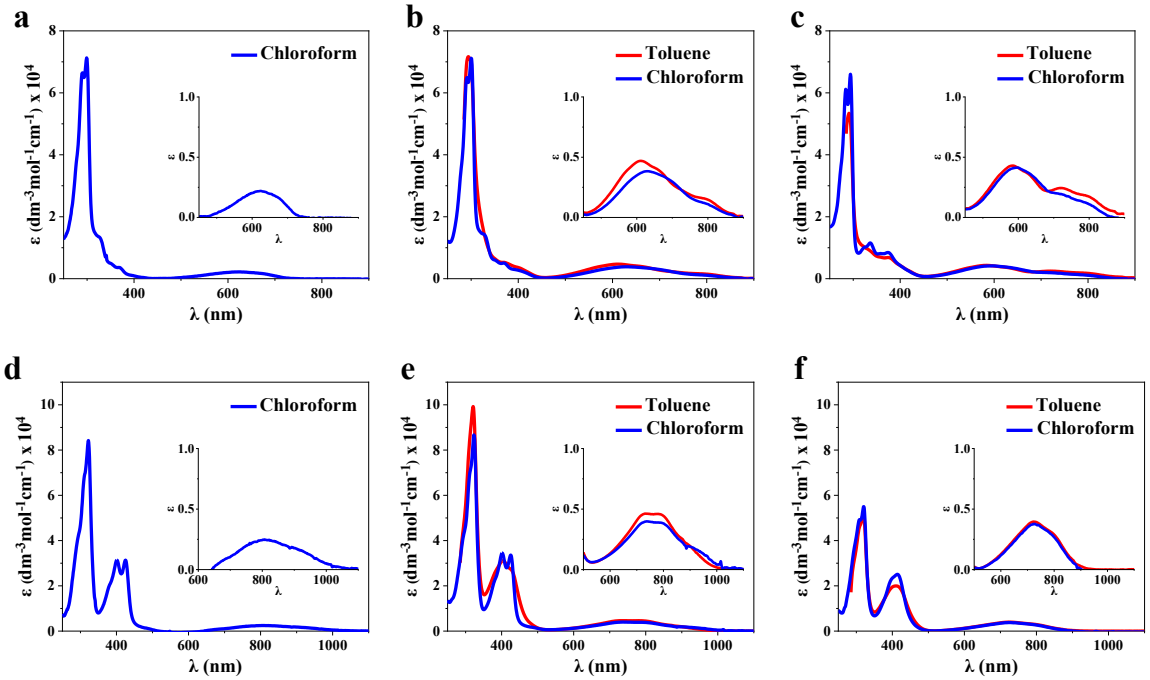


Figure 32: Solution absorption spectra for dialkyl-diFIDT-di(O) (a – c) and dialkyl-diFIDT-di(C(CN)$_2$) (d – f) analogues in toluene and chloroform. a) 2,7-didodecyl-diFIDT-di(O)[a]. b) 2,7-bis(2-ethylhexyl)-diFIDT-di(O). c) 3,8-dihexyl-diFIDT-di(O). d) 2,7-didodecyl-diFIDT-di(C(CN)$_2$)[a]. e) 2,7-bis(2-ethylhexyl)-diFIDT-di(C(CN)$_2$). f) 3,8-dihexyl-diFIDT-di(C(CN)$_2$). [a]toluene spectra not recorded due to low solubility.

Electrochemical studies of the **dialkyl-diFIDT-di(O)** and **dialkyl-diFIDT-di(C(CN)$_2$)** analogues were performed by cyclic voltammetry (CV) using a 0.1 M solution of Bu_4NPF_6 in DCM solutions and a ferrocene (Fc/Fc^+) internal standard. Potentials were swept from 0 V to a positive maximum, then swept back to a negative maximum before returning to 0 V. In line with best practice, energy levels were estimated from $E^{1/2}$ (when reversibility is observed) or

E^i (when irreversibility is observed), where $E^{1/2}$ is the half-wave potential, E^i is the inflection-point potential.[124] HOMO = - ($E^{1/2\ or\ i}$ + 4.8) eV and LUMO = - ($E^{1/2\ or\ i}$ + 4.8) eV for oxidation and reduction respectively, with the ferrocene/ferrocenium reference redox system at 4.8 eV below the vacuum level. Electrochemical data for **2,7-didodecyl-diFIDT-di(O)** and **2,7-didodecyl-diFIDT-di(C(CN)$_2$)** were not recorded due to poor solubility. Oxidation and reduction potentials are summarised in **Table 6**.

No major differences in the cyclic voltammograms were observed between either **dialkyl-diFIDT-di(O)** and **dialkyl-diFIDT-di(C(CN)$_2$)** analogues, reflecting the negligible impact of alkyl chains on the electrochemical properties, akin to that observed with the optoelectronic properties (described above). In particular, the cyclic voltammograms displayed two chemically reversible reductions along with one or two irreversible oxidations (**Figure 33**). **Table 6** highlights that extracted HOMO and LUMO energy levels for both **dialkyl-diFIDT-di(O)** and **dialkyl-diFIDT-di(C(CN)$_2$)** analogues were unchanged between alkyl groups.

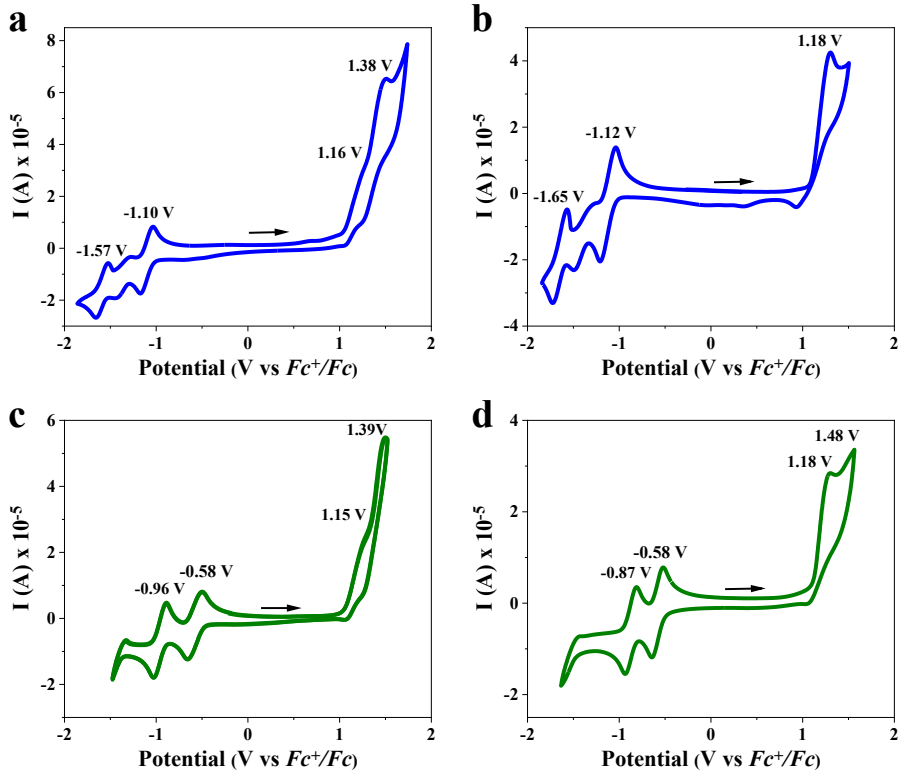


Figure 33: Cyclic voltammagrams of dialkyl-diFIDT-di(O) and dialkyl-diFIDT-di(C(CN)$_2$) analogues, showing corresponding $E^{1/2\ or\ i}$ potentials.

Table 6: Summary of material properties of diFIDT-di(O) and diFIDT-diC(CN)$_2$ compared to the non-fluorinated analogues.

OSC	*HOMO*[a)]	*LUMO*[a)]	λ_{max} *(solution)*
	[eV]	[eV]	[nm]
2,7-didodecyl-diFIDT-di(O)	-[b)]	-[b)]	625, 299, 290[c)]
2,7-didodecyl-diFIDT-di(C(CN)$_2$)	-[b)]	-[b)]	804, 425, 401, 322[c)]
2,7-bis(2-ethylhexyl)-diFIDT-di(O)	- 5.96	- 3.70	612 ,294[c)]
			629, 300, 291[d)]
2,7-bis(2-ethylhexyl)-diFIDT-di(C(CN)$_2$)	- 5.95	- 4.22	739, 404, 321[c)]
			744, 425, 401, 323[d)]
3,8-dihexyl-diFIDT-di(O)	- 5.98	- 3.68	583, 291[c)]
			597, 374, 336, 294[d)]
3,8-dihexyl-diFIDT-di(C(CN)$_2$)	- 5.98	- 4.22	723, 410, 319[c)]
			726, 414, 320[d)]

[a]extracted from CV measurements, [b]no CV data or solution UV-Vis in toluene due to poor solubility, [c]in toluene, [d]in chloroform.

3.4 Crystal Structures

Single crystals were grown for a subset of analogues via the solvent vapour exchange method using either chloroform/methanol (**2,7-bis(2-ethylhexyl)-diFIDT-di(O)** and **3,8-dihexyl-diFIDT-di(C(CN)$_2$)**) or chlorobenzene/methanol (**3,8-dihexyl-diFIDT-di(O)**) mixtures. Crystals of sufficient quality could not be obtained for **2,7-didodecyl-diFIDT-di(O)** and **2,7-didodecyl-diFIDT-di(C(CN)$_2$)**, likely due to the low solubility. Furthermore, only fine powders were achieved for **2,7-bis(2-ethylhexyl)-diFIDT-di(C(CN)$_2$)**.

2,7-bis(2-ethylhexyl)-diFIDT-di(O) crystallised in the triclinic *P*1 space group. The IDT core was completely coplanar, in agreement with the DFT calculations. The 2-ethyhexyl side-chains on the thienyl α-position lie outside the plane. Additional 'floating' atoms indicate some minor disorder in the alkyl chain positioning (**Figure 34a**). Specific short contacts are observed between stacks, including F···F (3.02 Å), S···F (3.16 Å), S···O (3.30 Å) and O···H (2.61 Å) interactions (**Figure 34b**).

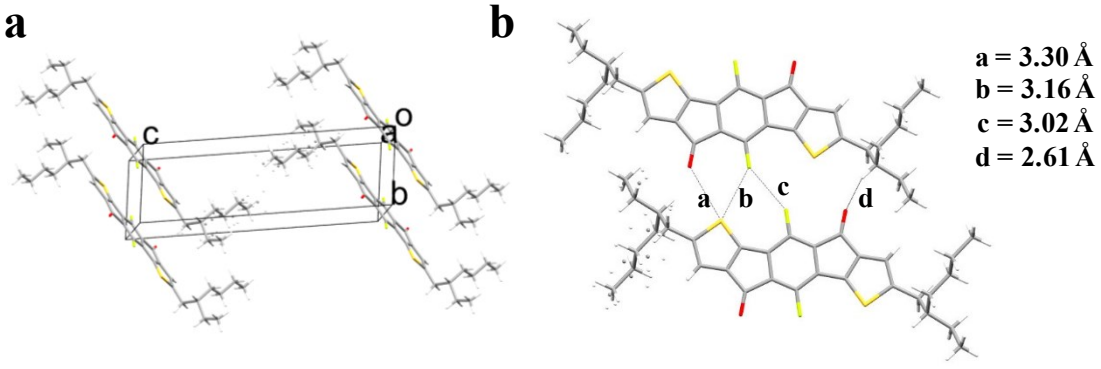


Figure 34: a) Unit cell of 2,7-bis(2-ethylhexyl)-diFIDT-di(O). b) Intermolecular short contacts.

A pseudo-brickwork arrangement, with π-π stacking along the *b* and *a* axes with very partial alkyl chain interdigitation (**Figure 35**). The additional branching ethyl chain thus appears effective at suppressing efficient alkyl side-chain interactions when compared to **2,7-dihexyl-diFIDT-di(O)** (Section 2.4). Such an effect may account for the improved solubility, as discussed in Section 3.2.2. There is co-facial packing of the conjugated core within a stack, with an interplanar stacking distance of 3.51 Å and a slipping distance of 5.03 Å (angle 54.9 °) along the *b* axis and interplanar stacking distance of 2.81 Å and a slipping distance of 5.16 Å (angle 69.5 °) along the *a* axis (**Figure A69**).

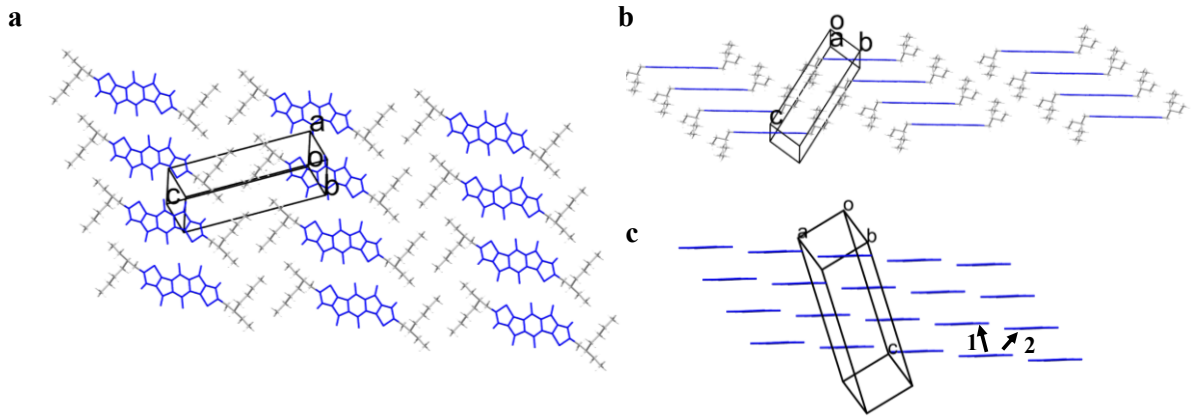


Figure 35: Crystal packing motifs of 2,7-bis(2-ethylhexyl)-diFIDT-di(O). a) top-view. b) side-view, along the molecular short-axis. c) side-view, along the molecular long-axis, indicating the two possible charge transfer pathways.

As for crystal structures discussed in previous chapters, the electron transfer integrals were calculated. A larger value indicates better overlap between frontier molecular orbitals on neighbouring units (LUMO – LUMO, in the case of electron transport) and therefore the potential for more efficient charge transfer. **2,7-bis(2-ethylhexyl)-diFIDT-di(O)** displays a 1-dimensional (1D) charge transfer pathway, despite the pseudo-brickwork stacking arrangement. An electron transfer integral of only 4 meV is found for the main π-stack (along the *b* axis, **1** in **Figure 35c**), whereas a much higher value (76 meV) is found for the π-stack along the *a* axis (**2** in **Figure 35c**).

3,8-dihexyl-diFIDT-di(O) crystallised in the monoclinic *P*2/c space group. The IDT core was completely coplanar, in agreement with the DFT calculations. The hexyl chains on the thienyl *β*-position lie outside the plane at an angle of 79.1 ° (**Figure 36a**). Specific short contacts are observed between stacks, including S···S (3.58 Å), S···F (3.25 Å) and S···O (3.32 Å) interactions (**Figure 36b**).

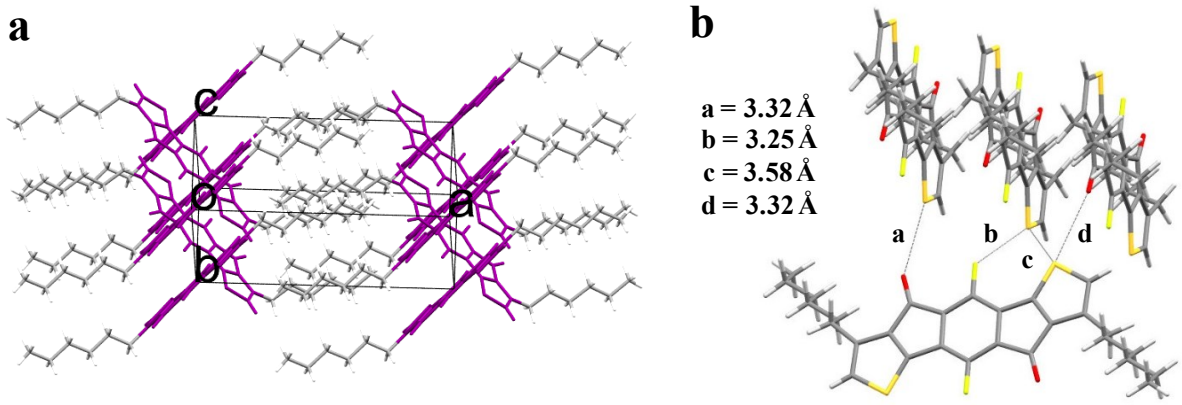


Figure 36: a) Unit cell of 3,8-dihexyl-diFIDT-di(O). b) Intermolecular short contacts.

A planar slipped π-π stacking arrangement is formed along the *b* axis, however adjacent stacks (along the molecular short axis) are arranged almost perpendicular to each other (85.3 °) with good inter-stack registry. Alkyl chain interdigitation is observed between stacks (**Figure 37**). This is in contrast to **2,7-dihexyl-diFIDT-di(O)**, which displays a planar slipped π-π stacking motif without such tilting (Section 2.4). There is co-facial packing of the conjugated core within a stack, along the *b* axis, with an interplanar stacking distance of 3.40 Å and a slipping distance of 3.29 Å (angle 44.1 °) (**Figure A72**). These values are smaller compared to **2,7-dihexyl-diFIDT-di(O)** (interplanar stacking distance of 3.49 Å, slipping distance of 4.34 Å). These observations signify a substantial change in packing motif upon repositioning of alkyl chains from the 2,7- to 3,8-positions. **3,8-Dihexyl-diFIDT-di(O)** displays a 1-dimensional (1D) charge transfer pathway, with an electron transfer integral of 66 meV for the main π-stack.

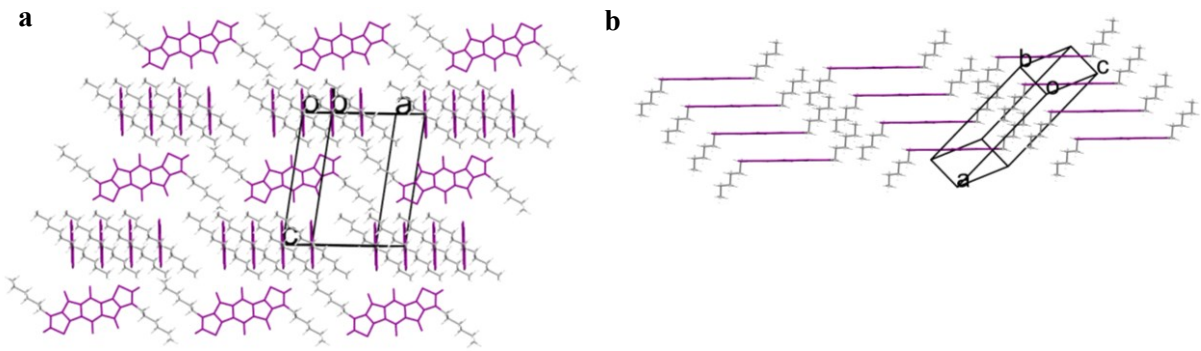


Figure 37: Crystal packing motifs of 3,8-dihexyl-diFIDT-di(O).

3,8-dihexyl-diFIDT-di(C(CN)$_2$) crystallised in the monoclinic P2$_1$/c space group (**Figure 38a**). The IDT core was distorted, in agreement with the DFT calculations. In particular, the dicyanomethylene groups are bent out-of-plane slightly with the IDT (5.4 °). This distortion is less pronounced than that present in **2,7-dihexyl-IDT-di(C(CN)$_2$)** (7.5 °) though a larger apparent twist of the dicyanomethylene groups is observed (**Figure 38b**). The hexyl chains on the thienyl β-position lie outside the plane at an angle of 78.5 ° but are not fully chain extended. In addition, 'floating' atoms indicate some minor disorder in the alkyl chain positioning. Solely intramolecular short contacts are observed, including N···F (2.76 Å), C···F (2.60 Å), S···F (3.16 Å), N···H (2.45 Å) and C···H (2.53 Å) interactions (**Figure 38c**).

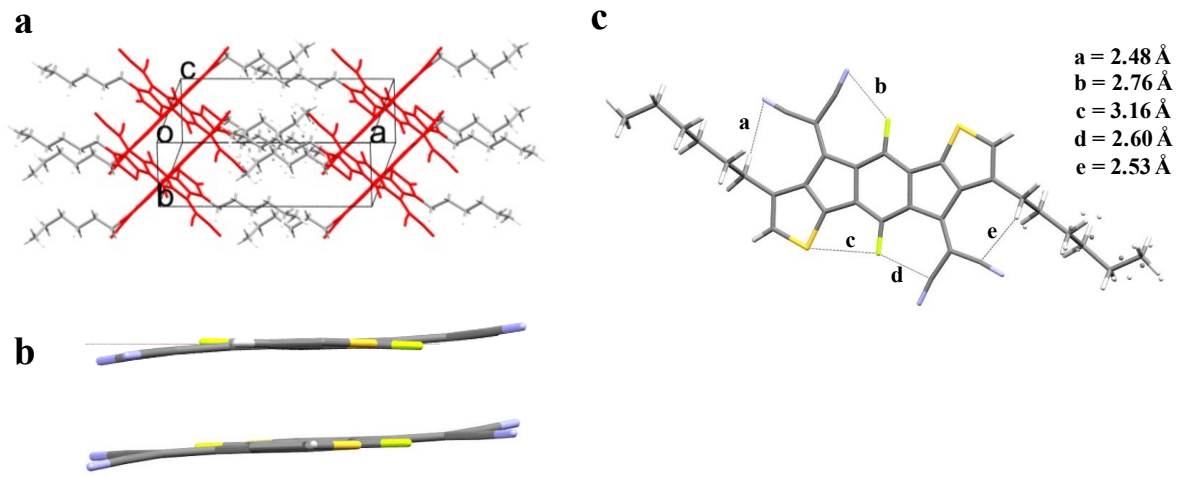


Figure 38: a) Unit cell of 3,8-dihexyl-diFIDT-di(C(CN)$_2$). b) Planarity of 2,7-dihexyl-diFIDT-di(C(CN)$_2$) (top) versus 3,8-dihexyl-diFIDT-di(C(CN)$_2$) (bottom), with alkyl chains removed for clarity (viewed along the long axis). c) Intramolecular short contacts.

A planar slipped π-π stacking arrangement is formed along the *b* axis, however adjacent stacks (along the molecular short axis) are arranged almost perpendicular to each other (88.6 °) with some inter-stack registry. Alkyl chain interdigitation is observed between stacks along the long axis as well as partial interdigitation along the short axis (**Figure 39**). This is similar to the 2,7-dihexyl analogue, **2,7-dihexyl-diFIDT-di(C(CN)$_2$)**, but with better inter-stack registry. There is co-facial packing of the conjugated core within a stack, with an interplanar stacking distance of 3.45 Å and a slipping distance of 3.37 Å (angle 44.3 °) (**Figure A75**). These values are similar to **2,7-dihexyl-diFIDT-di(C(CN)$_2$)** (interplanar stacking distance of 3.43 Å, slipping distance of 2.73 Å).

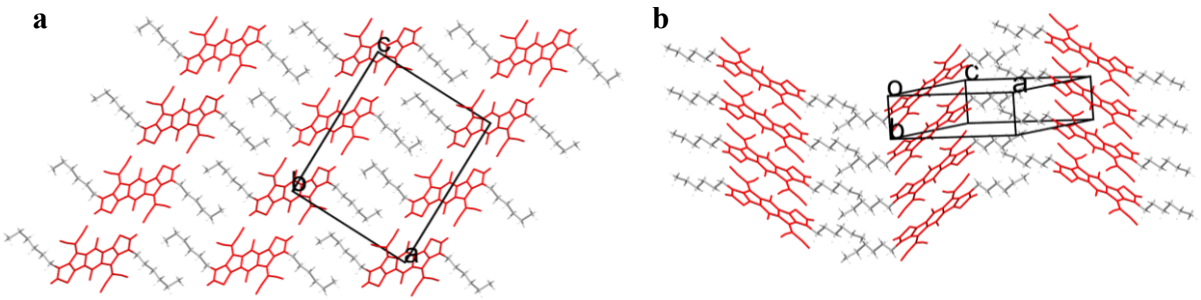


Figure 39: Crystal packing motifs of 3,8-dihexyl-diFIDT-di(C(CN)$_2$).

3,8-dihexyl-diFIDT-di(C(CN)$_2$) displays a one-dimensional (1D) charge transfer pathway, with an electron transfer integral of only 19 meV for the main π-stack, indicating that charge transfer is highly disfavoured. This value is dramatically lower than **2,7-dihexyl-diFIDT-di(C(CN)$_2$)** (129 meV), in spite of both possessing similar interplanar stacking distances. While a larger slipping distance for **3,8-dihexyl-diFIDT-di(C(CN)$_2$)** would certainly suggest a lower expected transfer integral, the near-zero value reflects the non-linear relationship between molecular displacement and transfer integral. This phenomenon has been widely studied, showing that, while transfer integral generally decreases with increasing displacement, there is an oscillation between local maxima and minima.[140,141] These minima (near-zero integral values) occur where lobes of the LUMO on one molecule are positioned over nodes of the LUMO on the neighbouring molecule, resulting in no net stabilising interactions between the LUMOs. **Figure 40** illustrates the poor LUMO – LUMO overlap for **3,8-dihexyl-diFIDT-di(C(CN)$_2$)**, highlighted by the small area of darker shading.

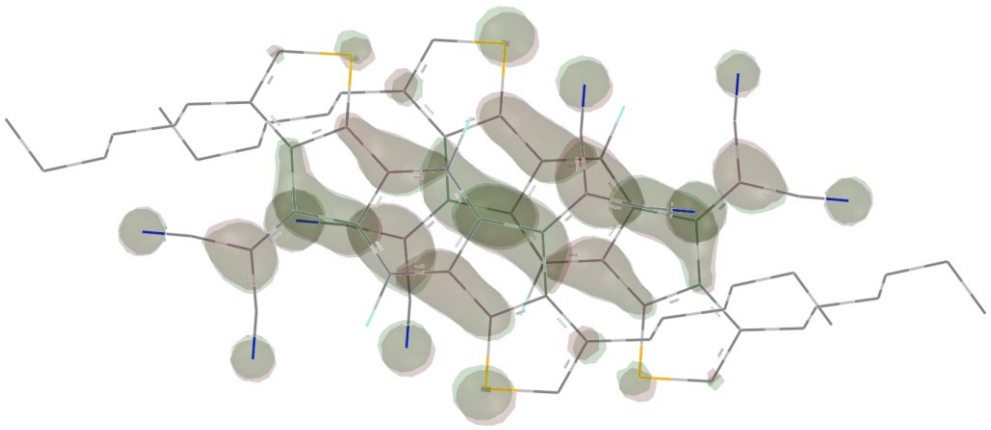


Figure 40: Top view of LUMOs on neighbouring 3,8-dihexyl-diFIDT-di(C(CN)$_2$) molecules in the π-stack , with darker shading highlighting areas of LUMO – LUMO overlap.

Interestingly, an appreciable electron mobility is still realised when utilising **3,8-dihexyl-diFIDT-di(C(CN)$_2$)** in OFET devices (*vide infra*). This observation highlights a disparity between the relative molecular orientations in the single crystal and those in the thin-film of

the OFET devices. A non-perfect correlation between the single crystal structures and thin-films is an important factor to remember when trying to draw conclusions. Additionally, the common conception that the high order of a single crystal represents the optimum molecular arrangement for charge transfer is not true in this case.

3.5 Thermal Properties

The thermal behaviour of the three new **dialkyl-diFIDT-di(O)** and three new **dialkyl-diFIDT-di(C(CN)$_2$)** analogues was investigated by TGA (**Figure 41a** and **Figure 41b** respectively) and DSC (**Figure 42a** and **Figure 42b** respectively). Key data are summarised in **Table 7**.

All three **dialkyl-diFIDT-di(O)** analogues exhibit high thermal stability, with the onset of decomposition (T_d) (temperature at which 5 % mass loss is reached) occurring at 360 – 370 °C. This is in line with that observed for **2,7-dihexyl-diFIDT-di(O)** (T_d = 360 °C). No specific trend was observed by changing the alkyl chain, indicating that the nature of the alkyl chains contributed minimally to thermal stability. All three **dialkyl-diFIDT-di(C(CN)$_2$)** analogues exhibited lower thermal stability than the **dialkyl-diFIDT-di(O)** analogues. Again, there was no specific trend for the 2,7-disubstituted analogues, however the depression was particularly severe for the 3,8-dihexyl analogue, where a 70 °C decrease was observed versus the **dialkyl-diFIDT-di(O)** analogue.

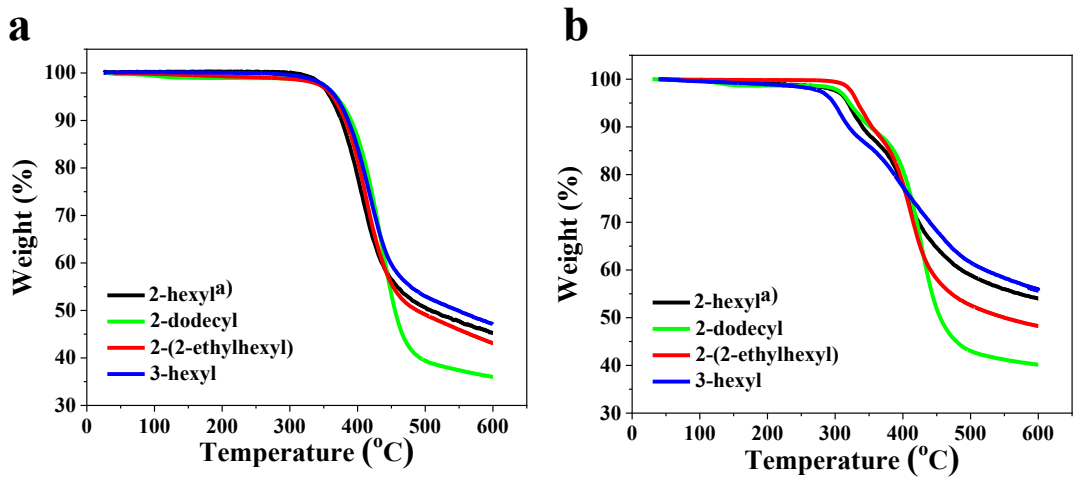


Figure 41: TGA plots for a) 2,7-dihexyl-[a)], 2,7-didodecyl-, 2,7-bis(2-ethylhexyl)- and 3,8-dihexyl-diFIDT-di(O). b) 2,7-dihexyl-[a)], 2,7-didodecyl-, 2,7-bis(2-ethylhexyl)- and 3,8-dihexyl-diFIDT-di(C(CN)$_2$). [a)]data from Chapter 2.

All three **dialkyl-diFIDT-di(O)** analogues displayed strong melting and crystallisation transitions which were stable upon repeated thermal cycling (**Figure A76**). Additional lower temperature non-reproducible melting transitions suggest the presence of polymorphs in the powder. Furthermore, along with the isotropic transition observed at 191 °C, **2,7-didodecyl-diFIDT-di(O)** exhibited a weak reproducible endotherm at ~ 177 °C, suggesting a crystal-to-crystal or crystal-to-mesophase transition. In all cases the melting points were lower compared to **2,7-dihexyl-diFIDT-di(O)**. Extension of the alkyl side-chain to dodecyl chains resulted in a relatively large decrease (~ 30 °C) while replacement with a branched chain had a smaller impact (8 °C). The effects of these side-chains may be suppressed somewhat due to the relative increase in molecular weight. Repositioning of the hexyl chains from the 2,7- to 3,8-positions also caused a significant decrease (45 °C). The decrease indicated that this simple modification resulted in a large disruption to the intermolecular interactions.

All three **dialkyl-diFIDT-di(C(CN)$_2$)** analogues displayed strong melting and crystallisation transitions but were unstable upon repeated thermal cycling, with changes occurring in the peak positions and intensity. The melting points of all three **dialkyl-diFIDT-di(C(CN)$_2$)** analogues

were higher than the corresponding **dialkyl-diFIDT-di(O)**, highlighting the stronger intermolecular interactions induced by the strong dicyanomethylene EWGs. A minimal increase for the branched side-chain (8 °C) perhaps indicated that disruption from branching offsets the dicyanomethylene somewhat. **3,8-Dihexyl-diFIDT-di(C(CN)$_2$)** (T_m = 238 °C) displayed a large increase in T_m versus the corresponding diketone (T_m = 176 °C). For all three analogues, T_m values were lower than **2,7-dihexyl-diFIDT-di(C(CN)$_2$)**, as was observed for the **dialkyl-diFIDT-di(O)** analogues.

Extending the alkyl chain to dodecyl chains caused a moderate increase in melting temperature of **2,7-didodecyl-diFIDT-di(C(CN)$_2$)** versus the **2,7-didodecyl-diFIDT-di(O)** analogue (25 °C), similar to that observed for C_6H_{13} (27 °C). In addition to this however, the DSC thermogram of **2,7-didodecyl-diFIDT-di(C(CN)$_2$)** contained a strong reproducible endotherm at lower temperature (T_m ~ 173 °C). The presence of multiple endotherms (upon heating) and exotherms (upon cooling) is indicative of typical liquid-crystalline behaviour.[142] A similar effect has been reported previously by Ozdemir et al. concerning an electron-deficient indenofluorene OSC.[143] Polarised optical microscopy was used in order to probe these transitions further. Upon heating, no obvious change was observed above 173 °C. Heating the sample to 220 °C resulted in the formation of an isotropic black liquid. Upon cooling (2 °C min^{-1}) partial slow crystallisation to a birefringent solid was observed. Further cooling to below 85 °C appeared to show a further crystallisation to a more ordered state. These results support possible liquid-crystalline behaviour, however the irreversible formation of an amorphous black substance indicates that **2,7-didodecyl-diFIDT-di(C(CN)$_2$)** is unstable upon melting in air. This fact made confirmation of liquid-crystalline behaviour difficult.

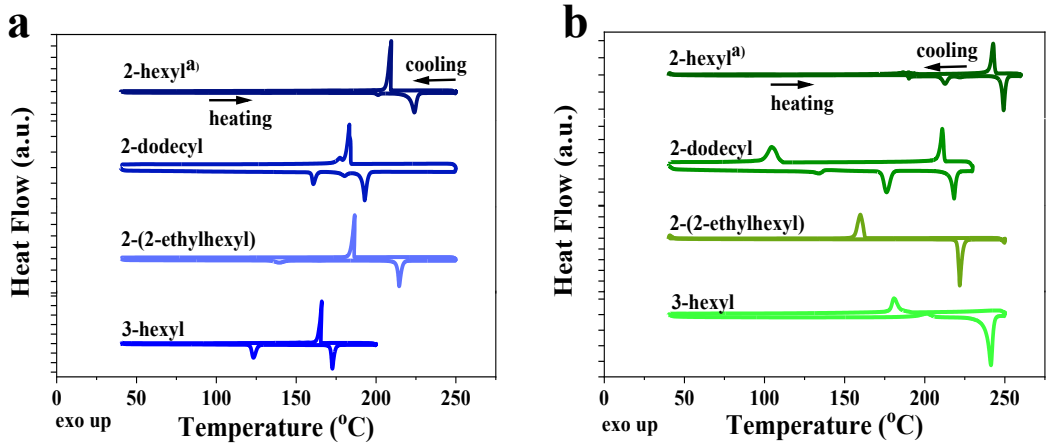


Figure 42: DSC plots (1st Cycle) for a) 2,7-dihexyl-[a)], 2,7-didodecyl-, 2,7-bis(2-ethylhexyl)- and 3,8-dihexyl-diFIDT-di(O). b) 2,7-dihexyl-[a)], 2,7-didodecyl-, 2,7-bis(2-ethylhexyl)- and 3,8-dihexyl-diFIDT-di(C(CN)$_2$). [a)]data from Chapter 2.

Overall, while modification of the side-chains could impart minor improvements to the thermal stability, it appears all three alkyl side-chains had an overall negative impact on the intermolecular interactions, as evidenced by a reduction in T_m versus the 2,7-dihexyl analogues. In particular, repositioning of the C_6H_{13} chains from the 2,7-positions to the 3,8-positions impacted thermal properties drastically, indicating a profound change in crystal packing. Lengthening the side-chain induced suspected liquid-crystalline behaviour. Such a property may be advantageous for film-forming properties.

Table 7: Summary of TGA and DSC data for diFIDT-di(O) and diFIDT-di(C(CN)$_2$) analogues.

Alkyl Side-Chain	*diFIDT-di(O)*			*diFIDT-di(C(CN)$_2$)*		
	T_d [°C]	T_m [°C]	ΔH_m [J g^{-1}]	T_d [°C]	T_m [°C]	ΔH_m [J g^{-1}]
2,7-dihexyl[a)]	**360**	**221**	**83**	**319**	**248**	**59**
2,7-didodecyl	**369**	**177, 191**	**-**[b)]	**321**	**173, 216**	**44, 41**
2,7-bis(2-ethylhexyl)	**364**	**213**	**70**	**333**	**221**	**62**
3,8-dihexyl	**368**	**176**	**63**	**298**	**238**	**79**

[a)]data from Chapter 2. [b)]overlap of peaks prevented accurate extraction of ΔH_m.

3.6 OFET Performance

OFET devices incorporating the **dialkyl-diFIDT-di(C(CN)$_2$)** OSCs were fabricated via spin-coating and/or blade-coating. This enabled the effects of the alkyl side-chain on device performance to be investigated, in particular for comparison to the high performing **2,7-dihexyl-diFIDT-di(C(CN)$_2$)** analogue explored in Chapter 2. Key parameters are summarised in **Table 8**. No functioning devices using the corresponding diketones were able to be fabricated, hence they will not be discussed here. Both spin-coated and blade-coated devices were fabricated following the same procedure to that outlined in Chapter 2, unless otherwise stated. We are still awaiting the majority of device data, owing to delays due to the global covid-19 crisis. As a result, analyses of device performance are limited. In particular, we are unable to explore the effects of the 2,7-bis(2-ethylhexyl) side-chains nor make any comparisons between spin-coated and blade-coated devices.

Devices with all **dialkyl-diFIDT-di(C(CN)$_2$)** analogues tested exhibit unipolar electron transport. Hence, there appears to be no dependence of majority carrier on the type of alky side-chain, unlike that observed by Xu et al. for **dialkyl-IDT-di(O)** (Section 3.1). The saturated mobility is extracted from the linear part of the square root of the drain current (**Figure A77a**

& A78a). Absence of any double slope in the plot confirms the reliability of the data. Also, the saturated mobility value remains relatively constant with gate voltage above V_T (**Figure A78c**).

In all cases, saturated electron mobilities of ≥ 0.1 $cm^2 V^{-1} s^{-1}$ were achieved. This highlights the intrinsically effective charge transport properties of the **diFIDT-di(C(CN)$_2$)** core. However, performance was not observed to improve versus **2,7-dihexyl-diFIDT-di(C(CN)$_2$)** for any modification to the alkyl side-chains tested. A slight reduction in the performance of spin-coated devices using **2,7-didodecyl-diFIDT-di(C(CN)$_2$)** may be attributable to poorer control of thin-film morphology upon deposition due to reduced solubility. Despite improved solution-processability of **3,8-dihexyl-diFIDT-di(C(CN)$_2$)** versus **2,7-dihexyl-diFIDT-di(C(CN)$_2$)**, blade-coated devices also showed reduced performance. This may reflect the poorer π-π overlap within stacks as well as increased disorder of the side-chains, indicated from single crystal analysis (Section 3.5), however a more detailed comparison of the thin-film morphologies is needed.

Table 8: Summary of OFET device performance for dialkyl-diFIDT-di(C(CN)$_2$) analogues in bottom contact-top gate contact configuration (best values in brackets).

Alkyl Side-Chain	*Deposition*	V_T	μ_{linear}	$\mu_{saturated}$	I_{on}/I_{off}
		[V]	[$cm^2 V^{-1} s^{-1}$]	[$cm^2 V^{-1} s^{-1}$]	
2,7-dihexyl-[a)]	Spin-coated	8.2	0.12	0.33 (0.33)	10^2
	Blade-coated	12.4	0.01	0.34 (0.49)	10^2-10^3
2,7-didodecyl-	Spin-coated[b)]	43	0.12	0.21 (0.24)	10^4
	Blade-coated	-[c)]	-[c)]	-[c)]	-[c)]
2,7-bis(2-ethylhexyl)-	Spin-coated	-[c)]	-[c)]	-[c)]	-[c)]
	Blade-coated	-[c)]	-[c)]	-[c)]	-[c)]
3,8-dihexyl-	Spin-coated	-[c)]	-[c)]	-[c)]	-[c)]
	Blade-coated	17.2	0.04	0.14 (0.20)	10^3

[a)]data from Chapter 2, [b)]annealed at 200 °C, [c)]awaiting device data.

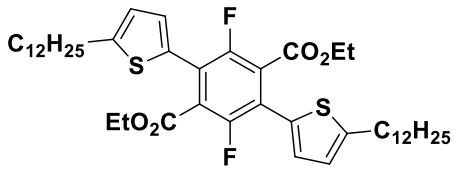
3.7 Conclusion

Three novel **dialkyl-diFIDT-di(O)** and **dialkyl-diFIDT-di(C(CN)$_2$)** OSCs were synthesised, following the general route outlined in Chapter 2, in comparable yields. Knoevenagel condensation to access **2,7-didodecyl-diFIDT-di(C(CN)$_2$)** required the use of toluene as a solvent at elevated temperature (as opposed to DCM at room temperature) due to limited solubility of **2,7-didodecyl-diFIDT-di(O)**. Repositioning the side-chains to the 3,8-positions impacted the Friedel-Crafts intramolecular acylation step, with short reaction times identified as crucial to avoiding the formation of dimeric/oligomeric side-products. Extension of the side chain length is seen to decrease processability significantly, such that characterisation and/or device fabrication of both **2,7-didodecyl-diFIDT-di(O)** and **2,7-didodecyl-diFIDT-di(C(CN)$_2$)** is hindered. Conversely, introduction of branched side-chains conveys a major improvement to handling and processability. This is most likely as a result of suppressed side-chain interdigitation, as apparent from the single crystal analysis of **2,7-bis(2-ethylhexyl)-diFIDT-di(O)**. There is also a surprising improvement in solubility upon repositioning of the hexyl chains to the 3,8-positions.

As expected, optoelectronic and electrochemical properties are little affected by the choice of side-chain, owing to the minimal impact they have on the π-system. LUMO energy levels remain in the range of - 4.22 eV to - 4.24 eV. A lack of data means the effects side-chain engineering on device performance remain to be fully determined. However, from the data that was obtained, it appears that **2,7-dihexyl-diFIDT-di(C(CN)$_2$)** (Chapter 2) remains the highest performing. Poorer solution-processability (**2,7-didodecyl-diFIDT-di(C(CN)$_2$)**) and poorer frontier molecular orbital overlap (**3,8-dihexyl-diFIDT-di(C(CN)$_2$)**) are presented as possible explanations. In spite of these issues, unipolar saturated electron mobilities of > 0.1 $cm^2 V^{-1} s^{-1}$ were still observed.

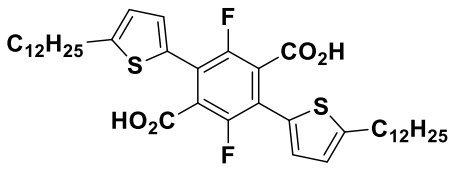
3.8 Experimental

Diethyl 2,5-difluoro-3,6-bis(5-dodecylthiophen-2-yl)terephthalate ([7]):



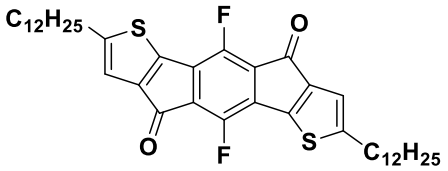
A mixture of 2,5-Dibromo-3,6-difluoroterephthalic acid diethyl ester (**[2]**) (2.5 g, 6.0 mmol), (5-dodecylhexyl)thiophen-2-yl)trimethylstannane (**[6]**) (6.0 g, 14.4 mmol) in anhydrous DMF (40 mL) were degassed for 45 mins. Tetrakis(triphenylphosphine)palladium(0) (347 mg, 0.3 mmol, 0.05 equiv) was added and the mixture degassed for a further 15 mins. The mixture was stirred at 100 °C for 17 hours. The mixture was diluted with DCM (100 mL) and the crude reaction mixture passed through a plug of 15 % KF in silica, eluting with DCM. The solvent was then concentrated in vacuo. DCM (100 mL) was added and the organic phase washed with water (4 x 50 mL) and brine (50 mL). The combined organics were dried over anhydrous magnesium sulfate, filtered and the solvent removed in vacuo. The crude product was purified by silica gel chromatography (petroleum ether 4:1 DCM). The product was collected and dried under vacuum to give the product (2.96 g, 64 %) as pale yellow needle crystals. ^{1}H NMR (400 MHz, $CDCl_3$, δ): 7.01 (d, ^{3}J = 3.5 Hz, 2 H, ArH), 6.76 (d, ^{3}J = 3.5 Hz, 2 H, ArH), 4.26 (q, ^{3}J = 7.2 Hz, 4 H, CH_2), 2.83 (t, ^{3}J = 7.5 Hz, 4 H, CH_2), 1.69 (p, ^{3}J = 7.5 Hz, 4 H, CH_2), 1.40 – 1.22 (m, 36 H, CH_2), 1.18 (t, J = 7.1 Hz, 6 H, CH_3), 0.93 – 0.83 (m, 6H). ^{13}C NMR (101 MHz, $CDCl_3$): δ 163.94, 152.01 (dd, ^{1}J = 250 Hz, ^{4}J = 4.0 Hz, CF), 149.41, 129.44, 128.43, 125.10 – 124.86 (m, CF), 124.47, 122.00 – 121.79 (m, CF), 62.41, 32.06, 31.73, 30.22, 29.81, 29.78, 29.70, 29.50, 29.26, 22.83, 14.26, 13.96 (some overlapping carbons). ^{19}F NMR (377 MHz, $CDCl_3$, δ): - 119.91 (s, CF). HRMS (APCI) m/z: $[M+H]^+$ calcd. for $C_{44}H_{64}F_2O_4S_2$, 758.4209; found, 758.4203.

***2,5-Bis(5-dodecylthiophen-2-yl)-3,6-difluoroterephthalic acid ([8])**:*



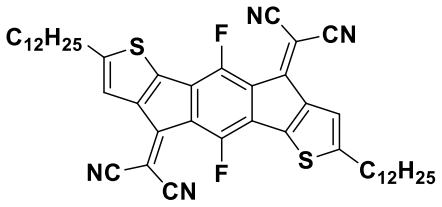
Diethyl 2,5-difluoro-3,6-bis(5-dodecylthiophen-2-yl)terephthalate ***([7])*** (2.5 g, 3.29 mmol) was suspended in *tert*-butanol (50 mL). KOH (1.48 g, 26.35 mmol) was added as a single portion. The suspension was heated to reflux overnight. Upon heating a solution followed by a suspension was observed. The reaction was cooled to room temperature and aqueous hydrochloric acid (2.0 M, 75 mL) was added with stirring for 5 mins. The resulting precipitate was filtered, washed with plenty of water and dried in an oven at 140 °C to give the product (2.15 g, 93 %) as a cream brick-like solid. ^{1}H NMR (400 MHz, DMSO-d_6, 120 °C, δ): 7.13 (d, ^{3}J = 3.6 Hz, 2 H, ArH), 6.90 (d, ^{3}J = 3.6 Hz, 2 H, ArH), 2.86 (t, ^{3}J = 7.8 Hz, 4 H, CH_2), 1.70 (p, ^{3}J = 7.8 Hz, 4 H, CH_2), 1.45 – 1.24 (m, 36 H, CH_2), 0.88 (t, ^{3}J = 6.8 Hz, 6 H, CH_3). ^{13}C NMR (101 MHz, DMSO-d_6, 120 °C, δ): 163.25, 150.38 (dd, ^{1}J = 247 Hz, ^{4}J = 3 Hz, CF), 148.13, 128.87, 127.15, 125.14 – 124.88 (m, CF), 123.94, 119.95 – 119.71 (m, CF), 30.52, 30.18, 28.64, 28.23, 28.21, 28.14, 27.92, 27.86, 27.75, 21.21, 12.90 (some overlapping carbons). ^{19}F NMR (377 MHz, DMSO-d_6, 120 °C, δ): - 120.01 (s, CF). HRMS (APCI) m/z: $[M+H]^+$ calcd. for $C_{40}H_{57}F_2O_4S_2$, 703.3661; found, 703.3652.

***2,7-Didodecyl-5,10-difluoro-s-indaceno[1,2-b:5,6-b']dithiophene-4,9-dione (2,7-didodecyl-diFIDT-di(O))**:*



2,5-Difluoro-3,6-di-(5-dodecylthiophen-2-yl-terephthalic acid ***([8])*** (2.0 g, 2.80 mmol) was suspended in anhydrous DCM (40 mL) and catalytic anhydrous DMF (0.11 mL, 1.4 mmol). Thionyl chloride (1.24 mL, 17.1 mmol) was added dropwise over 15 minutes. The reaction heated to 50 °C overnight. Solvent was removed to give an orange oil which was used in the next step without further purification. The acyl chloride was redissolved in anhydrous DCM (50 mL) and then added to a suspension of anhydrous $AlCl_3$ (1.93 g) in DCM (50 mL) at 0 °C. The resultant mixture was allowed to warm to room temperature and stirred overnight. The mixture was poured into cold aqueous hydrochloric acid (2.0 M, 100 mL), causing a deep blue precipitate to form which was collected by filtration. Washing with aqueous hydrochloric acid (2.0 M), water, and acetone followed by drying in vacuo afforded a cyan blue solid (1.37 g, 85 %). m.p. 191 °C. ^{1}H NMR (500 MHz, TCE-d_2, 120 °C, δ): 6.90 (s, 2 H, ArH), 2.88 (t, ^3J = 7.5 Hz, 4 H, CH_2), 1.78 (p, ^3J = 7.4 Hz, 4 H, CH_2), 1.56 – 1.31 (m, 36 H, CH_2), 1.01 – 0.91 (t, ^3J = 6.9 Hz 6 H, CH_3). ^{13}C NMR (126 MHz, TCE-d_2, 120 °C, δ): 181.33, 154.17, 149.26, 146.13 (dd, ^1J = 265 Hz, ^4J = 2.5 Hz, CF), 140.57, 129.44 – 129.23 (m, CF), 127.27 – 127.10 (m, CF), 117.89, 31.58, 30.92, 30.42, 29.29, 29.26, 29.14, 28.95, 28.92, 28.68, 22.28, 13.59 (some carbons overlapping. ^{19}F NMR (471 MHz, TCE-d_2, 120 °C, δ): - 129.39 (s, CF). IR (cm^{-1}) 1715 (C=O). HRMS (APCI) m/z: $[M+H]^+$ calcd. for $C_{40}H_{53}O_2S_2F_2$, 667.3450; found, 667.3464.

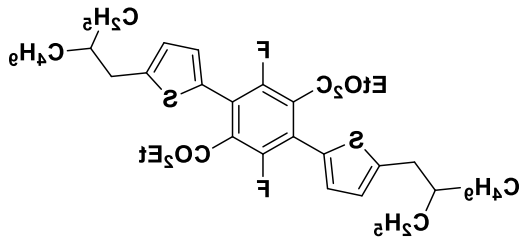
2,2'-(5,10-Difluoro-2,7-didodecyl-s-indaceno[1,2-b:5,6-b']dithiophene-4,9-diylidene)dimalononitrile (2,7-didodecyl-diFIDT-di(C(CN)$_2$)):



2,7-Didodecyl-5,10-difluoro-s-indaceno[1,2-b:5,6-b']dithiophene-4,9-dione (200 mg, 0.3 mmol) and malononitrile (200 mg, 3.0 mmol) were suspended in anhydrous toluene (40 mL).

Pyridine (2.72 mL, 33.6 mmol) was added and the mixture stirred overnight at 80 °C. Solids dissolved upon heating. Aqueous hydrochloric acid (2.0 M, 40 mL) was added and the resulting precipitate was filtered and washed with water, methanol and acetone to give a green brick-like solid. The crude product was reprecipitated in the minimum amount of hot chloroform with methanol, filtered, washed with methanol and dried to give a pale green solid (150 mg, 66 %). m.p. 216 °C. ^{1}H NMR (400 MHz, TCE-d_2, δ): 7.32 (s, 2 H, ArH), 2.84 (t, ^{3}J = 7.6 Hz, 4 H, CH_2), 1.69 (p, ^{3}J = 7.6 Hz, 4 H, CH_2), 1.43- 1.20 (m, 36 H, CH_2), 0.88 (t, ^{3}J = 6.9 Hz, 6 H, CH_3). ^{13}C NMR (101 MHz, TCE-d_2, 120 °C, δ): 155.04, 152.32, 149.31, 144.28, 139.50, 119.97, 113.14, 111.88, 81.83, 31.59, 30.90, 30.69, 29.29, 29.26, 29.14, 28.95, 28.91, 28.70, 22.29, 13.60 (some carbons missing due to poor solubility). ^{19}F NMR (377 MHz, TCE-d_2, δ): - 108.11 (s, CF). IR (cm^{-1}) 2222 (C≡N). HRMS (APCI) m/z: [M+H]+ calcd. for $C_{46}H_{52}F_2N_4S_2$, 762.3596; found, 762.3587.

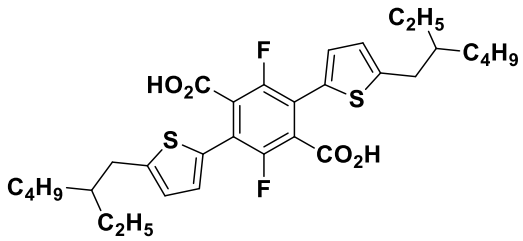
***Diethyl 2,5-difluoro-3,6-bis(5-(2-ethylhexyl)thiophen-2-yl)terephthalate ([10])**:*



A mixture of 2,5-dibromo-3,6-difluoroterephthalic acid diethyl ester ***([2])*** (2.65 g, 6.4 mmol), (5-(2-ethylhexyl)thiophen-2-yl)trimethylstannane ***([9])*** (5.5 g, 15.31 mmol) in anhydrous DMF (40 mL) were degassed for 45 mins. Tetrakis(triphenylphosphine)palladium(0) (368 mg, 0.32 mmol, 0.05 equiv) was added and the mixture degassed for a further 15 mins. The mixture was stirred at 100 °C for 17 hours. The mixture was diluted with DCM (100 mL) and the crude reaction mixture passed through a plug of 15 % KF in silica, eluting with DCM. The solvent was then concentrated in vacuo. DCM (100 mL) was added and the organic phase washed with

water (4 x 50 mL) and brine (50 mL). The combined organics were dried over anhydrous magnesium sulfate, filtered and the solvent removed in vacuo. The crude product was purified by silica gel chromatography (petroleum ether 4:1 DCM). The product was collected and dried under vacuum to give diethyl 2,5-difluoro-3,6-bis(5-(2-ethylhexyl)thiophen-2-yl)terephthalate (3.28 g, 80 %) as an orange oil. ^{1}H NMR (400 MHz, $CDCl_3$, δ): 7.01 (d, ^{3}J = 3.6 Hz, 2 H, ArH), 6.75 (d, ^{3}J = 3.6 Hz, 2 H, ArH), 4.25 (q, ^{3}J = 7.1 Hz, 4 H, CH_2), 2.77 (d, ^{3}J = 6.7 Hz, 4 H, CH_2), 1.62 – 1.54 (m, 2 H, CH), 1.39 – 1.24 (m, 16 H, CH_2), 1.18 (t, ^{3}J = 7.1 Hz, 6 H, CH_3), 0.89 (t, ^{3}J = 7.4 Hz, 12 H, CH_3). ^{13}C NMR (101 MHz, $CDCl_3$, δ): 163.97, 152.03 (dd, ^{1}J = 250 Hz, ^{4}J = 4.0 Hz, CF), 147.99, 129.38, 128.68, 125.53, 125.05 – 124.78 (m, CF), 121.98 – 121.68 (m, CF), 62.42, 41.58, 34.17, 32.51, 28.99, 25.65, 23.13, 14.26, 13.94, 10.96. ^{19}F NMR (377 MHz, $CDCl_3$, δ): - 119.96 (s, CF). HRMS (ES^+) m/z: $[M+H]^+$ calcd. for $C_{36}H_{48}F_2O_4S_2$, 647.3045; found, 647.3057.

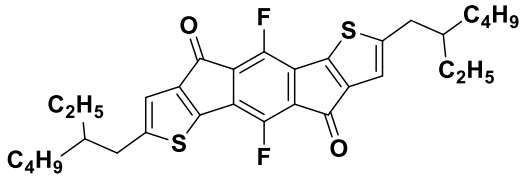
***2,5-Bis(5-2-(ethylhexyl)thiophen-2-yl)-3,6-difluoroterephthalic acid ([11])**:*



Diethyl 2,5-difluoro-3,6-bis(5-(2-ethylhexyl)thiophen-2-yl)terephthalate ***([10])*** (3.00 g, 4.64 mmol) was suspended in *tert*-butanol (100 mL). KOH (2.60 g, 46.40 mmol) was added as a single portion. The suspension was heated to reflux overnight. Upon heating a solution followed by a suspension was observed. The reaction was cooled to room temperature and the solvent removed. The crude was redissolved in ethanol (100 mL) and aqueous hydrochloric acid (2.0 M, 75 mL) was added with stirring for 5 mins. The resulting precipitate was filtered, washed with plenty of water and dried in a vacuum oven at 100 °C (150 mbar) to give 2.60 g

(95 %) of cream solid. ^{1}H NMR (400 MHz, DMSO-d_6, δ): 7.13 (d, ^{3}J = 3.6 Hz, 2 H, ArH), 6.91 (d, ^{3}J = 3.6 Hz, 2 H, ArH), 2.77 (d, ^{3}J = 6.9 Hz, 4 H, CH_2), 1.61 – 1.51 (m, 2 H, CH), 1.37 – 1.19 (m, 16 H, CH_2), 0.90 – 0.81 (m, 12 H, CH_3). ^{13}C NMR (101 MHz, DMSO-d_6, δ): 164.47, 150.58 (dd, ^{1}J = 246 Hz, ^{4}J = 3.5 Hz, CF), 147.28, 129.53, 127.84, 126.07, 125.60 – 125.26 (m, CF), 120.20 – 119.93 (m, CF), 40.77, 33.27, 31.79, 28.22, 25.05, 22.46, 13.97, 10.60. ^{19}F NMR (377 MHz, DMSO-d_6, δ): - 120.82 (s, CF). HRMS (CI) m/z: $[M+H]^+$ calcd. for $C_{32}H_{40}F_2O_4S_2$, 591.2409; found, 591.2389.

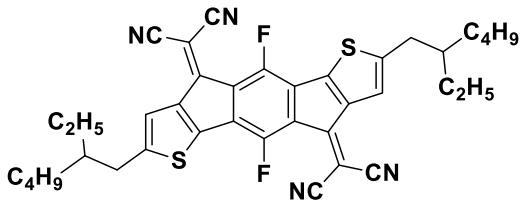
2,7-Bis(2-ethylhexyl)-5,10-difluoro-s-indaceno[1,2-b:5,6-b']dithiophene-4,9-dione (2,7-bis(2-ethylhexyl)-diFIDT-di(O)):



2,5-Difluoro-3,6-di-(5-(2-ethylhexyl)thiophen-2-yl-terephthalic acid ***([11])*** (2.7 g, 4.57 mmol) was suspended in anhydrous DCM (60 mL) and catalytic anhydrous DMF (0.2 mL, 2.28 mmol). Thionyl chloride (3.33 mL, 45.7 mmol) was added dropwise over 15 minutes. The reaction heated to 50 °C overnight. Solvent was removed to give an orange oil which was used in the next step without further purification. The acyl chloride was redissolved in anhydrous DCM (80 mL) and then added to a suspension of anhydrous $AlCl_3$ (6.19 g, 45.7 mmol) in DCM (100 mL) at 0 °C. The resultant mixture was allowed to warm to room temperature and stirred overnight. The mixture was poured into cold aqueous hydrochloric acid (2.0 M, 100 mL) and the organic phase extracted with chloroform (2 x 75 mL). The organic phase was washed with water (100 mL) and brine (100 mL) followed by drying over Na_2SO_4 and removal of solvent in vacuo. The crude solid was filtered and washed with methanol and acetone followed by drying in vacuo to afford a green/blue solid (2.11 g, 88 %). m.p. 213 °C. ^{1}H NMR (400 MHz,

$CDCl_3$, δ): 6.81 (s, 2 H, ArH), 2.74 (d, 4 H, ^3J = 6.8 Hz, CH_2), 1.59 (m, 2 H, CH), 1.33 (m, 16 H, CH_2), 0.90 (m, 12 H, CH_3). ^{13}C NMR (101 MHz, $CDCl_3$, δ): 182.31, 152.88, 150.03 (dd, ^1J = 265 Hz, ^4J = 2.4 Hz, CF), 140.40, 129.60 (m, CF), 127.12 (m, CF), 119.31, 41.49, 34.74, 32.40, 28.94, 25.55, 23.09, 14.24, 10.91. ^{19}F NMR (377 MHz, $CDCl_3$, δ): - 120.82 (s, CF). IR (cm^{-1}) 1707 (C=O). HRMS (CI) m/z: $[M-H]^-$ calcd. for $C_{32}H_{36}F_2O_2S_2$, 554.2119; found, 554.2119.

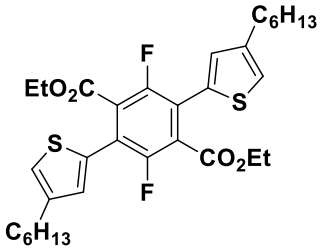
2,2'-(2,7-Bis(2-ethylhexyl)-5,10-difluoro-s-indaceno[1,2-b:5,6-b']dithiophene-4,9-diylidene)dimalononitrile (2,7-bis(2-ethylhexyl)-diFIDT-di(C(CN)$_2$)):



2,7-Bis(2-ethylhexyl)-5,10-difluoro-s-indaceno[1,2-b5,6-b']dithiophene-4,9-dione (300 mg, 0.54 mmol) and malononitrile (357 mg, 5.41 mmol) were dissolved in anhydrous DCM (40 mL). Pyridine (4.9 mL, 61 mmol) was added and the mixture stirred overnight at 30 °C. The reaction was tracked by TLC (1:1 petroleum ether/DCM). Aqueous hydrochloric acid (2.0 M, 100 mL) was added and the crude product extracted with chloroform (2 x 50 mL). The combined organic extracts were washed with water (2 x 50 mL) and brine (50 mL), dried over anhydrous sodium sulfate, filtered and concentrated under reduced pressure. The crude solid was filtered and washed with methanol and acetone, then dried in vacuo to give a grass green solid (272 mg, 77 %). m.p. 221 °C. ^{1}H NMR (400 MHz, $CDCl_3$, δ): 7.32 (s, 2 H, ArH), 2.79 (d, ^3J = 6.3 Hz, 4 H, CH_2), 1.61 (m, 2H, CH), 1.33 (m, 16 H, CH_2), 0.92 (m, 12 H, CH_3). ^{13}C NMR (101 MHz, $CDCl_3$, δ): 154.09, 149.23, 147.91 (dd, ^1J = 265 Hz, ^4J = 2.5 Hz, CF), 144.81, 139.45, 127.62 (m, CF), 127.21 (m, CF), 121.31, 113.47, 112.32, 81.87, 41.52, 35.06, 32.43, 28.92, 25.63, 23.08, 14.24, 10.92. ^{19}F NMR (377 MHz, $CDCl_3$, δ): - 108.11 (s, CF). IR (cm^{-1})

2222 (C≡N). HRMS (APCI) m/z: $[M+H]^+$ calcd. for $C_{38}H_{37}F_2N_4S_2$, 651.2422; found, 651.2420.

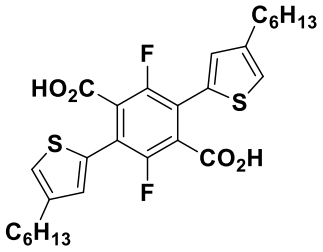
***Diethyl 2,5-difluoro-3,6-bis(4-hexylthiophen-2-yl)terephthalate ([13])**:*



A mixture of 2,5-Dibromo-3,6-difluoroterephthalic acid diethyl ester ***([2])*** (4.2 g, 6.9 mmol), (4-hexylthiophen-2-yl)trimethylstannane ***([12])*** (11 g, 16 mmol) in anhydrous DMF (80 mL) were degassed for 45 mins. Tetrakis(triphenylphosphine)palladium(0) (584 mg, 0.51 mmol, 0.05 equiv) was added and the mixture degassed for a further 15 mins. The mixture was stirred at 100 °C for 17 hours. The mixture was diluted with DCM (100 mL) and the crude reaction mixture passed through a plug of 15 % KF in silica, eluting with DCM. The solvent was then concentrated in vacuo. DCM (150 mL) was added and the organic phase washed with water (4 x 100 mL) and brine (100 mL). The combined organics were dried over anhydrous magnesium sulfate, filtered and the solvent removed in vacuo. The crude product was purified by silica gel chromatography (petroleum ether 2:1 DCM). The product was collected and dried under vacuum to give diethyl 2,5-difluoro-3,6-bis(4-hexylthiophen-2-yl)terephthalate (4.95 g, 83 %) as a pale orange solid. ^{1}H NMR (400 MHz, $CDCl_3$, δ): 7.07 (d, ^3J = 1.5 Hz, 2 H, ArH), 7.04 (d, ^3J = 1.5 Hz, 2 H, ArH), 4.24 (q, ^3J = 7.5 Hz, 4 H, CH_2), 2.61 (t, ^3J = 7.5 Hz, 4 H, CH_2), 1.66 – 1.58 (m, 4 H, CH_2), 1.39 – 1.27 (m, 12 H, CH_2), 1.18 (t, ^3J = 7.2 Hz, 6 H, CH_3), 0.90 (t, ^3J = 6.9 Hz, 6 H, CH_3). ^{13}C NMR (101 MHz, $CDCl_3$, δ): 163.76, 152.07 (dd, ^1J = 252 Hz, ^4J = 4.5 Hz, CF), 143.62, 130.96, 130.81, 125.33 – 125.05 (m, CF), 123.07, 122.26 – 122.02 (m, CF),

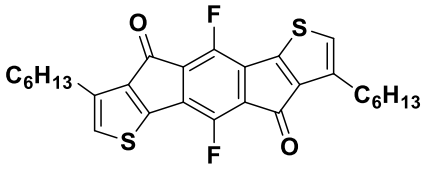
62.43, 31.69, 30.56, 30.48, 29.06, 22.73, 14.19, 13.93. ^{19}F NMR (377 MHz, $CDCl_3$, δ): - 119.73 (s, CF). HRMS (ES-TOF) m/z: $[M+H]^+$ calcd. for $C_{32}H_{41}O_4S_2F_2$, 591.2430; found, 591.2414.

***2,5-Bis(4-hexylthiophen-2-yl)-3,6-difluoroterephthalic acid ([14])**:*



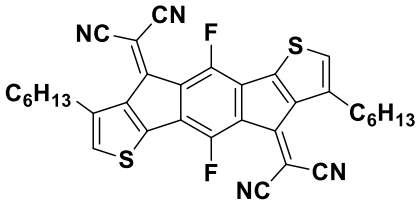
Diethyl 2,5-difluoro-3,6-bis(4-hexylthiophen-2-yl)terephthalate ***([13])*** (4.9 g, 8.29 mmol) was suspended in ethanol (200 mL). KOH (6.52 g, 116.12 mmol) was added as a single portion. The suspension was heated to reflux overnight. Upon heating a solution followed by a suspension was observed. The reaction was cooled to room temperature and aqueous hydrochloric acid (2.0 M, 250 mL) was added with stirring for 5 mins. The resulting precipitate was filtered, washed with plenty of water and dried in an oven at 140 °C to give 4.18 g (94%) of greenish solid. ^{1}H NMR (400 MHz, DMSO-d_6, δ): 14.17 (s, 2 H, CO_2H), 7.42 (d, ^3J = 1.5 Hz, 2 H, ArH), 7.17 (d, ^3J = 1.5 Hz, 2 H, ArH), 2.59 (t, ^3J = 7.7 Hz, 4 H, CH_2), 1.63 – 1.55 (m, 4 H, CH_2), 1.35 – 1.25 (m, 12 H, CH_2), 0.86 (t, ^3J = 7.0 Hz, 6 H, CH_3). ^{13}C NMR (101 MHz, DMSO-d_6, δ): 164.33, 150.67 (dd, ^1J = 247 Hz, ^4J = 3.4 Hz, CF), 142.98, 130.86, 129.76, 125.69 – 125.38 (m, CF), 123.90, 120.43 – 120.16 (m, CF), 31.03, 29.86, 29.59, 28.32, 22.04, 13.92. ^{19}F NMR (377 MHz, DMSO-d_6, δ): - 120.75 (s, CF). HRMS (ES-TOF) m/z: $[M+H]^+$ calcd. for $C_{28}H_{33}O_4S_2F_2$, 535.1788; found, 535.1794.

***3,8-Dihexyl-5,10-difluoro-s-indaceno[1,2-b:5,6-b']dithiophene-4,9-dione (3,8-dihexyl-diFIDT-di(C(CN)$_2$))**:*



2,5-Difluoro-3,6-di-(4-hexylthiophen-2-yl-terephthalic acid (4.0 g, 7.48 mmol) was suspended in anhydrous DCM (100 mL) and catalytic amount of anhydrous DMF (0.29 mL, 3.74 mmol). Thionyl chloride (10.90 mL, 149.62 mmol) was added dropwise over 15 minutes. The reaction was heated to 50 °C overnight. After cooling to room temperature, the solvent was removed under reduced pressure to give an orange oil which is used in the next step without further purification. The acyl chloride was redissolved in anhydrous DCM (100 mL) and then added to a suspension of anhydrous $AlCl_3$ (10.12 g) in DCM (100 mL) at 0 °C. The resultant mixture was allowed to warm to room temperature and stirred for 4 hrs. Aqueous hydrochloric acid (2.0 M, 400 mL) was added and the crude product extracted with chloroform (2 x 150 mL). The combined organic extracts were rinsed with water (2 x 150 mL) and brine (150 mL), dried over anhydrous sodium sulfate, filtered and concentrated under reduced pressure. The residue was reprecipitated in the minimum amount of hot DCM with methanol, filtered, washed with methanol and acetone then dried in vacuo to give a cyan blue solid (2.95 g, 78 %). m.p. 172 °C. ^{1}H NMR (400 MHz, $CDCl_3$, δ): 6.91 (s, 2 H, Ar H), 2.72 (t, ^{3}J = 7.7 Hz, 4 H, CH_2), 1.65 (m, 4 H, CH_2), 1.32 (m, 12 H, CH_2), 0.88 (t, ^{3}J = 6.8 Hz, 6 H, CH_3). ^{13}C NMR (101 MHz, $CDCl_3$, δ): 182.30, 152.21, 146.56 (dd, ^{1}J = 265 Hz, ^{4}J = 2.4 Hz, CF), 140.89, 139.04, 129.19 (m, CF), 128.30 (m, CF), 127.14, 31.70, 29.49, 29.07, 28.35, 22.73, 14.23. ^{19}F NMR (377 MHz, $CDCl_3$, δ): - 129.64 (s, CF). IR (cm^{-1}) 1700 (C=O). HRMS (ES-TOF) m/z: $[M+H]^+$ calcd. for $C_{28}H_{28}F_2O_2S_2$, 498.1499; found, 498.1503.

2,2'-(5,10-Difluoro-3,8-dihexyl-s-indaceno[1,2-b:5,6-b']dithiophene-4,9-diylidene)dimalononitrile (3,8-dihexyl-diFIDT-di(C(CN)$_2$)):



3,8-Dihexyl-5,10-difluoro-s-indaceno[1,2-b:5,6-b']dithiophene-4,9-dione (200 mg, 0.4 mmol) and malononitrile (264 mg, 4.0 mmol) were dissolved in anhydrous DCM (20 mL). Pyridine (0.39 mL, 4.8 mmol) and $TiCl_4$ (0.44 mL, 4 mmol) were added and the mixture stirred overnight at room temperature. Aqueous hydrochloric acid (2.0 M, 20 mL) was added and the crude product extracted with chloroform (2 x 50 mL). The combined organic extracts were rinsed with water (2 x 50 mL) and brine (50 mL), dried over anhydrous sodium sulfate, filtered and concentrated under reduced pressure. The residue was reprecipitated in the minimum amount of hot DCM with methanol, filtered, washed with methanol and dried to give a deep green solid (123 mg, 52 %). m.p. 238 °C. ^{1}H NMR (400 MHz, $CDCl_3$, δ): 7.03 (s, 2 H, Ar H), 3.01 (t, ^{3}J = 6.8 Hz, 4 H, CH_2), 1.62 (m, 4 H, CH_2), 1.31 (m, 12 H, CH_2), 0.89 (t, ^{3}J = 7.7 Hz, 6 H, CH_3). ^{13}C NMR (101 MHz, $CDCl_3$, 50 °C, δ): 154.84, 148.32, 147.65 (dd, ^{1}J = 265 Hz, ^{4}J = 2.4 Hz, CF), 141.70, 138.86, 130.18 (m, CF), 128.82, 126.65 (m, CF), 114.42, 113.11, 82.28, 31.87, 31.78, 30.47, 28.70, 22.68, 14.08. ^{19}F NMR (377 MHz, $CDCl_3$, δ): - 106.23 (s, CF). IR (cm^{-1}) 2222 (C≡N). HRMS (ES-TOF) m/z: $[M+H]^+$ calcd. for $C_{30}H_{28}F_2N_4S_2$, 594.1723; found, 594.1731.

4. *N*-Cyanoimine as an alternative electron-withdrawing group to dicyanomethylene

Single crystal characterisation was carried out by Dr. Andrew J. P. White (Imperial College London). Analysis of transfer integrals and intermolecular interactions was performed by Dr. Karl J. Thorley (University of Kentucky). OFET device fabrication and testing was performed by Dr. Aniruddha Basu (KAUST).

4.1 Introduction

The work in previous chapters focused on the use of the popular dicyanomethylene EWG to produce a variety of highly electron-deficient **dialkyl-diFIDT** OSCs. While dicyanomethylene is an attractive choice for n-type OSCs owing to its strong electron-withdrawing ability, this group can dramatically reduce solubility and induce steric interactions, as is exemplified in Chapter 2 and Chapter 3. As a result, we were motivated to investigate alternative EWGs compatible in Knoevenagel condensation reactions that would be able to effectively stabilise the LUMO energy level while avoiding the problems associated with dicyanomethylene. Initial efforts focused on the introduction of EWGs commonly used in the synthesis of NFAs, including ethyl 2-cyanoacetate (**1**), 2-(3-oxo-2,3-dihydro-1H-inden-1-ylidene)malononitrile (**2**) and 3-ethyl-2-thioxothiazolidin-4-one (**3**) (**Figure 43**).[144–146]

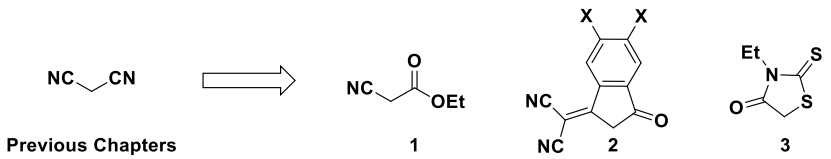


Figure 43: Common EWGs used in NFAs.

Ethyl 2-cyanoacetate (**1**) was seen as an attractive alternative to dicyanomethylene as the structural similarity suggested it could also effectively stabilise the LUMO, albeit to a slightly lesser extent (ester versus nitrile). In addition, **1** possesses a site for further alkylation, potentially improving processability. We ultimately deemed this functionality unsuitable due to insufficient electron-withdrawing ability, with DFT calculations indicating a LUMO energy level ~ 0.5 eV higher with **1** versus dicyanomethylene. 2-(3-oxo-2,3-dihydro-1H-inden-1-ylidene)malononitrile (**2**) is a very popular unit for use in NFAs, where a wide variety of analogues have been reported (X = H, F, Cl, Me).[147] This group is used on the periphery of acceptor – donor – acceptor (A – D – A) NFAs to lower the LUMO (due to its strong electron-withdrawing ability) and improve π-π stacking.[148] However, it was deemed unsuitable for our purposes due to the steric bulk resulting in extensive twisting at the bridging point, as shown by the optimised DFT structure in **Figure 44**. Such twisting would likely be detrimental to device performance due to disruption to π-π stacking interactions.

3-Ethyl-2-thioxothiazolidin-4-one (**3**) was seen as a good alternative to **2** due to potentially reduced torsion owing to its smaller size. This was confirmed by DFT calculations, where the optimised structure displayed far smaller torsion compared to **2** (**Figure 44**). **3** also bears a site for alkylation to improve solubility. Again, this unit was discounted due to insufficient electron-withdrawing ability.

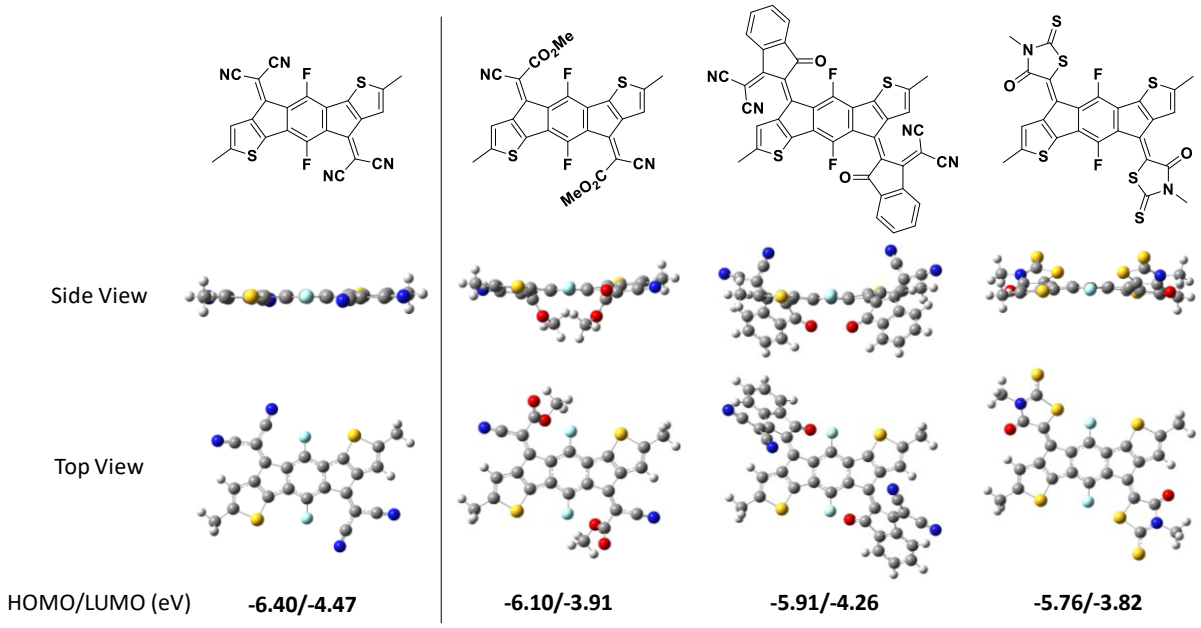


Figure 44: Optimised structures for 2,7-dialkyl-diFIDT-di(X), where X = 1, 2 or 3, compared to 2,7-dialkyl-diFIDT-di(C(CN)$_2$) (Chapter 2), calculated by DFT.

Despite these judgements, attempted were still made to react **2,7-dihexyl-diFIDT-di(O)** with both **2** and **3,** though both were unsuccessful (**Figure 45**). No reaction occurred in the absence of $TiCl_4$, suggesting a steric barrier, while dark brown mixtures were formed upon the addition of $TiCl_4$. It is reasonable to assume that the presence of additional carbonyl functionality in **1** and **2** led to competing condensation reactions (e.g. dimerisation of **2**) and/or decomposition.

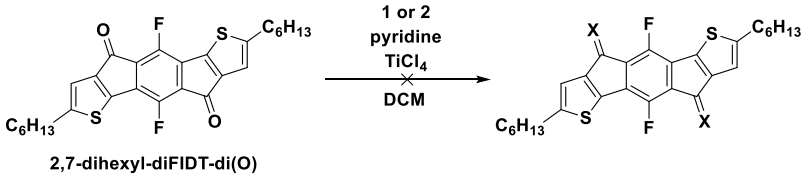


Figure 45: Failed Knoevenagel condensation of 2,7-dihexyl-diFIDT-di(O) with 1 and 2.

Due to the issues described above, another alternative EWG was sought. Reports of a less common *N*-cyanoimine EWG for use in OSCs have been published.[149–151] Recently, Peltier et al. showed that **2,7-dihexyl-IDT-di(N(CN))** boasted an equally deep LUMO energy level (-4.13 eV) to the corresponding **2,7-dihexyl-IDT-di(C(CN)$_2$)** (- 4.10 eV), in addition to improved solubility in common organic solvents.[152] These results prompted us to explore the

use of *N*-cyanoimine with the fluorinated core. DFT calculations were performed to establish ground state conformation and HOMO/LUMO energy levels. In particular, the asymmetry of the *N*-cyanoimine linkage meant that three distinct stereoisomers were possible. **Figure 46** importantly demonstrates that the compound should be planar, suggesting the *N*-cyanoimine groups do not introduce any undesired steric interactions. This is in contrast to that predicted using groups **1** – **3** as discussed previously. The *Z*,*Z*-isomer was predicted to be the most stable, as indicated by a lower HOMO energy level. These calculations predicted a LUMO energy level (- 4.25 eV) which is slightly higher than the corresponding dicyanomethylene (- 4.47 eV), suggesting a slightly weaker electron-withdrawing ability of the *N*-cyanoimine.

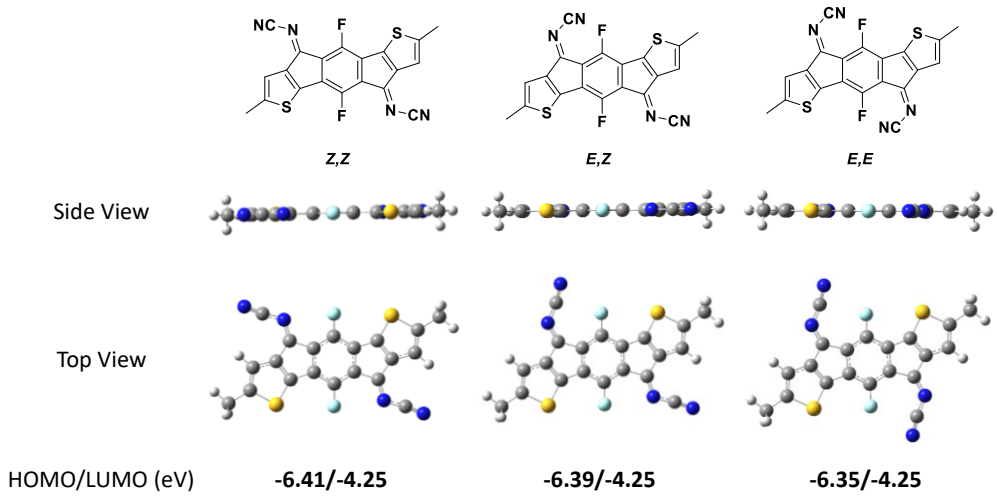


Figure 46: Optimised Structures for diFIDT-di(C(CN)) isomers, calculated by DFT.

Though the *Z*,*Z*-isomer was predicted to be thermodynamically favourable, the asymmetry of this group could still pose a problem under the reaction conditions. Due to the lack of stereoselectivity in the Knoevenagel condensation reaction, there is the possibility of forming a mixture of stereoisomers (as illustrated in **Figure 46**). This could cause issues with purification, since such a mixture would be difficult to separate. Having said that, a number of reports have highlighted that some stereocontrol can be achieved owing to steric effects (e.g. one bulky EWG and one less bulky EWG).[153–155] High stereoselectivity has also been

achieved by employing chiral aminocatalysts.[156,157] With respect to **2,7-dihexyl-IDT-di(O)**, Peltier et al. report the formation of isomerically pure ***Z,Z*-2,7-dihexyl-IDT-di(N(CN))** by single crystal analysis, indicating stereoselectivity in this system.

In this Chapter, a series of novel **dialkyl-diFIDT-di(N(CN))** OSCs were synthesised in order to investigate their physiochemical properties and device performance. Synthesis of **2,7-dihexyl-diFIDT-di(N(CN))**, in the first instance, allowed a direct comparison to the already reported non-fluorinated analogue, **2,7-dihexyl-IDT-di(N(CN))**. This again allowed the effect of fluorination to be investigated, akin to the work outlined in Chapter 2 for **2,7-dihexyl-diFIDT-di(C(CN)$_2$)**. Subsequently, synthesis of **dialkyl-diFIDT-di(N(CN))** OSCs bearing 2,7-bis(2-ethylhexyl) and 3,8-dihexyl chains would enable a number of comparisons to be made regarding the effects of side-chain engineering, akin to those performed in Chapter 3. 2,7-Didodecyl analogues were not considered due to poor solubility. Finally, a comparison between *N*-cyanoimine with the corresponding dicyanomethylene compounds (Chapter 2 & 3) could also be made. This multifaceted approach ensured a comprehensive review of the potential of *N*-cyanoimine as an EWG in the context of n-type OSC materials, building on the initial work done by Peltier et al.

4.2 Synthesis

2,7-Dihexyl-diFIDT-di(N(CN)), **2,7-bis(2-ethylhexyl)-diFIDT-di(N(CN))** and **3,8-dihexyl-diFIDT-di(N(CN))** were synthesised following a modified literature procedure (**Figure 47)**.[152,158] The diketone starting materials were synthesised according to the routes outline in Section 2.2 and Section 3.2 for the 2,7-dihexyl and 2,7-bis(2-ethylhexyl)/3,8-dihexyl analogues respectively. The diketones were reacted with $TiCl_4$ and bis(trimethylsilyl)carbodiimide in a Knoevenagel-type condensation reaction at room temperature to give **2,7-dihexyl-diFIDT-**

di(N(CN)) (50 %), **2,7-bis(2-ethylhexyl)-diFIDT-di(N(CN))** (90 %) and **3,8-dihexyl-diFIDT-di(N(CN))** (51 %) respectively after purification by recrystallisation.

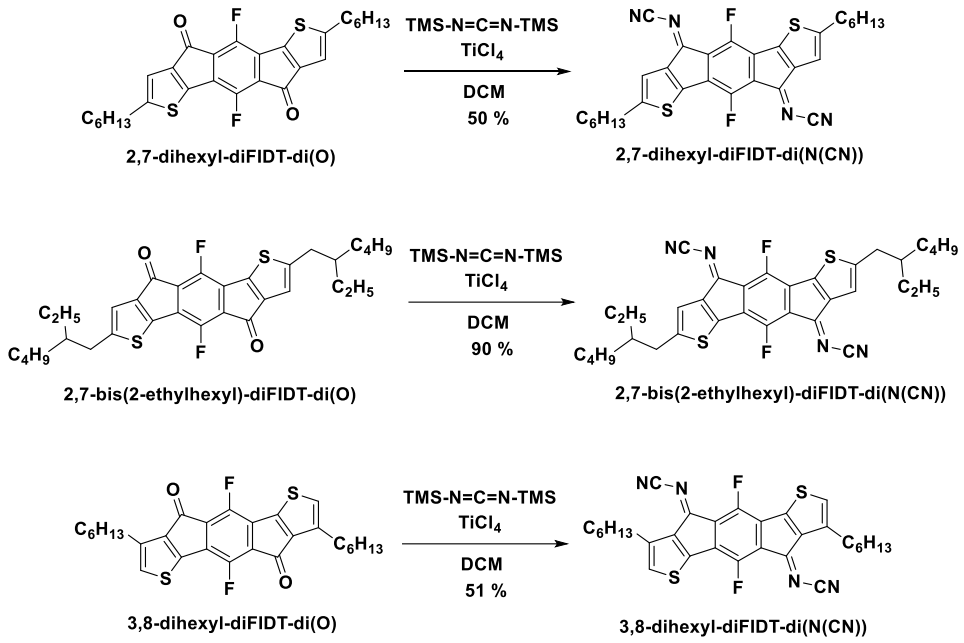


Figure 47: Synthesis of dialkyl-diFIDT-di(N(CN)) analogues.

The chemical structures of **2,7-dihexyl-diFIDT-di(N(CN))**, **2,7-bis(2-ethylhexyl)-diFIDT-di(N(CN))** and **3,8-dihexyl-diFIDT-di(N(CN))** were verified by ^{1}H NMR, ^{19}F NMR, ^{13}C NMR, IR and HRMS. Single crystal growth was achieved for **2,7-dihexyl-diFIDT-di(N(CN))** and **3,8-dihexyl-diFIDT-di(N(CN)** but not **2,7-bis(2-ethylhexyl)-diFIDT-di(N(CN))**, which afforded only fine powders.

To the best of our knowledge, the mechanism for this reaction has not been discussed in any recent literature and remains unclear. **Figure 48** outlines a possible mechanism. A modified mechanism may involve pre-functionalisation of biscarbimide by $TiCl_4$.[159]

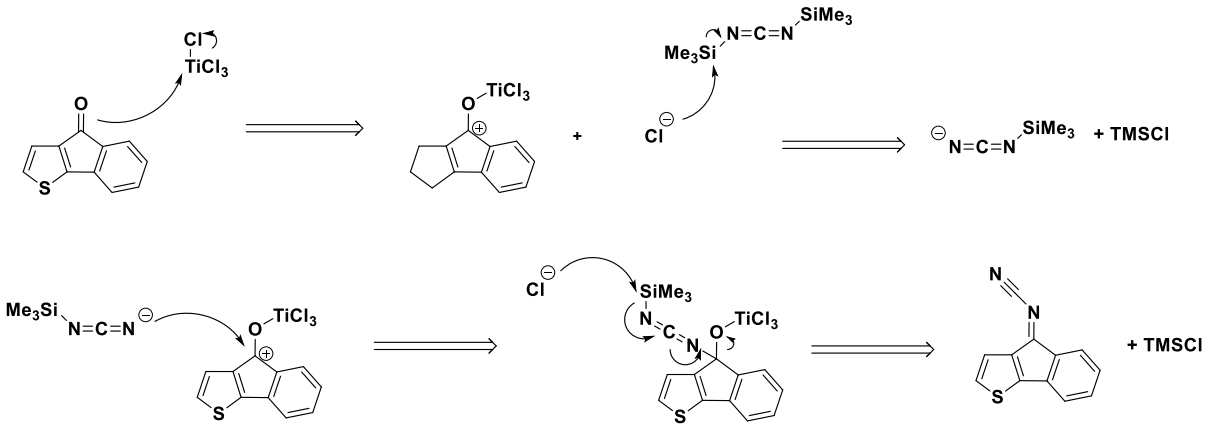


Figure 48: Proposed mechanism for synthesis of N-cyanoimine

All three *N*-cyanoimine analogues displayed unexpectedly low solubility in chlorobenzene (at 25 °C) (full procedure outlined in General Experimental, Chapter 8), specifically when compared to the corresponding dicyanomethylene analogues (**Table 9**). This was contrary to what was observed by Peltier et al. for the non-fluorinated analogues. Interestingly, **2,7-dihexyl-diFIDT-di(N(CN))** and **2,7-bis(2-ethylhexyl)-diFIDT-di(N(CN))** exhibited similar solubilities (1.25 – 1.4 mg mL^{-1}), indicating, in this instance, that the introduction of a branching chain was not beneficial for solubility. This was unlike that observed for **2,7-bis(2-ethylhexyl)-diFIDT-di($C(CN)_2$)**, where a large enhancement was observed. **2,7-bis(2-ethylhexyl)-diFIDT-di(N(CN))** was far less soluble than **2,7-bis(2-ethylhexyl)-diFIDT-di($C(CN)_2$)**. **3,8-Dihexyl-diFIDT-di(N(CN))** displayed the lowest solubility (0.55 – 0.65 mg mL^{-1}). This was again contrary to what was previously observed for **3,8-dihexyl-diFIDT-di($C(CN)_2$)**, where repositioning of the alkyl side-chains from 2,7- to 3,8-positions improved solubility significantly. These observations highlight the complex structure – property relationships present in OSC materials. Specifically, they indicate markedly different aggregation properties induced by the use of *N*-cyanomine EWGs at the bridging positions, compared to dicyanomethylene groups.

Table 9: Solubility of dialkyl-diFIDT-di(N(CN)) analogues in chlorobenzene versus the corresponding dialkyl-diFIDT-di(C(CN)$_2$).

Alkyl Side-Chain	*Solubility* [mg mL^{-1}, 25 °C]	
	diFIDT-di(C(CN)$_2$)	*diFIDT-di(N(CN))*
2,7-dihexyl	**4.0**	**1.25 – 1.4**
2,7-bis(2-ethylhexyl)	**40**	**1.25 – 1.4**
3,8-dihexyl	**10 – 13**	**0.55 – 0.65**

4.3 Optoelectronic and Electrochemical Properties

The absorption spectra for all **dialkyl-diFIDT-di(N(CN))** analogues in solution (toluene and chloroform, 10^{-5} M) were recorded (**Figure 49**). As for all **dialkyl-diFIDT-di(C(CN)$_2$)** analogues, the *N*-cyanoimine analogues displayed strong well-defined absorption bands at shorter wavelengths (250 – 450 nm) as well as broad weak absorption at longer wavelengths (550 – 900 nm). Spectra predicted by TD-DFT calculations are shown in **Figure A88**. From the onset of absorption at the longer wavelengths (around 850 – 900 nm), optical gaps of ~ 1.4 eV could be extracted. **3,8-dihexyl-diFIDT-di(N(CN))** displays a markedly reduced absorption intensity at shorter wavelengths, similar to that observed for **3,8-dihexyl-diFIDT-di(C(CN)$_2$)** (**Figure 49c**). This feature thus appears aligned with positioning of the alkyl side-chains in the 3,8-positions.

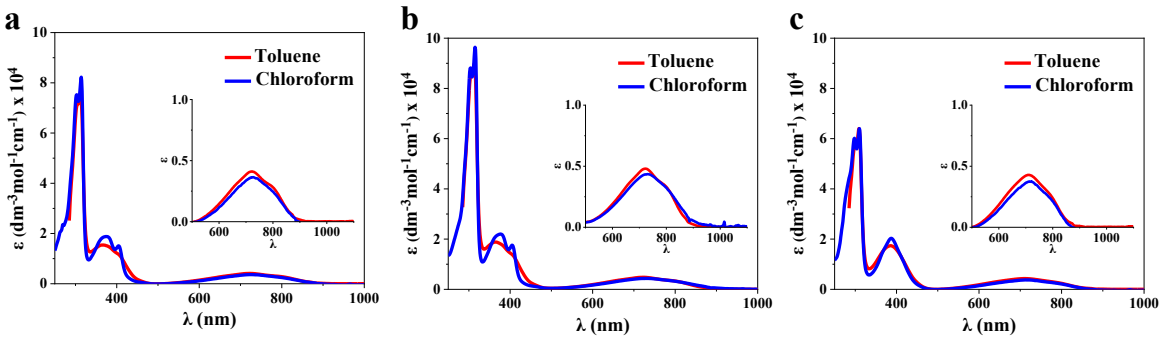


Figure 49: Solution absorption spectra for dialkyl-diFIDT-di(N(CN)) analogues in toluene and chloroform. a) 2,7-dihexyl-diFIDT-di(N(CN)). b) 2,7-bis(2-ethylhexyl)-diFIDT-di(N(CN)). c) 3,8-dihexyl-diFIDT-di(N(CN)).

Electrochemical studies of the **dialkyl-diFIDT-di(N(CN))** analogues were performed by cyclic voltammetry (CV) using a 0.1 M solution of Bu_4NPF_6 in DCM solutions and a ferrocene (Fc/Fc^+) internal standard. Potentials were swept from 0 V to a positive maximum, then swept back to a negative maximum before returning to 0 V. In line with best practice, energy levels were estimated from $E^{1/2}$ (when reversibility is observed) or E^i (when irreversibility is observed), where $E^{1/2}$ is the half-wave potential, E^i is the inflection-point potential.[124] HOMO = - ($E^{1/2\ or\ i}$ + 4.8) eV and LUMO = - ($E^{1/2\ or\ i}$ + 4.8) eV for oxidation and reduction respectively, with the ferrocene/ferrocenium reference redox system at 4.8 eV below the vacuum level. Electrochemical data for **2,7-dihexyl-IDT-di(N(CN))** was taken from Peltier et al., where $E^{1/2}$ for the first reduction peak was extracted to provide a better comparison.[152] Oxidation and reduction potentials are summarised in **Table 10**.

No major differences in the cyclic voltammograms were observed between **dialkyl-diFIDT-di(N(CN))** analogues, reflecting the negligible impact of alkyl chains on the electrochemical properties, as already noted in previous chapters. The cyclic voltammograms displayed two chemically reversible reductions along with one or two irreversible oxidations (**Figure 50**). These compounds displayed deep LUMO energy levels (- 4.16 eV to - 4.19 eV), indicating the suitability of *N*-cyanoimine as an effective EWG. Direct comparison between the LUMO

energy levels of **2,7-dihexyl-IDT-di(N(CN))** and **2,7-dihexyl-diFIDT-di(N(CN))** demonstrated a small depression (0.16 eV) from the introduction of fluorine groups onto the central phenyl moiety. Additionally, LUMO energy levels were < 0.1 eV higher than the corresponding **dialkyl-diFIDT-di(C(CN)$_2$)** analogues (- 4.22 eV to - 4.24 eV, Section 2.3 and Section 3.3), indicating a similar ability to stabilise the reduced state. This is much closer in energy than predicted by DFT (Section 4.1) and in good agreement with Peltier et al., who reported little or no difference between the LUMO energy levels of **2,7-dialkyl-IDT-di(C(CN)$_2$)** and **2,7-dialkyl-IDT-di(N(CN))**. Conversely, slightly deeper HOMO energy levels (~ 0.1 eV) are observed for **dialkyl-diFIDT-di(N(CN))** compared to **dialkyl-diFIDT-di(C(CN)$_2$)**, resulting in a small widening of the electrochemical gap (< 0.2 eV). This maybe reflects having the electron-withdrawing imine moiety in close vicinity to the electron-rich IDT core and/or a smaller π-system compared to **dialkyl-diFIDT-di(C(CN)$_2$)**.

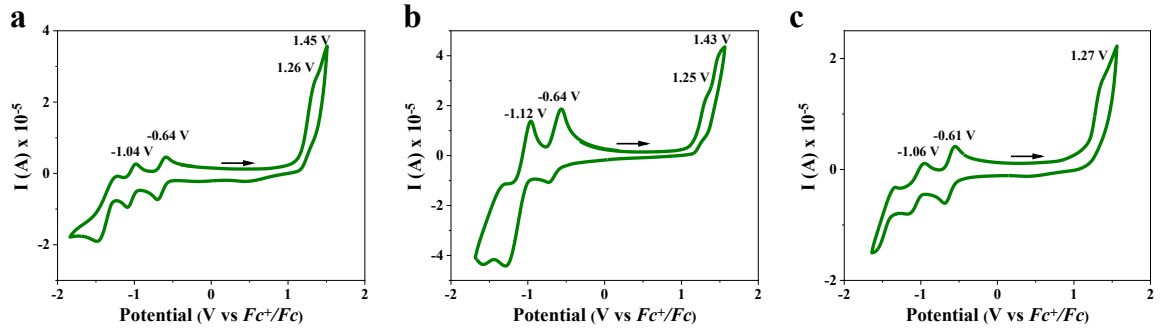


Figure 50: Cyclic voltammagrams of dialkyl-diFIDT-diN(CN)) analogues, showing corresponding $E^{1/2}$ or i potentials. a) 2,7-dihexyl-diFIDT-di(N(CN)). b) 2,7-bis(2-ethylhexyl)-diFIDT-di(N(CN)). c) 3,8-dihexyl-diFIDT-di(N(CN)).

Table 10: Summary of material properties of dialkyl-diFIDT-di(N(CN)) analogues, compared to the non-fluorinated analogues.

OSC	*HOMO*[a)]	*LUMO*[a)]	λ_{max} *(solution)*
	[eV]	[eV]	[nm]
2,7-dihexyl-IDT-di(N(CN))[b)]	- 5.72	- 4.00[c)]	711, 322[d)]
2,7-dihexyl-diFIDT-di(N(CN))	- 6.06	- 4.16	719, 365, 312[e)]
			726, 405, 373, 314, 303[f)]
2,7-bis(2-ethylhexyl)-diFIDT-di(N(CN))	- 6.05	- 4.16	722, 364, 313[e)]
			729, 405, 377, 315, 304[f)]
3,8-dihexyl-diFIDT-di(N(CN))	- 6.07	- 4.19	708, 386, 309[e)]
			713, 387, 310, 298[f)]

[a)]extracted from CV measurements, [b)]all data taken from Peltier et al.[110], [c)]reanalysed as $E^{1/2}$, [d)]in THF, [e)]in toluene, [f)]in chloroform.

4.4 Crystal Structures

Single crystals of **2,7-dihexyl-diFIDT-di(N(CN))** and **3,8-dihexyl-diFIDT-di(N(CN))** were grown via the solvent vapour exchange method using chlorobenzene/methanol mixtures. Similar attempts with **2,7-bis(2-ethylhexyl)-diFIDT-di(N(CN))** were unsuccessful, resulting in only fine powders. The crystal structure for **2,7-dihexyl-IDT-di(N(CN))** was downloaded from the Cambridge Crystallographic Data Centre for comparison.

2,7-dihexyl-diFIDT-di(N(CN)) crystallised in the monoclinic $P2_1/n$ space group. The IDT core was completely coplanar, in agreement with the DFT calculations (**Figure 51a**). *N*-cyanoimine groups are bent out-of-plane slightly with the IDT (2.3 °). This distortion is more pronounced than that present in **2,7-dihexyl-IDT-di(N(CN))** (1.3 °) (**Figure 51b**). The hexyl chains on the thienyl α-position lie outside the plane with a dihedral angle of 88 °. A single

N···H (2.61 Å) short contact is observed between stacks, along with intramolecular C···C (3.20 Å) and N···F (2.96 Å) interactions (**Figure 51c**).

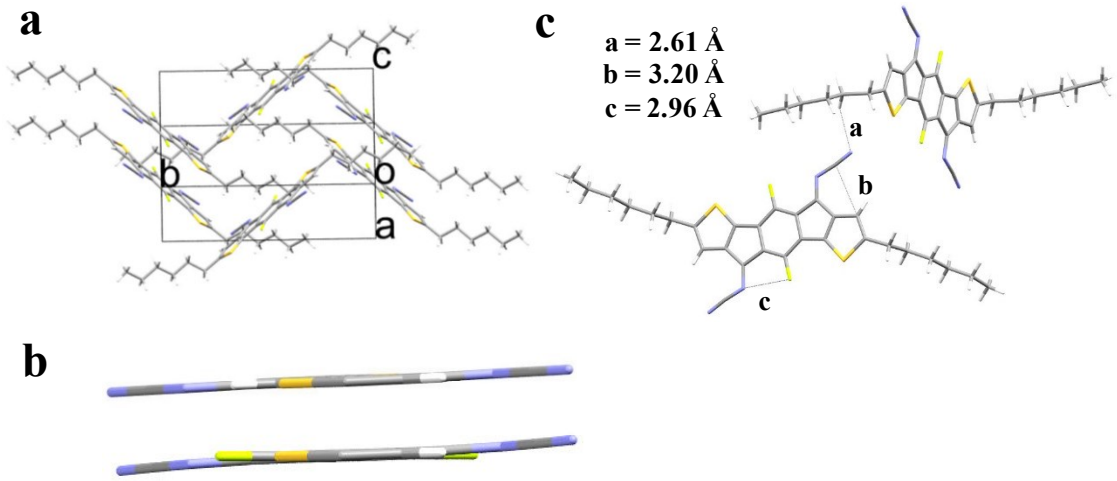


Figure 51: a) Unit cell of 2,7-dihexyl-diFIDT-di(N(CN)). b) Planarity of 2,7-dihexyl-IDT-di(N(CN)) (top) versus 2,7-dihexyl-diFIDT-di(N(CN)) (bottom), with alkyl chains removed for clarity (viewed along the long axis). c) Inter- and intramolecular short contacts.

A planar slipped π-π stacking arrangement is formed along the *a* axis, however adjacent stacks (along the molecular short axis) are arranged almost perpendicular to each other (85.3 °) with poor inter-stack registry. Alkyl chain interdigitation is observed between stacks along the long axis (**Figure 52a** & **c**). This is in contrast to the non-fluorinated analogue **2,7-dihexyl-IDT-di(N(CN))**, which displays a planar slipped π-π stacking motif without such tilting (**Figure 52b** & **d**). This change in packing motif upon core fluorination is akin to that described in Chapter 2, whereby a similar change was realised upon fluorination of **2,7-dihexyl-IDT-di(C(CN)$_2$)**. There is co-facial packing of the conjugated core within a stack, along the *a* axis, with an interplanar stacking distance of 3.41 Å and a slipping distance of 3.24 Å (angle 43.6 °) (**Figure A91**). These values are similar to **2,7-dihexyl-IDT-di(N(CN))** (interplanar stacking distance of 3.41 Å, slipping distance of 3.51 Å).

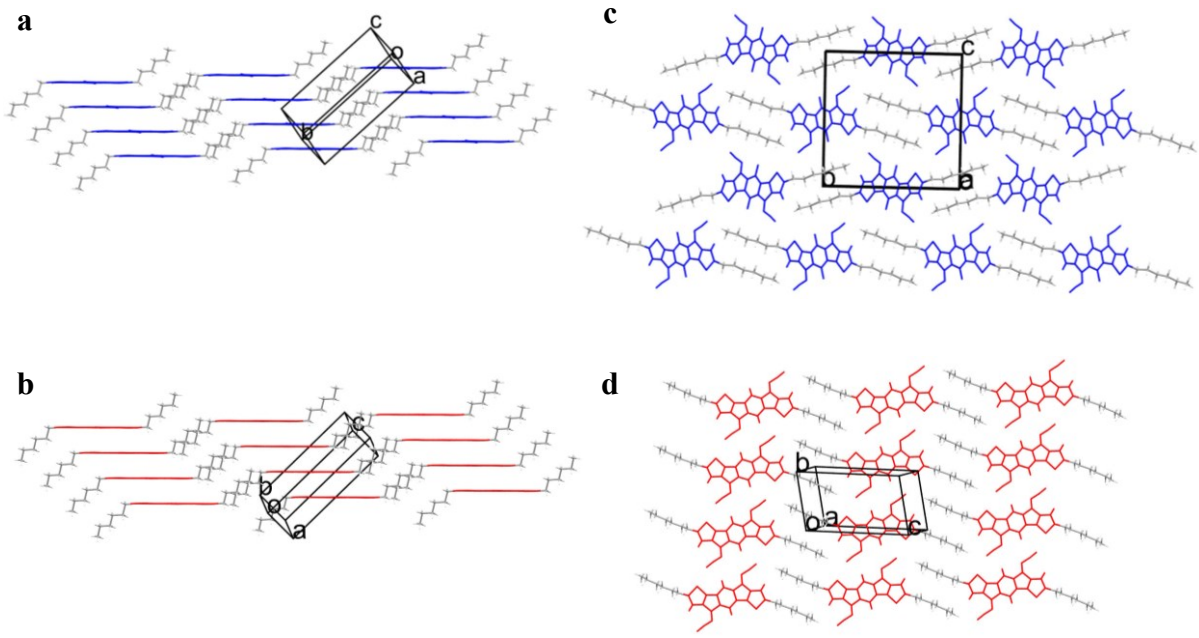


Figure 52: a) & c) Crystal packing motifs of 2,7-dihexyl-diFIDT-di(N(CN)). b) & d) Crystal packing motifs of 2,7-dihexyl-IDT-di(N(CN)).

As for crystal structures discussed in previous chapters, the electron transfer integrals were calculated. A larger value indicates better overlap between frontier molecular orbitals on neighbouring units (LUMO – LUMO in the case of electron transport) and therefore the potential for more efficient charge transfer. **2,7-Dihexyl-diFIDT-di(N(CN))** displays a one-dimensional (1D) charge transfer pathway, with an electron transfer integral of 106 meV for the main π-stack. This value is high, and larger than that calculated for **2,7-dihexyl-IDT-di(N(CN))** (87 meV), indicating that core fluorination is again beneficial for charge transfer, as was observed for **2,7-dihexyl-diFIDT-di(C(CN)$_2$)** (Section 2.4). However, this value is smaller than **2,7-dihexyl-diFIDT-di(C(CN)$_2$)** (129 meV), suggesting that the use of *N*-cyanoimine in place of dicyanomethylene is disadvantageous for charge transfer. This observation may go some way to explaining the reduced electron mobility observed in OFET devices (*vide infra*).

SAPT0 analysis was performed, as described in the previous chapters. This allows the total interaction energies between molecular pairs extracted from the crystal structures to be decomposed into the respective non-covalent interactions. Analysis was performed on molecular pairs of **2,7-dihexyl-IDT-di(N(CN))** and **2,7-dihexyl-diFIDT-di(N(CN))** from their respective crystal packing motifs. In addition, the **2,7-dihexyl-IDT-di(N(CN))** molecules in their crystal packing were altered by substitution of the central protons for fluorine atoms, thus leading to the hypothetical **2,7-dihexyl-diFIDT-di(N(CN))** molecules in the **2,7-dihexyl-IDT-di(N(CN))** packing. Similarly, **2,7-dihexyl-IDT-di(N(CN))** molecules were placed in the **2,7-dihexyl-diFIDT-di((N(CN))** packing. This allowed the specific effect of F substitution to be isolated.

In the **2,7-dihexyl-diFIDT-di(N(CN))** packing, the substitution of F with H makes very little difference to pairwise interaction energies (**Figure 53a**). The main difference in packing originates from the in-plane edge-to-edge interaction of the **2,7-dihexyl-IDT-di(N(CN))** crystal, between adjacent molecules (**Figure 53b**). The non-fluorinated derivative results in an interaction stabilisation 8.33 kcal mol^{-1} stronger than the fluorinated one. This difference is the result of a large steric repulsion by the inclusion of fluorine, which is too large to fit into the close packing between the *N*-cyanoimine groups. The repulsion is to such an extent that the overall interaction becomes slightly positive (E_{SAPT} = + 0.20 kcal mol^{-1}). Thus, **2,7-dihexyl-diFIDT-di(N(CN))** prefers to adopt the crystal packing where intermolecular interactions involving the fluorine atom are minimised. This is a similar effect to that observed for **2,7-dihexyl-diFIDT-di(C(CN)$_2$)** (Section 2.4).

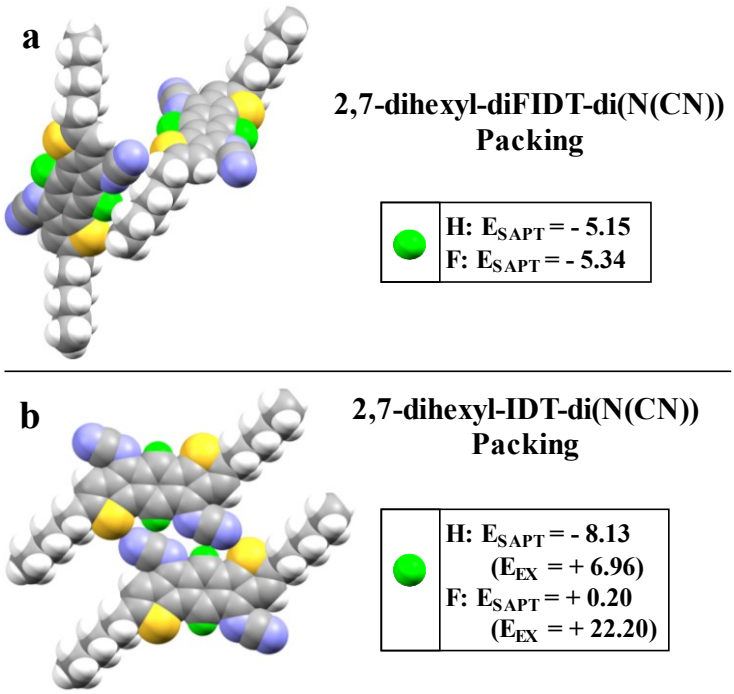


Figure 53: In-plane longitudinal interaction in a) 2,7-dihexyl-diFIDT-di(N(CN)) crystal packing and b) 2,7-dihexyl-IDT-di(N(CN)) crystal packing. Total SAPT energies (E_{SAPT}) and repulsive exchange energies (E_{EX}) are given for 2,7-dihexyl-IDT-di(N(CN)) and 2,7-dihexyl-diFIDT-di(N(CN)) molecules in each packing motif. All energies in kcal mol^{-1}. Atom colours: yellow = sulfur, green = hydrogen or fluorine, purple = nitrogen.

3,8-dihexyl-diFIDT-di(N(CN)) crystallised in the triclinic *P*1 space group. The IDT core was completely coplanar, in agreement with the DFT calculations. The hexyl side-chains on the thienyl *β*-position lie outside the plane with a dihedral angle of 80 ° (**Figure 54a**). *N*-cyanoimine groups are bent out-of-plane with the IDT (13.7 °) (**Figure 54b**). This is greater than that for **2,7-dihexyl-diFIDT-di(N(CN))**, indicating increased steric crowding due to the proximity of the alkyl chains in the 3,8-positions. One intermolecular S···F (3.27 Å) short contact was observed, along with several intramolecular interactions, including N···F (2.91 Å), N···H (2.55 Å) and C···H (2.59 Å) (**Figure 54c**).

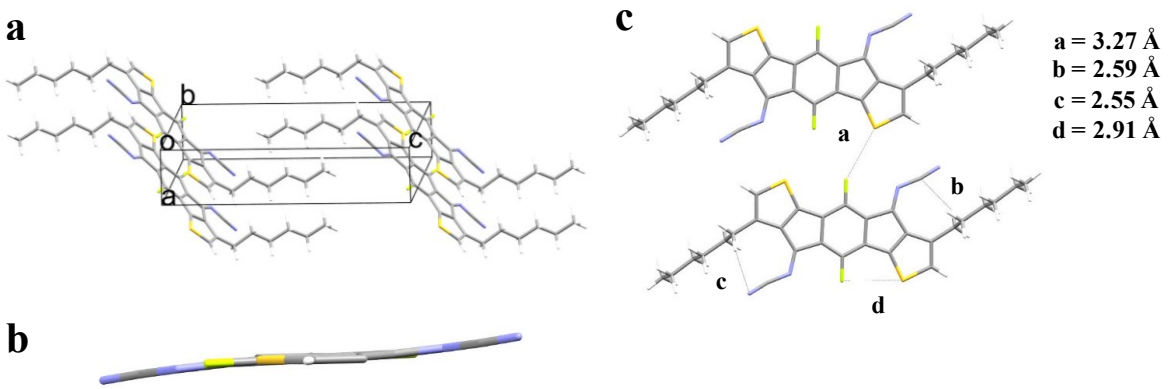


Figure 54: a) Unit cell of 3,8-dihexyl-diFIDT-di(N(CN)). b) Planarity, with alkyl chains removed for clarity (viewed along the long axis). c) Inter- and intramolecular short contacts.

A planar slipped π-π stacking arrangement is formed along the *a* axis and alkyl chain interdigitation observed between stacks (**Figure 55**). Stacks are arranged coplanar along the short axis. This is contrasting to that observed for **2,7-dihexyl-diFIDT-di(N(CN))**, where a perpendicular arrangement is present. Hence, the position of the alkyl chain is shown to have a significant impact on crystal packing, in a similar fashion to that observed in Chapter 3 with the **dialkyl-diFIDT-di(C(CN)$_2$)** analogues. There is co-facial packing of the conjugated core within a stack, along the *a* axis, with an interplanar stacking distance of 3.39 Å and a slipping distance of 3.25 Å (angle 43.8 °) (**Figure A96**). These values are almost identical to those found for **2,7-dihexyl-diFIDT-di(N(CN))**.

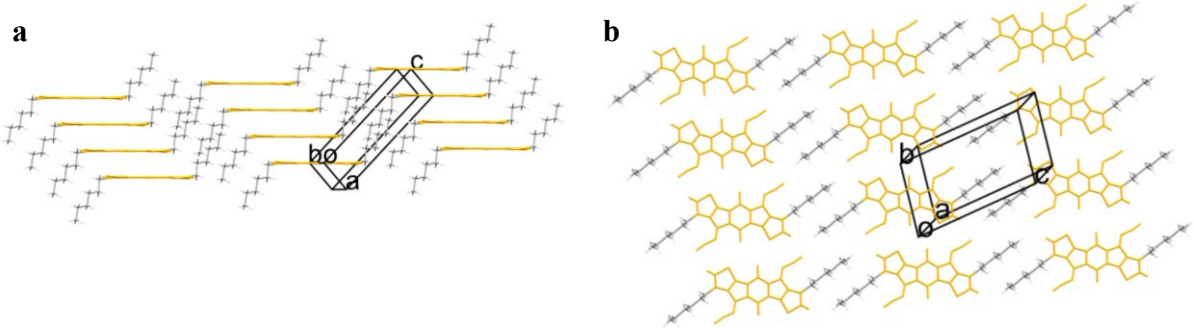


Figure 55: Crystal packing motifs for 3,8-dihexyl-diFIDT-di(N(CN)).

3,8-Dihexyl-diFIDT-di(N(CN)) displays a one-dimensional (1D) charge transfer pathway, with an electron transfer integral of 11 meV for the main π-stack. This is much lower than for **2,7-dihexyl-diFIDT-di(N(CN))** (106 meV), which indicates that there is a poorer LUMO – LUMO interaction. This negative impact upon repositioning the alkyl side-chains from the 2,7-positions to the 3,8-positions is similar to that observed with **2,7-dihexyl-diFIDT-di(C(CN)$_2$)/3,8-dihexyl-diFIDT-di(C(CN)$_2$)** (Section 3.4), though less drastic. Unlike with the dicyanomethylene analogues, the almost identical interplanar stacking distances and slipping distances for **2,7-dihexyl-diFIDT-di(C(CN)$_2$)** and **3,8-dihexyl-diFIDT-di(C(CN)$_2$)** make such a large difference in transfer integral more surprising. However, these results highlight the sensitivity of charge transfer to the relative positioning of the frontier molecular orbitals on neighbouring molecules.

4.1 Thermal Properties

The thermal behaviour of the three **dialkyl-diFIDT-di(N(CN))** analogues was investigated by TGA (**Figure 56**) and DSC (**Figure 57**). Key data are summarised in **Table 11**.

All three **diFIDT-di(N(CN))** analogues exhibited high thermal stabilities (T_d > 320 °C) (temperature at which 5 % mass loss is reached), though a distinct drop in mass (~ 1 % loss) can be seen at around 250 – 275 °C. This feature was also present for the non-fluorinated analogue (**2,7-dihexyl-IDT-di(N(CN))**), as previously reported by Peltier et al. though not explicitly discussed.[152] A T_d of 364 °C reported for **2,7-dihexyl-IDT-di(N(CN))** was > 40 °C higher than **2,7-dihexyl-diFIDT-di(N(CN))** (T_d = 321 °C). This indicated that core fluorination was detrimental for thermal stability. Thermal stabilities were almost identical for **2,7-dihexyl-** and **2,7-bis(2-ethylhexyl)-diFIDT-di(N(CN))** compared to their dicyanomethylene analogues. Repositioning of the hexyl side-chains from 2,7-position to 3,8-position led to a small increase

in thermal stability (13 °C). **3,8-dihexyl-diFIDT-di(N(CN))** was also substantially more stable (T_d = 334 °C) than the dicyanomethylene analogue (T_d = 298 °C). These trends seem to reflect the differences observed by single crystal analysis.

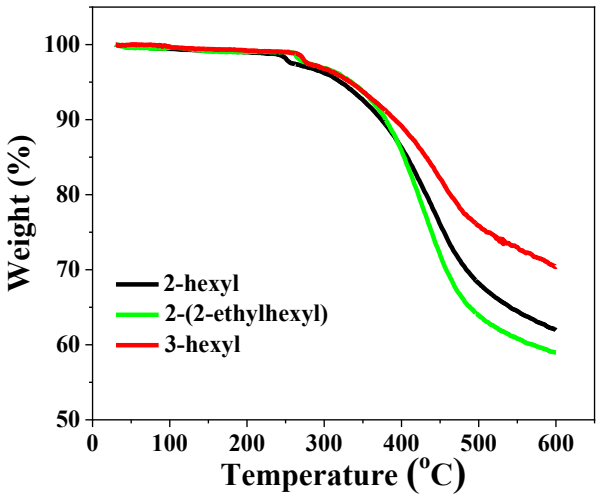


Figure 56: TGA plots for 2,7-dihexyl-, 2,7-bis(2-ethylhexyl)- and 3,8-dihexyl-diFIDT-di(N(CN)).

DSC of the **dialkyl-diFIDT-di(N(CN))** analogues were recorded to up to 200 °C only (**Figure 57**). Heating to 250 °C was shown to degrade the samples, corresponding well with the onset of mass loss in the TGA. Neither **2,7-dihexyl-** nor **2,7-bis(2-ethylhexyl)-diFIDT-di(N(CN))** display any thermal transitions up to 200 °C, suggesting degradation may occur before melting. Non-fluorinated **2,7-dihexyl-IDT-di(N(CN))** was reported to exhibit a weak crystal-to-mesophase transition in this temperature range.

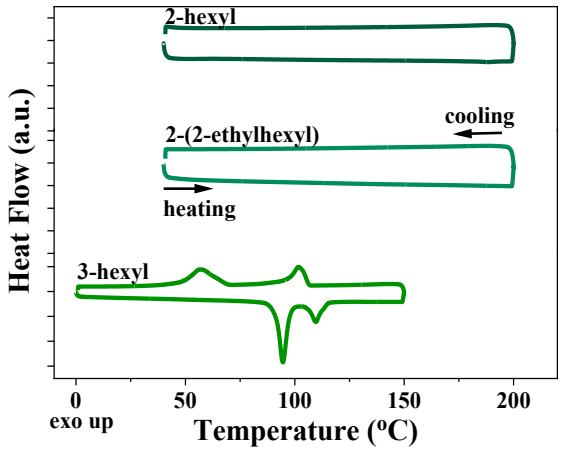


Figure 57: DSC plots (1st Cycle) for 2,7-dihexyl-, 2,7-bis(2-ethylhexyl)- and 3,8-dihexyl-diFIDT-di(N(CN)).

Conversely, **3,8-dihexyl-diFIDT-di(N(CN))** displayed two low enthalpy, reproducible endotherms around 100 °C, which appeared stable upon repeated thermal cycling (**Figure 58**). Peltier et al. detail similar transitions for **2,7-dihexyl-IDT-di(N(CN))**, identifying the formation of an undefined mesophase.[152] POM analysis of these transitions in **3,8-dihexyl-diFIDT-di(N(CN))** showed the persistence of a solid-like state up to 225 °C, supporting the notion that the isotropic transitions in these OSCs lie beyond the decomposition temperature (~ 250 °C). The inability to cool the samples from the melt, coupled with the low enthalpy of the transitions, meant that no further information about these thermal transitions could be gleaned from POM.

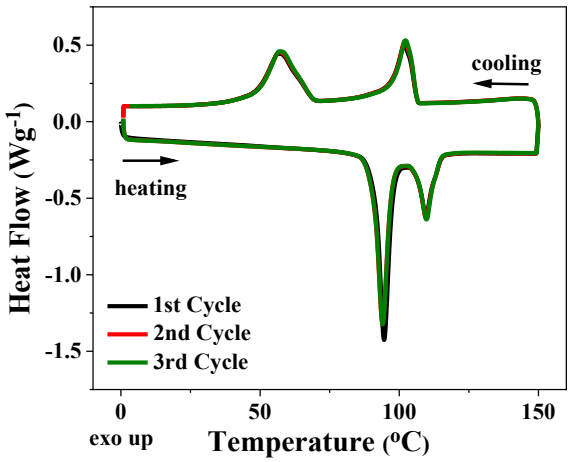


Figure 58: DSC plots (all cycles) for 3,8-dihexyl-diFIDT-di(N(CN)).

Table 11: Summary of TGA and DSC data for diFIDT-di(N(CN)) analogues versus diFIDT-di(C(CN)$_2$).

Alkyl Side-Chain	*diFIDT-di(C(CN)$_2$)*[a]			*diFIDT-di(N(CN))*		
	T_d [°C]	T_m [°C]	ΔH_m [J g^{-1}]	T_d [°C]	T_m [°C]	ΔH_m [J g^{-1}]
2,7-dihexyl	**319**	**248**	**59**	**321**	-[b]	-[b]
2,7-bis(2-ethylhexyl)	**333**	**221**	**62**	**335**	-[b]	-[b]
3,8-dihexyl	**298**	**238**	**79**	**334**	**92, 110**	**19, 11**

[a] data from Chapter 2 and Chapter 3, [b] no transitions observed in DSC.

4.2 OFET Performance

OFET devices incorporating the **dialkyl-diFIDT-di(N(CN))** OSCs were fabricated blade-coating. We are still awaiting the majority of device data, owing to delays due to the global covid-19 crisis. Key results are summarised in **Table 12**. Previous reports using the non-fluorinated **2,7-dihexyl-IDT-di(N(CN))** devices fabricated via vacuum deposition achieved only low mobilities (up to 1.4 x 10^{-3} cm^2 V^{-1} s^{-1}).[152] Devices with all **dialkyl-diFIDT-di(N(CN))** analogues exhibit unipolar electron transport, reflecting the role of the deep LUMO level in allowing stable electron transport. Also, a deep HOMO energy level (~ - 6.05 eV) imparts a large energy level offset with the S/D electrode helping to suppress competing hole injection and possible ambipolar behaviour. These features mirror that observed for **dialkyl-diFIDT-di(C(CN)$_2$)** analogues, supporting the applicability of *N*-cyanoimine-functionalised OSCs for use as transistor materials.

The saturated mobility is extracted from the linear part of the square root of the drain current (**Figure A97a** & **A98a**). Absence of any double slope in the plot endorses the reliability of the data, although a weak gate voltage-dependence of the saturated mobility above V_T suggests some device non-idealities (**Figure A97c** & **A98c**). The best performance was obtained for **2,7-dihexyl-diFIDT-di(N(CN))** devices, annealed at 200 °C, with a saturated electron mobility up to 0.13 cm^2 V^{-1} s^{-1} (average 0.09 cm^2 V^{-1} s^{-1}) across 8 devices. The performance of pristine

devices was over an order of magnitude lower (average 0.003 $cm^2 V^{-1} s^{-1}$). Lower saturated mobilities were achieved with the **3,8-dihexyl-diFIDT-di(N(CN))** (up to 0.03 $cm^2 V^{-1} s^{-1}$), which could maybe be attributed to poorer film quality. In contrast to **2,7-dihexyl-diFIDT-di(N(CN))**, no difference in performance was realised between pristine devices and devices annealed at 200 °C for **3,8-dihexyl-diFIDT-di(N(CN))**. Avoiding the need for thermal annealing is attractive in an industrial setting due to potentially reducing the energy consumption during manufacture.

All devices display performance at least an order of magnitude higher than previously reported for the vacuum-processed, non-fluorinated **2,7-dihexyl-IDT-di(N(CN))**. Having said that, **dialkyl-diFIDT-di(N(CN))** devices all display lower performance than the dicyanomethylene analogues (Section 2.6 & 3.6). Furthermore, the large variations in the threshold voltages suggest the presence of interfacial traps and a strong relation to the local processing conditions. This issue was also observed for all **dialkyl-diFIDT-di($C(CN)_2$)** devices and thus appears mutual to all devices fabricated by blade-coating. Due to the negligible difference in electrical properties (see Section 4.4), the inferior performance of **dialkyl-diFIDT-di(N(CN))** devices is likely ascribed device fabrication issues.

Table 12: Summary of OFET device performance for dialkyl-diFIDT-di(N(CN)) analogues in bottom contact-top gate contact configuration (best values in brackets).

Alkyl Side-chain	*Deposition*	V_T	μ_{linear}	$\mu_{saturated}$	I_{on}/I_{off}
		[V]	[$cm^2 V^{-1} s^{-1}$]	[$cm^2 V^{-1} s^{-1}$]	
2,7-dihexyl- [a]	Spin-coated	- [b]	- [b]	- [b]	- [b]
	Blade-coated	45.5	0.02	0.09 (0.13)	10^4
2,7-bis(2-ethylhexyl)-	Spin-coated	- [b]	- [b]	- [b]	- [b]
	Blade-coated	- [b]	- [b]	- [b]	- [b]
3,8-dihexyl-	Spin-coated	- [b]	- [b]	- [b]	- [b]
	Blade-coated	23.7	0.01	0.03 (0.03)	10^3

[a] annealed at 200 °C, [b] awaiting data.

4.3 Conclusion

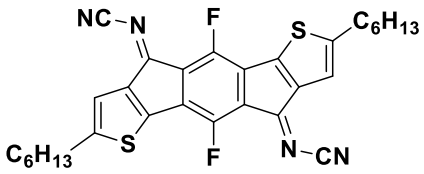
Three novel **dialkyl-diFIDT-di(N(CN))** OSCs bearing 2,7-dihexyl, 2,7-bis(2-ethylhexyl) and 3,8-dihexyl side-chains have been synthesised from the corresponding diketones via a Knoevenagel condensation reaction in moderate to high yields (50 – 90 %). The products could be isolated by simple hot recrystallisation. All three compounds displayed unexpectedly poor solubility in chlorobenzene (at 25 °C) and solubilities were markedly lower than the corresponding **dialkyl-diFIDT-di(C(CN)$_2$)** analogue explored in previous chapters. This was in contrast to that reported for the non-fluorinated analogues.

Single crystal analysis of the 2,7-dihexyl- and 3,8-dihexyl- analogues showed that they arrange into highly ordered planar slipped stacking arrangements with very close π-π stacking distances (~ 3.40 Å) and minimal π-π slippage. Furthermore, these strong aggregation properties are reflected in the thermal properties, where no melting point was observed up to ~ 250 °C. Clear degradation was observed above this point, possibly indicating limited thermal stability of the *N*-cyanoimine group itself. Introduction of the *N*-cyanoimine groups was confirmed to be effective at stabilising the LUMO (- 4.16 eV to - 4.19 eV) albeit slightly less so than dicyanomethylene (Chapters 2 and 3). Optoelectronic properties were similar also.

A subset of OFET devices incorporating **dialkyl-diFIDT-di(N(CN))** were fabricated and displayed good unipolar electron mobility, with μ_{sat} up to 0.13 cm^2 V^{-1} s^{-1} for **2,7-dihexyl-diFIDT-di(N(CN))** via scalable blade-coating. Performance was lower with the 3,8-dihexyl-side-chains (up to 0.03 cm^2 V^{-1} s^{-1}), which may be attributed to poorer thin film quality due to stronger aggregation properties. Device performance was lower than that observed for the **dialkyl-diFIDT-di(C(CN)$_2$)** analogues.

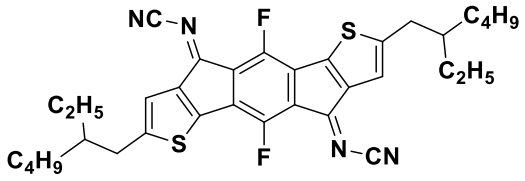
4.4 Experimental

2,2'-(5,10-Difluoro-2,7-dihexyl-s-indaceno[1,2-b:5,6-b']dithiophene-4,9-diylidene)dicyanoimine (2,7-dihexyl-diFIDT-di(N(CN))):



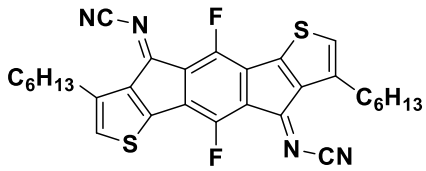
To solution of 5,10-difluoro-2,7-dihexyl-s-indaceno[1,2-b:5,6-b']dithiophene-4,9-dione (200 mg, 0.4 mmol) in anhydrous DCM (20 mL) at 0 °C was added $TiCl_4$ (0.44 mL, 4 mmol) dropwise. The resulting mixture was stirred for 10 mins at 0 °C. To this was added dropwise a solution bis(trimethylsilyl)carbodiimide (0.91 mL, 4 mmol) in anhydrous DCM (5 mL). The mixture was allowed to warm to room temperature and stirred for 4 hrs to give a deep red mixture. $TiCl_4$ (0.22 mL, 2 mmol) and bis(trimethylsilyl)carbodiimide (0.45 mL, 2 mmol) were added and the mixture was allowed to stir overnight. TLC (2/1 petroleum ether/DCM) confirmed the reaction was complete. Water was then added (100 mL) and the mixture was extracted with chloroform (2 x 50 mL). The combined organic extracts were rinsed with water (2 x 50 mL) and brine (50 mL), dried over anhydrous sodium sulfate, filtered and concentrated under reduced pressure. The crude solid was filtered and washed with methanol and acetone then dried in vacuo to give a dark, crystalline solid (110 mg, 50 %). m.p. N/A. ^{1}H NMR (400 MHz, $CDCl_3$, δ): 7.36 (s, 2 H, ArH), 2.82 (t, ^3J = 7.7 Hz, 4 H, CH_2), 1.70 (m, 4 H, CH_2), 1.33 (m, 12 H, CH_2), 0.90 (t, ^3J = 6.9 Hz, 6 H, CH_3). ^{13}C NMR (126 MHz, TCE-d_2, 120 °C, δ): 173.97, 155.42, 147.67, 147.59 (d, ^1J = 270 Hz, CF), 137.56, 129.93 – 129.45 (m, CF), 128.77 – 128.25 (m, CF), 119.61, 113.41, 31.08, 30.88, 30.55, 28.31, 22.09, 13.49. ^{19}F NMR (377 MHz, $CDCl_3$, δ): - 124.30 (s, CF). IR (cm^{-1}) 2179 (C≡N), 1602 (C=N-R). HRMS (ES-TOF) m/z: $[M+H]^+$ calcd. for $C_{30}H_{28}F_2N_4S_2$, 546.1723; found, 546.1734.

2,2'-(2,7-Bis(2-ethylhexyl)-5,10-difluoro-s-indaceno[1,2-b:5,6-b']dithiophene-4,9-diylidene)dicyanoimine (2,7-bis(2-ethylhexyl)-diFIDT-di(N(CN))):



To solution of 2,7-bis(2-ethylhexyl)-5,10-difluoro-s-indaceno[1,2-b5,6-b']dithiophene-4,9-dione (300 mg, 0.54 mmol) in anhydrous DCM (40 mL) at 0 °C was added $TiCl_4$ (0.6 mL, 5.41 mmol) dropwise. The resulting mixture was stirred for 10 mins at 0 °C. To this was added dropwise a solution bis(trimethylsilyl)carbodiimide (1.23 mL, 5.41 mmol) in anhydrous DCM (20 mL). The mixture was allowed to warm to room temperature and stirred for 4 hrs to give a deep red mixture. $TiCl_4$ (0.3 mL, 2.70 mmol) and bis(trimethylsilyl)carbodiimide (0.61 mL, 2.70 mmol) were added and the mixture was allowed to stir overnight. TLC (4/1 petroleum ether/DCM) confirmed the reaction was complete. Water was then added (100 mL) and the mixture was extracted with chloroform (2 x 50 mL). The combined organic extracts were rinsed with water (2 x 50 mL) and brine (50 mL), dried over anhydrous sodium sulfate, filtered and concentrated under reduced pressure. The crude solid was filtered and washed with methanol and acetone then dried in vacuo to give a dark, crystalline solid (295 mg, 90 %). m.p. N/A. ^{1}H NMR (400 MHz, $CDCl_3$, δ): 7.34 (s, 2H, ArH), 2.76 (d, 4H, ^3J = 6.8 Hz, CH_2), 1.61 (m, 2H, CH), 1.33 (m, 16H, CH_2), 0.91 (m, 12H, CH_3). ^{13}C NMR (126 MHz, TCE-d_2, 120 °C, δ): δ 177.34, 157.57, 151.22, 151.01 (d, ^1J = 268 Hz, CF), 140.90, 133.13 (m, CF), 131.97 (m, CF), 123.84, 116.79, 44.76, 38.36, 35.91, 32.09, 29.17, 25.94, 16.91, 13.91. ^{19}F NMR (377 MHz, $CDCl_3$, δ): - 124.26 (s, CF). IR (cm^{-1}) 2177 (C≡N), 1602 (C=N-R). HRMS (APCI) m/z: $[M+H]^+$ calcd. for $C_{34}H_{37}F_2N_4S_2$, 603.2422; found, 603.2425.

2,2'-(5,10-Difluoro-3,8-dihexyl-s-indaceno[1,2-b:5,6-b']dithiophene-4,9-diylidene)dicyanoimine (3,8-dihexyl-diFIDT-di(N(CN))):



To solution of 5,10-difluoro-3,8-dihexyl-s-indaceno[1,2-b:5,6-b']dithiophene-4,9-dione (200 mg, 0.4 mmol) in anhydrous DCM (20 mL) at 0 °C was added $TiCl_4$ (0.44 mL, 4 mmol) dropwise. The resulting mixture was stirred for 10 mins at 0 °C. To this was added dropwise a solution bis(trimethylsilyl)carbodiimide (0.91 mL, 4 mmol) in anhydrous DCM (5 mL). The mixture was allowed to warm to room temperature and stirred for 4 hrs to give a deep red mixture. $TiCl_4$ (0.22 mL, 2 mmol) and bis(trimethylsilyl)carbodiimide (0.45 mL, 2 mmol) were added and the mixture was allowed to stir overnight. TLC (2/1 petroleum ether/DCM) confirmed the reaction was complete. Water was then added (100 mL) and the mixture was extracted with chloroform (2 x 50 mL). The combined organic extracts were rinsed with water (2 x 50 mL) and brine (50 mL), dried over anhydrous sodium sulfate, filtered and concentrated under reduced pressure. The crude solid was filtered and washed with methanol and acetone then dried in vacuo to give a dark green, crystalline solid (112 mg, 51 %). m.p. N/A. ^{1}H NMR (400 MHz, $CDCl_3$, 50 °C, δ): 6.97 (2H, s, Ar H), 2.86 (4H, m, CH_2), 1.64 (4H, m, CH_2), 1.33 (12H, m, CH_2), 0.90 (6H, t, ^3J = 6.6 Hz, CH_3). ^{13}C NMR (101 MHz, TCE-d_2, 120 °C, δ): 170.45, 150.71, 146.90 (d, ^1J = 267 Hz, CF), 141.63, 138.89, 128.04, 112.31, 31.25, 29.55, 28.87, 28.41, 22.15, 13.54 (some carbon signals missing due to poor solubility). ^{19}F NMR (377 MHz, $CDCl_3$, 50 °C, δ): - 100.00 (s, CF). IR (cm^{-1}) 2179 (C≡N). HRMS (ES-TOF) m/z: $[M+H]^+$ calcd. for $C_{30}H_{28}F_2N_4S_2$, 546.1723; found, 546.1714.

5. Further modifications of 2,7-dialkyl-diFIDT-di(O)

5.1 End-functionalisation via Direct (Hetero)arylation

Single crystal characterisation was carried out by Dr. Andrew J. P. White (Imperial College London). Analysis of transfer integrals and intermolecular interactions was performed by Dr. Karl J. Thorley (University of Kentucky).

5.1.1 Introduction

While end-functionalisation of IDT is widespread, most notably in the formation of high performing NFAs for OPV, end-functionalisation of **IDT-di(O)** analogues has so far been limited. Seminal work by Zhao et al. coupled the **IDT-di(O)** core with thiophene units of varying lengths via traditional Stille cross coupling, as shown in **Figure 59a**.[108] The focus of this end-functionalisation was to modify the crystal packing and processability. More recently, Song et al. have reported a diketopyrrolopyrrole (DPP)-flanked IDT-di($C(CN)_2$), **DDPP-IDT-di($C(CN)_2$)** (**Figure 59b**).[160] This unit was predicted to be planar and possessed a very deep LUMO energy level (- 4.31 eV) and narrow band gap (0.95 eV), suggesting applicability as an ambipolar OSC. The synthesis required coupling of DPP to a 2,5-dibromoterephthalate ester with subsequent multi-step ring closure and bridge functionalisation to give the **IDT-di($C(CN)_2$)** core.

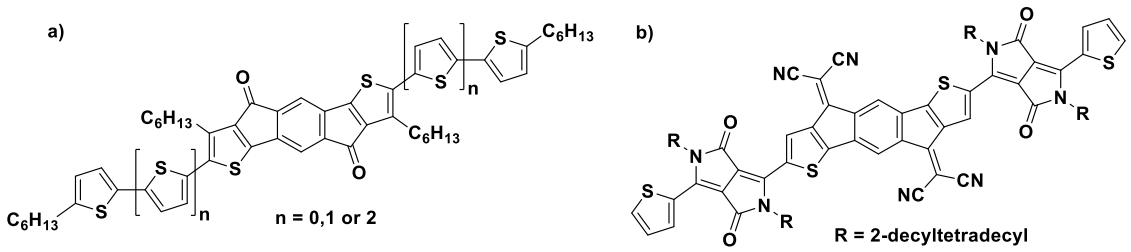


Figure 59: End Functionalisation of IDT-di(X) in the literature.

OSCs comprise assemblies of aromatic/heteroaromatic units connected by carbon – carbon bonds, to form extended π-conjugated systems. As a result, materials chemists employ Pd-catalysed cross-coupling reactions routinely to create these carbon – carbon bonds. Recently, there has been increasing utilisation of direct (hetero)arylation reactions for the synthesis of OSCs, in which C-H bond activation is exploited. Direct (hetero)arylation is seen as an attractive alternative to traditional cross-couplings primarily due to an absence of the necessity for pre-functionalisation of monomer to give a metallated precursor (e.g. Ar-SnR_3 for Stille or Ar-$B(OR)_2$ for Suzuki). This allows a reduced number of synthetic steps as well as avoidance of unstable organolithium compounds and/or toxic by-products (particularly organotin compounds in the case of Stille coupling). A central issue with direct (hetero)arylation is the sensitivity of C-H activation in different aromatic systems, necessitating extensive screening of conditions to optimise yields. In contrast, traditional cross-coupling methods such as Stille and Suzuki generally work over a range of conditions (aromatic system, catalyst, temperature etc.). Overall, direct (hetero)arylation can be more economical and environmentally friendly, making it an attractive approach despite the added optimisation. This has led to increasing adoption, particularly for polymerisations, by what is known as direct (hetero)arylation polymerisation (DHAP).[161,162] Comparable material properties and device performance can be achieved compared to polymers prepared via classical cross-couplings.[163]

Previous chapters focused solely on functionalisation at the 4,9-bridging point as a tool to introduce EWGs, in an effort to decrease the LUMO energy level. However, positioning of the

alkyl side-chain away from the reactive 2,7-positions, as with **3,8-dihexyl-diFIDT-dione**, allows scope for additional end-functionalisation. As a result, we were motivated to explore if direct arylation could be applied for use with **3,8-dihexyl-diFIDT-dione**, which contains C-H functionality at the thienyl α-position (**Figure 60**). Direct arylation was seen as particularly attractive for use with **3,8-dihexyl-diFIDT-dione** due to:

1) Existing literature examples of direct (hetero)arylation with IDT
2) Difficulties with traditional pre-functionisation (e.g. to Ar-B(OR)$_2$ or Ar-SnR$_3$)

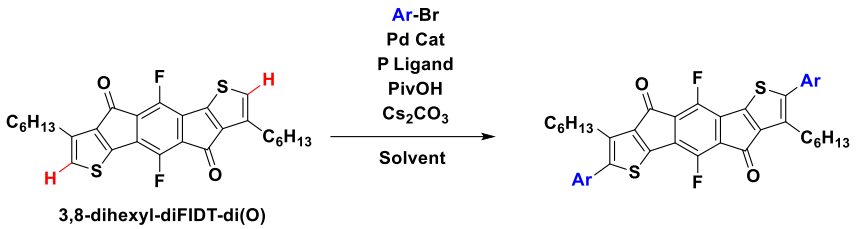


Figure 60: General scheme for direct (hetero)arylation of 3,8-dihexyl-diFIDT-dione.

Of particular interest was the possibility of cross-coupling with electron-deficient Ar-Br units, which could serve as a new route to lowering the LUMO energy level as well as tuning the aggregation properties. The use of commercially available Ar-Br units would also ensure economy both in cost and avoidance of additional synthetic steps. This methodology could allow potential access to a wide library of new electron-deficient OSCs. A selection of possible Ar-Br units is shown in **Figure 61**.

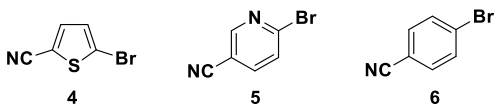


Figure 61: Selection of commercially-available electron-deficient Ar-Br Units.

Units bearing nitrile groups were considered due to their strong electron-withdrawing nature. Location of the nitrile group in the *para*-position, as opposed to the *ortho*- or *meta*- positions, would help minimise steric hinderance, promoting a more planar arrangement. This was

expected to be beneficial for charge transport by ensuring close π-π stacking. Torsional twisting between IDT and the adjacent aryl group was further predicted to decrease from **6** → **5** (due to removal of an *ortho*-H) and **6** → **4** (due to 6-membered ring versus 5-membered ring and reduced aromaticity). **5** was also attractive due to additional electron-deficiency from the pyridyl group, in contrast to the electron-rich thiophene in **4** for example, potentially aiding the lowering of the LUMO energy level. Optimised structures for **3,8-dialkyl-diFIDT-di(O)** bearing groups **4** – **6** are shown in **Figure 62**.

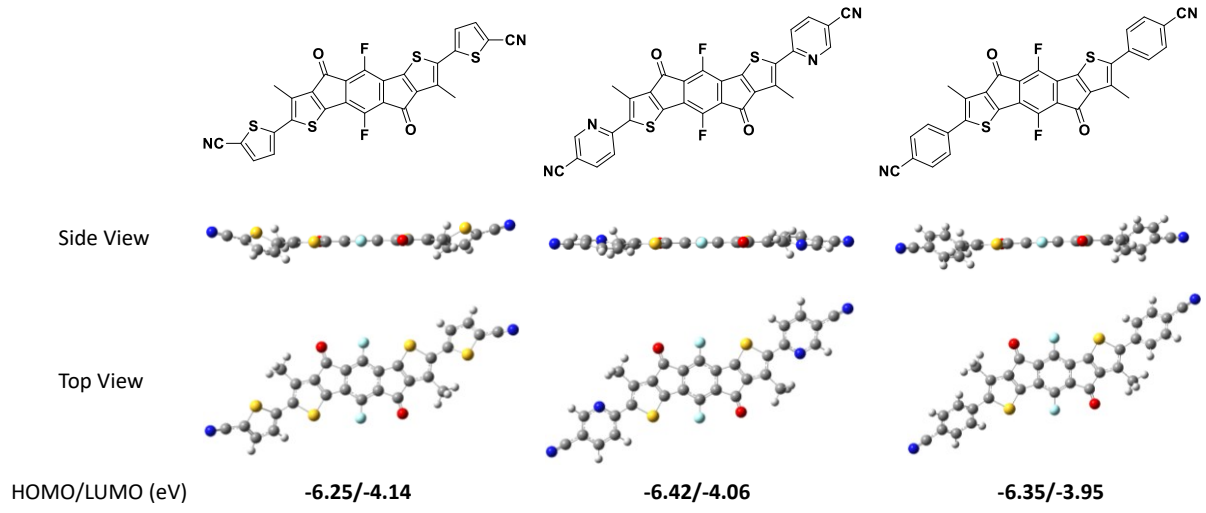


Figure 62: Optimised structures for a selection of end-functionalised diFIDT-di(O) analogues, calculated by DFT.

Direct (hetero)arylations using electron-deficient thiophenes have been reported to suffer from so called *β*-defects, whereby additional C-H bonds are activated towards coupling.[164,165] This phenomenon has been widely studied with regards to DHAP reactions for polymeric OSCs.[166,167] *β*-defects result in branching of the polymer chains which can have hugely detrimental effects on device performance and processability. **4** contains activated *β*-protons due to the presence of the nitrile and bromo substituents so was liable to unwanted competing C-H activation. Indeed, attempts to use **4** in direct (hetero)arylation with **3,8-dihexyl-diFIDT-di(O)** appeared to suffer from such a problem. As a result, successful coupling to give **2,7-**

bis(thiophene-2-carbonitrile)-3,8-dihexyl-diFIDT-di(O) was not achieved. Additionally, couplings using **5** appeared to be very sluggish with very poor conversion. Only a couple reports of direct heteroarylation reactions utilising halopyridines have been reported, to the best of our knowledge.[168,169] This indicates that this reaction could be improved with modifications to the reaction conditions, though may be difficult. Time demands meant that this was not pursued further.

In this chapter the synthesis and characterisation of **2,7-bis(4-benzonitrile)-3,8-dihexyl-diFIDT-di(O)** is reported, successfully prepared via the direct (hetero)arylation approach. Potential applicability of such modifications to produce novel OSCs is explored by analysis of the optoelectronic and thermal properties, along with the crystal structure analysis.

5.1.2 Synthesis

2,7-bis(4-benzonitrile)-3,8-dihexyl-diFIDT-di(O) was synthesised following the route outlined in **Figure 63**. **3,8-dihexyl-diFIDT-di(O)** was coupled with 4-bromobenzonitrile via direct (hetero)arylation conditions to give **2,7-bis(4-benzonitrile)-3,8-dihexyl-diFIDT-di(O)** in low yield (36 %) after purification via column chromatography. Direct arylation conditions (palladium catalyst, phosphorous ligand, organic acid and base) were chosen based on literature reports of the direct (hetero)arylation of IDT.[170] It was observed that high catalyst loading (0.2 equiv) was needed to ensure full conversion to the disubstituted product, with lower loadings (0.05 equiv) resulting in mainly the monosubstituted product. Neither longer reaction times nor higher temperatures (at low catalyst loading) improved conversion. A low isolated yield despite consumption of starting material (as indicated by TLC) may indicate the presence of undesired side-reactions. Further optimisation of the reaction conditions was not performed, though a more extensive screening of conditions may enable a higher yielding reaction. **2,7-bis(4-benzonitrile)-3,8-dihexyl-diFIDT-di(O)** was freely soluble in common organic solvents

(such as chloroform, DCM and THF). The chemical structure was verified by ^{1}H NMR, ^{19}F NMR, ^{13}C NMR, IR, HRMS and XRD.

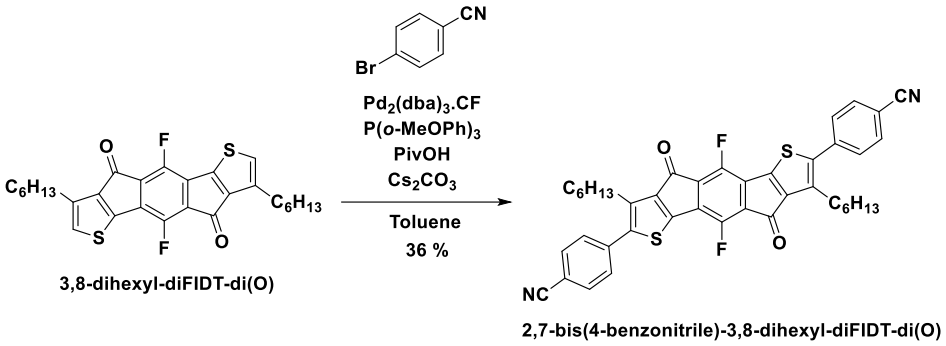


Figure 63: Synthesis of 2,7-bis(4-benzonitrile)-3,8-dihexyl-diFIDT-di(O).

We note that subsequent functionalisation of the bridging group in a similar manner to that explored in the preceding chapters was unsuccessful (**Figure 64**). We suggest that there may be a competitive activation of the nitrile group by $TiCl_4$, resulting in a mix of by-products.[171,172] This work was not followed up.

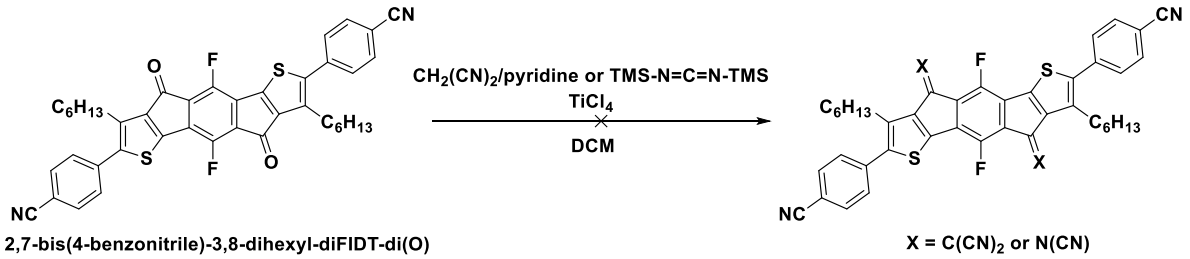


Figure 64: Unsuccessful bridge functionalisation of 2,7-bis(4-benzonitrile)-3,8-dihexyl-diFIDT-di(O).

5.1.3 Optoelectronic and Electrochemical Properties

The absorption spectra for **2,7-bis(4-benzonitrile)-3,8-dihexyl-diFIDT-di(O)** in solution (toluene and chloroform, 10^{-5} M) were recorded (**Figure 65a**). Similar to all **diFIDT-di(X)** analogues, the end-functionalised **3,8-dihexyl-diFIDT-di(O)** displayed a strong absorption band at shorter wavelengths (250 – 450 nm) as well as broad weak absorption at longer wavelengths (550 – 900 nm). There is a small increase in the intensity of the longer wavelength

absorption compared to **3,8-dihexyl-diFIDT-di(O)**, supported by improved HOMO – LUMO overlap (f = 0.181) predicted by TD-DFT (**Figure A102**). A small red-shift indicates a small reduction in the optical gap of **2,7-(4-benzonitrile)-3,8-dihexyl-diFIDT-di(O)** versus **3,8-dihexyl-diFIDT-di(O)**, corresponding well with electrochemical data.

Electrochemical studies of the **2,7-(4-benzonitrile)-3,8-dihexyl-diFIDT-di(O)** were performed by cyclic voltammetry (CV) using a 0.1 M solution of Bu_4NPF_6 in DCM solutions and a ferrocene (Fc/Fc^+) internal standard. Potentials were swept from 0 V to a positive maximum, then swept back to a negative maximum before returning to 0 V. In line with best practice, energy levels were estimated from $E^{1/2}$ (when reversibility is observed) or E^i (when irreversibility is observed), where $E^{1/2}$ is the half-wave potential, E^i is the inflection-point potential.[124] HOMO = - ($E^{1/2\ or\ i}$ + 4.8) eV and LUMO = - ($E^{1/2\ or\ i}$ + 4.8) eV for oxidation and reduction respectively, with the ferrocene/ferrocenium reference redox system at 4.8 eV below the vacuum level. Oxidation and reduction potentials are summarised in **Table 13**.

The cyclic voltammogram displayed two chemically reversible reductions along with two partially reversible/irreversible oxidation. (**Figure 65b**). A LUMO of - 3.80 eV corresponded to a minor stabilisation (0.12 eV) versus **3,8-dihexyl-diFIDT-di(O)**. This value is much smaller than predicted by DFT (Section 5.1.1), though not unexpected due to the substantial torsion of the 4-benzonitrile groups with respect to the IDT, as also predicted by DFT. Such torsion was confirmed by single crystal analysis (Section 5.1.4). A LUMO of - 3.80 eV is insufficient to impart thermodynamic stability of the reduced state in ambient conditions. This data demonstrates that end-functionalisation in the manner explored here is alone only capable of having a minor influence on energetics, particularly in comparison to the bridge-functionalisation explored in earlier chapters.

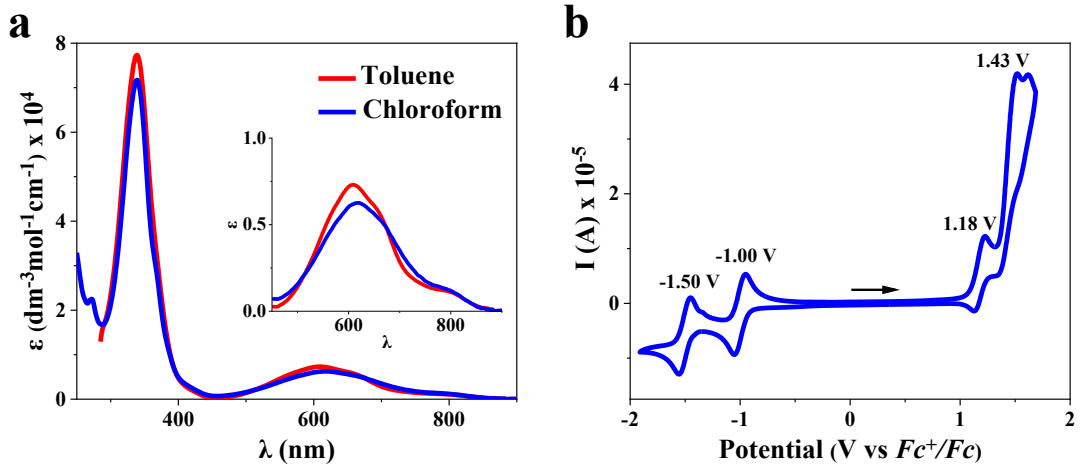


Figure 65: a) Solution absorption spectra in toluene and chloroform and b) Cyclic voltammogram, showing corresponding $E^{1/2}$ or i potentials, of 2,7-bis(4-benzonitrile)-3,8-dihexyl-diFIDT-di(O).

Table 13: Summary of material properties of 3,8-dihexyl-diFIDT-di(O) and 2,7-(4-benzonitrile)-3,8-dihexyl-diFIDT-di(O).

OSC	*HOMO*[a]	*LUMO*[a]	λ_{max} *(solution)*
	[eV]	[eV]	[nm]
3,8-dihexyl-IDT-di(O)[b]	- 5.98	- 3.68	583, 291[c]
			597, 374, 336, 294[d]
2,7-(4-benzonitrile)-3,8-dihexyl-diFIDT-di(O)	- 5.98	- 3.80	609, 339[c]
			618, 339[d]

[a] extracted from CV measurements, [b] data from Chapter 3, [c] in toluene, [d] in chloroform.

5.1.4 Crystal Structure

Single crystals were grown via the solvent vapour exchange method using a chlorobenzene/methanol mixture. **2,7-(4-benzonitrile)-3,8-dihexyl-diFIDT-di(O)** crystallised in the triclinic *P*1 space group containing two independent molecules, **A** (red) and **B** (blue) (**Figure 66a**). The structure also included a disordered arrangement of embedded solvent molecules (chlorobenzene), which were removed using SQUEEZE.[173]

The IDT core display some minor distortions from planarity. The hexyl side-chains on the thienyl *β*-position lie outside the plane in an L-configuration, with the alkyl C1 – C2 plane at 75.6 ° (molecule **A**) and 77.9 ° (molecule **B**) to the IDT plane. Additional 'floating' atoms indicate some minor disorder in the alkyl chain positioning. Full chain extension appears to be prevented by the alkyl chain and benzonitrile group of the neighbouring molecules (**Figure 66b**). Benzonitrile groups within a molecule are twisted 42.5 ° (molecule **A**) and 43.4 ° (molecule **B**) relative to the IDT plane, however are coplanar with each other (**Figure 66c**). This torsion indicates significant steric interactions between the benzonitrile groups and the IDT core, as predicted by DFT calculations (Section 5.1.1).

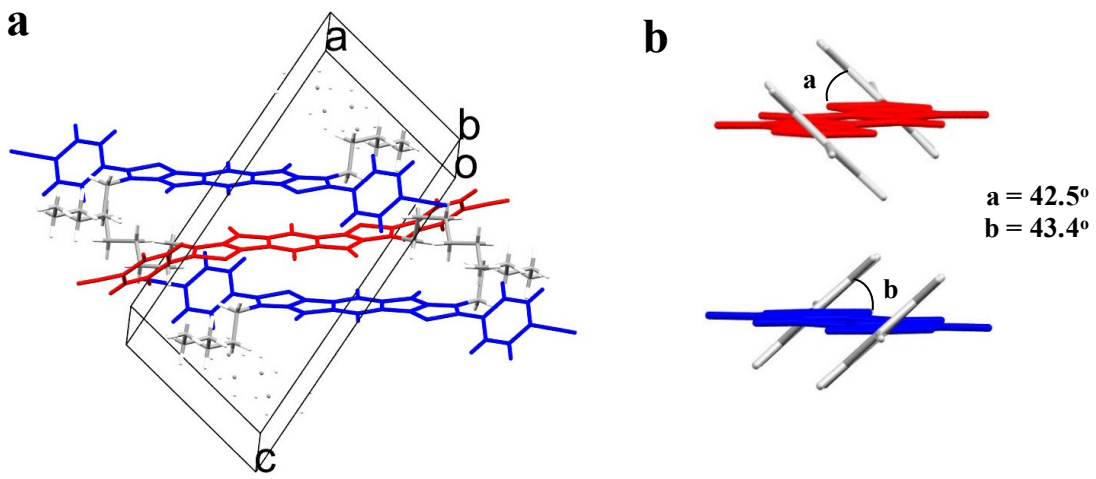


Figure 66: a) Unit cell of 2,7-(4-benzonitrile)-3,8-dihexyl-diFIDT-di(O), showing molecule A (red) and molecule B (blue). b) Torsion of benzonitrile groups out of the IDT plane for molecule A (red) and molecule B (blue), with alkyl chains removed for clarity.

A planar slipped π-π stacking arrangement is formed along the *a* axis, consisting of an alternating arrangement of molecule **A** and molecule **B**. Molecule **A** and molecule **B** sit in a shallow X-configuration relative to each other. There is almost co-facial packing of the conjugated core within a stack, along the *a* axis (**Figure 67a** & **c**). There is an angle of 1.8 ° between the planes of molecule **A** and molecule **B**. An average interplanar stacking distance of 3.35 Å (maximum = 3.51 Å, minimum 3.19 Å) and an average slipping distance of 3.35 Å

(angle 43.9 °) were observed. This amounted to a small decrease in interplanar stacking distance compared to **3,8-dihexyl-diFIDT-di(O)** (3.40 Å) and similar slipping distance (3.29 Å, angle 44.1 °).

One weak intramolecular C···H (molecule **A** = 2.70 Å, molecule **B** = 2.69 Å) short contact is observed between the benzonitrile and alkyl chain (**Figure 67b**). No alkyl chain interdigitation is observed, leading to loosely associated stacks. It is interesting that no direct π-π interactions exist between the two 4-benzonitrile units and/or between 4-benzonitrile and the diFIDT-di(O) core.

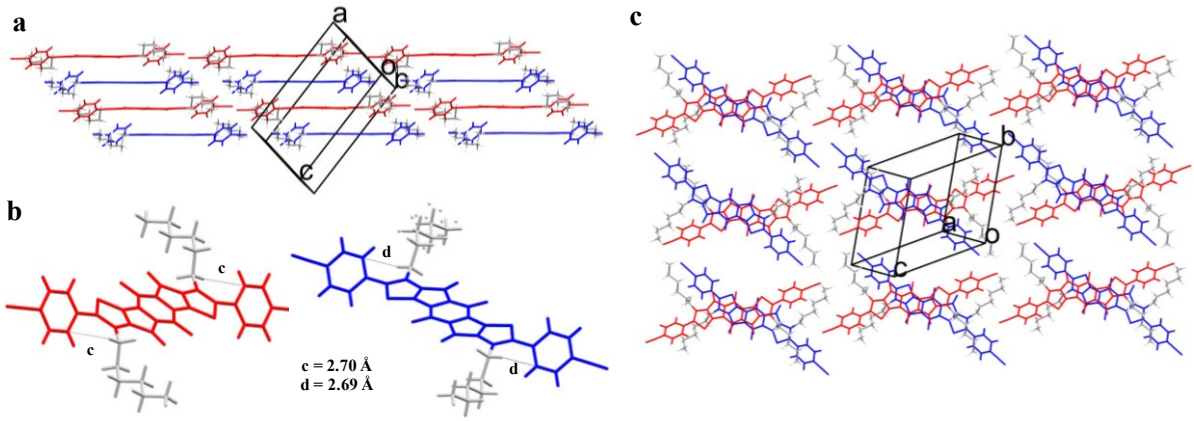


Figure 67: a) & b) Crystal packing motifs of 2,7-(4-benzonitrile)-3,8-dihexyl-diFIDT-di(O), showing molecule A (red) and molecule B (blue). a) X-configuration. b) Planar slipped stacking. c) Intramolecular short contacts in molecule A and molecule B.

As for crystal structures discussed in previous chapters, the electron transfer integral was calculated. A larger value indicates better overlap between frontier molecular orbitals on neighbouring units (LUMO-LUMO in the case of electron transport) and therefore the potential for more efficient charge transfer. **2,7-(4-benzonitrile)-3,8-dihexyl-diFIDT-di(O)** displays a one-dimensional (1D) charge transfer pathway, with an electron transfer integral (B3LYP/6-31G(d)) of 61 meV for the main π-stack. This value is fairly high despite the X-configuration

of molecule **A** and molecule **B**, and only slightly reduced compared to **3,8-dihexyl-diFIDT-di(O)** (66 meV).

5.1.5 Thermal Properties

The thermal behaviour of **2,7-bis(4-benzonitrile)-3,8-dihexyl-diFIDT-di(O)** was investigated by TGA (**Figure 68a**) and DSC (**Figure 68b**).

2,7-bis(4-benzonitrile)-3,8-dihexyl-diFIDT-di(O) displayed a very high thermal stability, with a T_d of 399 °C (temperature at which 5 % mass loss is reached) (**Figure Xa**). This corresponded to a 31 °C increase versus **3,8-dihexyl-diFIDT-di(O)** (T_d = 368 °C), indicating that end-functionalisation was beneficial for thermal stability. A single sharp melting endotherm was observed (T_m = 229 °C, ΔH_m = 57 J g^{-1}), which appeared to be stable to repeated thermal cycling. The subsequent crystallisation exotherm observed upon cooling broadened and split into multiple peaks as the heating/cooling cycles proceeded. This indicated the formation of multiple polymorphs, potentially due to the cooling rate being too high. The melting temperature of **2,7-bis(4-benzonitrile)-3,8-dihexyl-diFIDT-di(O)** (T_m = 229 °C) was higher than **3,8-dihexyl-diFIDT-di(O)** (T_m = 176 °C). While this increase could indicate the enhancement of intermolecular interactions, for instance from additional π-π stacking by the 4-benzonitrile moieties, a large increase in molecular weight (700.86 g mol^{-1} versus 498.65 g mol^{-1}) could also be a contributing factor. Analysis of the crystal packing (Section 5.1.4) suggests it may be the latter.

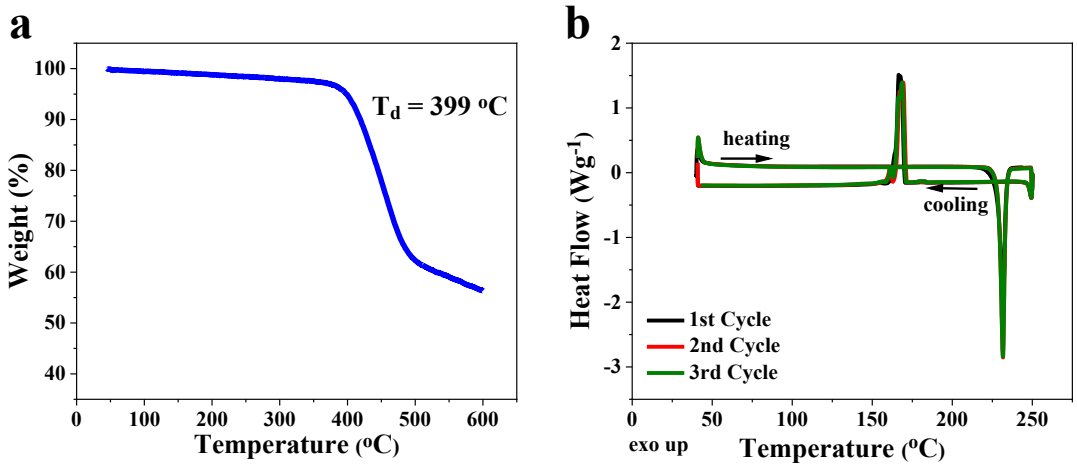


Figure 68: a) TGA plot and b) DSC plots (all cycles) for 2,7-bis(4-benzonitrile)-3,8-dihexyl-diFIDT-di(O).

5.1.6 Conclusion

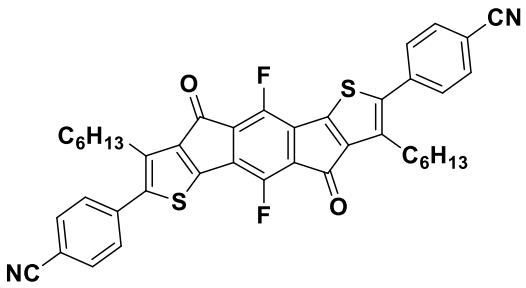
2,7-bis(4-benzonitrile)-3,8-dihexyl-diFIDT-di(O) was prepared via the direct (hetero)arylation approach, utilising C-H activation of **3,8-dihexyl-diFIDT-di(O)**, in a low yield (36 %). This amounts to the first known use of C-H activation on an electron-deficient IDT core. The low yield highlights one of the issues associated with direct arylation cross couplings (reagent sensitivity) and is expected to improve upon optimisation of the reaction conditions. Usage of this methodology for the introduction of more attractive functionality (e.g. thiophene- or pyridine-containing groups) is so far unsuccessful. Post-functionalisation at the bridging unit was also unsuccessful. Instead, we propose that direct (hetero)arylation with **3,8-dihexyl-diFIDT-di(C(CN)$_2$)** directly may be preferable.

Introduction of the 4-benzonitrile groups at the 2,7-positions of **3,8-dihexyl-diFIDT-di(O)** appears to have only a minor impact on the electronic properties. The UV-Vis spectrum of **2,7-bis(4-benzonitrile)-3,8-dihexyl-diFIDT-di(O)** in solution is largely similar to **3,8-dihexyl-diFIDT-di(O)**, with a small red-shift in absorption. In addition, a LUMO energy level (- 3.80 eV) is calculated from CV measurements, amounting to a small stabilisation versus **3,8-dihexyl-diFIDT-di(O)** (- 3.68 eV) and less pronounced than predicted by DFT.

Conversely, the 4-benzonitrile groups are shown to have a profound effect on the physical properties. High thermal stability (T_d = 399 °C) and melting temperature (T_m = 229 °C) indicate the OSC should be stable to common device fabrication conditions. These values are significantly higher than **3,8-dihexyl-diFIDT-di(O)** (T_d = 368 °C and T_m = 176 °C), which is attributed primarily to the increase in molecular weight. Single crystal analysis shows that **2,7-bis(4-benzonitrile)-3,8-dihexyl-diFIDT-di(O)** forms a planar slipped π-π stacking arrangement, with significant torsional twisting at the 2,7-position (~ 43 °) between 4-benzonitrile and IDT. Two independent molecules exist in the packing motif, arranged in an X-configuration. The findings indicate that **2,7-bis(4-benzonitrile)-3,8-dihexyl-diFIDT-di(O)** is likely poorly suited for use in n-type transistor applications, owing to a rather high lying LUMO energy level. This is in spite of a relatively high electron transfer integral between the π-stacks (61 meV).

5.1.7 Experimental

4,4'-(5,10-Difluoro-3,8-dihexyl-4,9-dioxo-4,9-dihydro-s-indaceno[1,2-b5,6-b']dithiophene-2,7-diyl)dibenzonitrile (2,7-bis(4-benzonitrile)-3,8-dihexyl-diFIDT-di(O)):



To a mixture of 3,8-dihexyl-5,10-difluoro-s-indaceno[1,2-b5,6-b']dithiophene-4,9-dione (200 mg, 0.4 mmol), 4-bromobenzonitrile (218 mg, 1.2 mmol), $Pd_2(dba)_3$.CF (80 mg, 0.08 mmol, 0.2 equiv), tri(*o*-anisyl)phosphine (84 mg, 0.24 mmol), pivalic acid (40 mg, 0.4 mmol), and caesium carbonate (392 mg, 1.2 mmol) in a 20 mL microwave vial was added toluene (5 mL).

The reaction mixture was degassed under nitrogen and premixed for 15 mins, then was heated to 130 °C and stirred vigorously overnight. After cooling to room temperature, the mixture was added to water and extracted with chloroform and the combined organic fractions dried over Na_2SO_4 and filtered. The solvent was removed. The crude product was purified by column chromatography on silica (4:1 DCM/petroleum ether) to give a blue solid (102 mg, 36 %). m.p. 229 °C. ^{1}H NMR (400 MHz, $CDCl_3$, δ): 7.76 (d, ^3J = 8.4 Hz, 4 H, Ar H), 7.55 (d, ^3J = 8.4 Hz, 4 H, Ar H), 2.78 (t, ^3J = 7.5 Hz, 4 H, CH_2), 1.68 – 1.61 (m, 4 H, CH_2), 1.26 (m, 12 H, CH_2), 0.8 (t, ^3J =6.6 Hz, 6 H, CH_3). ^{13}C NMR (101 MHz, $CDCl_3$, δ): 182.18, 150.94, 146.66 (dd, ^1J = 267 Hz, ^4J = 2.6 Hz, CF), 143.30, 140.29, 137.99, 137.78, 132.86, 132.86, 129.58, 129.48 – 129.25 (m, CF), 127.69 – 127.49 (m, CF), 118.43, 112.35, 31.48, 30.14, 29.30, 26.82, 22.68, 14.16. ^{19}F NMR (377 MHz, $CDCl_3$, δ): - 128.73 (s, CF). IR (cm^{-1}) 2225 (C≡N), 1707 (broad, C=O). HRMS (ES-TOF) m/z: $[M+H]^+$ calcd. for $C_{42}H_{34}N_4F_2O_2S_2$ 700.2030, found 700.2021.

5.2 Nucleophilic Aromatic Substitution (S_NAr) of the Fluorine Group

Preparation of dimethyldioxirane (DMDO) for the synthesis of the **2,7-bis(2-ethylhexyl)-diSO$_2$RIDT-di(O)** was carried out by Martina Rimmele (Imperial College London).

5.2.1 Introduction

Aromatic nucleophilic substitution (S_NAr) reactions are utilised extensively in the pharmaceutical industry due to their high atom economy and mild conditions.[174] These reactions involve attack by a nucleophile on an aromatic unit, leading to the substitution of a leaving group. Traditionally, this reaction is believed to proceed via an addition-elimination mechanism (**Figure 69**).[175]

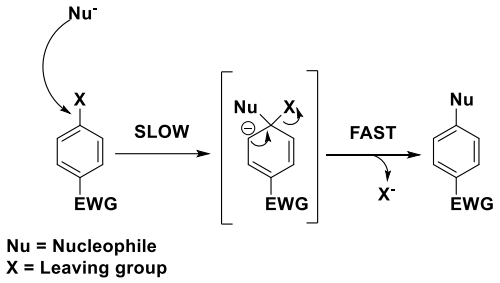


Figure 69: General Mechanism for S_NAr Reactions.

The nucleophile (Nu^-) first adds to the aromatic unit, resulting in a negatively-charged tetrahedral intermediate known as a Meisenheimer complex. The loss of aromaticity results in the addition step being rate-limiting. Next, elimination of the leaving group (X^-) proceeds quickly to regain the aromaticity, leading to an overall substitution of X for Nu. These reactions are promoted by the presence of EWGs, which are able to stabilise the negatively charged intermediate. Unusually, fluorine is preferred as a leaving group since the high electronegativity serves to further stabilise the negatively-charged intermediate. C – X bond

breaking is not the rate-limiting step (unlike, for instance, in S_N1/S_N2 reactions), meaning the higher C – F bond energy is not a factor. It should be noted that recent theoretical and experimental investigations have put into doubt the wide applicability of this two-step mechanism.[176–178]

Utilisation of S_NAr reactions for modifications of organic semiconductors has been explored previously in the Heeney group, focusing on substitutions of fluorinated benzothiadiazole (BT) and benzotriazole (BTz) units.[179,180] In an original study, Casey et al. utilised a double S_NAr reaction of a difluoro-BT (**diFBT**) unit to give the novel dithioalkyl-BT (**diSRBT**) in moderate yield using an alkyl thiol (RSH) and a mild base (K_2CO_3) in DMF. These units were then used in copolymers for use as donors in organic solar cells. The substitution was shown to effectively improve the solubility, aiding polymer processing. Subsequent studies by Creamer et al. expanded this work to include substitution using alcohols (ROH) and primary amines (RNH_2) (**Figure 70a**).[181] This methodology has further been shown to be effective for post-polymerisation functionalisation with multi-functional thiols for emissive conjugated polymer nanoparticles (**Figure 70b**).[182] Post-polymerisation functionalisation is particularly attractive as reactive functional groups can be introduced that are unlikely to survive the polymerisation conditions.

Casey et al. also employed the S_NAr methodology to increase the electron-accepting of the BT unit by substitution of the fluorine groups with strongly electron-withdrawing cyano groups.[183] Cyanation was shown to cause a large stabilisation of the LUMO in germole copolymers such that OFET devices displayed a complete shift from unipolar hole transport to unipolar electron transport. A follow-up study highlighted that systematic tuning of the LUMO energy level via cyano substitution with the same germole copolymer enabled optimisation of

solar cell performance.[184] Cyanation has likewise been shown to be applicable to fluorinated BTz acceptor units (**Figure 70a**).[185]

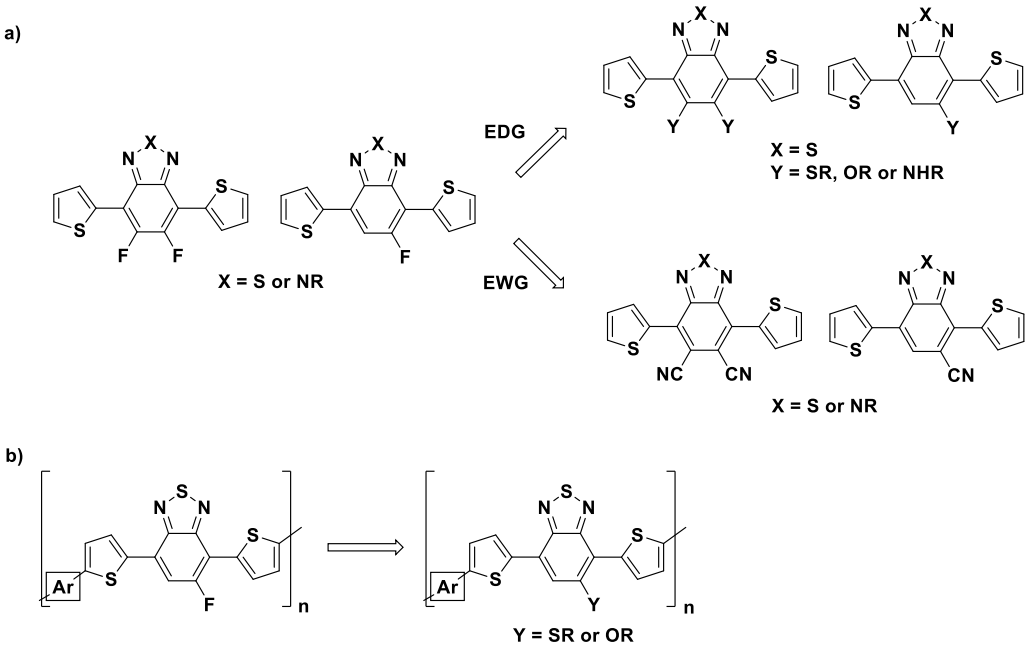


Figure 70: Summary of S_NAr work performed previously in the Heeney group.

The success of this work prompted consideration of whether this methodology could be applied to the electron-deficient units outlined in this thesis. The presence of EWGs in the *ortho*-positions to the fluorine groups of the central phenyl ring indicated possible reactivity towards S_NAr reactions (**Figure 71**).

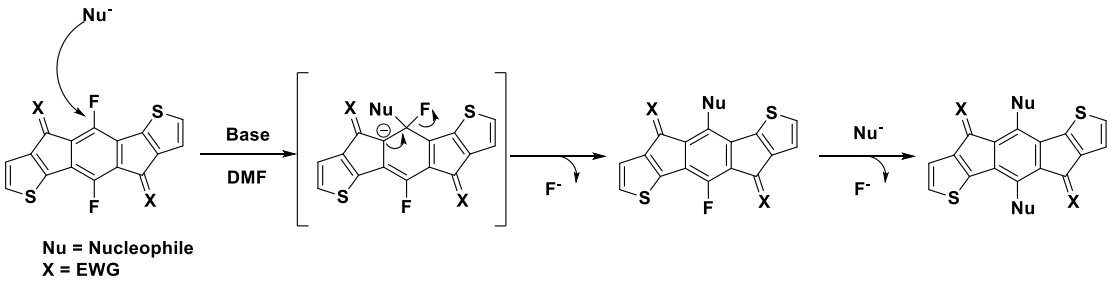


Figure 71: Mechanism for S_NAr on diFIDT-di(X).

The initial aim was to investigate whether cyano substitution was possible on **dialkyl-diFIDT-di(O)**, to form the highly electron-deficient **dialkyl-diCNIDT-di(O)**. **Dialkyl-diCNIDT-**

di(O) was predicted to be planar with a large stabilisation of the LUMO energy level (~ 0.35 eV) versus **dialkyl-diFIDT-di(O)** (**Figure 72**). This suggested suitability for n-type applications. However, test reactions were deemed unsuccessful. A likely explanation was the possibility for undesired nucleophilic addition at the carbonyl group. Cyanides are well-known to form cyanohydrins with ketones, for instance in the benzoin condensation reaction.[186] This proposal was supported by analysis of the NMR and IR data – fluorine signals remained in the ^{19}F NMR whereas a C≡N stretch appeared in the IR, without the presence of a C=O stretch.

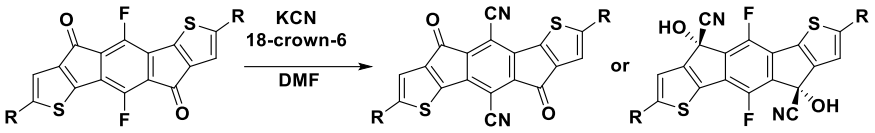


Figure 72: Possible products from reaction of diFIDT-di(O) with cyanide.

This resulted in attention being transferred to substitution using thiols instead. Competing reaction at the carbonyl was expected to be suppressed due to the softer nature of the thiolate nucleophile. In this chapter partial adoption of the S_NAr methodology for use with **dialkyl-diFIDT-di(O)** is reported. In particular, substitution of the fluorine groups with alkyl thiol groups is reported to give the novel **dialkyl-diSRIDT-di(O)**. Furthermore, selective full oxidation of the alkyl thiol groups under mild conditions enables conversion from moderate EDGs (thiol) to strong EWGs (sulfone), to afford **dialkyl-diSO_2R-IDT-di(O)**. DFT calculations predicted a large stabilisation of the LUMO (~ 0.4 eV) versus **dialkyl-diFIDT-di(O)**, which was larger than that for **dialkyl-diCNIDT-di(O)** (**Figure 73**). Some distortion from planarity was also observed, highlighting the increased steric bulk of the SO_2R group. With analysis of the optoelectronic and thermal properties, the suitability of the **diSO_2R-IDT-di(O)** for use in organic electronic devices is investigated.

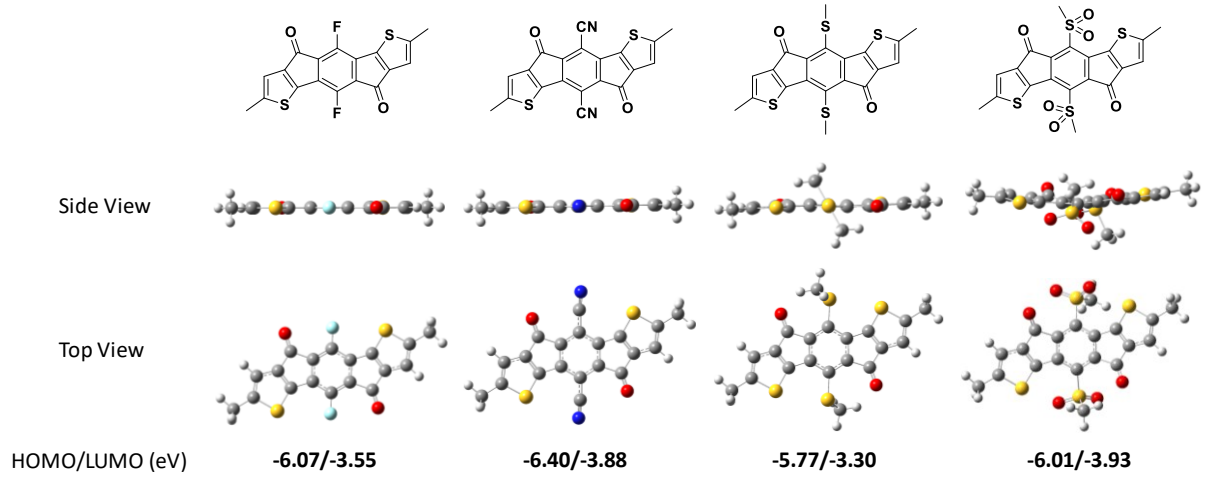


Figure 73: Optimised Structures for diFIDT-di(O) (left), diCNIDT-di(O) (middle left), diSRIDT-di(O) (middle right) and diSO₂RIDT-di(O) (right), calculated by DFT.

5.2.2 Synthesis

2,7-bis(2-ethylhexyl)-diSRIDT-di(O) and **2,7-bis(2-ethylhexyl)-diSO₂RIDT-di(O)** were synthesised following the synthetic route outlined in **Figure 74**. Substitution of the fluorine groups was achieved by heating with octane-1-thiol in the presence of a weak base (K_2CO_3), in a polar aprotic solvent (DMF). The product was purified using column chromatography to give **2,7-bis(2-ethylhexyl)-diSRIDT-di(O)** in a moderate yield (66 %) as a blue solid. Subsequently, the thioether was oxidised cleanly to the corresponding disulfone using dimethyldioxirane (DMDO) in DCM at room temperature. DMDO was prepared previously by Martina Rimmele following a literature procedure.[187] The progress of the reaction was tracked via TLC. Simple removal of the solvent followed by purification by column chromatography gave **2,7-bis(2-ethylhexyl)-diSO₂RIDT-di(O)** in moderate yield (61 %) as a tacky turquoise film. Both **2,7-bis(2-ethylhexyl)-diSRIDT-di(O)** and **2,7-bis(2-ethylhexyl)-diSO₂RIDT-di(O)** were freely soluble in common organic solvents (e.g. chloroform, THF, dichloromethane etc.). The chemical structures were verified by ^{1}H NMR, ^{13}C NMR, IR and HRMS. In particular, IR and HRMS were decisive in confirming full oxidation to the sulfone as opposed to only partial oxidation to the sulfoxide. **2,7-bis(2-ethylhexyl)-diSRIDT-di(O)** formed hair-

like bunched blue needles by vapour phase diffusion from a chlorobenzene/methanol mixture, though they were of insufficient quality for XRD analysis.

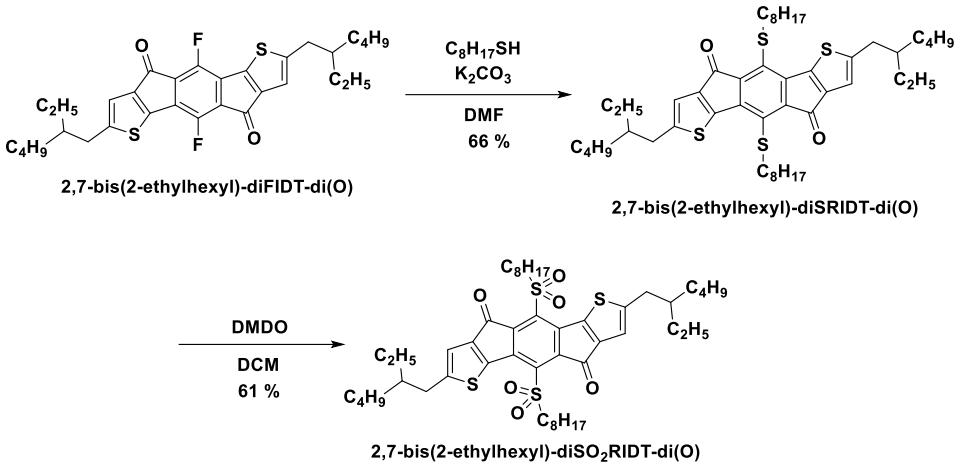


Figure 74: Synthesis of 2,7-bis(2-ethylhexyl)-diSRIDT-di(O) and 2,7-bis(2-ethylhexyl)-diSO₂RIDT-di(O).

We note that substitution of the fluorine groups of neither **dialkyl-diFIDT-di(C(CN)$_2$)** nor **dialkyl-diFIDT-di(N(CN))** were successful. ^{1}H NMR indicated the presence of the thioether group/s (**Figure A109**) while multiple signals were apparent in the ^{19}F NMR (**Figure A110**). The problem is likely to be competing base-catalysed 1,4-addition of the thiol at the bridging point (**Figure 75**).[188] Such thiol-Michael addition 'click' reactions have been widely studied.

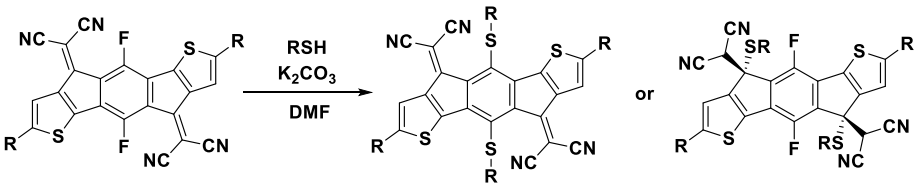


Figure 75: Possible products from reaction of diFIDT-di(C(CN)₂) with thiol.

5.2.3 Optoelectronic and Electrochemical Properties

The absorption spectra for **2,7-bis(2-ethylhexyl)-diSRIDT-di(O)** and **2,7-bis(2-ethylhexyl)-diSO$_2$RIDT-di(O)** in solution (toluene and chloroform, 10^{-5} M) were recorded (**Figure 76**). Similar to **2,7-bis(2-ethylhexyl)-diFIDT-di(O)**, **2,7-bis(2-ethylhexyl)-diSRIDT-di(O)** displayed a stronger absorption band at shorter wavelengths (250 – 400 nm) as well as broad

weak absorption at longer wavelengths (500 – 850 nm) (**Figure 76b**). Unlike the fluorinated analogue though is the presence of two distinct, overlapping peaks at shorter wavelengths. This is not predicted by TD-DFT, though a broadening is observed, resulting from overlap between a larger number of states (**Figure A111a**). Moreover, the molar absorption coefficient of these peaks is roughly half that of the fluorinated analogue (~ 7 x 10^4 dm^3 mol^{-1} cm^{-1} vs ~ 3.5 x 10^4 dm^3 mol^{-1} cm^{-1}). A weak red-shift of the longer wavelength absorption indicated a small narrowing of the optical gap versus **2,7-bis(2-ethylhexyl)-diFIDT-di(O)**.

The absorption spectra for **2,7-bis(2-ethylhexyl)-diSO_2RIDT-di(O)** was markedly different from **2,7-bis(2-ethylhexyl)-diSRIDT-di(O)**, most notably by the absence of a short wavelength absorption in the 450 – 900 nm region (**Figure 76c**). This possibly reflects that disruption to the planarity of the aromatic core due to the large SO_2R groups limits HOMO-LUMO orbital overlap drastically. Such optical transparency is very attractive for cathode interlayer applications, as has been demonstrated by Miao et al. on a structurally similar IDT-based material.[189] In the near-UV region there are two distinct, overlapping peaks, as seen in the spectrum of **2,7-bis(2-ethylhexyl)-diSRIDT-di(O)**, though they red shifted. In addition to this is a sharp absorption < 300 nm. Molar absorption coefficients of these peaks are further reduced versus that of **2,7-bis(2-ethylhexyl)-diSRIDT-di(O)** in agreement with the predicted spectrum calculated by TD-DFT (**Figure A111b**).

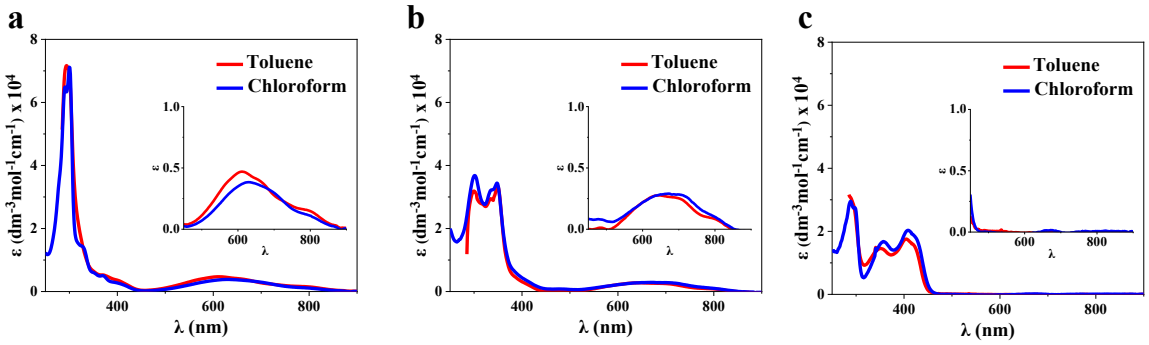


Figure 76: Solution absorption spectra for a) 2,7-bis(2-ethylhexyl)-diFIDT-di(O)[a]. b) 2,7-bis(2-ethylhexyl)-diSRIDT-di(O). c) 2,7-bis(2-ethylhexyl)-diSO$_2$RIDT-di(O) in toluene and chloroform. [a]Data taken from Chapter 3.

Electrochemical studies of the **2,7-bis(2-ethylhexyl)-diSRIDT-di(O)** and **2,7-bis(2-ethylhexyl)-diSO$_2$RIDT-di(O)** were performed by cyclic voltammetry (CV) using a 0.1 M solution of Bu_4NPF_6 in DCM solutions and a ferrocene (Fc/Fc^+) internal standard. Potentials were swept from 0 V to a positive maximum, then swept back to a negative maximum before returning to 0 V. In line with best practice, energy levels were estimated from $E^{1/2}$ (when reversibility is observed) or E^i (when irreversibility is observed), where $E^{1/2}$ is the half-wave potential, E^i is the inflection-point potential.[124] HOMO = - ($E^{1/2\ or\ i}$ + 4.8) eV and LUMO = - ($E^{1/2\ or\ i}$ + 4.8) eV for oxidation and reduction respectively, with the ferrocene/ferrocenium reference redox system at 4.8 eV below the vacuum level. Oxidation and reduction potentials are summarised in **Table 14**.

The cyclic voltammogram of **2,7-bis(2-ethylhexyl)-diSRIDT-di(O)** displayed one chemically reversible reduction along with two partially reversible oxidations. (**Figure 77b**). Unlike **2,7-bis(2-ethylhexyl)-diFIDT-di(O)** and all other fluorinated analogues, a second reduction is not observed in this case, most likely occurring outside of the potential window for DCM. A LUMO of - 3.49 eV corresponded to a moderate destabilisation (0.21 eV) versus **2,7-bis(2-ethylhexyl)-diFIDT-di(O)**. This modification is also shown to destabilise the HOMO (- 5.70 eV), reflecting the change from highly electronegative fluorine groups to electron-donating

thioether groups. A slightly greater destabilisation of the HOMO versus the LUMO results in a small decrease in the electrochemical gap compared to **2,7-bis(2-ethylhexyl)-diFIDT-di(O)**, corresponding well with the optoelectronic data.

The cyclic voltammogram of **2,7-bis(2-ethylhexyl)-diSO$_2$RIDT-di(O)** exhibits two chemically reversible reductions along with two partially reversible/irreversible oxidations. (**Figure 77c**). A LUMO of - 3.87 eV corresponds to large stabilisation (0.38 eV) versus **2,7-bis(2-ethylhexyl)-diSRIDT-di(O)**, reflecting the change from electron-donating to electron-withdrawing upon oxidation of the thioether groups to sulfone groups. Furthermore, a small stabilisation of the LUMO was seen versus **2,7-bis(2-ethylhexyl)-diFIDT-di(O)** (0.17 eV). A LUMO of - 3.87 eV demonstrates that, as with end-functionalisation (Section 5.1.3), substitution of the fluorine groups in the manner explored here is alone insufficient to impart thermodynamic stability in ambient conditions. The HOMO is also stabilised, albeit less so (0.25 eV), compared to **2,7-bis(2-ethylhexyl)-diSRIDT-di(O)** resulting in a small narrowing of the electrochemical gap.

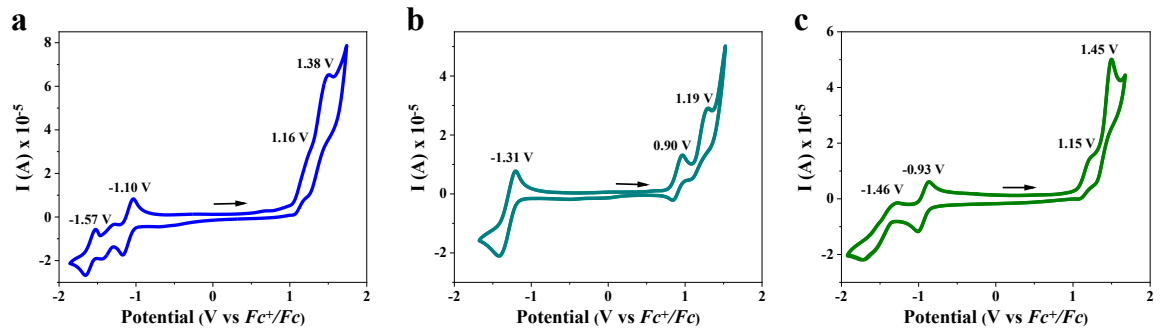


Figure 77: Cyclic voltammograms of sulfur-substituted analogues, showing corresponding $E^{1/2\ or\ i}$ potentials. a) 2,7-bis(2-ethylhexyl)-diFIDT-di(O)[a)]. b) 2,7-bis(2-ethylhexyl)-diSRIDT-di(O). c) 2,7-bis(2-ethylhexyl)-diSO$_2$RIDT-di(O). [a)]Data taken from Chapter 3.

Table 14: Summary of material properties of 3,8-dihexyl-diFIDT-di(O) and 2,7-(4-benzonitrile)-3,8-dihexyl-diFIDT-di(O).

OSC	*HOMO*[a)]	*LUMO*[a)]	λ_{max} *(solution)*
	[eV]	[eV]	[nm]
2,7-bis(2-ethylhexyl)-diFIDT-di(O)[b)]	- 5.96	- 3.70	612, 294[c)]
			629, 300, 291[d)]
2,7-bis(2-ethylhexyl)-diSRIDT-di(O)	- 5.70	- 3.49	648, 349, 300[c)]
			672, 348, 301[d)]
2,7-bis(2-ethylhexyl)-diSO$_2$RIDT-di(O)	- 5.95	- 3.87	406, 351, 285[c)]
			408, 357, 289[d)]

[a)]extracted from CV measurements, [b)]data from Chapter 3, [c)]in toluene, [d)]in chloroform.

5.2.4 Thermal Properties

The thermal behaviour of **2,7-bis(2-ethylhexyl)-diSRIDT-di(O)** and **2,7-bis(2-ethylhexyl)-diSO$_2$RIDT-di(O)** were investigated by TGA (**Figure 78**) and DSC (**Figure 79**). Key data are summarised in **Table 15**.

2,7-bis(2-ethylhexyl)-diSRIDT-di(O) exhibited high thermal stability (T_d = 346 °C), albeit slightly lower than the fluorinated analogue (T_d = 364 °C) (**Figure 78b**). Conversion to the disulfone analogue, **2,7-bis(2-ethylhexyl)-diSO$_2$RIDT-di(O)**, resulted in a pronounced decrease in decomposition temperature (49 °C) (**Figure 78c**).

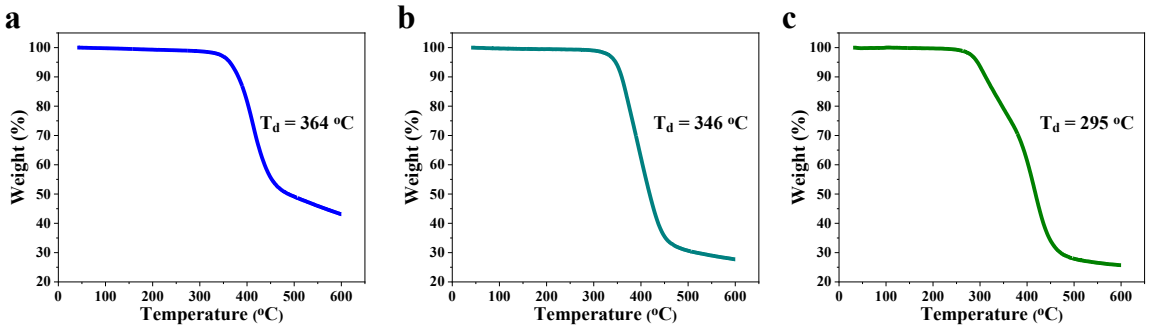


Figure 78: TGA plots for 2,7-bis(2-ethylhexyl)-diFIDT-di(O)[a], 2,7-bis(2-ethylhexyl)-diSRIDT-di(O) and 2,7-bis(2-ethylhexyl)-diSO$_2$RIDT-di(O). [a]Data from Chapter 3.

2,7-bis(2-ethylhexyl)-diSRIDT-di(O) exhibited a single reversible endotherm (T_m = 82 °C) that appeared stable upon thermal cycling (up to 250 °C in this analysis) (**Figure 79b**). This corresponded to a significant decrease in melting point compared to **2,7-bis(2-ethylhexyl)-diFIDT-di(O)** (T_m = 213 °C) thus indicating that substitution of the core fluorine groups causes disruption to the intermolecular interactions between aromatic cores. Fluorine groups have been shown to introduce some stabilising S···F interactions in the crystal analysis of **2,7-bis(2-ethylhexyl)-diFIDT-di(O)** (see Section 3.4), so replacement of these groups for thiol groups could remove such interactions. While S···S intermolecular interactions have been widely reported as influential in the literature, we are unable to say if that is true in this case since we were unable to grow single crystals.[190] The defining factor is likely the addition of the C_8H_{17} linear chains, which are expected to orientate out-of-plane (as indicated by DFT calculations, see Section 5.2.1) and disrupt close packing of the aromatic cores. A similar observation has been made recently by Riaz et al., where substitution of the fluorine groups for alkoxy and alkyl thiol groups in a resulted in a large decrease in melting point.[191] It could be expected that the use of shorter alkyl thiol chains (e.g. ethanethiol) may help limit the melting point depression.

Oxidation of the thioether groups to sulfone groups resulted in a further decrease in melting temperature (T_m = 77 °C). A cold crystallisation was observed in the first heating cycle (**Figure**

79c) which immediately melts. This feature introduces some error into the T_m value stated above. The cold crystallisation is absent in subsequent cycles, where a reversible melting endotherm is instead observed at a slightly lower temperature (T_m = 61 °C). Disruption to the planarity of the aromatic core by the large SO_2R groups (as indicated by DFT calculations, see Section 5.2.1) may explain the decrease in melting temperature, although small, compared to **2,7-bis(2-ethylhexyl)-diSRIDT-di(O)**, due to the resulting weaker intermolecular interactions.

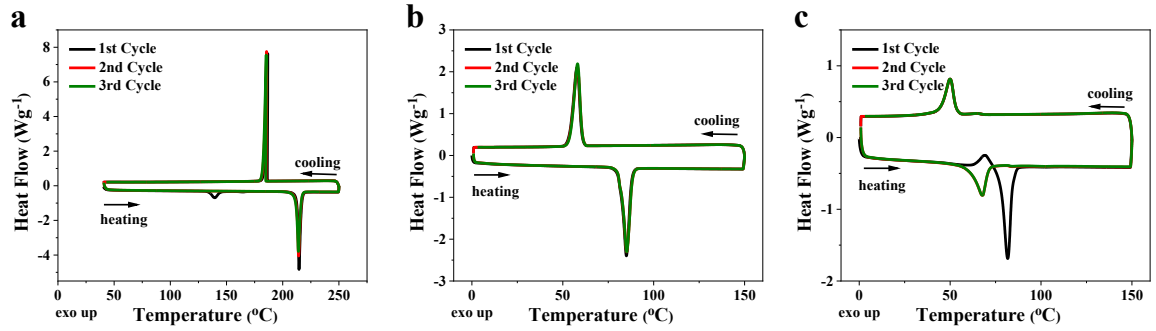


Figure 79: DSC plots (all cycles) for 2,7-bis(2-ethylhexyl)-diFIDT-di(O)[a], 2,7-bis(2-ethylhexyl)-diSRIDT-di(O) and 2,7-bis(2-ethylhexyl)-diSO₂RIDT-di(O). [a]Data from Chapter 3.

Table 15: Summary of TGA and DSC data for 2,7-bis(2-ethylhexyl)-diFIDT-di(O)[a], 2,7-bis(2-ethylhexyl)-diSRIDT-di(O) and 2,7-bis(2-ethylhexyl)-diSO₂RIDT-di(O).

OSC	T_d [°C]	T_m [°C]	ΔH_m [J g^{-1}]
2,7-bis(2-ethylhexyl)-diFIDT-di(O)[a)]	**364**	**213**	**70**
2,7-bis(2-ethylhexyl)-diSRIDT-di(O)	**346**	**82**	**52**
2,7-bis(2-ethylhexyl)-diSO₂RIDT-di(O)	**295**	**77 (61[b)])**	**37 (19[b)])**

[a)]data from Chapter 3. [b)]data taken from 2nd heating cycle.

5.2.5 Conclusion

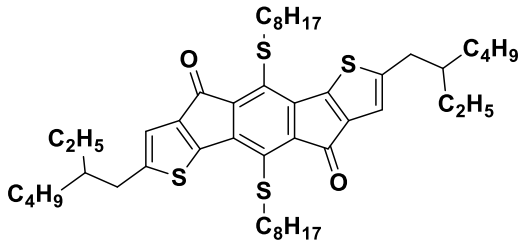
Nucleophilic aromatic substitution of the central fluorine groups in **dialkyl-diFIDT-di(O)** is shown to be feasible by reaction with an alkyl thiol. **2,7-bis(2-ethylhexyl)-diSRIDT-di(O)** is thus formed by reaction of **2,7-bis(2-ethylhexyl)-diFIDT-di(O)** with octane-1-thiol in

moderate yield (66 %). The same substitution is shown to be incompatible with the other diFIDT analogues (e.g. **dialkyl-diFIDT-di(C(CN)$_2$)** and **dialkyl-diFIDT-di(N(CN))**). We attribute this to competing 1,4-addition by the thiolate nucleophile at the bridging point. Consequently, this S_NAr methodology appears less robust than for fluorinated benzothiadiazole units, as has been previously explored within our research group. Full oxidation of the thioether groups to sulfones using DMDO gave **2,7-bis(2-ethylhexyl)-diSO$_2$RIDT-di(O)** in a moderate yield (61 %). This functionalisation is attractive due to the chemoselectivity of the oxidation, in addition to facile product purification.

Substitution of the fluorine groups for thioether groups led to a destabilisation of the LUMO (- 3.49 eV), reflecting the presence of the moderate electron-donating sulfur compared to highly electronegative fluorine. The additional alkyl side-chains and/or larger sulfur atoms of the thioether groups appear to disrupt intra- and intermolecular order, indicated by lower T_d (248 °C) and T_m (82 °C) as well as lower molar absorption coefficients of UV-Vis absorption. Oxidation of these groups to electron-withdrawing sulfone groups effectively depresses the LUMO energy level (- 3.87 eV), displaying improved stability versus **2,7-bis(2-ethylhexyl)-diFIDT-di(O)** (- 3.70 eV). Undesirably, the large SO_2R groups appear to disrupt intra- and intermolecular order even more greatly. T_d decreases noticeably (295 °C) in conjunction with a small decrease in melting temperature (T_m = 77 °C). Interestingly, long wavelength absorption (500 – 900 nm) is also completely suppressed. Such optical transparency in combination with the favourable energy levels suggest possible applicability of **2,7-dialkyl-diSO$_2$RIDT-di(O)** OSCs for use as cathode interlayers. Further investigations focusing on modifying the alkyl side-chains and/or thioalkyl chains could help probe aggregation effects. For instance, use of linear alkyl side-chains in the 2,7-positions and/or shorter thioalkyl side-chains would help improve order and packing, enabling single crystal analysis to be utilised.

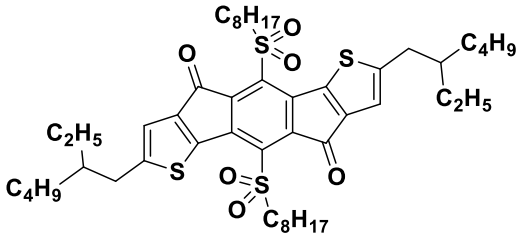
5.2.6 Experimental

2,7-Bis(2-ethylhexyl)-5,10-bis(octylthio)-s-indaceno[1,2-b:5,6-b']dithiophene-4,9-dione (**2,7-bis(2-ethylhexyl)-diSRIDT-di(O)**)*:*



To a suspension of 2,7-bis(2-ethylhexyl)-5,10-difluoro-s-indaceno[1,2-b5,6-b']dithiophene-4,9-dione (400 mg, 0.72 mmol) and anhydrous K_2CO_3 (300 mg, 2.16 mmol) in DMF (6 mL) in a 20 mL microwave vial, was added octane-1-thiol (0.5 mL, 2.88 mmol). The mixture was degassed for 10 mins and stirred vigorously overnight at 80 °C. The resulting deep blue solution was poured into water (150 mL) and the crude product extracted with chloroform (2 x 100 mL). The combined organic extracts were washed with water (3 x 100 mL) and brine (100 mL), dried over anhydrous sodium sulfate, filtered and concentrated under reduced pressure. The crude solid was purified by column chromatography (4:1 petroleum ether/DCM) yielding the product as a deep blue solid (384 mg, 66 %). m.p. 82 °C. ^{1}H NMR (400 MHz, $CDCl_3$, δ): 6.79 (s, 2H, ArH), 3.02 (t, 4H, ^3J = 7.5 Hz, CH_2), 2.71 (d, 4H, ^3J = 6.8 Hz, CH_2), 1.59 (m, 6H, CH_2 & CH), 1.31 (m, 36H, CH_2), 0.90 (m, 12H, CH_3), 0.84 (t, 6H, ^3J = 6.9 Hz, CH_3. ^{13}C NMR (101 MHz, $CDCl_3$, δ): 185.58, 154.44, 152.03, 147.05, 141.03, 138.00, 126.28, 118.81, 41.46, 36.62, 34.59, 32.47, 31.90, 30.24, 29.31, 29.21, 28.98, 28.91, 25.60, 23.13, 22.77, 14.27, 14.22, 10.94. IR (cm^{-1}) 1700 (C=O). HRMS (ES-TOF) m/z: $[M+H]^+$ calcd. for $C_{48}H_{71}O_2S_4$, 807.4337; found, 807.4357.

2,7-Bis(2-ethylhexyl)-5,10-bis(octylsulfonyl)-s-indaceno[1,2-b:5,6-b']dithiophene-4,9-dione (**2,7-bis(2-ethylhexyl)-diSO$_2$RIDT-di(O)**)*:*



To a solution of 2,7-bis(2-ethylhexyl)-5,10-bis(octylthio)-s-indaceno[1,2-b:5,6-b']dithiophene-4,9-dione (70 mg, 0.087 mmol) in DCM (10 mL) was added dimethyldioxirane (DMDO (15 mL, 0.077 M in acetone) dropwise at room temperature and the solution was stirred overnight. Solvent was then removed *in vacuo* and the resulting deep green crude product purified by silica gel chromatography (DCM) to afford the product as a sticky green solid (46 mg, 61 %). m.p. 61 °C. ^{1}H NMR (400 MHz, $CDCl_3$, δ): 6.82 (s, 2 H, ArH), 3.76 – 3.72 (m, 4 H, CH_2), 2.70 (d, ^{3}J = 6.9 Hz, 4 H, CH_2), 1.94- 1.86 (m, 4 H, CH_2), 1.65 – 1.57 (m, 2 H, CH), 1.50 – 1.43 (m, 4 H, CH_2), 1.39 – 1.20 (m, 32 H, CH_2), 0.91 – 0.84 (m, 18 H, CH_3). ^{13}C NMR (101 MHz, $CDCl_3$, δ): 182.62, 156.31, 151.11, 142.39, 142.33, 140.61, 132.27, 118.96, 56.43, 41.36, 34.48, 32.46, 31.80, 29.11, 29.06, 28.91, 28.54, 25.63, 23.11, 22.72, 22.57, 14.25, 14.19, 10.89. IR (cm^{-1}) 1718 (C=O), 1137 (S=O). HRMS (APCI) m/z: $[M+H]^+$ calcd. for $C_{48}H_{71}O_6S_4$, 871.4128; found, 871.4028.

6. Novel nonacyclic IDT-based OSCs

This chapter builds on the work carried out with Woyuan Yuo as part of her Master of Science research project at Imperial College London.[192]

6.1 Introduction

Extension of the π-conjugation by the addition of fused (hetero)aromatic rings is a popular tool employed to modify the performance of OSCs. Intense research activity has yielded a vast library of these ladder-type OSCs, including OSCs containing up to 23 fused rings.[82,193] There have also been a number of reports on fully conjugated polymers.[194,195] Such highly fused ladder-type systems are sought as they can improve the charge transport properties by promoting π-π interactions between neighbouring molecules in the solid state while limiting the reorganisation energy. The fusion of multiple (hetero)aromatic units together leads to high-lying frontier molecular orbitals and hence applicability as p-type materials, achieving mobilities up to 43 $cm^2 V^{-1} s^{-1}$ at present.[196] Incorporation of electron-deficient moieties is required to lower the frontier molecular orbital energies in order to access ambipolar and/or n-type behaviour, as is discussed in full in Section 1.5.

Motivation for this project was to explore π-extension, with attention again focused on IDT, for the purpose of accessing novel higher-order ladder-type molecular OSCs with potential ambipolar or n-type properties. Alkylation at the bridging points on the central IDT moiety

would allow for facile control of material processability, while functionalisation at the peripheral bridging points would serve to tune the energy levels, as well as improving π-π interactions. Optimised structures calculated by DFT predicted fully coplanar aromatic cores (**Figure 80**), whilst analysis of the frontier molecular orbitals indicate that the LUMO is highly localised on the peripheral bridging points and phenyl groups. This indicated that functionalisation of the peripheral bridging points could be employed to effectively and selectively stabilise the LUMO (**Figure A112**).

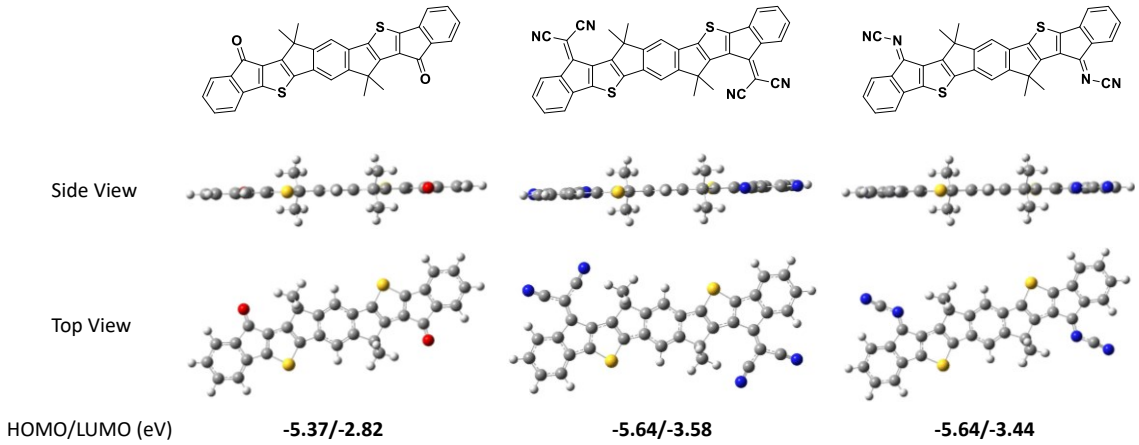


Figure 80: Optimised Structures for IDT-difluorenone (left), IDT-difluorenylidene-di(C(CN)$_2$) (middle) and IDT-difluorenylidene-di(N(CN)) (right), calculated by DFT.

In this chapter, a new class of fused nonacyclic IDT-based OSCs are synthesised along with the investigation of their physiochemical properties and device performance. C-H activation of the IDT precursor using direct arylation conditions is employed, reducing the number of synthetic steps as well as avoiding the use of toxic reagents, followed by a multi-step ring closure to afford the novel **IDT-difluorenone**. Functionalisation of the bridging positions with EWGs, including dicyanomethylene and *N*-cyanoimine, enabled modulation of the electronic and physical properties.

6.2 Synthesis

IDT-difluorenone was synthesised following a similar methodology to that used in Chapter 2 and Chapter 3 for **dialkyl-diFIDT-di(C(CN)$_2$)** compounds, whereby ring-closure was achieved beginning from an aromatic ester (**Figure 81**). To begin, deprotonation of the 4,9-dihydro-*s*-indaceno[1,2-*b*:5,6-*b′*]dithiophene (IDT) (**[15]**) was followed by the nucleophilic substitution to yield 4,4,9,9-tetrahexadecyl-4,9-dihydro-s-indaceno[1,2-b:5,6-b']dithiophene (**[16]**) in moderate yield (59 %). **[16]** was then utilised in a direct (hetero)arylation cross-coupling, exploiting C-H activation, with methyl 2-bromobenzoate (**[17]**) to afford 2,2'-(4,4,9,9-tetrahexadecyl-4,9-dihydro-s-indaceno[1,2-b:5,6-b']dithiophene-2,7-diyl)dibenzoate (**[18]**) (70 %) after purification by silica gel chromatography. Direct arylation conditions (Pd catalyst, P ligand, organic acid and base) were chosen based on literature reports of direct (hetero)arylation of IDT.[170] Saponification with KOH in *tert*-butanol afforded the diacid (**[19]**) (82 %), which was converted to the acid chloride by treatment with oxalyl chloride in DCM in the presence of a catalytic amount of DMF. After solvent removal, the resulting water-sensitive material was used directly without purification. Ring closure was achieved by a Lewis acid-promoted intramolecular Friedel-Crafts acylation with $AlCl_3$ to afford the diketone, **IDT-difluorenone**, in high yield (88 %) after purification by silica gel chromatography. **IDT-difluorenone** is a low melting-point sticky solid and freely soluble in common organic solvents (e.g. chloroform, THF, dichloromethane etc.). Degradation of **IDT-difluorenone** in chloroform was observed over a period of a week or so, evidenced by a change in colour from purple to orange/red as well as additional shifts arising in the proton NMR (**Figures A121** & **A122**). This indicated sensitivity to light and/or acid though degradation could be avoided by storing as a solid in the absence of light. Such instability is commonly observed with higher (hetero)acenes, most notably pentacene, and is usually attributed to photoinduced oxidation and/or dimerisation/oligomerisation.[197–199] It is unclear if that is true in this case.

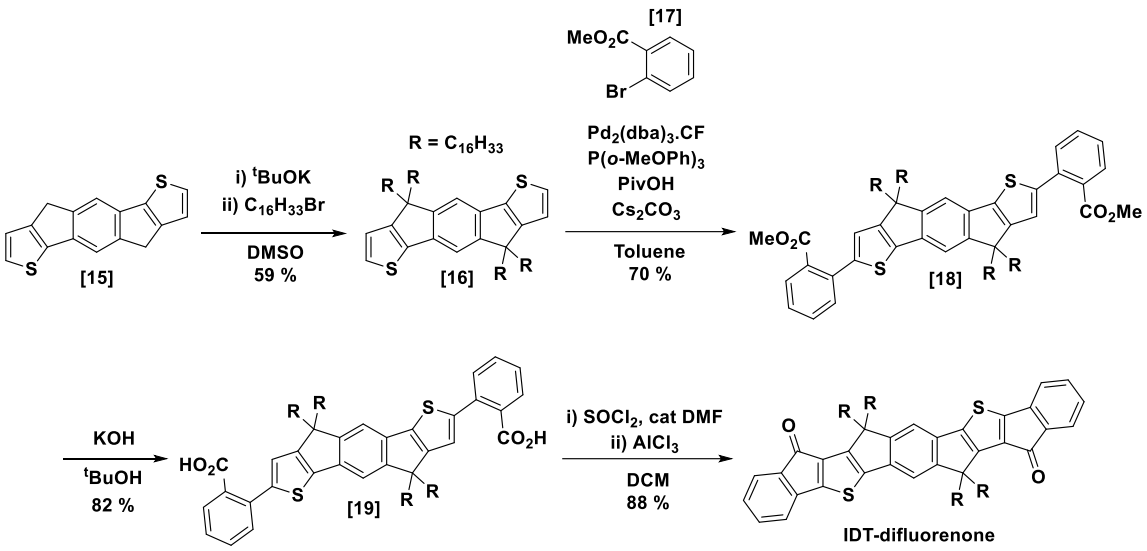


Figure 81: Synthesis of IDT-difluorenone.

Knoevenagel condensation with malononitrile, pyridine and $TiCl_4$ at room temperature afforded 2,2'-(4,4,9,9-tetrahexadecyl-4,9-dihydro-s-indaceno[1,2-b:5,6-b']dithiophene-2,7-diyl)difluorene-ylidene)dimalononitrile (**IDT-difluorenylidene-di(C(CN)$_2$)**) in moderate yield (52 %) after purification by silica gel chromatography followed by reprecipitation from chloroform/methanol (**Figure 82**). **IDT-difluorenylidene-di(C(CN)$_2$)** displayed reduced solubility compared to the corresponding ketone. No reaction was observed, including at elevated temperature, without the addition of $TiCl_4$. This indicated substantial steric hindrance at the ketone, possibly from the large hexadecyl alkyl side-chains. The diketone was also reacted with $TiCl_4$ and bis(trimethylsilyl)carbodiimide in a Knoevenagel-type condensation reaction at room temperature to give **IDT-difluorenylidene-di(N(CN))** (74 %) after reprecipitation from chloroform/methanol (**Figure 82**). Neither **IDT-difluorenylidene-di(C(CN)$_2$)** nor **IDT-difluorenylidene-di(N(CN))** exhibited the degradation associated with **IDT-difluorenone**, indicating that introduction of the strongly electron-withdrawing dicyanomethylene or *N*-cyanoimine functionality was effective at increasing the air and/or photo-stability of these large fused heteroacenes. Similar modifications have been widely employed to improve stability in numerous (hetero)acenes.[200,201]

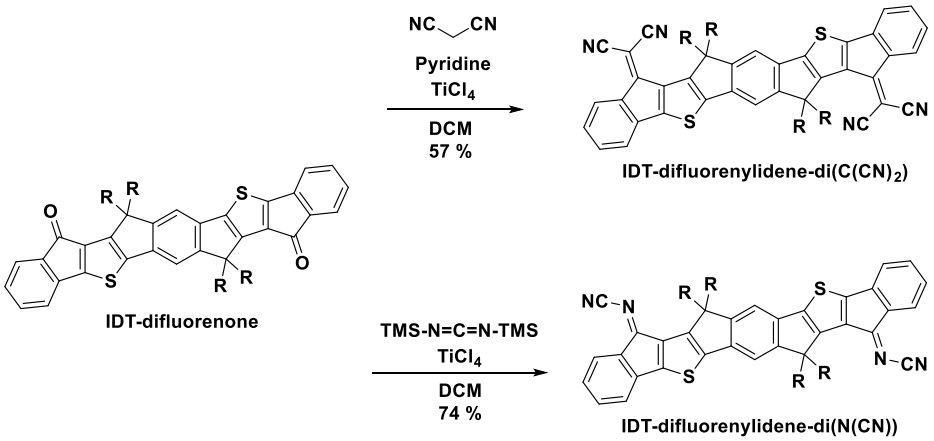


Figure 82: Synthesis of IDT-difluorenylidene-di(C(CN)$_2$) and IDT-difluorenylidene-di(N(CN)).

The chemical structures of **IDT-difluorenone**, **IDT-difluorenylidene-di(C(CN)$_2$)** and **IDT-difluorenylidene-di(N(CN))** were verified by ^{1}H NMR, ^{19}F NMR, ^{13}C NMR, IR and HRMS. Single crystal growth was unsuccessful, giving only fine powders in all cases.

6.3 Optoelectronic and Electrochemical Properties

The absorption spectra for **IDT-difluorenylidene-di(C(CN)$_2$)** and **IDT-difluorenylidene-di(N(CN))** in solution (toluene and chloroform, 10^{-5} M) were recorded (**Figure 83**). The spectra of **IDT-difluorenone** were not recorded owing to instability in solution (as noted in Section 6.1). In general, these compounds displayed strong, sharp absorption bands at shorter wavelengths (250 – 450 nm, ε up to 7 x 10^4 dm^3 mol^{-1} cm^{-1}) as well as broad weak absorption at longer wavelengths (500 – 900 nm, ε ~ 0.25 x 10^4 dm^3 mol^{-1} cm^{-1}). Such optical transparency is potentially very attractive for cathode interlayer applications. TD-DFT calculations indicate that HOMO to LUMO and HOMO-1 to LUMO+1 transitions contribute to the long wavelength absorption, and overlap is very poor. The is particularly evident for **IDT-difluorenylidene-di(C(CN)$_2$)** where f = 0.05 for this absorption (**Figure A127**).

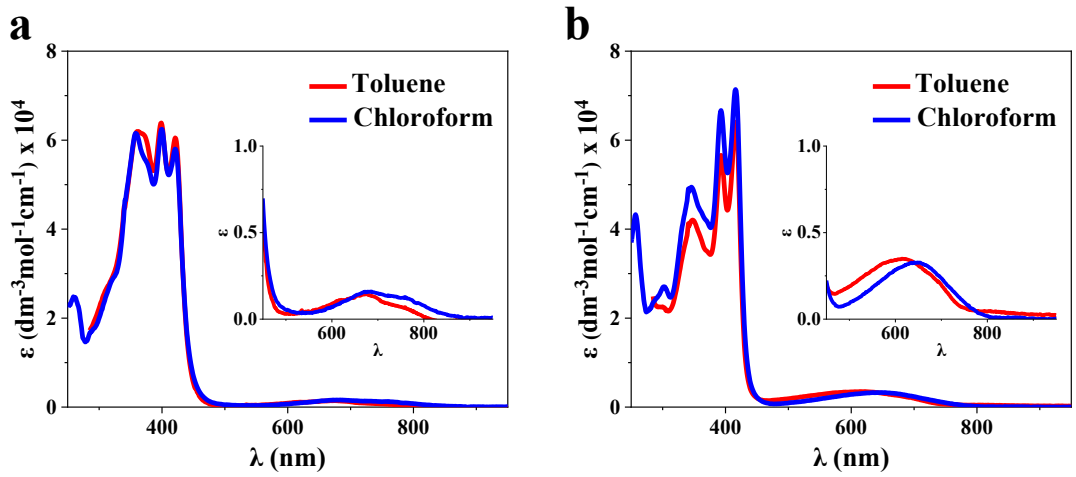


Figure 83: Solution absorption spectra for a) IDT-difluorenylidene-di(C(CN)$_2$) and b) IDT-difluorenylidene-di(N(CN)) in toluene and chloroform.

Electrochemical studies of all three nonacyclic OSCs were performed by cyclic voltammetry (CV) using a 0.1 M solution of Bu_4NPF_6 in DCM solutions and a ferrocene (Fc/Fc^+) internal standard. Potentials were swept from 0 V to a positive maximum, then swept back to a negative maximum before returning to 0 V. In line with best practice, energy levels were estimated from $E^{1/2}$ (when reversibility is observed) or E^i (when irreversibility is observed), where $E^{1/2}$ is the half-wave potential, E^i is the inflection-point potential.[124] HOMO = - ($E^{1/2\ or\ i}$ + 4.8) eV and LUMO = - ($E^{1/2\ or\ i}$ + 4.8) eV for oxidation and reduction respectively, with the ferrocene/ferrocenium reference redox system at 4.8 eV below the vacuum level. Oxidation and reduction potentials are summarised in **Table 16**.

The cyclic voltammogram of **IDT-difluorenone** displayed no reductions potentials. DFT calculations predicted a LUMO of - 2.84 eV (Section 6.1) which would suggest that, if a stable reduction does exist, the reduction potential may lie outside the potential window for the solvent used. On the other hand, a chemically reversible oxidation was observed, corresponding to a relatively high HOMO level of - 5.34 eV (**Figure 84a**). These results are indicative of a p-type OSC thus indicate that **IDT-difluorenone** is a fairly electron-rich unit. This is understandable from the chemical structure, whereby there is a highly π-extended system of

nine fused (hetero)aromatic rings. The ketone functionality appears insufficient in stabilising the LUMO to any great extent.

IDT-difluorenylidene-di(C(CN)$_2$) and **IDT-difluorenylidene-di(N(CN))**, unlike **IDT-difluorenone**, each display a chemically reversible reduction , corresponding to LUMO energy levels of - 3.62 eV and - 3.48 eV respectively (**Figure 84b** & **c**). This indicated that these strong EWGs are effective at stabilising the LUMOs. As predicted by DFT (Section 6.1), dicyanomethylene is seen to be a stronger stabilising group than the *N*-cyanoimine. While this is true, the LUMO energy levels remain fairly high in both cases. This indicates that these OSCs are likely to be inappropriate for unipolar n-type applications and suited more favourably as ambipolar or p-type OSCs.

In comparison, these modifications had a negligible effect on the HOMO energy levels (0.03 eV differential between **IDT-difluorenone** and **IDT-difluorenylidene-di(C(CN)$_2$)**. This reflects the locality of the LUMO at the bridging position (as suggested by DFT calculations, Section 6.1), allowing selective tuning of the LUMO by modulation of the bridging functionality.

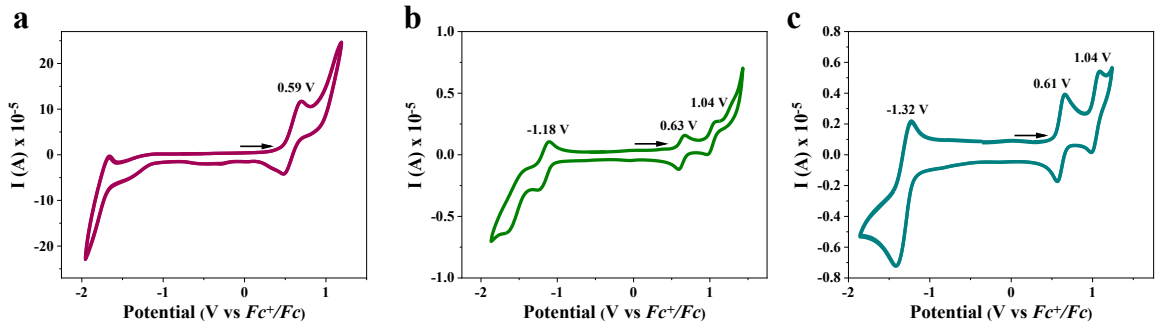


Figure 84: Cyclic voltammograms of IDT-based nonacycles, showing corresponding $E^{1/2\ or\ i}$ potentials. a) IDT-difluorenone. b) IDT-difluorenylidene-di(C(CN)$_2$). c) IDT-difluorenylidene-di(N(CN)).

Table 16: Summary of material properties of 3,8-dihexyl-diFIDT-di(O) and 2,7-(4-benzonitrile)-3,8-dihexyl-diFIDT-di(O).

OSC	HOMO[a)]	LUMO[a)]	λ_{max} (solution)
	[eV]	[eV]	[nm]
IDT-difluorenone	- 5.39	-[b)]	-[c)]
IDT-difluorenylidene-di(C(CN)$_2$)	- 5.42	- 3.62	676, 421, 399, 361[d)]
			678, 421, 400, 358, 259[e)]
IDT-difluorenylidene-di(N(CN))	-5.41	- 3.48	621, 416, 393, 348[d)]
			641, 416, 393, 346, 257[e)]

[a)]extracted from CV measurements, [b)]data from Chapter 3, [c)]UV-Vis spectra not reported, [d)]in toluene, [e)]in chloroform.

6.4 Thermal Properties

The thermal behaviour of **IDT-difluorenone**, **IDT-difluorenylidene-di(C(CN)$_2$)** and **IDT-difluorenylidene-di(N(CN))** was investigated by TGA (**Figure 85**) and DSC (**Figure 86**). Key data are summarised in **Table 17**.

All three novel fused IDT materials exhibit high thermal stabilities. Functionalisation of the bridging group with dicyanomethylene or *N*-cyanomine improved thermal stability compared to **IDT-difluorenone** (T_d = 343 °C) (temperature at which 5 % mass loss is reached). The lack of any notable degradation of **IDT-difluorenone** up to ~ 250 °C in the nitrogen environment of the TGA analysis supports the idea of oxidative instability being the cause of the degradation discussed in Section 6.2. **IDT-difluorenylidene-di(N(CN))** displayed a particularly high T_d of 380 °C.

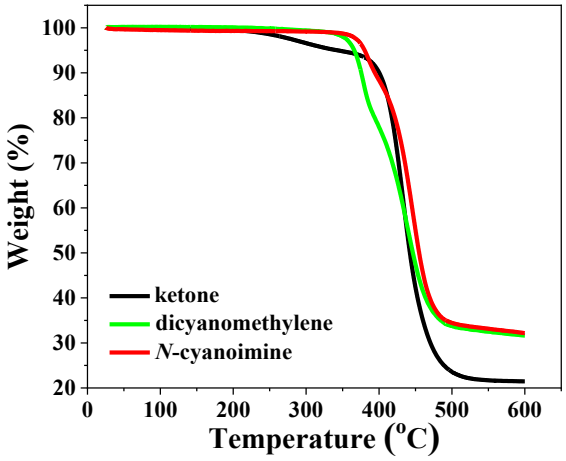


Figure 85: TGA plots for IDT-difluorenone, IDT-difluorenylidene-di(C(CN)$_2$) and IDT-difluorenylidene-di(N(CN)).

IDT-difluorenone displayed a low temperature reproducible endotherm (T_m = 74 °C) which appeared stable upon thermal cycling (**Figure 86a**). The low melting point suggests weak intermolecular interactions between neighbouring fused aromatic units. This is in contrast to **IDT-difluorenylidene-di(C(CN)$_2$)** and **IDT-difluorenylidene-di(N(CN))**, where two distinct reproducible thermal transitions are observed – a low enthalpy lower temperature transition and a higher enthalpy higher temperature transition (**Figure 86b** & **c**). These thermal characteristics are indicative of the formation of a liquid-crystalline (LC) mesophase or a crystal-to-crystal transition. A low enthalpy crystal-to-mesophase/crystal-to-crystal transition, suggest that the mesophases are highly ordered and stable across a wide temperature range. With **IDT-difluorenylidene-di(C(CN)$_2$)**, an initial endothermic transition was observed at 143 °C (ΔH_m = 8 J g^{-1}) followed by a second at 302 °C. This OSC appears unstable upon heating to such a high temperature, as evidenced by a decrease in ΔH_m of these melting transitions as the material was thermally cycled. This could be justified by the vicinity of T_m (302 °C) to T_d (366 °C). The corresponding transitions in **IDT-difluorenylidene-di(N(CN))** occur at considerably lower temperatures (58 °C and 210 °C respectively) than in **IDT-difluorenylidene-di(C(CN)$_2$)** indicating stronger intermolecular interactions in the latter. Additionally, these transitions

appear stable upon repeated thermal cycling, presumably since the transitions occur well below T_d (380 °C) in this case. Such a low temperature thermal transition as possessed by **IDT-difluorenylidene-di(N(CN))** may be undesirable for achieving thermally-robust device performance.

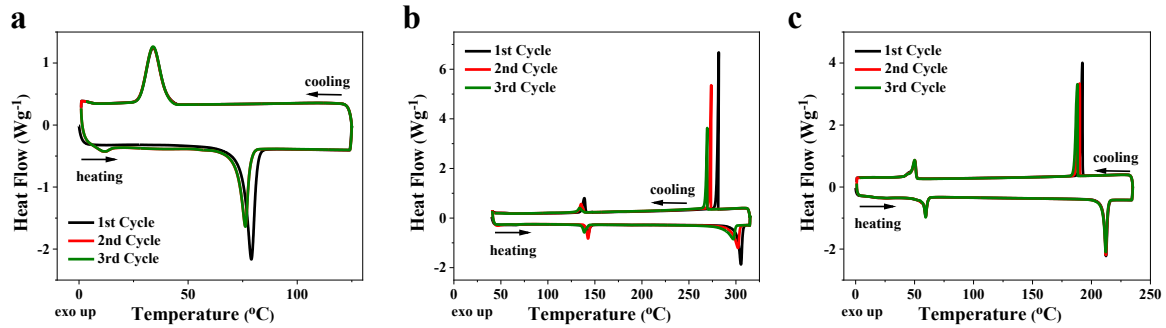


Figure 86: DSC plots (all cycles) for IDT-difluorenone, IDT-difluorenylidene-di(C(CN)₂) and IDT-difluorenylidene-di(N(CN)).

The possible liquid-crystalline (LC) properties of **IDT-difluorenylidene-di(N(CN))** were probed further using polarised optical microscopy (POM). The higher temperature endothermic transition was confirmed as corresponding to the melting temperature, by the observation of an isotropic liquid above 210 °C. Upon slow cooling from the melt (2 °C min^{-1}), rapid crystallisation occurred below 180 °C to a highly ordered birefringent solid. The absence of any clear Schlieren or focal conic texture made identification as a LC mesophase difficult. No visible change was observed upon further cooling below 45 °C, however this was may be unsurprising due to the low enthalpy associated with this transition, suggesting minimal structure change. From these observations, we are unable to conclude if the mesophase was a crystalline or a highly ordered LC phase.

Table 17: Summary of TGA and DSC data (1st cycle) for IDT-difluorenone, IDT-difluorenylidene-di(C(CN)2) and IDT-difluorenylidene-di(N(CN)).

OSC	T_d [°C]	T_m [°C]	ΔH_m [J g^{-1}]
IDT-difluorenone	**343**	**74**	**53**
IDT-difluorenylidene-di(C(CN)$_2$)	**366**	**143, 302**	**8, 48**
IDT-difluorenylidene-di(N(CN))	**380**	**58, 210**	**11, 35**

6.5 Conclusion

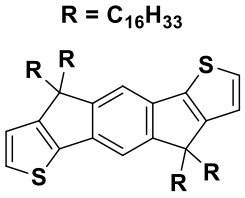
Three novel nonacyclic ladder-type molecular OSCs have been synthesised by π-extension of IDT, following a multi-step ring-closure. Initial coupling of an aromatic ester with IDT was achieved by direct (hetero)arylation conditions in good yield (70 %), exploiting C-H activation on the IDT. Degradation of **IDT-difluorenone** is observed over the period of a week or so however can be avoided by storage as a solid in the absence of light. This issue was absent upon conversion to **IDT-difluorenylidene-di(C(CN)$_2$)** or **IDT-difluorenylidene-di(N(CN))**. **IDT-difluorenylidene-di(C(CN)$_2$)** and **IDT-difluorenylidene-di(N(CN))** display very weak longer wavelength absorptions across most of the visible region (> 450 nm) with strong, sharp absorption features at shorter wavelengths (< 450 nm) – attractive for cathode interlayer applications. HOMO energy levels as extracted from CV measurements are ~ - 5.4 eV for all three OSCs. **IDT-difluorenone** does not display a reduction, suggesting a LUMO > - 2.8 eV. **IDT-difluorenylidene-di(C(CN)$_2$)** and **IDT-difluorenylidene-di(N(CN))** on the other hand display single reversible reductions (- 3.62 eV and - 3.48 eV respectively). These results show that the LUMO energy level can be selectively modulated by functionalisation of the peripheral bridging points, with practically no effect on the HOMO. The LUMOs of **IDT-difluorenylidene-di(C(CN)$_2$)** and **IDT-difluorenylidene-di(N(CN))** appear insufficiently low for effective n-type transport.

All three OSCs display high thermal stabilities (T_d > 340 °C), with stabilities seemingly being improved upon functionalisation of the peripheral bridging points with dicyanomethylene or *N*-cyanoimine groups. This functionalisation also caused a large increase in melting points, from a T_m of 74 °C for **IDT-difluorenone** up to 302 °C and 210 °C for **IDT-difluorenylidene-di(C(CN)$_2$)** and **IDT-difluorenylidene-di(N(CN))** respectively. These features infer a large increase in intermolecular interactions between the π-conjugated units. **IDT-difluorenylidene-di(C(CN)$_2$)** and **IDT-difluorenylidene-di(N(CN))** display additional lower temperature low-enthalpy thermal transitions characteristic of crystal-to-mesophase or crystal-to-crystal transitions.

Fabrication of devices using **IDT-difluorenylidene-di(C(CN)$_2$)** and **IDT-difluorenylidene-di(N(CN))** is in process to investigate the mode of charge transport possible (p-type, n-type or ambipolar) as well as general performance. These results will help inform us if this molecular design is suitable for accessing efficient transistor OSCs.

6.6 Experimental

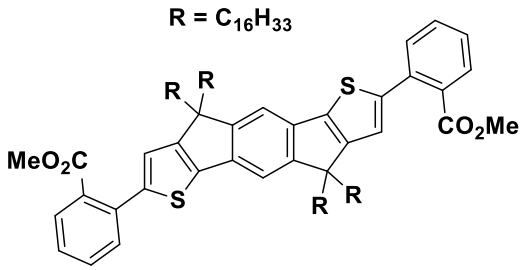
4,9-Dihydro-4,4,9,9-tetrahexadecyl-s-indaceno[1,2-b:5,6-b']-dithiophene ([16]):



To a suspension of 4,9-dihydro-s-indaceno[1,2-b:5,6-b']dithiophene (**[15]**) (3.00 g, 11.26 mmol) in anhydrous DMSO (50 mL) was added sodium tert-butoxide (7.56 g, 67.67 mmol) in parts. The reaction mixture was heated at 80 °C for 2 hours, followed by the addition of 1-bromohexadecane (20.61 g, 67.50 mmol) dropwise. After complete addition, the resultant

mixture was heated at 88 °C overnight to give a dark greenish brown solution. Then the mixture was cooled to room temperature and poured into ice-water. The precipitate was collected by filtration and washed with water and methanol to give a dark brown solid. The crude product was purified by column chromatography on silica, eluting with hexane to give an off-white solid (7.74 g, 59 %). ^{1}H NMR (400 MHz, $CDCl_3$, δ): 7.28 (s, 2H, ArH), 7.25 (d, ^{3}J = 4.8 Hz, 2H, ArH), 6.96 (d, ^{3}J = 4.8 Hz, 2H, ArH), 2.02 – 1.92 (m, 4H, CH_2), 1.89 – 1.80 (m, 4H, CH_2), 1.33 – 1.04 (m, 104H, CH_2), 0.88 (m, 20H, CH_2 and CH_3). ^{13}C NMR (101 MHz, $CDCl_3$, δ): 155.23, 153.39, 141.80, 135.72, 126.23, 121.86, 113.27, 53.80, 39.28, 32.09, 30.18, 29.87, 29.85, 29.82, 29.78, 29.75, 29.52, 24.33, 22.85, 14.27 (some carbons overlapping). HRMS (APCI) m/z: $[M+H]^+$ calcd. for $C_{80}H_{139}S_2$, 1164.0313; found, 1164.0310.

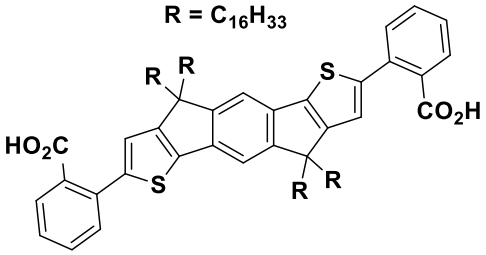
Dimethyl 2,2'-(4,4,9,9-tetrahexadecyl-4,9-dihydro-s-indaceno[1,2-b:5,6-b']dithiophene-2,7-diyl)dibenzoate ([18]):



To a mixture of 4,4,9,9-tetrahexadecyl-4,9-dihydro-s-indaceno[1,2-b:5,6-b'] dithiophene (**[16]**) (2.00 g, 1.72 mmol), methyl 2-bromobenzoate (**[17]**) (1.2 mL, 8.55 mmol), $Pd_2(dba)_3$.CF (90 mg, 0.40 mmol, 0.2 equivs), tri(o-anisyl)phosphine (120 mg, 0.34 mmol), pivalic acid (170 mg, 1.66 mmol), and caesium carbonate (1.66 g, 5.10 mmol) was added toluene (50 mL) to dissolve the contents. The reaction mixture was degassed under nitrogen and premixed for 30 minutes, then was heated to 130 °C and stirred vigorously overnight to give a yellow-brown fluorescence solution. The mixture was added to water (100 mL) and extracted with DCM (3 x 50 mL). The solvent was removed to yield an orange-brown crude oil. The crude product was purified by

column chromatography on silica (5:1 petroleum ether/DCM) to give a highly fluorescent orange solid (1.72 g, 70 %). ^{1}H NMR (400 MHz, $CDCl_3$, δ): 7.72 (dd, ^{3}J = 7.8, 1.1 Hz, 2H, ArH), 7.59 (dd, ^{3}J = 7.7, 1.0 Hz, 2H, ArH), 7.53 (td, ^{3}J = 7.5, 1.4 Hz, 2H, ArH), 7.41 (td, ^{3}J = 7.5, 1.4 Hz, 2H, ArH), 7.30 (s, 2H, ArH), 6.91 (s, 2H, ArH), 3.75 (s, 6H, CH_3), 1.99 (td, ^{3}J = 12.6, 4.7 Hz, 4H, CH_2), 1.90 (td, ^{3}J = 12.7, 6.4 Hz, 4H, CH_2), 1.34 -1.09 (m, 112 H, CH_2), 0.89 (t, ^{3}J = 6.9 Hz, 12H, CH_3). ^{13}C NMR (101 MHz, $CDCl_3$, δ): 170.02, 155.63, 152.94, 143.31, 142.30, 135.93, 134.70, 131.76, 131.08, 130.80, 129.56, 127.54, 121.34, 113.29, 54.25, 52.33, 39.39, 32.07, 30.28, 29.85, 29.81, 29.62, 29.51, 24.43, 22.84, 14.26 (some carbons overlapping). HRMS (ES-TOF) m/z: $[M+H]^+$ calcd. for $C_{96}H_{150}O_4S_2$, 1432.37; found, 1432.11.

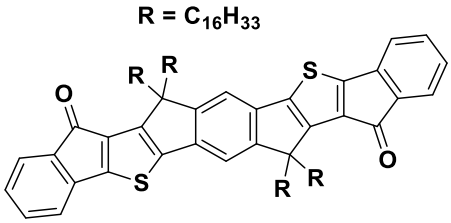
2,2'-(4,4,9,9-Tetrahexadecyl-4,9-dihydro-s-indaceno[1,2-b:5,6-b']dithiophene-2,7-diyl)dibenzoic acid ([19]):



To a suspension of dimethyl 2,2'-(4,4,9,9-tetrahexadecyl-4,9-dihydro-s-indaceno [1,2-b:5,6-b']dithiophene-2,7-diyl)dibenzoate ***([18])*** (1.70 g, 1.19 mmol) in *tert*-butanol (100 mL) and water (15 mL) was added potassium hydroxide (0.93 g, 16.62 mmol). The reaction mixture was refluxed at 90 °C overnight. The solvent was removed reduced pressure and the crude was re-dissolved in ethanol (100 mL). HCl (2 M, 50 mL) was added to acidify the solution and the resulting precipitate was collected by filtration, washed with water and dried in a vacuum oven at 100 °C (150 mbar) to afford a pale yellow solid (1.36 g, 82 %). ^{1}H NMR (400 MHz, $CDCl_3$, δ): 7.90 (dd, ^{3}J = 7.5, 1.0 Hz, 2H, ArH), 7.59 – 7.52 (m, 4H), 7.26 (s, 2H), 6.98 (s, 2H), 1.96 (td, ^{3}J = 12.5, 4.5 Hz, 4 H, CH_2), 1.83 (td, ^{3}J = 12.5, 4.5 Hz, 4 H, CH_2), 1.32 – 1.02 (m, 112H,

CH_2), 0.89 (t, ^3J = 6.9 Hz, 12H, CH_3). ^{13}C NMR (101 MHz, $CDCl_3$, δ): 170.02, 155.62, 152.93, 143.31, 142.30, 135.93, 134.70, 131.76, 131.07, 130.80, 129.56, 127.53, 121.33, 113.29, 54.25, 52.32, 39.39, 32.07, 30.28, 29.85, 29.81, 29.62, 29.51, 24.43, 22.84, 14.26 (some carbons overlapping).

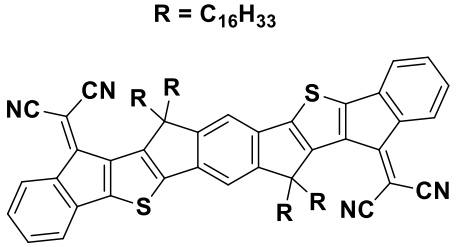
2,2'-(4,4,9,9-Tetrahexadecyl-4,9-dihydro-s-indaceno[1,2-b:5,6-b']dithiophene-2,7-diyl)difluorenone (IDT-difluorenone):



To a suspension of 2,2'-(4,4,9,9-tetrahexadecyl-4,9-dihydro-s-indaceno[1,2-b:5,6-b']dithiophene-2,7-diyl)dibenzoic acid 4 (1.00 g, 0.71 mmol) in anhydrous DCM (40 mL) was added a catalytic amount of anhydrous DMF (0.30 mL) and then oxalyl chloride (0.60 mL, 7.12 mmol) dropwise. The reaction mixture was stirred at room temperature for 5 minutes and then refluxed overnight. The solvent was removed by reduced pressure to yield an orange solid which was used in the next step without further purification. The acyl chloride was redissolved in anhydrous DCM (40 mL). The resultant solution was added dropwise to a suspension of $AlCl_3$ (0.95 g, 7.12 mmol) in anhydrous DCM (40 mL) at 0 °C. The mixture was stirred at room temperature for 3 hours. After removal of half of the solvent by reduced pressure, HCl (2 M) in ice was added to the above solution. The solution was extracted with ethyl acetate (3 x 80 mL) and brine (3 x 80 mL). The collected organic layer was dried over $MgSO_4$. After removal of the solvent, the residue was purified by column chromatography on silica gel (petroleum ether/ethyl acetate 25:1) to afford a dark reddish purple solid (0.86 g, 88 %). m.p. 74 °C. ^1H NMR (400 MHz, $CDCl_3$, δ): 7.44 (d, ^3J = 7.1 Hz, 2H, ArH), 7.34 (t, ^3J = 7.5 Hz, 2H,

ArH), 7.24 (s, 2H, ArH), 7.18 – 7.10 (m, 4H, ArH), 2.30 (td, ^{3}J = 12.8, 4.8 Hz, 4H, CH_2), 1.98 (td, ^{3}J = 12.8, 4.8 Hz, 4H, CH_2), 1.41 – 0.96 (m, 104H, CH_2), 0.87 (t, ^{3}J = 6.8 Hz, 12H, CH_3), 0.81 – 0.59 (m, 8H, CH_2). ^{13}C NMR (101 MHz, $CDCl_3$, δ): 160.14, 152.57, 150.44, 146.16, 140.37, 138.39, 136.36, 136.01, 134.15, 134.15, 128.21, 123.59, 118.92, 113.18, 77.48, 77.16, 76.84, 54.82, 38.60, 32.07, 29.86, 29.80, 29.67, 29.51, 29.36, 24.18, 22.84, 14.27 (some carbons overlapping). IR (cm^{-1}) 1711 (C=O). HRMS (APCI) m/z: $[M+H]^+$ calcd. for $C_{94}H_{143}O_2S_2$, 1368.0479; found, 1368.0474.

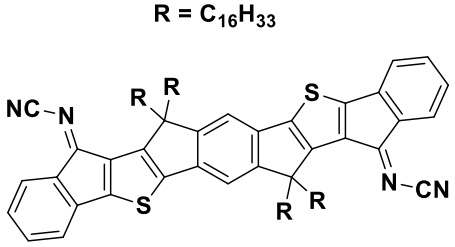
2,2'-(4,4,9,9-Tetrahexadecyl-4,9-dihydro-s-indaceno[1,2-b:5,6-b']dithiophene-2,7-diyl)difluorene-ylidene)dimalononitrile (IDT-difluorenylidene-di(C(CN)$_2$)):



To a solution of 2,2'-(4,4,9,9-tetrahexadecyl-4,9-dihydro-s-indaceno[1,2-b:5,6-b']dithiophene-2,7-diyl)difluorenone (0.32 g, 0.232 mmol), and malononitrile (0.15 g, 2.32 mmol) in anhydrous DCM (40 mL), pyridine (0.23 mL, 2.78 mmol) was added, the resultant solution was stirred for 10 minutes. Then $TiCl_4$ (0.25 mL, 2.32 mmol) was added dropwise to the mixture. The colour of the solution changed to dark green immediately after the complete addition of $TiCl_4$. The reaction mixture was stirred at room temperature overnight. The solution was extracted with chloroform and brine. The collective organic layer was dried over $MgSO_4$. After removal of the solvent, methanol was added, and the crude product was filtered and washed with methanol and acetone to give a deep green solid. This solid was dissolved in hot chloroform and reprecipitated in methanol to give a pale green solid (0.20 g, 57 %). m.p. 302 °C. ^{1}H NMR (400 MHz, $CDCl_3$, δ): 8.37 (d, ^{3}J = 7.5 Hz, 2H, ArH), 7.34 (t, ^{3}J = 7.5 Hz, 2H,

ArH), 7.23 (s, 2H, ArH), 7.20 – 7.14 (m, 4H, ArH), 2.78 (ddd, ^{3}J = 13.8, 11.7, 4.7 Hz, 4H, CH_2), 2.04 (ddd, ^{3}J = 13.8, 11.7, 4.6 Hz, 4H, CH_2), 1.35 – 1.00 (m, 104H, CH_2), 0.87 (t, ^{3}J = 6.9 Hz, 12H, CH_3), 0.80 – 0.54 (m, 8H, CH_2). ^{13}C NMR (101 MHz, TCE-d_2, 120 °C, δ): 157.69, 155.97, 153.89, 149.28, 146.92, 137.95, 137.75, 135.04, 133.55, 128.07, 126.51, 118.88, 115.43, 114.30, 111.83, 76.55, 56.89, 38.16, 31.59, 29.35, 29.30, 29.12, 28.96, 28.89, 23.77, 22.28, 13.60 (some carbons overlapping). IR (cm^{-1}) 2222 (C≡N), 1554 (C=C). HRMS (APCI) m/z: $[M+H]^+$ calcd. for $C_{100}H_{143}N_4S_2$, 1464.0704; found, 1464.0732.

2,2'-(4,4,9,9-Tetrahexadecyl-4,9-dihydro-s-IDT-2,7-diyl)difluorene-ylidene)dicyanoimine (IDT-difluorenylidene-di(N(CN)):



To solution of 2,2'-(4,4,9,9-tetrahexadecyl-4,9-dihydro-s-IDT-2,7-diyl)difluorenone (130 mg, 0.1 mmol) in anhydrous DCM (40 mL) at 0 °C was added $TiCl_4$ (0.11 mL, 1 mmol) dropwise. The resulting mixture was stirred for 10 mins at 0 °C. To this was added dropwise a solution bis(trimethylsilyl)carbodiimide (0.23 mL, 1 mmol) in anhydrous DCM (10 mL). The mixture was allowed to warm to room temperature and stirred for 4 hrs to give a deep red mixture. $TiCl_4$ (0.12 mL, 0.5 mmol) and bis(trimethylsilyl)carbodiimide (0.23 mL, 1 mmol) were added and the mixture was allowed to stir overnight. TLC (2/1 DCM/petroleum ether) confirmed the reaction was complete. Water was then added (100 mL) and the mixture was extracted with chloroform (2 x 50 mL). The combined organic extracts were rinsed with water (2 x 50 mL) and brine (50 mL), dried over anhydrous sodium sulfate, filtered and concentrated under reduced pressure. The crude solid was suspended in methanol, filtered and washed with

methanol and acetone then dried in vacuo to give a dark, crystalline solid. This solid was reprecipitated from the minimum amount of hot chloroform in methanol to give a grass green solid (100 mg, 74 %). m.p. 210 °C. ^{1}H NMR (400 MHz, $CDCl_3$, δ): 8.29 (d, ^{3}J = 7.5 Hz, 2H, ArH), 7.35 (td, ^{3}J = 7.7, 1.0 Hz, 2H, ArH), 7.24 (s, 2H, ArH), 7.16 (td, ^{3}J = 7.7, 1.0 Hz, 2H, ArH), 7.11 (d, ^{3}J = 7.3 Hz, 2H, ArH), 2.39 – 2.26 (m, 4H, CH_2), 2.01 – 1.89 (m, 4H, CH_2), 1.33 – 0.96 (m, 104H, CH_2), 0.87 (t, ^{3}J = 6.9 Hz, 12H, CH_3), 0.76 – 0.54 (m, 8H, CH_2). ^{13}C NMR (101 MHz, $CDCl_3$, δ): 177.09, 158.37, 152.70, 150.59, 146.75, 139.58, 136.81, 136.28, 135.20, 134.64, 128.65, 127.01, 119.59, 114.13, 113.16, 55.28, 37.94, 32.07, 29.86, 29.81, 29.79, 29.64, 29.51, 29.34, 24.09, 22.84, 14.26 (some carbons overlapping). IR (cm^{-1}) 2175 (C≡N). HRMS (APCI) m/z: $[M+H]^+$ calcd. for $C_{96}H_{143}N_4S_2$, 1417.0782; found, 1417.0770.

7. General Conclusion

Through extensive modifications to **dialkyl-IDT-di(O)**, a library of novel **dialkyl-diFIDT-di(X)** (where X = EWG) molecular OSCs have been synthesised. Suitability for use as n-type materials in OFET applications has been supported by deep LUMO energy levels (< - 4 eV), high crystallinity, high thermal stability and solution processability.

Fluorination of the central phenyl moiety has been shown to be effective at depressing the LUMO energy levels versus the non-fluorinated analogues, as well as improving π-π stacking interactions in the single crystals – highlighted by improved electron transfer integrals. Additionally, an unexpected improvement in solubility is observed upon such fluorination – a result contrary to that generally observed in the literature. A combination of computational calculations and crystal analysis indicate that this may be due to backbone torsion, resulting from the positioning of the fluorine group in close proximity to the strongly electron withdrawing group. This was the case for both **2,7-dihexyl-diFIDT-di(C(CN)$_2$)** and **2,7-dihexyl-diFIDT-di(N(CN))**.

Modification by side-chain engineering was sought in an attempt to improve device performance. Within the set of different alkyl side-chains employed, 2,7-dihexyl side-chains proved optimal, affording unipolar saturated electron mobilities of up to 0.49 $cm^2 V^{-1} s^{-1}$ for **2,7-dihexyl-diFIDT-di(C(CN)$_2$)**. Crucially, devices showed ideal/near-ideal behaviour, ensuring accurate and reliable mobilities could be extracted.

Three different EWGs positioned at the 4,9-bridging positions were explored to stabilise the LUMO energy levels – ketone, dicyanomethylene and *N*-cyanoimine. Ketone functionality proved insufficient to achieve highly stable LUMO energy levels (- 3.7 eV to - 3.8 eV). Additionally, no working OFET devices were obtained using any ketone analogue. In contrast,

the use of dicyanomethylene or *N*-cyanoimine functionality resulted in effectively stabilised the LUMO (- 4.15 eV to - 4.25 eV). OFET devices based on both **2,7-dialkyl-diFIDT-di(C(CN)$_2$)** and **2,7-dialkyl-diFIDT-di(N(CN))** displayed unipolar n-type transport, with mobilities > 0.1 $cm^2 V^{-1} s^{-1}$. Dicyanomethylene proved marginally superior to *N*-cyanoimine in depressing the LUMO energy levels, as well as providing higher electron transfer integrals and ultimately higher OFET mobility.

Two further approaches to functionalisation of **dialkyl-diFIDT-di(X)** have been pursued – end-functionalisation and fluorine substitution. End-functionalisation by direct arylation cross-coupling proved difficult, though ultimately successful, yielding **2,7-bis(4-benzonitrile)-3,8-dihexyl-diFIDT-di(O)**. Substitution of the fluorine groups by S_NAr has been shown to work using a thiolate nucleophile, though cyanide substitution was unsuccessful. This methodology appears limited in scope due to competing reactivity of the EWGs at the 4,9-positions. Having said that, substitution using functionalised thiols may be an interesting route to pursue.

Finally, a route to a novel class of ladder-type molecular OSCs based on IDT has been developed. A highly localised LUMO, at the periphery of the unit, allows selective tuning of the LUMO energy level by functionalisation of the peripheral bridging positions. Furthermore, suppressed HOMO-LUMO orbital overlap instils good optical transparency in the absorption spectra.

Greater understanding of the findings from this work would be aided by further investigation into the thin-film properties, using techniques including AFM and GIWAXS, since molecular ordering and orientation in the thin-film has a large effect on performance. Fluorination has been shown in this thesis to induce significant changes to the crystal packing and may also greatly influence molecular orientation at the OSC – dielectric interface, as reported in the literature.[60,202] Beyond this, the use of these small molecules in small molecule – polymer

blended OFET devices may be a route to higher performance, by improving processing and thin-film morphology.

A number of possible future target molecules can be anticipated, based on the insights gathered in this thesis, which may allow improvements to device performance also. In particular, further side-chain engineering and/or π-extension (**Figure 87a** & **d**), end-functionalisation with stronger EWGs (**Figure 87b**) and/or substitution with functionalised thiols (**Figure 87c**) are proposed.

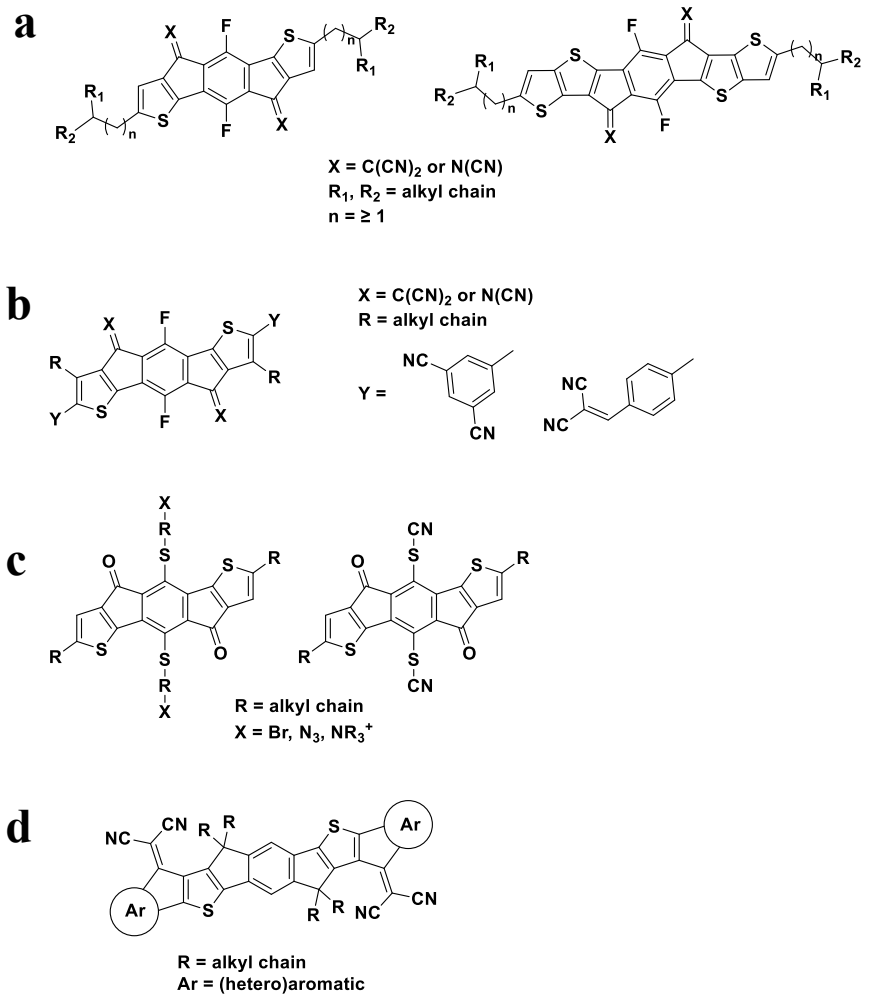


Figure 87: Possible future targets based on work from a) Chapters 2-4, b) and c) Chapter 5 and d) Chapter 6.

8. General Experimental

***Solubility Testing**:* To a 6 mL glass vial containing a small stirrer bar and 1.00 ± 0.02 mg of the respective OSC was added 0.1 mL chlorobenzene via a micropipette. The mixture was then stirred (400 rpm) at 25 °C for 20 minutes. If solid remained, more solvent was added, and the process repeated until complete dissolution. The testing was repeated 3 times for each compound to ensure reproducibility.

***DFT Calculations**:* DFT/TD-DFT calculations were carried out using the B3LYP hybrid functional and the 6-311+G(d,p) basis set in the GAUSSIAN09 software package. Alkyl chains were replaced with a methyl group to simplify calculations and reduce computational time. Structures were optimised, and a frequency analysis was performed. *Transfer Integrals:* Electron transfer integrals (LUMO-LUMO overlap, B3LYP/6-31G*) for molecular pairs from crystal structures of the specified OSC, calculated using the approach of Valeev et al. with Gaussian 16 Rev A.03 software.[203] *Symmetry Adapted Perturbation Theory (SAPT0) calculations:* Symmetry adapted perturbation interaction energies (SAPT0/jun-cc-pvdz) were calculated for molecular pairs from crystal structures using Psi4 software. In each case, H and F atoms were first allowed to relax geometrically to allow for error in positioning hydrogen atoms from x-ray diffraction data, and to allow the *in silico* substitution of H and F atoms. Total SAPT0 energies (E_{SAPT}) are decomposed into electrostatic (E_{ES}, Keesom interaction), exchange (E_{EX}, Pauli repulsion), induction (E_{IND}, Debye interaction) and dispersion (E_{DISP}, London interaction) energies. All energies are in kcal mol^{-1}.

***Characterisation**:* ^{1}H, ^{19}F, and ^{13}C NMR spectra were recorded on a Bruker AV-400 (400 MHz), using the residual solvent resonance of chloroform-*d* or 1,1,2,2-tetrachloroethane-d_2 and are given in ppm. Electrospray and chemical ionisation mass spectrometry were performed

with a Waters LCT Premier (ES-TOF) and a Micromass Autospec Premier mass spectrometer respectively. UV–vis spectra were recorded on a UV-1800 Shimadzu UV–vis spectrometer. TGA measurements, using ≥ 2 mg of material, were conducted under nitrogen between 25 °C and 600 °C at a scan rate of 10 K min^{-1} with a Mettler Toledo TGA/DSC 1LF/UMX instrument. DSC measurements, using ~ 3 mg of material, were conducted under nitrogen at scan rate of 10 °C min^{-1} with a TA DSC-Q20 instrument. The melting temperatures (T_m) were extracted from the DSC data as the extrapolated onset temperature of the major endotherm of the 1st heating cycle, unless otherwise stated.

Single Crystal Growth and Analysis*:* OSC solutions in chloroform or chlorobenzene (0.5 mg in 0.75 mL) were placed in 2 mL glass vials. These vials were placed into a larger vial containing methanol (2.5 mL) which was then sealed. Equilibration via vapour diffusion occurred over 3 – 5 d after which crystals were analysed. Crystallographic data were collected using Agilent Xcalibur PX Ultra A, and the structures were refined using the SHELXTL and SHELX-2013 program systems.

Device Fabrication and Characterisation*:* All film preparation and characterisation steps were carried out under inert atmosphere. Organic thin film transistors (OTFTs) were fabricated in bottom-contact top-gate (BC-TG) configuration. *Spin-coated Devices:* Gold source-drain electrodes of 40 nm were deposited via thermal evaporation in high vacuum (10^{-6} mbar) resulting channel lengths in the range of 30 – 100 nm and width 1 mm. Prior to semiconductor deposition both source-drain substrate and solution were heated at 100 °C. The small molecule solution (5 mg mL^{-1} in chlorobenzene) was spin coated with spin speed of 2000 rpm for 30 sec and then annealed at various temperatures for 15 minutes. 900 nm of CYTOP were used as the dielectric layer followed by 40 nm of thermal evaporated aluminum which formed the gate electrode. Device fabrication and electrical measurements were performed in a nitrogen

glovebox. Transistor characterisation was carried out using an Agilent B2902 semiconductor parameter analyser. Mobility was extracted from the slope of $\sqrt{I_D}$ versus V_G. *Blade-coated Devices:* The Al/Au (5 nm/35 nm) source and drain electrodes were vapour-deposited using shadow mask on the glass. The small molecule solution (5 mg mL^{-1} in chlorobenzene) was blade coated on the substrates at 100 °C with the blade speed of 50 mm s^{-1} and then the substrates were kept at 100 °C for 5 mins. ~ 900 nm CYTOP film was deposited on top of the semiconductor by spin coating at 2000 rpm spin rate followed by annealing at 50 °C for 1hr. The capacitance of the CYTOP dielectric was measured 2.1 nF cm^{-2}. 70 nm Al was vapour-deposited at the top as the gate electrode. The current-voltage characteristics for the devices were measured using KEYSIGHT B2912A Precision Source/Measure Unit. *Air Stability Tests:* A series of spin-coated devices fabricated in N_2 (as above) were exposed in air for over 100 hours and the electrical characteristics were measured using an Agilent B920A semiconductor parameter analyser.

9. References

[1] K. Rose, S. Devarajan, *Kirk-Othmer Encyclopedia of Chemical Technology*, Wiley, Hoboken, NJ, **2006**.

[2] H. Shirakawa, E. J. Louis, A. G. MacDiarmid, C. K. Chiang, A. J. Heeger, *J. Chem. Soc. Chem. Commun.* **1977**, 578.

[3] H. Jia, T. Lei, *J. Mater. Chem. C* **2019**, *7*, 12809.

[4] S. Ahmad, *J. Polym. Eng.* **2014**, *34*, 279.

[5] H. J. Snaith, *J. Phys. Chem. Lett.* **2013**, *4*, 3623.

[6] T. Yajima, Y. Hikita, H. Y. Hwang, *Nat. Mater.* **2011**, *10*, 198.

[7] E. A. Jones, F. F. Wang, D. Costinett, *IEEE J. Emerg. Sel. Top. Power Electron.* **2016**, *4*, 707.

[8] J. Tian, C. Lai, G. Feng, D. Banerjee, W. Li, N. C. Kar, *Int. J. Sustain. Energy* **2020**, *39*, 88.

[9] H. Kwon, C. Y. Gao, X. Tang, J. Hong, C. E. Park, H. Kong, S. H. Kim, H. Yang, *Org. Electron.* **2019**, *77*, 105485.

[10] X. Cheng, M. Caironi, Y. Y. Noh, J. Wang, C. Newman, H. Yan, A. Facchetti, H. Sirringhaus, *Chem. Mater.* **2010**, *22*, 1559.

[11] M. P. Walser, W. L. Kalb, T. Mathis, B. Batlogg, *Appl. Phys. Lett.* **2009**, *95*, 233301.

[12] W. L. Kalb, T. Mathis, S. Haas, A. F. Stassen, B. Batlogg, *Appl. Phys. Lett.* **2007**, *90*,

92104.

[13] S. Huang, Y. Liu, Y. Zhao, Z. Ren, C. F. Guo, *Adv. Funct. Mater.* **2019**, *29*, 1805924.

[14] M. Zou, Y. Ma, X. Yuan, Y. Hu, J. Liu, Z. Jin, *J. Semicond.* **2018**, *39*, 11010.

[15] Q. Li, J. Zhang, Q. Li, G. Li, X. Tian, Z. Luo, F. Qiao, X. Wu, J. Zhang, *Front. Mater.* **2019**, *5*, 77.

[16] W. Gao, H. Ota, D. Kiriya, K. Takei, A. Javey, *Acc. Chem. Res.* **2019**, *52*, 523.

[17] M. Małachowski, J. Żmija, *Opto-Electronics Rev.* **2010**, *18*, 121.

[18] G. Horowitz, *Semiconducting Polymers*, (Eds: G. Hadziioannou, G. G. Malliaras), Wiley-VCH, Weinheim, Germany, 2007, Ch 12.

[19] H. Sirringhaus, *Adv. Mater.* **2014**, *26*, 1319.

[20] J. M. Montero, J. Bisquert, *Isr. J. Chem.* **2012**, *52*, 519.

[21] A. Facchetti, M. Yoon, T. J. Marks, *Adv. Mater.* **2005**, *17*, 1705.

[22] D. Braga, G. Horowitz, *Adv. Mater.* **2009**, *21*, 1473.

[23] K. A. Smith, B. Stewart, K. G. Yager, J. Strzalka, R. Verduzco, *J. Polym. Sci. Part B Polym. Phys.* **2014**, *52*, 900.

[24] X. Wang, B. Peng, P. Chan, *MRS Advances* **2016**, 1, 1637.

[25] C. Liu, Z. Liu, H. T. Lemke, H. N. Tsao, R. C. G. Naber, Y. Li, K. Banger, K. Müllen, M. M. Nielsen, H. Sirringhaus, *Chem. Mater.* **2010**, *22*, 2120.

[26] V. Coropceanu, J. Cornil, D. A. da Silva Filho, Y. Olivier, R. Silbey, J.-L. Brédas, *Chem.*

Rev. **2007**, *107*, 926.

[27] L.-L. Chua, J. Zaumseil, J.-F. Chang, E. C.-W. Ou, P. K.-H. Ho, H. Sirringhaus, R. H. Friend, *Nature* **2005**, *434*, 194.

[28] J. C. Ribierre, S. Watanabe, M. Matsumoto, T. Muto, T. Aoyama, *Appl. Phys. Lett.* **2010**, *96*, 83303.

[29] B. Sun, W. Hong, E. S. Thibau, H. Aziz, Z. H. Lu, Y. Li, *ACS Appl. Mater. Interfaces* **2015**, *7*, 18662.

[30] M. Nakano, I. Osaka, K. Takimiya, *Adv. Mater.* **2017**, *29*, 1602893.

[31] G. Adam, B. Munkhbat, P. Denk, C. Ulbricht, C. Hrelescu, M. C. Scharber, *Front. Mater.* **2016**, *3*, 39.

[32] N. Gasparini, A. Wadsworth, M. Moser, D. Baran, I. McCulloch, C. J. Brabec, *Adv. Energy Mater.* **2018**, *8*, 1703298.

[33] S. Rafique, S. M. Abdullah, K. Sulaiman, M. Iwamoto, *Renew. Sustain. Energy Rev.* **2018**, *84*, 43.

[34] C. Zhang, P. Chen, W. Hu, *Small* **2016**, *12*, 1252.

[35] C. F. Liu, X. Liu, W. Y. Lai, W. Huang, *Adv. Mater.* **2018**, *30*, 1802466.

[36] J. Zaumseil, *Adv. Funct. Mater.* **2019**, 1905269.

[37] M. Pärs, C. C. Hofmann, K. Willinger, P. Bauer, M. Thelakkat, J. Köhler, *Angew. Chemie - Int. Ed.* **2011**, *50*, 11405.

[38] A. V. Zasedatelev, A. V. Baranikov, D. Urbonas, F. Scafirimuto, U. Scherf, T. Stöferle,

R. F. Mahrt, P. G. Lagoudakis, *Nat. Photonics* **2019**, *13*, 378.

[39] M. J. Ford, M. Wang, S. N. Patel, H. Phan, R. A. Segalman, T. Q. Nguyen, G. C. Bazan, *Chem. Mater.* **2016**, *28*, 1256.

[40] A. F. Paterson, N. D. Treat, W. Zhang, Z. Fei, G. Wyatt-Moon, H. Faber, G. Vourlias, P. A. Patsalas, O. Solomeshch, N. Tessler, M. Heeney, T. D. Anthopoulos, *Adv. Mater.* **2016**, *28*, 7791.

[41] S. Riera-Galindo, F. Leonardi, R. Pfattner, M. Mas-Torrent, *Adv. Mater. Technol.* **2019**, *4*, 1900104.

[42] L. H. Chou, Y. Na, C. H. Park, M. S. Park, I. Osaka, F. S. Kim, C. L. Liu, *Polymer.* **2020**, *191*, 122208.

[43] G. Gryn'Ova, K. H. Lin, C. Corminboeuf, *J. Am. Chem. Soc.* **2018**, *140*, 16370.

[44] Z. F. Yao, J. Y. Wang, J. Pei, *Cryst. Growth Des.* **2018**, *18*, 7.

[45] X. Qiao, Q. Wu, H. Wu, D. Wang, H. Li, *Polym. Chem.* **2016**, *7*, 807.

[46] M. Pandey, N. Kumari, S. Nagamatsu, S. S. Pandey, *J. Mater. Chem. C* **2019**, *7*, 13323.

[47] C. Wang, H. Nakamura, H. Sugino, K. Takimiya, *Chem. Commun.* **2017**, *53*, 9594.

[48] D. Liu, Q. Miao, *Mater. Chem. Front.* **2018**, *2*, 11.

[49] Y. Mei, D. Fogel, J. Chen, J. W. Ward, M. M. Payne, J. E. Anthony, O. D. Jurchescu, *Org. Electron.* **2017**, *50*, 100.

[50] J. T. E. Quinn, J. Zhu, X. Li, J. Wang, Y. Li, *J. Mater. Chem. C* **2017**, *5*, 8654.

[51] Y. Wang, T. Michinobu, *J. Mater. Chem. C* **2018**, *6*, 10390.

[52] O. Inganäs, *Adv. Mater.* **2018**, *30*, 1800388.

[53] W. Cao, J. Xue, *Energy Environ. Sci.* **2014**, *7*, 2123.

[54] H. Klauk, U. Zschieschang, J. Pflaum, M. Halik, *Nature* **2007**, *445*, 745.

[55] H. Usta, A. Facchetti, T. J. Marks, *Acc. Chem. Res.* **2011**, *44*, 501.

[56] R. Di Pietro, D. Fazzi, T. B. Kehoe, H. Sirringhaus, *J. Am. Chem. Soc.* **2012**, *134*, 14877.

[57] J. Dhar, U. Salzner, S. Patil, *J. Mater. Chem. C* **2017**, *5*, 7404.

[58] B. A. Jones, A. Facchetti, M. R. Wasielewski, T. J. Marks, *J. Am. Chem. Soc.* **2007**, *129*, 15259.

[59] X. Xu, Y. Yao, B. Shan, X. Gu, D. Liu, J. Liu, J. Xu, N. Zhao, W. Hu, Q. Miao, *Adv. Mater.* **2016**, *28*, 5276.

[60] J.-H. Dou, Y.-Q. Zheng, Z.-F. Yao, Z.-A. Yu, T. Lei, X. Shen, X.-Y. Luo, J. Sun, S.-D. Zhang, Y.-F. Ding, G. Han, Y. Yi, J.-Y. Wang, J. Pei, *J. Am. Chem. Soc.* **2015**, *137*, 15947.

[61] E. G. Bittle, J. I. Basham, T. N. Jackson, O. D. Jurchescu, D. J. Gundlach, *Nat. Commun.* **2016**, *7*, 10908.

[62] H. H. Choi, K. Cho, C. D. Frisbie, H. Sirringhaus, V. Podzorov, *Nat. Mater.* **2017**, *17*, 2.

[63] C. Liu, G. Li, R. Di Pietro, J. Huang, Y. Y. Noh, X. Liu, T. Minari, *Phys. Rev. Appl.* **2017**, *8*, 34020.

[64] M. Waldrip, O. D. Jurchescu, D. J. Gundlach, E. G. Bittle, *Adv. Funct. Mater.* **2019**,

1904576.

[65] H. Phan, M. J. Ford, A. T. Lill, M. Wang, G. C. Bazan, T. Q. Nguyen, *Adv. Funct. Mater.* **2018**, *28*, 1707221.

[66] A. F. Paterson, S. Singh, K. J. Fallon, T. Hodsden, Y. Han, B. C. Schroeder, H. Bronstein, M. Heeney, I. Mcculloch, T. D. Anthopoulos, *Adv. Mater.* **2018**, *30*, 1801079.

[67] M. Stolar, T. Baumgartner, *Chem. Commun.* **2018**, *54*, 3311.

[68] C. Sun, S. Song, H. G. Song, S. M. Park, J. Y. Kim, Y. H. Kim, S. K. Kwon, *J. Nanosci. Nanotechnol.* **2017**, *17*, 5792.

[69] X. Wu, C. Sun, H. gun Song, Y. H. Kim, *J. Inf. Disp.* **2018**, *19*, 1.

[70] I. F. Perepichka, D. F. Perepichka, *Handbook of Thiophene-Based Materials: Applications in Organic Electronics and Photonics*, Wiley, Chichester, UK, **2009**.

[71] G. Turkoglu, M. E. Cinar, T. Ozturk, *Top. Curr. Chem.* **2017**, *375*, 84.

[72] O. Gidron, M. Bendikov, *Angew. Chemie - Int. Ed.* **2014**, *53*, 2546.

[73] A. Islam, Z. Liu, R. Peng, W. Jiang, T. Lei, W. Li, L. Zhang, R. Yang, Q. Guan, Z. Ge, *Chinese J. Polym. Sci.* **2017**, *35*, 171.

[74] Y. Lin, H. Fan, Y. Li, X. Zhan, *Adv. Mater.* **2012**, *24*, 3087.

[75] C. Sutton, C. Risko, J. L. Brédas, *Chem. Mater.* **2016**, *28*, 3.

[76] H. T. Black, D. F. Perepichka, *Angew. Chemie - Int. Ed.* **2014**, *53*, 2138.

[77] E. D. Głowacki, H. Coskun, M. A. Blood-Forsythe, U. Monkowius, L. Leonat, M. Grzybowski, D. Gryko, M. S. White, A. Aspuru-Guzik, N. S. Sariciftci, *Org. Electron.*

2014, *15*, 3521.

[78] N. Gospodinova, E. Tomšík, *Prog. Polym. Sci.* **2015**, *43*, 33.

[79] T. Lei, J. Y. Wang, J. Pei, *Chem. Mater.* **2014**, *26*, 594.

[80] Z. Ma, H. Geng, D. Wang, Z. Shuai, *J. Mater. Chem. C* **2016**, *4*, 4546.

[81] B. Movaghar, L. O. Jones, M. A. Ratner, G. C. Schatz, K. L. Kohlstedt, *J. Phys. Chem. C* **2019**, *123*, 29499.

[82] J. Chen, K. Yang, X. Zhou, X. Guo, *Chem. - An Asian J.* **2018**, *13*, 2587.

[83] Z. Liu, G. Zhang, D. Zhang, *Acc. Chem. Res.* **2018**, *51*, 1422.

[84] W. Zhang, J. Smith, S. E. Watkins, R. Gysel, M. McGehee, A. Salleo, J. Kirkpatrick, S. Ashraf, T. Anthopoulos, M. Heeney, I. McCulloch, *J. Am. Chem. Soc.* **2010**, *132*, 11437.

[85] J. Kirkpatrick, C. B. Nielsen, W. Zhang, H. Bronstein, R. S. Ashraf, M. Heeney, I. McCulloch, *Adv. Energy Mater.* **2012**, *2*, 260.

[86] C. Liang, H. Wang, *Org. Electron.* **2017**, *50*, 443.

[87] H. Usta, C. Risko, Z. Wang, H. Huang, M. K. Deliomeroglu, A. Zhukhovitskiy, A. Facchetti, T. J. Marks, *J. Am. Chem. Soc.* **2009**, *131*, 5586.

[88] M. R. Rao, A. Desmecht, D. F. Perepichka, *Chem. - A Eur. J.* **2015**, *21*, 6193.

[89] D. Venkateshvaran, M. Nikolka, A. Sadhanala, V. Lemaur, M. Zelazny, M. Kepa, M. Hurhangee, A. J. Kronemeijer, V. Pecunia, I. Nasrallah, I. Romanov, K. Broch, I. McCulloch, D. Emin, Y. Olivier, J. Cornil, D. Beljonne, H. Sirringhaus, *Nature* **2014**, *515*, 384.

[90] L. Biniek, B. C. Schroeder, C. B. Nielsen, I. McCulloch, *J. Mater. Chem.* **2012**, *22*, 14803.

[91] K. Thorley, I. McCulloch, *J. Mater. Chem. C* **2018**, *6*, 12413.

[92] Y. Li, M. Gu, Z. Pan, B. Zhang, X. Yang, J. Gu, Y. Chen, *J. Mater. Chem. A* **2017**, *5*, 10798.

[93] X. Guo, M. Zhang, J. Tan, S. Zhang, L. Huo, W. Hu, Y. Li, J. Hou, *Adv. Mater.* **2012**, *24*, 6536.

[94] R. He, J. Xu, Y. Yang, P. Cai, D. Chen, L. Ying, W. Yang, Y. Cao, *Org. Electron.* **2014**, *15*, 2950.

[95] X. Xu, G. Zhang, Y. Li, Q. Peng, *Chinese Chem. Lett.* **2019**, *30*, 809.

[96] H. Fu, Z. Wang, Y. Sun, *Angew. Chemie - Int. Ed.* **2019**, *58*, 4442.

[97] W. Zhang, Y. Han, X. Zhu, Z. Fei, Y. Feng, N. D. Treat, H. Faber, N. Stingelin, I. Mcculloch, T. D. Anthopoulos, M. Heeney, *Adv. Mater.* **2016**, *28*, 3922.

[98] X. Zhang, H. Bronstein, A. J. Kronemeijer, J. Smith, Y. Kim, R. J. Kline, L. J. Richter, T. D. Anthopoulos, H. Sirringhaus, K. Song, M. Heeney, W. Zhang, I. McCulloch, D. M. DeLongchamp, *Nat. Commun.* **2013**, *4*, 2238.

[99] W. Zhao, S. Li, H. Yao, S. Zhang, Y. Zhang, B. Yang, J. Hou, *J. Am. Chem. Soc.* **2017**, *139*, 7148.

[100] Y. Yang, Z. G. Zhang, H. Bin, S. Chen, L. Gao, L. Xue, C. Yang, Y. Li, *J. Am. Chem. Soc.* **2016**, *138*, 15011.

[101] S. Li, L. Ye, W. Zhao, S. Zhang, S. Mukherjee, H. Ade, J. Hou, *Adv. Mater.* **2016**, *28*,

9423.

[102] G. Zhang, J. Zhao, P. C. Y. Chow, K. Jiang, J. Zhang, Z. Zhu, J. Zhang, F. Huang, H. Yan, *Chem. Rev.* **2018**, 118, 3447.

[103] A. Wadsworth, M. Moser, A. Marks, M. S. Little, N. Gasparini, C. J. Brabec, D. Baran, I. McCulloch, *Chem. Soc. Rev.* **2019**, *48*, 1596.

[104] J. Zhang, H. S. Tan, X. Guo, A. Facchetti, H. Yan, *Nat. Energy* **2018**, *3*, 720.

[105] X. Song, N. Gasparini, M. M. Nahid, H. Chen, S. M. Macphee, W. Zhang, V. Norman, C. Zhu, D. Bryant, H. Ade, I. McCulloch, D. Baran, *Adv. Funct. Mater.* **2018**, *28*, 1802895.

[106] H. Bristow, K. J. Thorley, A. J. P. White, A. Wadsworth, M. Babics, Z. Hamid, W. Zhang, A. F. Paterson, J. Kosco, J. Panidi, T. D. Anthopoulos, I. McCulloch, *Adv. Electron. Mater.* **2019**, *5*, 1900344.

[107] X. Li, F. Pan, C. Sun, M. Zhang, Z. Wang, J. Du, J. Wang, M. Xiao, L. Xue, Z. G. Zhang, C. Zhang, F. Liu, Y. Li, *Nat. Commun.* **2019**, *10*, 519.

[108] C. Zhao, Y. Zhang, M. K. Ng, *J. Org. Chem.* **2007**, *72*, 6364.

[109] H. Tian, Y. Deng, F. Pan, L. Huang, D. Yan, Y. Geng, F. Wang, *J. Mater. Chem.* **2010**, *20*, 7998.

[110] J. D. Peltier, B. Heinrich, B. Donnio, J. Rault-Berthelot, E. Jacques, C. Poriel, *ACS Appl. Mater. Interfaces* **2017**, *9*, 8219.

[111] Q. Zhang, M. A. Kelly, N. Bauer, W. You, *Acc. Chem. Res.* **2017**, *50*, 2401.

[112] M. Kim, S. U. Ryu, S. A. Park, K. Choi, T. Kim, D. Chung, T. Park, *Adv. Funct. Mater.*

2019, 1904545.

[113] Y. Gao, Y. Deng, H. Tian, J. Zhang, D. Yan, Y. Geng, F. Wang, *Adv. Mater.* **2017**, *29*, 1606217.

[114] F. Wang, Y. Dai, W. Wang, H. Lu, L. Qiu, Y. Ding, G. Zhang, *Chem. Mater.* **2018**, *30*, 5451.

[115] D. Deng, Y. Zhang, J. Zhang, Z. Wang, L. Zhu, J. Fang, B. Xia, Z. Wang, K. Lu, W. Ma, Z. Wei, *Nat. Commun.* **2016**, *7*, 13740.

[116] H. Medlej, A. Nourdine, H. Awada, M. Abbas, C. Dagron-Lartigau, G. Wantz, L. Flandin, *Eur. Polym. J.* **2014**, *59*, 25.

[117] H. Huang, L. Yang, A. Facchetti, T. J. Marks, *Chem. Rev.* **2017**, *117*, 10291.

[118] D. J. Crouch, P. J. Skabara, M. Heeney, I. McCulloch, S. J. Coles, M. B. Hursthouse, *Chem. Commun.* **2005**, 1465.

[119] M. D'Lavari, W. Mitchell, C. Wang, D. Sparrow (Merck KGaA), WO2015154845A1, **2015**.

[120] K. Feng, X. Zhang, Z. Wu, Y. Shi, M. Su, K. Yang, Y. Wang, H. Sun, J. Min, Y. Zhang, X. Cheng, H. Y. Woo, X. Guo, *ACS Appl. Mater. Interfaces* **2019**, *11*, 35924.

[121] P. Boufflet, Y. Han, Z. Fei, N. D. Treat, R. Li, D.-M. Smilgies, N. Stingelin, T. D. Anthopoulos, M. Heeney, *Adv. Funct. Mater.* **2015**, *25*, 7038.

[122] K. Kawashima, T. Fukuhara, Y. Suda, Y. Suzuki, T. Koganezawa, H. Yoshida, H. Ohkita, I. Osaka, K. Takimiya, *J. Am. Chem. Soc.* **2016**, *138*, 10265.

[123] J. H. Yun, S. Park, J. H. Heo, H. S. Lee, S. Yoon, J. Kang, S. H. Im, H. Kim, W. Lee,

B. Kim, M. J. Ko, D. S. Chung, H. J. Son, *Chem. Sci.* **2016**, *7*, 6649.

[124] E. M. Espinoza, J. A. Clark, J. Soliman, J. B. Derr, M. Morales, V. I. Vullev, *J. Electrochem. Soc.* **2019**, *166*, H3175.

[125] T. Kharandiuk, E. J. Hussien, J. Cameron, R. Petrina, N. J. Findlay, R. Naumov, W. T. Klooster, S. J. Coles, Q. Ai, S. Goodlett, C. Risko, P. J. Skabara, *Chem. Mater.* **2019**, *31*, 7070.

[126] S. K. Park, J. H. Kim, S. Y. Park, *Adv. Mater.* **2018**, *30*, 1704759.

[127] A. Y. Sosorev, *Phys. Chem. Chem. Phys.* **2017**, *19*, 25478.

[128] M. Nakano, I. Osaka, D. Hashizume, K. Takimiya, *Chem. Mater.* **2015**, *27*, 6418.

[129] G. Ji, W. Zhao, J. Wei, L. Yan, Y. Han, Q. Luo, S. Yang, J. Hou, C. Q. Ma, *J. Mater. Chem. A* **2019**, *7*, 212.

[130] H. Tian, Y. Deng, F. Pan, L. Huang, D. Yan, Y. Geng, F. Wang, *J. Mater. Chem.* **2010**, *20*, 7998.

[131] J. Mei, Z. Bao, *Chem. Mater.* **2014**, *26*, 604.

[132] A. Welford, S. Maniam, E. Gann, X. Jiao, L. Thomsen, S. J. Langford, C. R. McNeill, *Org. Electron.* **2019**, *75*, 105378.

[133] C. Zhang, Y. Zang, F. Zhang, Y. Diao, C. R. McNeill, C. an Di, X. Zhu, D. Zhu, *Adv. Mater.* **2016**, *28*, 8456.

[134] C. Zhang, D. Yuan, H. Wu, E. Gann, L. Thomsen, C. R. McNeill, C. an Di, X. Zhu, D. Zhu, *J. Mater. Chem. C* **2017**, *5*, 1935.

[135] B. Lim, H. Sun, J. Lee, Y.-Y. Noh, *Sci. Rep.* **2017**, *7*, 164.

[136] H. Xu, Y. C. Zhou, X. Y. Zhou, K. Liu, L. Y. Cao, Y. Ai, Z. P. Fan, H. L. Zhang, *Adv. Funct. Mater.* **2014**, *24*, 2907.

[137] J. Yu, B. Zhao, X. Nie, B. Zhou, Y. Li, J. Hai, E. Zhu, L. Bian, H. Wu, W. Tang, *New J. Chem.* **2015**, *39*, 2248.

[138] P. Kovacic, K. N. McFarland, *J. Polym. Sci. Polym. Chem. Ed.* **1979**, *17*, 1963.

[139] J. Lange, J. M. Kanabus-Kaminska, A. Krai, *Synth. Commun.* **1980**, *10*, 473.

[140] K. J. Thorley, C. Risko, *J. Mater. Chem. C* **2016**, *4*, 4040.

[141] J. L. Brédas, J. P. Calbert, D. A. Da Silva Filho, J. Cornil, *Proc. Natl. Acad. Sci. U. S. A.* **2002**, *99*, 5804.

[142] K. Sun, Z. Xiao, S. Lu, W. Zajaczkowski, W. Pisula, E. Hanssen, J. M. White, R. M. Williamson, J. Subbiah, J. Ouyang, A. B. Holmes, W. W. H. Wong, D. J. Jones, *Nat. Commun.* **2015**, *6*.

[143] R. Ozdemir, D. Choi, M. Ozdemir, H. Kim, S. T. Kostakoğlu, M. Erkartal, H. Kim, C. Kim, H. Usta, *ChemPhysChem* **2017**, *18*, 850.

[144] Y. Kim, C. E. Song, S. J. Moon, E. Lim, *RSC Adv.* **2015**, *5*, 62739.

[145] R. Xie, L. Ying, H. Liao, Z. Chen, F. Huang, Y. Cao, *Front. Chem.* **2018**, *6*, 45.

[146] S. Holliday, R. S. Ashraf, C. B. Nielsen, M. Kirkus, J. A. Röhr, C. H. Tan, E. Collado-Fregoso, A. C. Knall, J. R. Durrant, J. Nelson, I. McCulloch, *J. Am. Chem. Soc.* **2015**, *137*, 898.

[147] P. Cheng, G. Li, X. Zhan, Y. Yang, *Nat. Photonics* **2018**, *12*, 131.

[148] G. He, Z. Li, X. Wan, J. Zhou, G. Long, S. Zhang, M. Zhang, Y. Chen, *J. Mater. Chem. A* **2013**, *1*, 1801.

[149] S. Chen, Y. Zhao, A. Bolag, J. I. Nishida, Y. Liu, Y. Yamashita, *ACS Appl. Mater. Interfaces* **2012**, *4*, 3994.

[150] K. Takahashi, K. Kobayashi, *J. Org. Chem.* **2000**, *65*, 2577.

[151] A. S. Batsanov, M. R. Bryce, M. A. Coffin, A. Green, R. E. Hester, J. A. K. Howard, I. K. Lednev, N. Martín, A. J. Moore, J. N. Moore, E. Ortí, L. Sánchez, M. Savirón, P. M. Viruela, R. Viruela, T.-Q. Ye, *Chem. - A Eur. J.* **1998**, *4*, 2580.

[152] J.-D. Peltier, B. Heinrich, B. Donnio, O. Jeannin, J. Rault-Berthelot, E. Jacques, C. Poriel, *J. Mater. Chem. C* **2018**, *6*, 13197.

[153] M. Schwarz, *J. Chem. Soc. D Chem. Commun.* **1969**, 212.

[154] T. Inokuchi, H. Kawafuchi, *J. Org. Chem.* **2006**, *71*, 947.

[155] R. Tanikaga, N. Konya, T. Tamura, A. Kaji, *J. Chem. Soc. Perkin Trans. 1* **1987**, 825.

[156] A. Lee, A. Michrowska, S. Sulzer-Mosse, B. List, *Angew. Chemie - Int. Ed.* **2011**, *50*, 1707.

[157] B. Voigt, A. Matviitsuk, R. Mahrwald, *Tetrahedron* **2013**, *69*, 4302.

[158] S. Chen, Y. Zhao, A. Bolag, J. Nishida, Y. Liu, Y. Yamashita, **2012**, *4*, 3994.

[159] O. Lichtenberger, E. Pippel, J. Woltersdorf, R. Riedel, *Mater. Chem. Phys.* **2003**, *81*, 195.

[160] H. Song, Y. Deng, Y. Gao, Y. Jiang, H. Tian, D. Yan, Y. Geng, F. Wang, *Macromolecules* **2017**, *50*, 2344.

[161] A. Nitti, R. Po, G. Bianchi, D. Pasini, *Molecules* **2017**, *22*, 21.

[162] S. L. Suraru, J. A. Lee, C. K. Luscombe, *ACS Macro Lett.* **2016**, *5*, 724.

[163] L. G. Mercier, M. Leclerc, *Acc. Chem. Res.* **2013**, *46*, 1597.

[164] J. T. Blaskovits, P. A. Johnson, M. Leclerc, *Macromolecules* **2018**, *51*, 8100.

[165] H. Bohra, M. Wang, *J. Mater. Chem. A* **2017**, *5*, 11550.

[166] R. M. Pankow, L. Ye, B. C. Thompson, *Polym. Chem.* **2019**, *10*, 4561.

[167] A. E. Rudenko, B. C. Thompson, *J. Polym. Sci. Part A Polym. Chem.* **2015**, *53*, 135.

[168] W. Hagui, N. Besbes, E. Srasra, J. F. Soulé, H. Doucet, *RSC Adv.* **2016**, *6*, 17110.

[169] C. Kieffer, V. Babin, M. Jouanne, I. Slimani, Y. Berhault, R. Legay, J. Sopková-de Oliveira Santos, S. Rault, A. S. Voisin-Chiret, *Tetrahedron* **2017**, *73*, 5509.

[170] Y. Li, W. K. Tatum, J. W. Onorato, S. D. Barajas, Y. Y. Yang, C. K. Luscombe, *Polym. Chem.* **2017**, *8*, 5185.

[171] U. D. Patil, P. P. Mahulikar, *ISRN Org. Chem.* **2012**, 963195.

[172] X. Cheng, S. Pei, C. Xue, K. Cao, L. Hai, Y. Wu, *RSC Adv.* **2014**, *4*, 63897.

[173] A. L. Spek, *Acta Crystallogr. Sect. C Struct. Chem.* **2015**, *71*, 9.

[174] M. Baumann, I. R. Baxendale, *Beilstein J. Org. Chem.* **2013**, *9*, 2265.

[175] K. Blaziak, W. Danikiewicz, M. Mąkosza, *J. Am. Chem. Soc.* **2016**, *138*, 7276.

[176] C. N. Neumann, J. M. Hooker, T. Ritter, **2016**, *534*, 369.

[177] E. E. Kwan, Y. Zeng, H. A. Besser, E. N. Jacobsen, *Nat. Chem.* **2018**, *10*, 917.

[178] S. Rohrbach, A. J. Smith, J. H. Pang, D. L. Poole, T. Tuttle, S. Chiba, J. A. Murphy, *Angew. Chemie - Int. Ed.* **2019**, *58*, 16368.

[179] A. Casey, *Optoelectronic Properties of New Conjugated Materials*, Imperial College London **2016**.

[180] A. D. Creamer, *Development of One-Step Post-Polymerisation Methods for Semiconducting Polymers*, Imperial College London **2017**.

[181] A. Creamer, A. Casey, A. V Marsh, M. Shahid, M. Gao, M. Heeney, *Macromolecules* **2017**, *50*, 2736.

[182] A. Creamer, C. S. Wood, P. D. Howes, A. Casey, S. Cong, A. V Marsh, R. Godin, J. Panidi, T. D. Anthopoulos, C. H. Burgess, T. Wu, Z. Fei, I. Hamilton, M. A. McLachlan, M. M. Stevens, M. Heeney, *Nat. Commun.* **2018**, *9*, 23955.

[183] A. Casey, Y. Han, Z. Fei, A. J. P. White, T. D. Anthopoulos, M. Heeney, *J. Mater. Chem. C* **2015**, *3*, 265.

[184] A. Casey, S. D. Dimitrov, P. Shakya-Tuladhar, Z. Fei, M. Nguyen, Y. Han, T. D. Anthopoulos, J. R. Durrant, M. Heeney, *Chem. Mater.* **2016**, *28*, 5110.

[185] A. Casey, J. Green, P. Shakya Tuladhar, M. Kirkus, Y. Han, T. D. Anthopoulos, M. Heeney, *J. Mater. Chem. A* **2017**, *5*, 6465.

[186] A. Lapworth, *J. Chem. Soc. Trans.* **1904**, *85*, 1206.

[187] M. Rimmele, K. Ableidinger, A. V. Marsh, N. J. Cheetham, M. J. Taublaender, A.

Buchner, J. Prinz, J. Fröhlich, M. M. Unterlass, M. Heeney, F. Glöcklhofer, *Polym. Chem.* **2019**, *10*, 738.

[188] D. P. Nair, M. Podgórski, S. Chatani, T. Gong, W. Xi, C. R. Fenoli, C. N. Bowman, *Chem. Mater.* **2014**, *26*, 724.

[189] Y. Miao, H. Yu, Y. Zhang, X. Yan, J. Zhang, Y. Wang, *J. Mater. Chem. C* **2018**, *6*, 57.

[190] M. Bai, S. P. Thomas, R. Kottokkaran, S. K. Nayak, P. C. Ramamurthy, T. N. Guru Row, *Cryst. Growth Des.* **2014**, *14*, 459.

[191] S. Riaz, M. Edgar, M. R. J. Elsegood, L. Horsburgh, S. J. Teat, T. G. Warwick, G. W. Weaver, *Cryst. Growth Des.* **2019**, *19*, 5237.

[192] W. Luo, *New Class of IDT-based Small Molecules for OFETs*, Imperial College London **2019.**

[193] T. Zheng, Z. Cai, R. Ho-Wu, S. H. Yau, V. Shaparov, T. Goodson, L. Yu, *J. Am. Chem. Soc.* **2016**, *138*, 868.

[194] J. Lee, A. J. Kalin, T. Yuan, M. Al-Hashimi, L. Fang, *Chem. Sci.* **2017**, *8*, 2503.

[195] A. Onwubiko, W. Yue, C. Jellett, M. Xiao, H. Y. Chen, M. K. Ravva, D. A. Hanifi, A. C. Knall, B. Purushothaman, M. Nikolka, J. C. Flores, A. Salleo, J. L. Bredas, H. Sirringhaus, P. Hayoz, I. McCulloch, *Nat. Commun.* **2018**, *9*, 416.

[196] Y. Yuan, G. Giri, A. L. Ayzner, A. P. Zoombelt, S. C. B. Mannsfeld, J. Chen, D. Nordlund, M. F. Toney, J. Huang, Z. Bao, *Nat. Commun.* **2014**, *5*, 3005.

[197] A. Maliakal, K. Raghavachari, H. Katz, E. Chandross, T. Siegrist, *Chem. Mater.* **2004**, *16*, 4980.

[198] R. Mondal, C. Tönshoff, D. Khon, D. C. Neckers, H. F. Bettinger, *J. Am. Chem. Soc.* **2009**, *131*, 14281.

[199] W. Fudickar, T. Linker, *J. Am. Chem. Soc.* **2012**, *134*, 15071.

[200] X. Shi, C. Chi, *Chem. Rec.* **2016**, *16*, 1690.

[201] A. Naibi Lakshminarayana, A. Ong, C. Chi, *J. Mater. Chem. C* **2018**, *6*, 3551.

[202] A. Zhang, C. Xiao, Y. Wu, C. Li, Y. Ji, L. Li, W. Hu, Z. Wang, W. Ma, W. Li, *Macromolecules* **2016**, *49*, 6431.

[203] E. F. Valeev, V. Coropceanu, D. A. Da Silva Filho, S. Salman, J. L. Brédas, *J. Am. Chem. Soc.* **2006**, *128*, 9882.

10. Appendix

10.1 Chapter 2

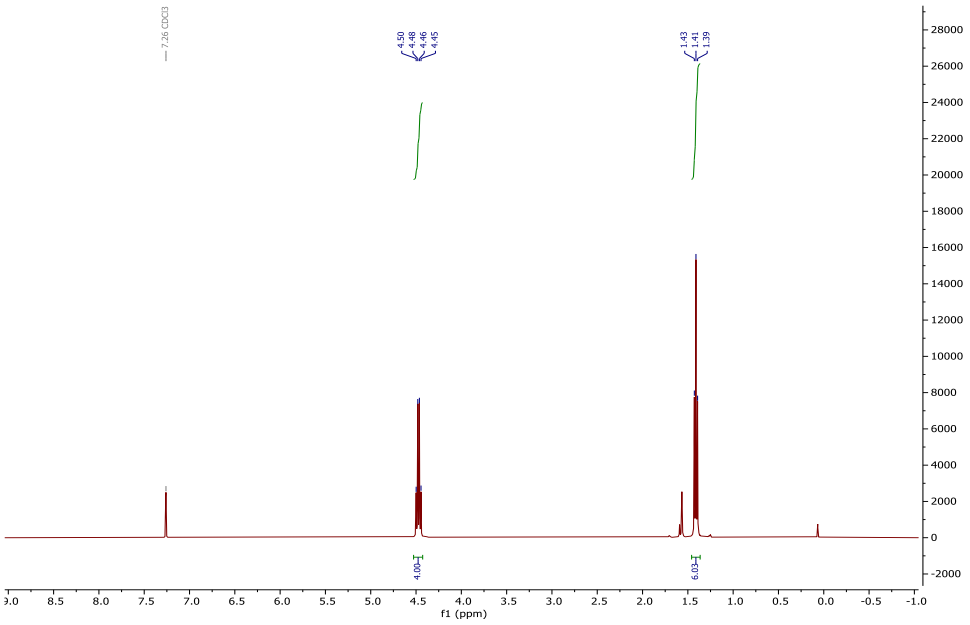


Figure A1: *^{1}H NMR of diethyl 2,5-dibromo-3,6-difluoroterephthalate* ***([2])*** *in $CDCl_3$.*

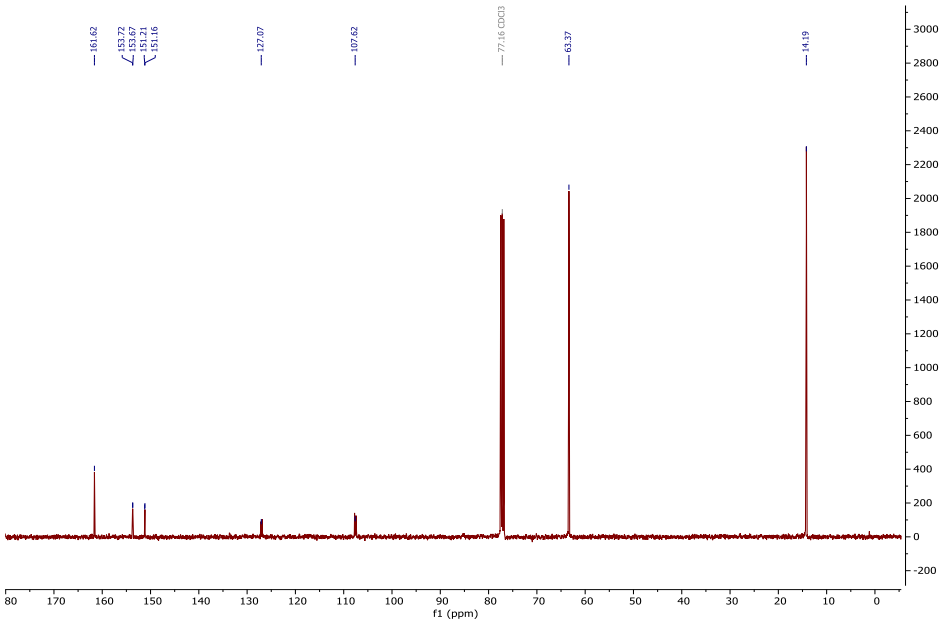


Figure A2: *^{13}C NMR of diethyl 2,5-dibromo-3,6-difluoroterephthalate* ***([2])*** *in $CDCl_3$.*

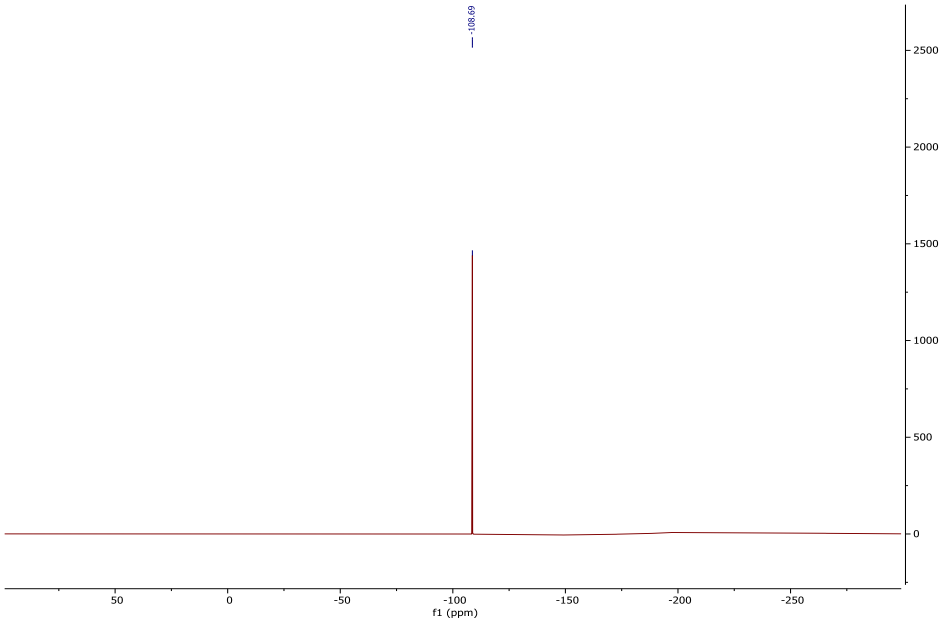


Figure A3: *^{19}F NMR of diethyl 2,5-dibromo-3,6-difluoroterephthalate (**[2]**) in $CDCl_3$.*

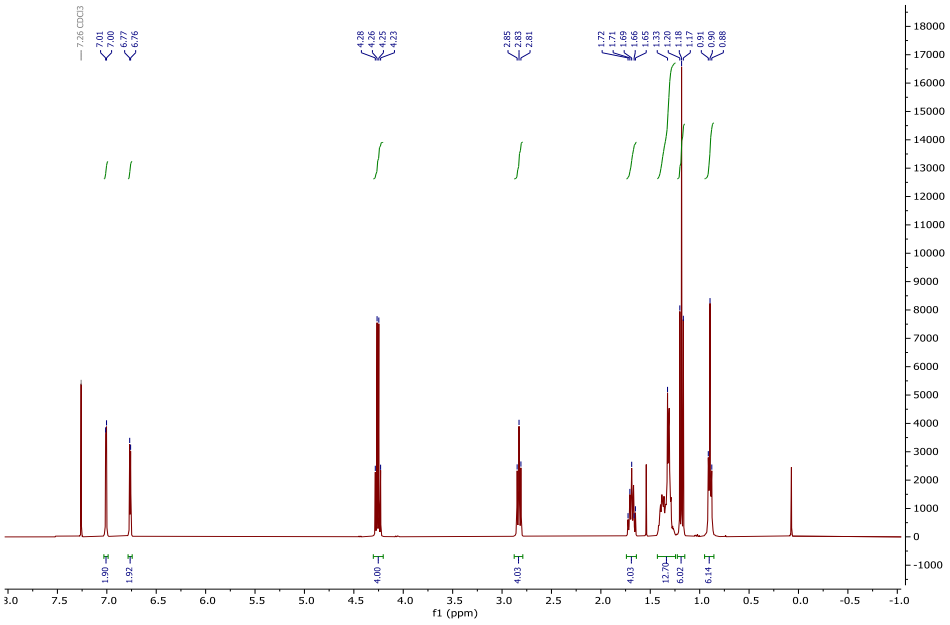


Figure A4: *^{1}H NMR of diethyl 2,5-difluoro-3,6-bis(5-hexylthiophen-2-yl)terephthalate (**[4]**) in $CDCl_3$.*

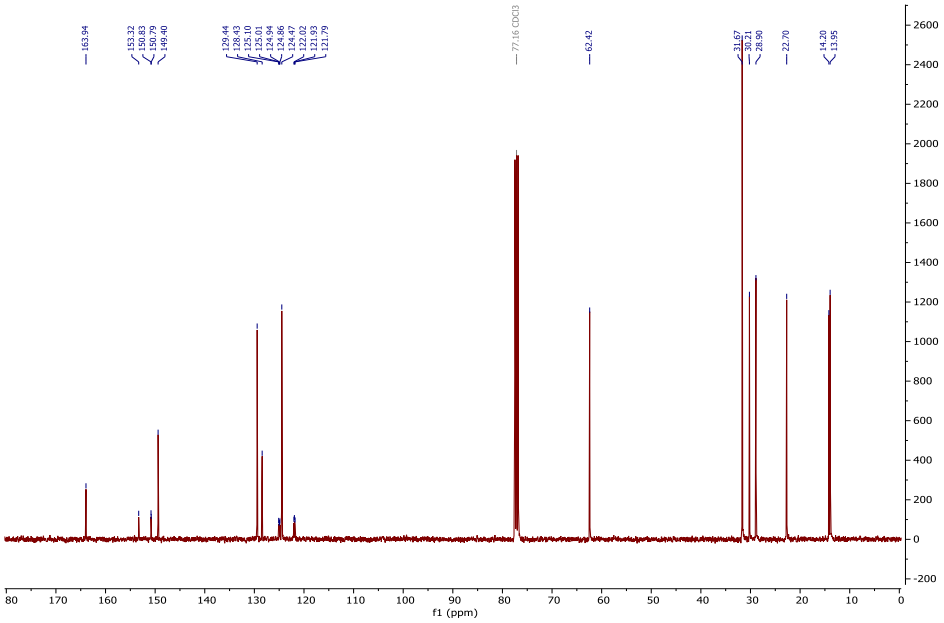


Figure A5: *^{13}C NMR of diethyl 2,5-difluoro-3,6-bis(5-hexylthiophen-2-yl)terephthalate (**[4]**) in $CDCl_3$.*

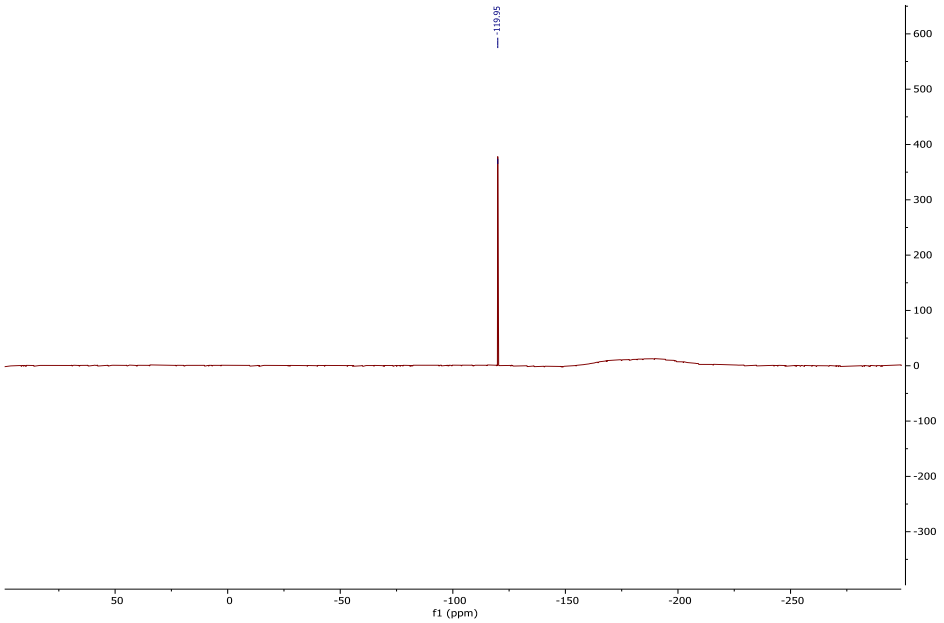


Figure A6: *^{19}F NMR of diethyl 2,5-difluoro-3,6-bis(5-hexylthiophen-2-yl)terephthalate (**[4]**) in $CDCl_3$.*

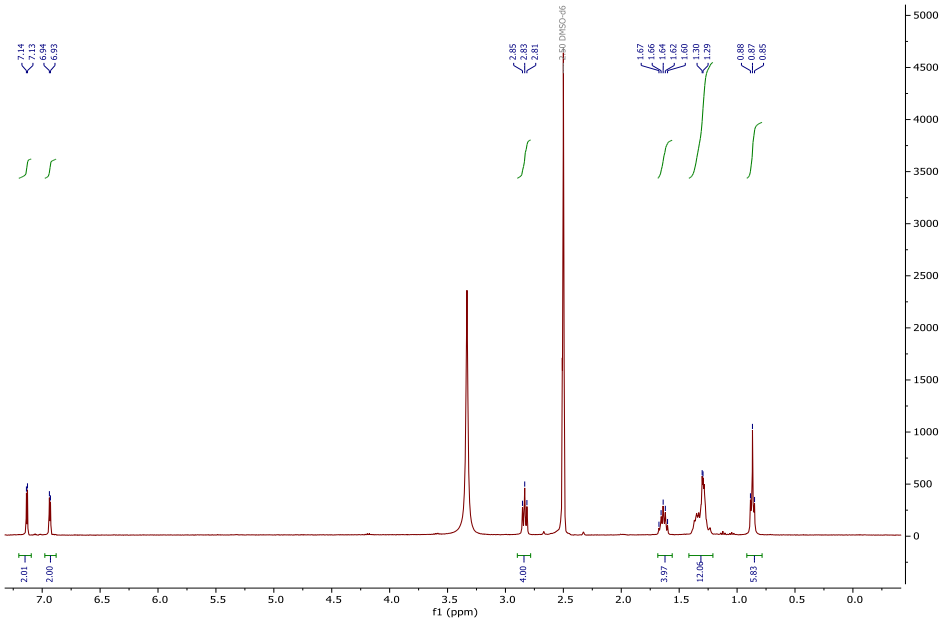


Figure A7: *^{1}H NMR of 2,5-bis(5-hexylthiophen-2-yl)-3,6-difluoroterephthalic acid (**[5]**) in DMSO-d_6.*

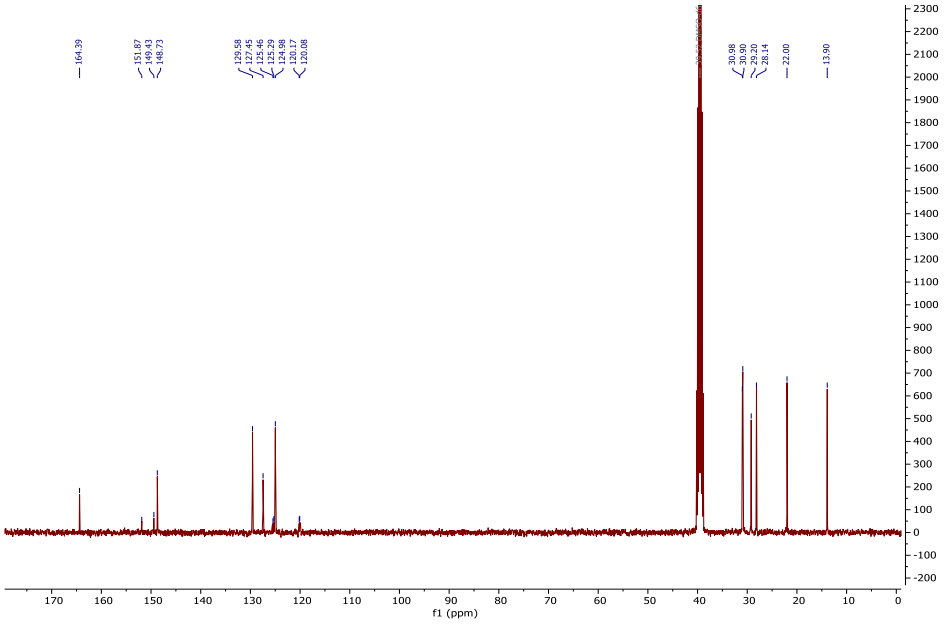


Figure A8: *^{13}C NMR of 2,5-bis(5-hexylthiophen-2-yl)-3,6-difluoroterephthalic acid (**[5]**) in DMSO-d_6.*

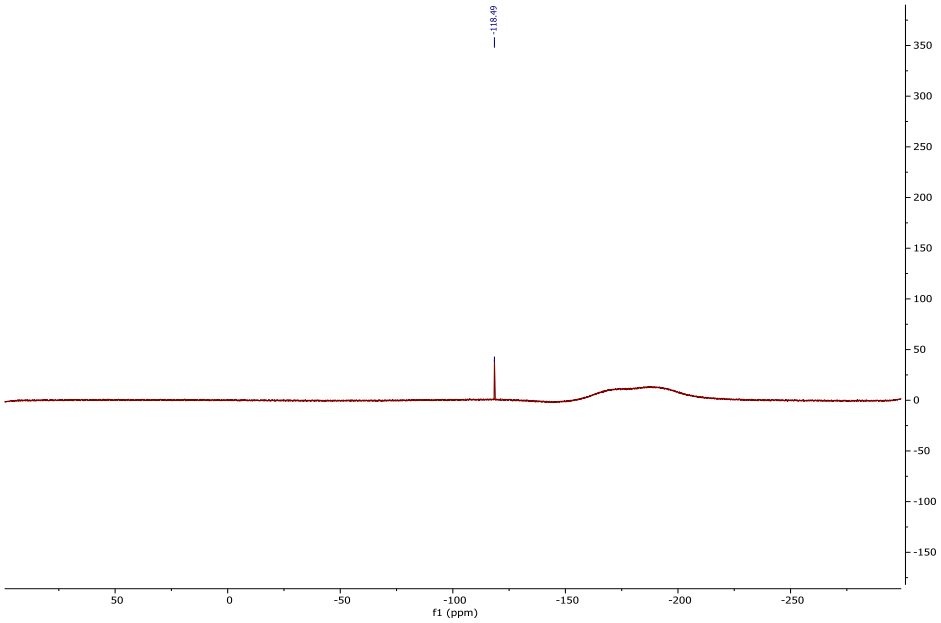


Figure A9: *^{19}F NMR of 2,5-bis(5-hexylthiophen-2-yl)-3,6-difluoroterephthalic acid (**[5]**) in $CDCl_3$.*

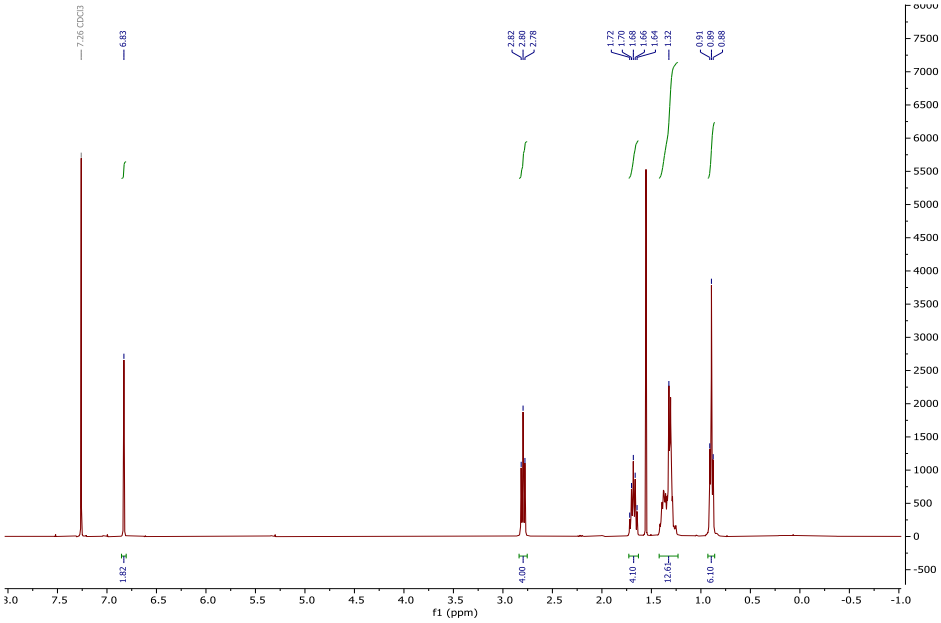


Figure A10: *^{1}H NMR of 2,7-dihexyl-5,10-difluoro-s-indaceno[1,2-b:5,6-b']dithiophene-4,9-dione (**2,7-dihexyl-diFIDT-di(O)**) in $CDCl_3$.*

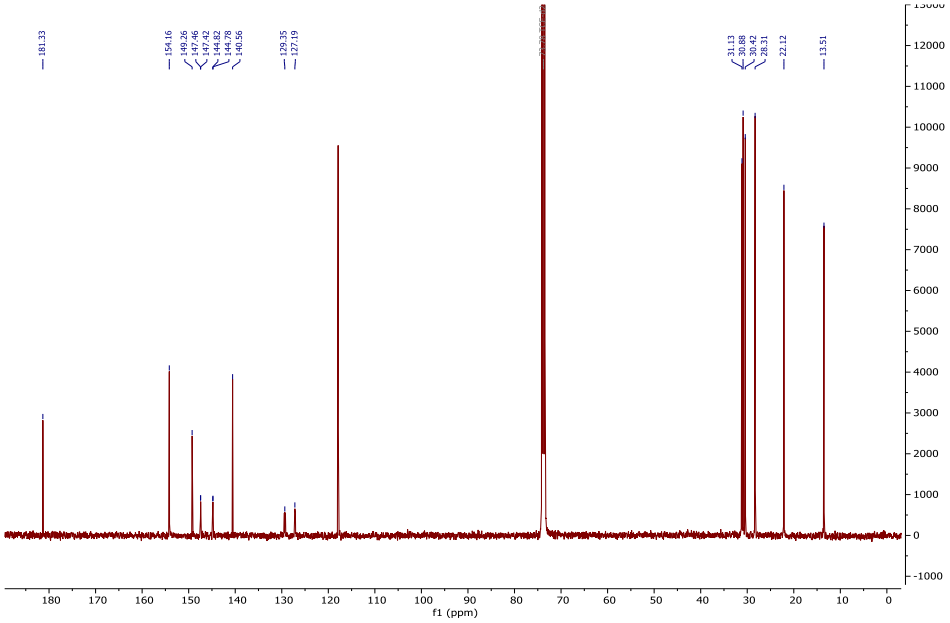


Figure A11: *^{13}C NMR of 2,7-dihexyl-5,10-difluoro-s-indaceno[1,2-b:5,6-b']dithiophene-4,9-dione (**2,7-dihexyl-diFIDT-di(O)**) in TCE-d_2 at 120 °C.*

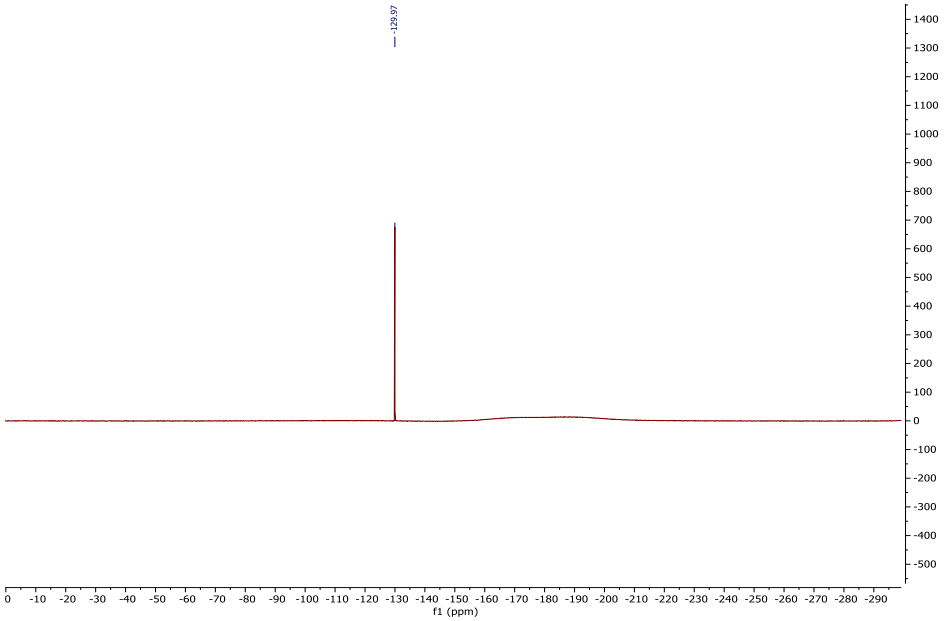


Figure A12: *^{19}F NMR of 2,7-dihexyl-5,10-difluoro-s-indaceno[1,2-b:5,6-b']dithiophene-4,9-dione (**2,7-dihexyl-diFIDT-di(O)**) in $CDCl_3$.*

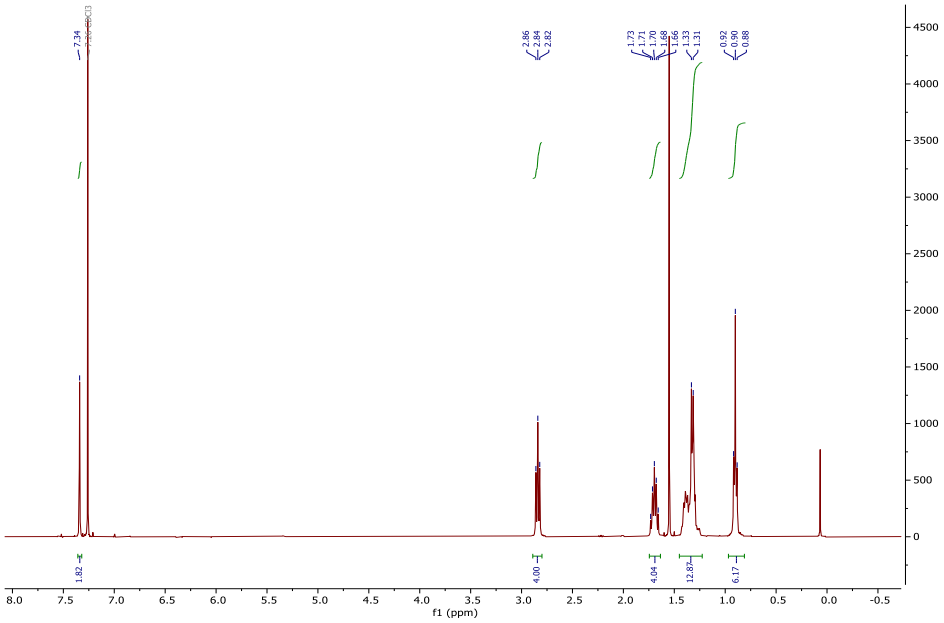


Figure A13: *^{1}H NMR of 2,2'-(5,10-difluoro-2,7-dihexyl-s-indaceno[1,2-b:5,6-b']dithiophene-4,9-diylidene)dimalononitrile (**2,7-dihexyl-diFIDT-di(C(CN)$_2$)**) in $CDCl_3$.*

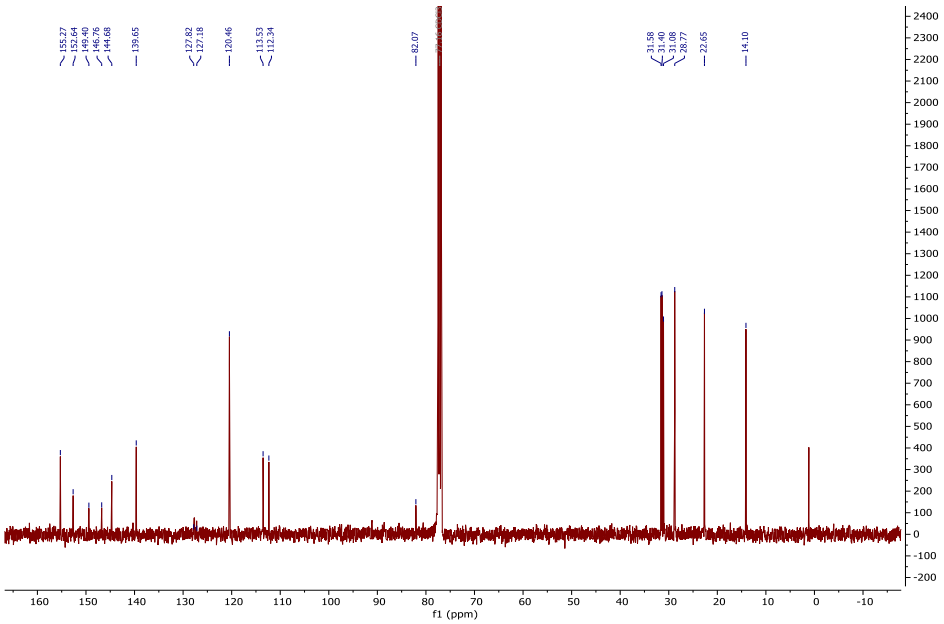


Figure A14: *^{13}C NMR of 2,2'-(5,10-difluoro-2,7-dihexyl-s-indaceno[1,2-b:5,6-b']dithiophene-4,9-diylidene)dimalononitrile (**2,7-dihexyl-diFIDT-di(C(CN)$_2$)**) in $CDCl_3$ at 50 °C.*

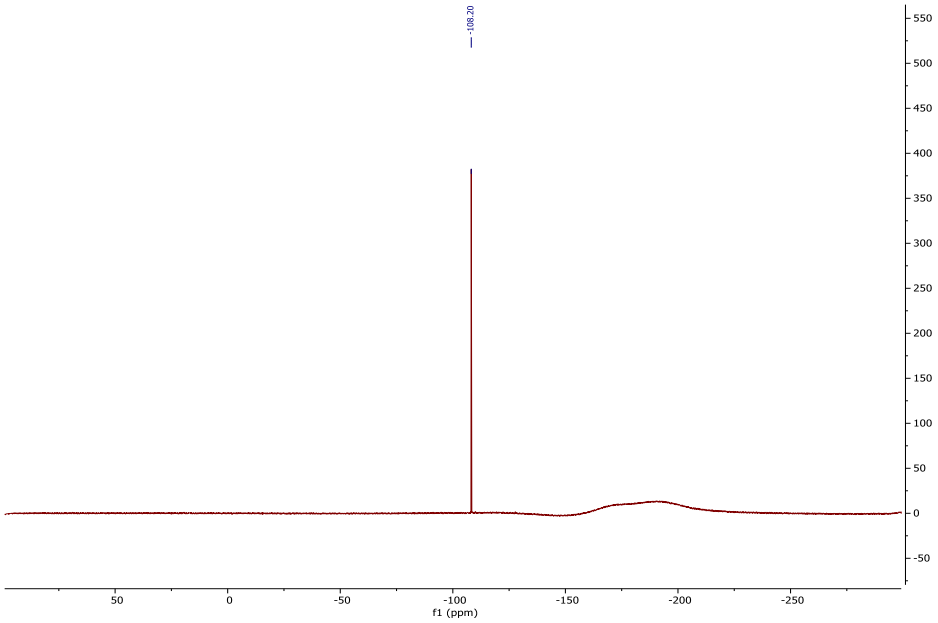


Figure A15: *^{19}F NMR of 2,2'-(5,10-difluoro-2,7-dihexyl-s-indaceno[1,2-b:5,6-b']dithiophene-4,9-diylidene)dimalononitrile (**2,7-dihexyl-diFIDT-di(C(CN)$_2$)**) in $CDCl_3$.*

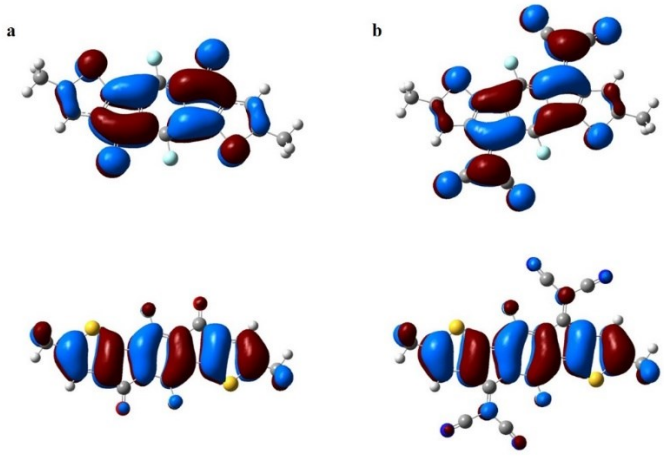
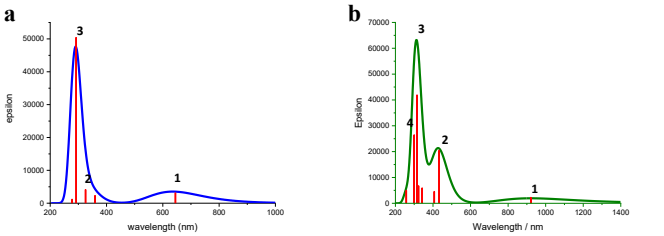


Figure A16: *Calculated HOMO (bottom) and LUMO (top) distributions for a) **diFIDT-di(O)** and b) **diFIDT-di(C(CN)$_2$)**, calculated by B3LYP/6-311+G(d,p).*



a)
1. HOMO→LUMO, 659 nm, f = 0.074
2. HOMO-7→LUMO, 327 nm, f = 0.097
   HOMO-3→LUMO
   HOMO→LUMO+2
3. HOMO-2→LUMO, 296 nm, f = 1.191
   HOMO-3→LUMO
   HOMO→LUMO+2

b)
1. HOMO→LUMO, 921 nm, f = 0.048
2. HOMO-2→LUMO, 433 nm, f = 0.439
   HOMO-1→LUMO+1
3. HOMO-5→LUMO, 315 nm, f = 0.898
   HOMO-4→LUMO
   HOMO→LUMO+2
4. HOMO-5→LUMO, 300 nm, f = 0.568
   HOMO-3→LUMO+1
   HOMO-1→LUMO+2
   HOMO→LUMO+2

Figure A17: *Predicted UV-vis spectra from TD-DFT energy calculations of a)* ***2,7-dialkyl-diFIDT-di(O)*** *and b)* ***2,7-dialkyl-diFIDT-di(C(CN)$_2$)*** *after geometry optimisation with DFT B3LYP/6-311+G(d,p), with selected excitations highlighted.*

The X-ray crystal structure of 2,7-dihexyl-diFIDT-di(O)

Crystal data for **2,7-dihexyl-diFIDT-di(O)**: $C_{28}H_{28}F_2O_2S_2$, M = 498.62, triclinic, P-1 (no. 2), a = 5.5764(5), b = 6.2336(4), c = 17.5850(16) Å, α = 93.089(6), β = 95.200(7), γ = 94.105(6)°, V = 606.06(8) Å^3, Z = 1 [Ci symmetry], D_c = 1.366 g cm–3, μ(Cu-Kα) = 2.323 mm–1, T = 173 K, blue/brown dichroic thin platy needles, Agilent Xcalibur PX Ultra A diffractometer; 2296 independent measured reflections (R_{int} = 0.0323), F^2 refinement,[^{X1,X2}] R_1(obs) = 0.0609, wR_2(all) = 0.1884, 1620 independent observed absorption-corrected reflections [$|F_o| > 4\sigma(|F_o|)$, completeness to θ_{full}(67.7°) = 98.4%], 155 parameters. CCDC 1965409.

The structure of **diFIDT-di(O)** was found to sit across a centre of symmetry at the middle of the central C_6F_2 ring.

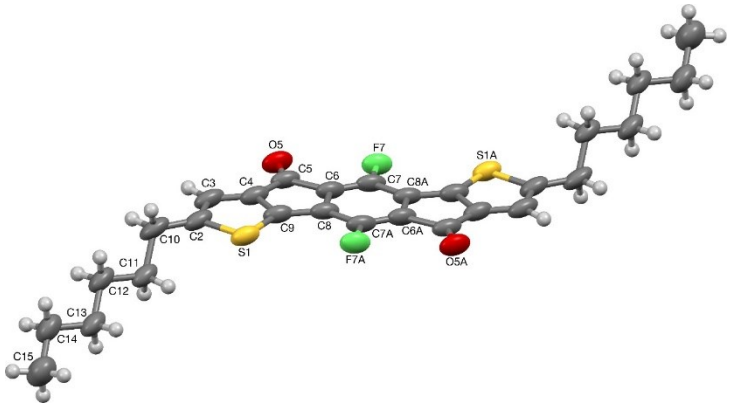


***Figure A18**: The crystal structure of **2,7-dihexyl-diFIDT-di(O)** (50 % probability ellipsoids). The molecule sits across a centre of symmetry at the middle of the central C_6F_2 ring.*

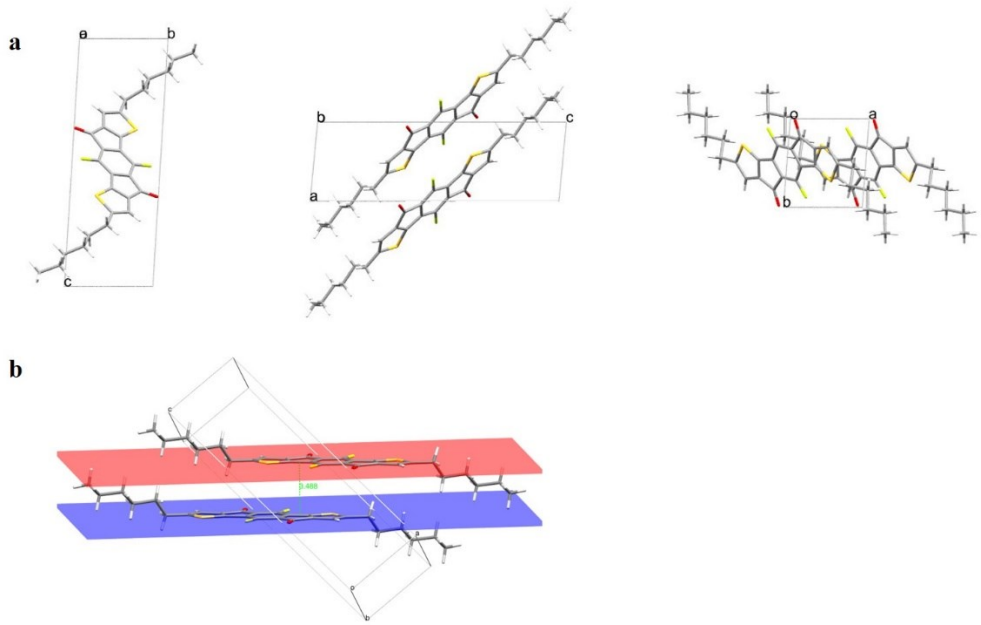
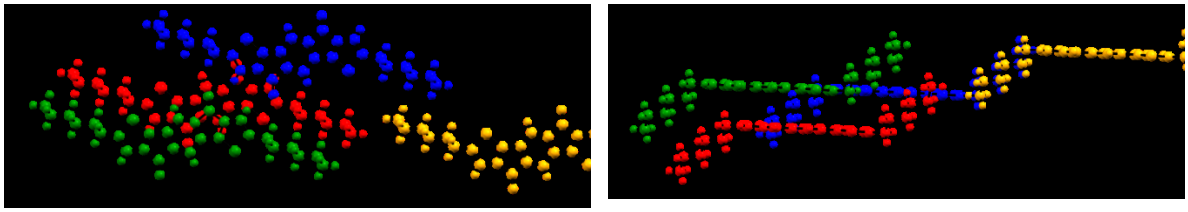
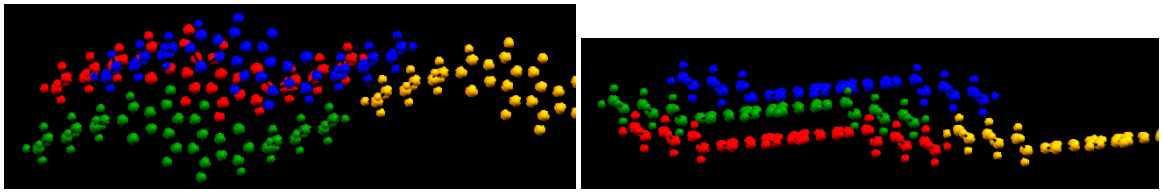


***Figure A19:** a) Unit cell of **2,7-dihexyl-diFIDT-di(O)** as viewed along the a-, b- and c-axes (left to right). b) Interplanar stacking distance.*



IDT-di(O)						
Crystal	X	ES	EX	IND	DISP	TOT
Blue/Green	H	-7.7	8.1	-2.5	-6.3	-8.4
Blue/Green	F	-8.0	8.0	-2.5	-6.3	-8.9
Blue/Red	H	-5.1	13.4	-2.0	-20.6	-14.3
Blue/Red	F	-7.9	19.3	-2.8	-22.2	-13.6
Red/Green	H	-7.5	20.0	-2.4	-30.3	-20.1
Red/Green	F	-7.1	19.6	-2.6	-30.6	-20.8

Figure A20: *SAPT0 energies for selective dimers of* ***2,7-dihexyl-IDT-di(O)*** *and* ***2,7-dihexyl-diFIDT-di(O)*** *in the* ***2,7-dihexyl-IDT-di(O)*** *crystal packing motif.*



diFIDT-di(O)						
Crystal	X	ES	EX	IND	DISP	TOT
Blue/Green	H	-7.0	12.6	-3.0	-15.7	-13.1
Blue/Green	F	-7.7	14.6	-3.4	-16.6	-13.2
Blue/Red	H	-9.5	24.7	-2.5	-36.1	-23.3
Blue/Red	F	-9.1	24.2	-2.7	-36.0	-23.6
Red/Green	H	-3.2	12.1	-2.0	-16.4	-9.5
Red/Green	F	-6.0	13.4	-2.1	-17.3	-11.9

Figure A21: *SAPT0 energies for selective dimers of* ***IDT-di(O)*** *and* ***diFIDT-di(O)*** *in the* ***diFIDT-di(O)*** *crystal packing motif.*

The X-ray crystal structure of 2,7-dihexyl-diFIDT-di(C(CN)$_2$)

Crystal data for **2,7-dihexyl-diFIDT-di(C(CN)$_2$)**: $C_{34}H_{28}F_2N_4S_2$, M = 594.72, monoclinic, $P2_1/n$ (no. 14), a = 10.9141(6), b = 4.5996(2), c = 29.1554(12) Å, β = 97.533(4)°, V = 1450.99(12) Å^3, Z = 2 [C_i symmetry], D_c = 1.361 g cm^{-3}, μ(Cu-Kα) = 2.027 mm^{-1}, T = 173 K, lustrous dark bronze platy needles, Agilent Xcalibur PX Ultra A diffractometer; 2787 independent measured reflections (R_{int} = 0.0611), F^2 refinement,[X1,X2] R_1(obs) = 0.0589, wR_2(all) = 0.1748, 1910 independent observed absorption-corrected reflections [$|F_o| > 4\sigma(|F_o|)$, completeness to θ_{full}(67.7°) = 98.6%], 191 parameters. CCDC 1965410.

The structure of **diFIDT-di(C(CN)$_2$)** was found to sit across a centre of symmetry at the middle of the central C_6F_2 ring.

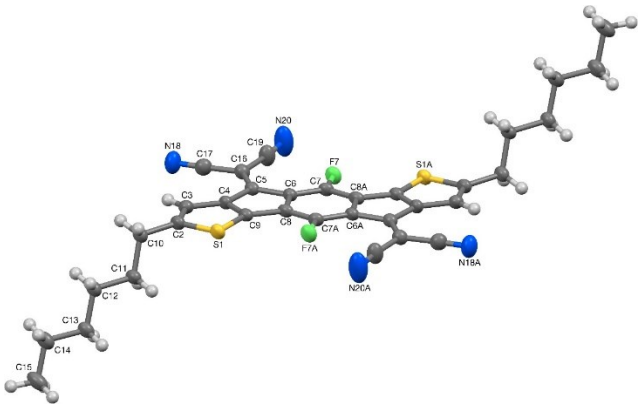


Figure A22: *The crystal structure of* ***2,7-dihexyl-diFIDT-di(C(CN)$_2$)*** *(50 % probability ellipsoids). The molecule sits across a centre of symmetry at the middle of the central C_6F_2 ring.*

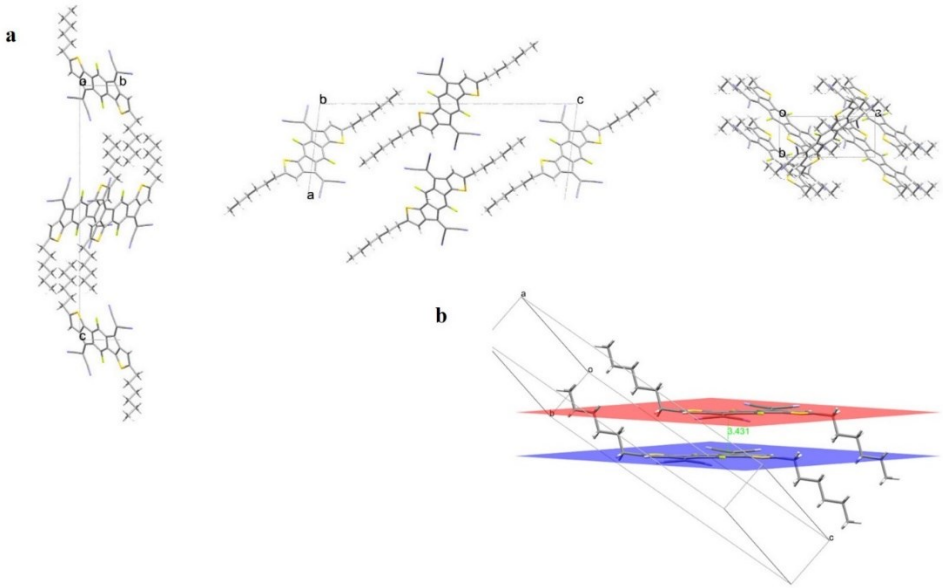
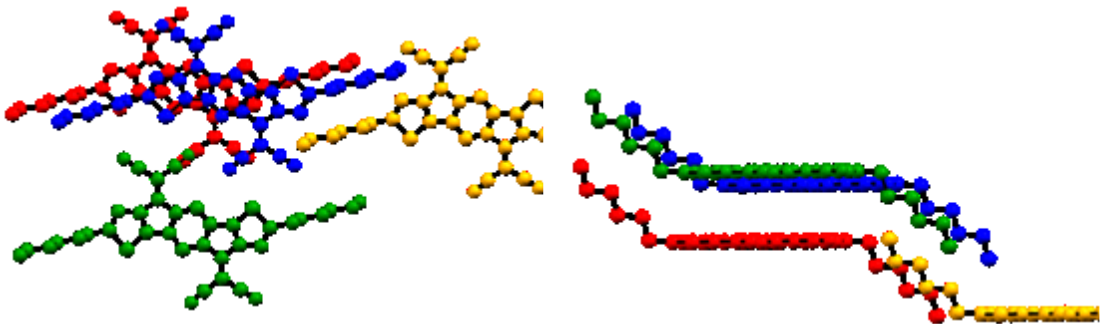
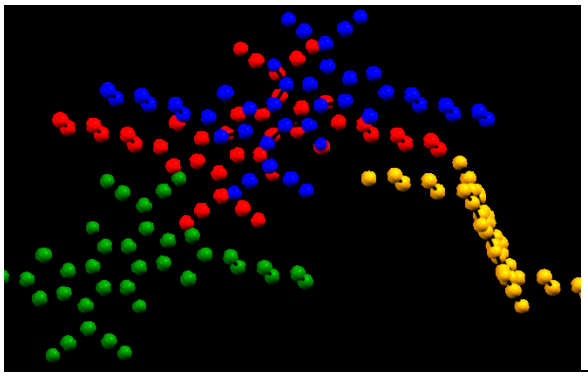


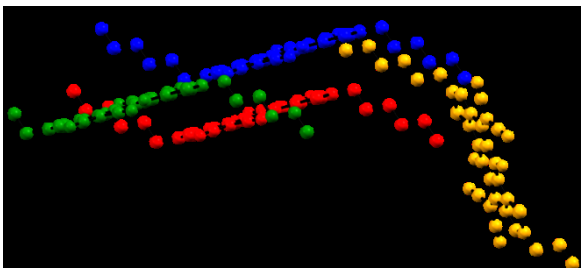
Figure A23: *a) Unit cell of* ***2,7-dihexyl-diFIDT-di(C(CN)$_2$)*** *as viewed along the a-, b- and c-axes (left to right). b) Interplanar stacking distance.*



2,7-dihexyl-IDT-di(C(CN)$_2$) **Crystal**	X	ES	EX	IND	DISP	TOT
Blue/Green	H	-12.0	17.1	-3.3	-14.9	-13.1
Blue/Green	F	-12.3	31.3	-3.6	-16.6	-1.3
Blue/Red	H	-10.1	30.3	-3.2	-50.6	-33.7
Blue/Red	F	-8.8	29.7	-3.5	-50.7	-33.3
Red/Green	H	-1.2	0.1	-0.1	-1.8	-3.1
Red/Green	F	-1.4	0.1	-0.2	-1.9	-3.3

Figure A24: *SAPT0 energies for selective dimers of* ***2,7-dihexyl-IDT-di(C(CN)$_2$)*** *and* ***2,7-dihexyl-diFIDT-di(C(CN)$_2$)*** *in the* ***2,7-dihexyl-IDT-di(C(CN)$_2$)*** *crystal packing motif.*





2,7-dihexyl-diFIDT-di(C(CN)$_2$) Crystal	X	ES	EX	IND	DISP	TOT
Blue/Green	H	-5.9	5.7	-1.6	-6.2	-7.9
Blue/Green	F	-6.0	5.7	-1.6	-6.2	-8.1
Blue/Red	H	-12.3	37.5	-3.9	-56.1	-34.7
Blue/Red	F	-11.3	36.8	-4.2	-56.3	-35.0
Red/Green	H	-5.0	8.9	-1.6	-12.9	-10.7
Red/Green	F	-5.6	8.9	-1.7	-13.0	-11.4

Figure A25: *SAPT0 energies for selective dimers of* ***2,7-dihexyl-IDT-di(C(CN)$_2$)*** *and* ***diFIDT-di(C(CN)$_2$)*** *in the* ***diFIDT-di(C(CN)$_2$)*** *crystal packing motif.*

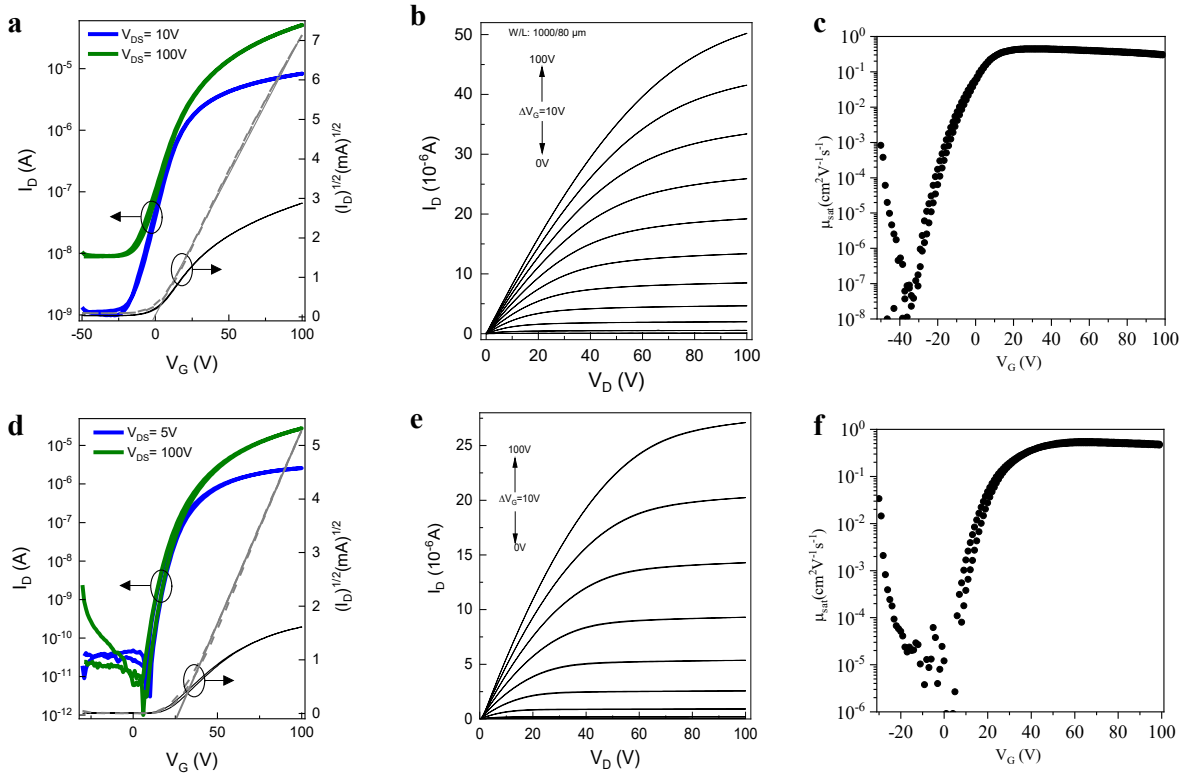


Figure A26: *Device data for best performing BC-TG blade-coated devices of* ***2,7-dihexyl-diFIDT-diC(CN)$_2$****. a-c) highest mobility device. d-f) low threshold voltage device.*

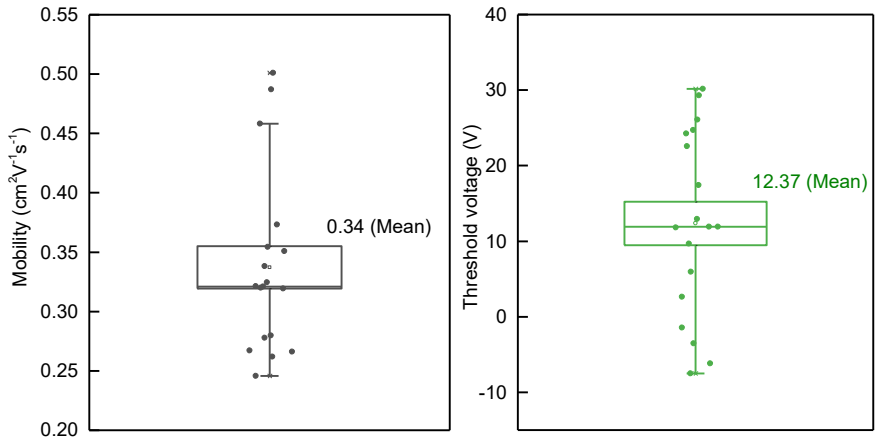


Figure A27: *Statistical distribution of electron mobility (left) and threshold voltage (right) extracted from 18 BC-TG OTFTs based on blade-coated* ***2,7-dihexyl-diFIDT-di(C(CN)$_2$)*** *layers that have been post-annealed at 100°C and tested in N_2.*

10.2 Chapter 3

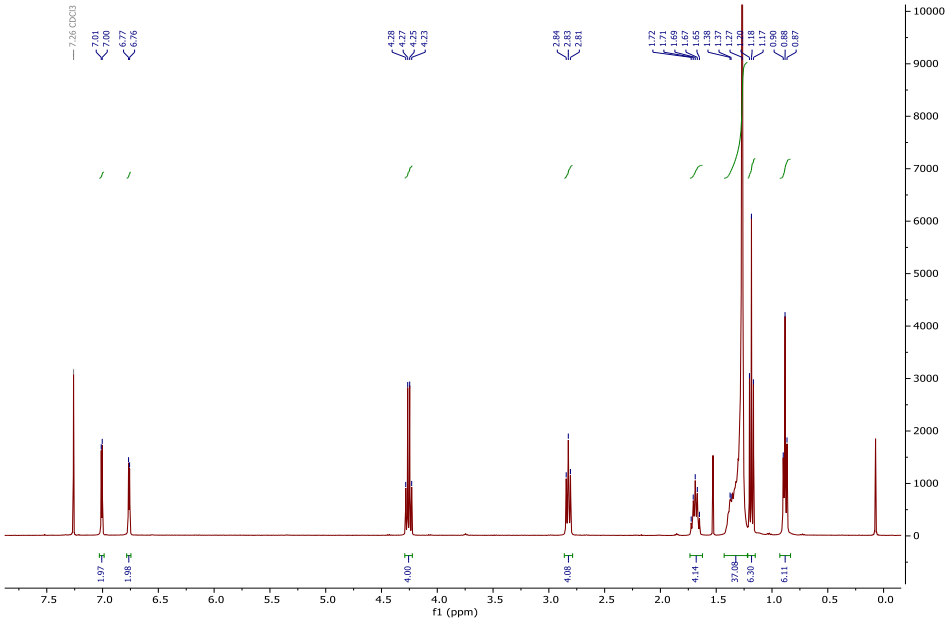


Figure A28: *[1]H NMR of diethyl 2,5-difluoro-3,6-bis(5-dodecylthiophen-2-yl)terephthalate in $CDCl_3$.*

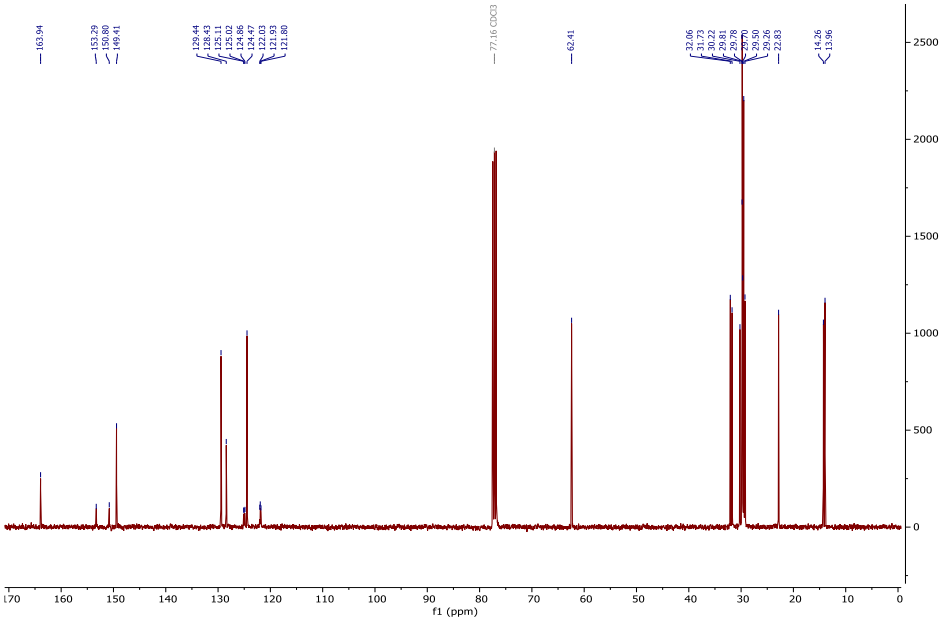


Figure A29: *[13]C NMR of diethyl 2,5-difluoro-3,6-bis(5-dodecylthiophen-2-yl)terephthalate in $CDCl_3$.*

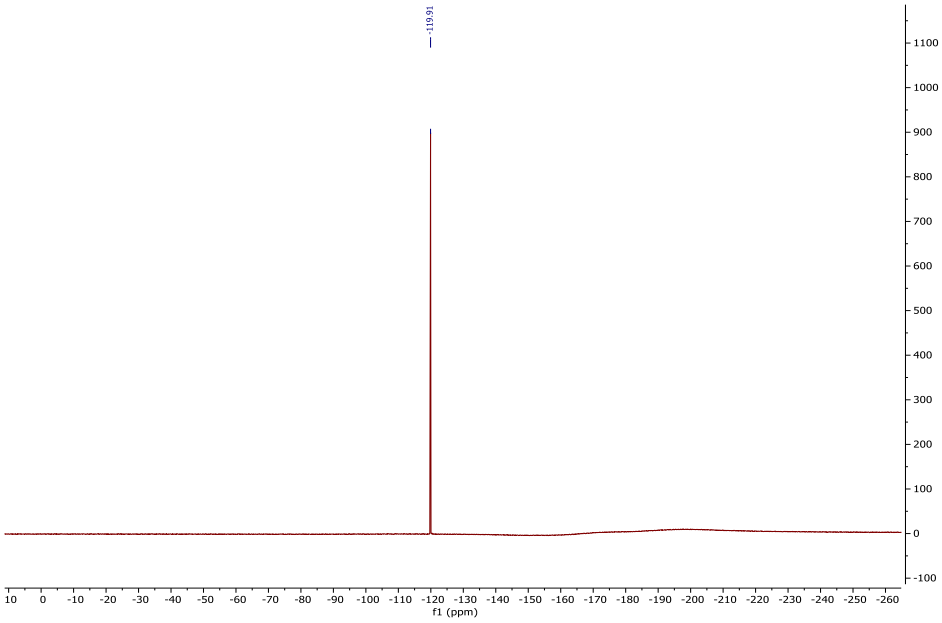


Figure A30: *[19]F NMR of diethyl 2,5-difluoro-3,6-bis(5-dodecylylthiophen-2-yl)terephthalate in $CDCl_3$.*

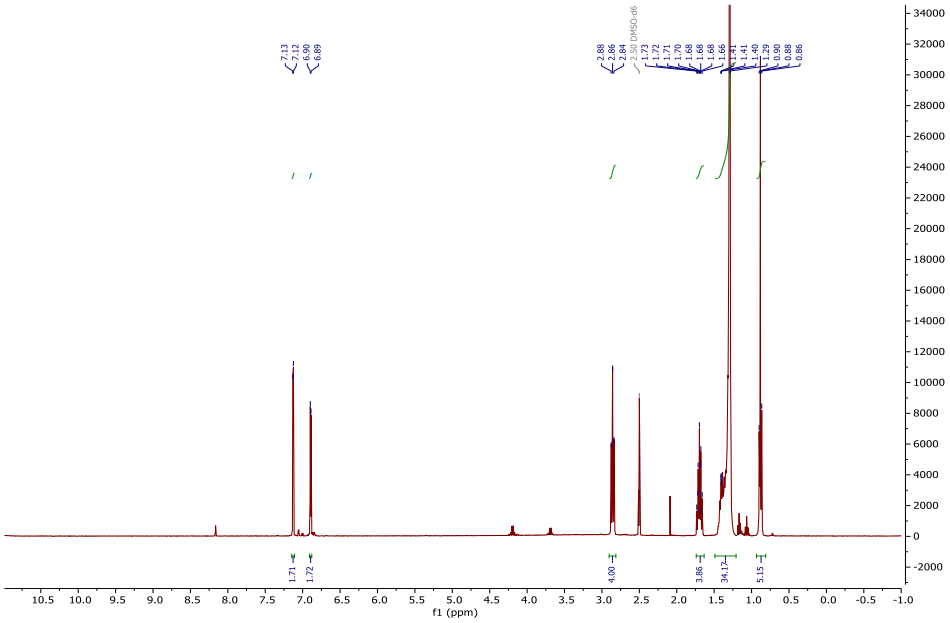


Figure A31: *[1]H NMR of 2,5-bis(5-dodecylthiophen-2-yl)-3,6-difluoroterephthalic acid in DMSO-d_6* at 120 °C.

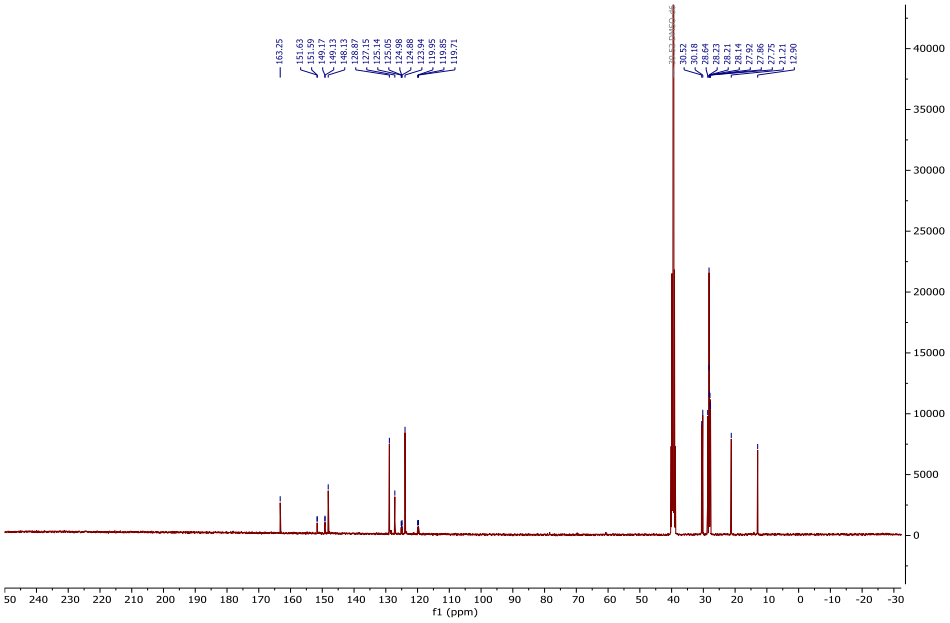


Figure A32: *^{13}C NMR of 2,5-bis(5-dodecylthiophen-2-yl)-3,6-difluoroterephthalic acid in DMSO-d_6* at 120 °C.

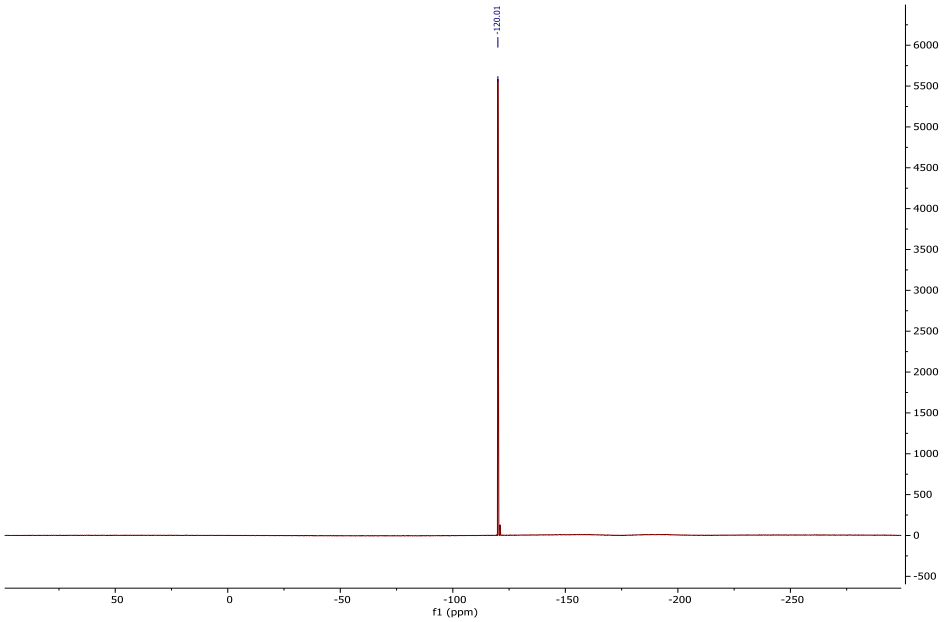


Figure A33: *^{19}F NMR of 2,5-bis(5-dodecylthiophen-2-yl)-3,6-difluoroterephthalic acid in DMSO-d_6* at 120 °C.

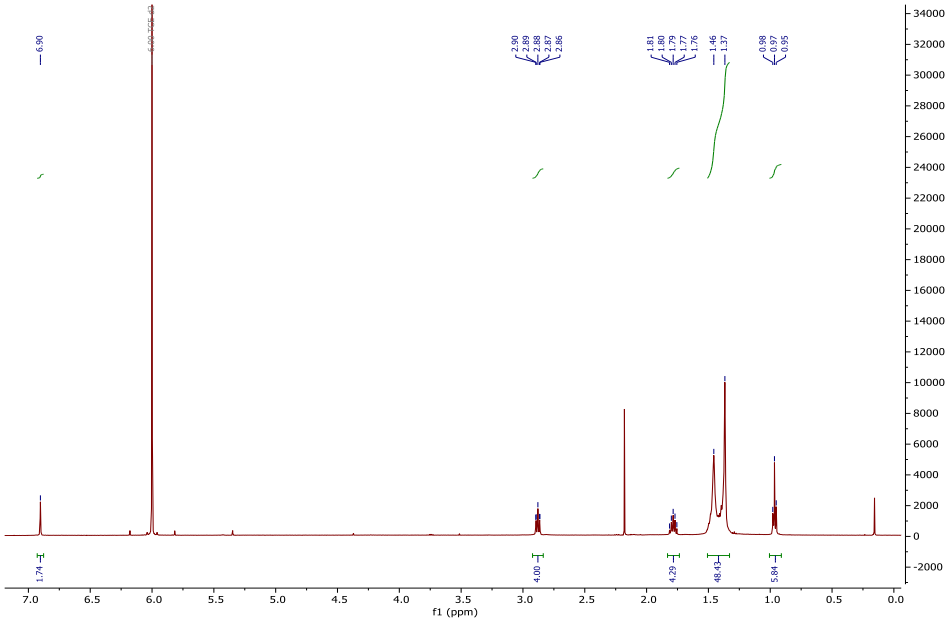


Figure A34: *^{1}H NMR of 2,7-didodecyl-5,10-difluoro-s-indaceno[1,2-b:5,6-b']dithiophene-4,9-dione (**2,7-didodecyl-diFIDT-di(O)**) in TCE-d_2 at 120 °C.*

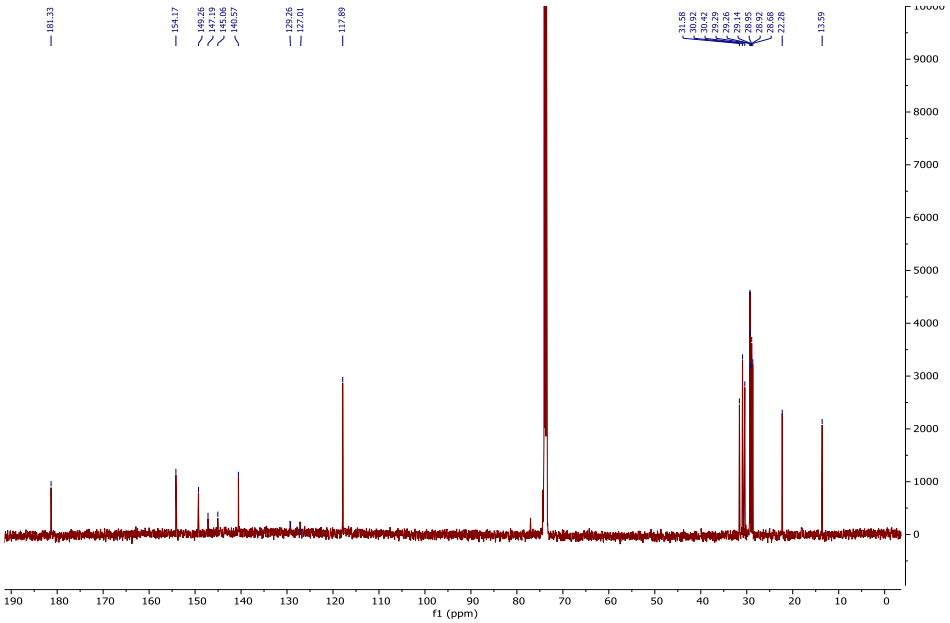


Figure A35: *^{13}C NMR of 2,7-didodecyl-5,10-difluoro-s-indaceno[1,2-b:5,6-b']dithiophene-4,9-dione (**2,7-didodecyl-diFIDT-di(O)**) in TCE-d_2 at 120 °C.*

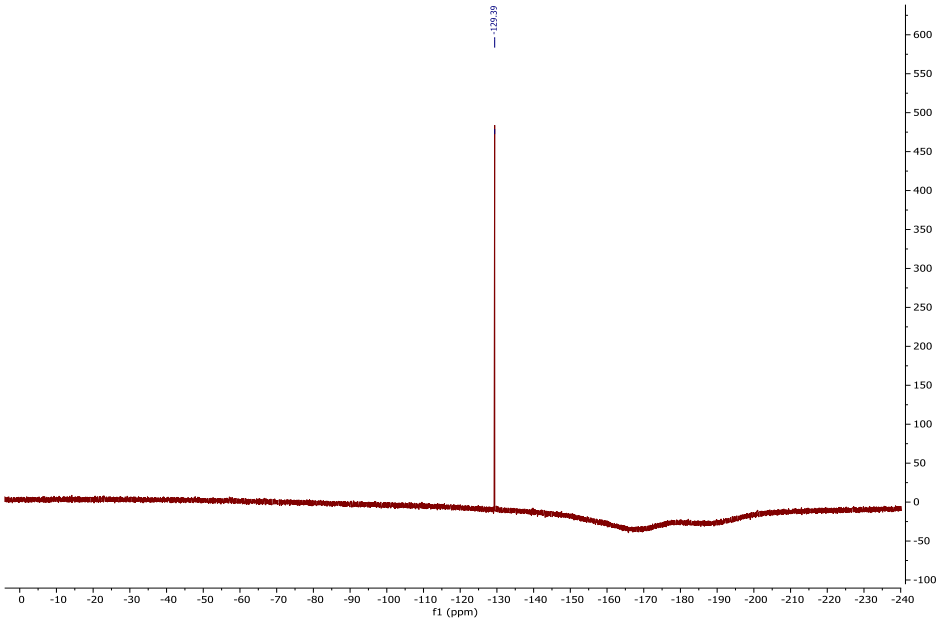


Figure A36: *^{19}F NMR of 2,7-didodecyl-5,10-difluoro-s-indaceno[1,2-b:5,6-b']dithiophene-4,9-dione (**2,7-didodecyl-diFIDT-di(O)**) in TCE-d_2 at 120 °C.*

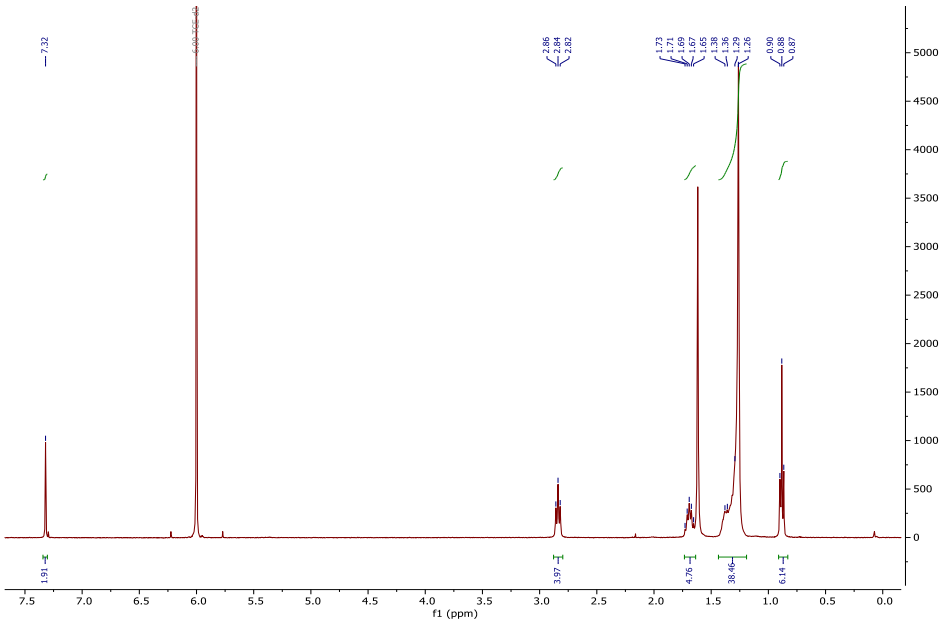


Figure A37: *^{1}H NMR of 2,2'-(5,10-difluoro-2,7-didodecyl-s-indaceno[1,2-b:5,6-b']dithiophene-4,9-diylidene)dimalononitrile (**2,7-didodecyl-diFIDT-di(C(CN)$_2$)**) in TCE-d_2 at 120 °C.*

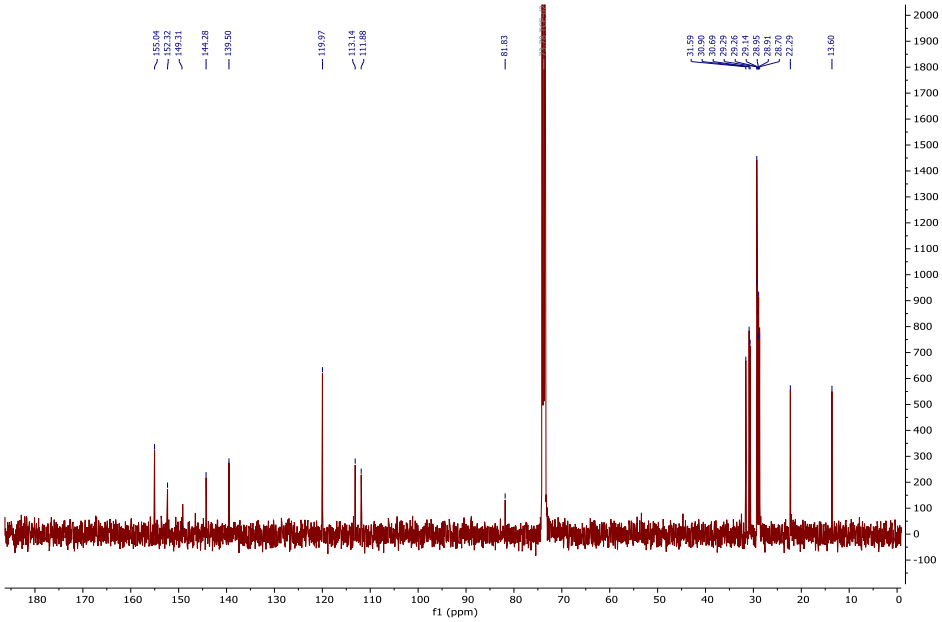


Figure A38: *^{13}C NMR of 2,2'-(5,10-difluoro-2,7-didodecyl-s-indaceno[1,2-b:5,6-b']dithiophene-4,9-diylidene)dimalononitrile (**2,7-didodecyl-diFIDT-di(C(CN)$_2$)**) in TCE-d$_2$ at 120 °C.*

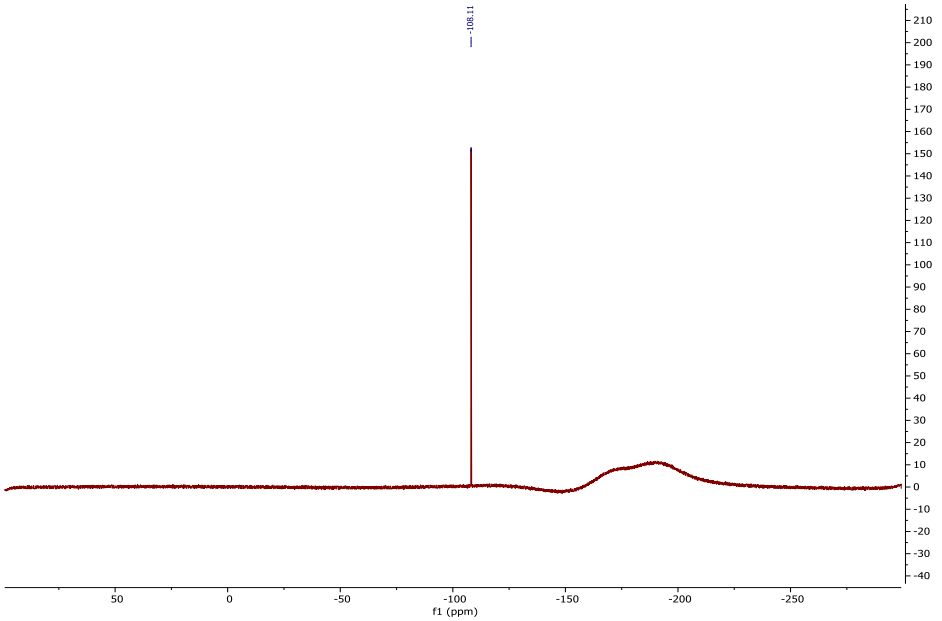


Figure A39: *^{19}F NMR of 2,2'-(5,10-difluoro-2,7-didodecyl-s-indaceno[1,2-b:5,6-b']dithiophene-4,9-diylidene)dimalononitrile (**2,7-didodecyl-diFIDT-di(C(CN)$_2$)**) in TCE-d$_2$ at 120 °C.*

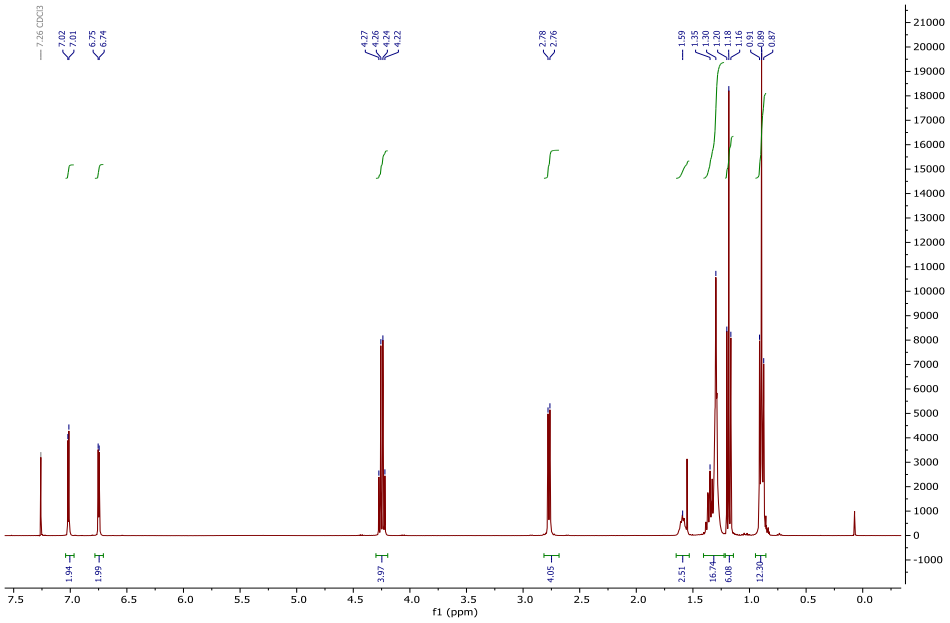


Figure A40: *^{1}H NMR of diethyl 2,5-difluoro-3,6-bis(5-(2-ethylhexyl)thiophen-2-yl)terephthalate in $CDCl_3$.*

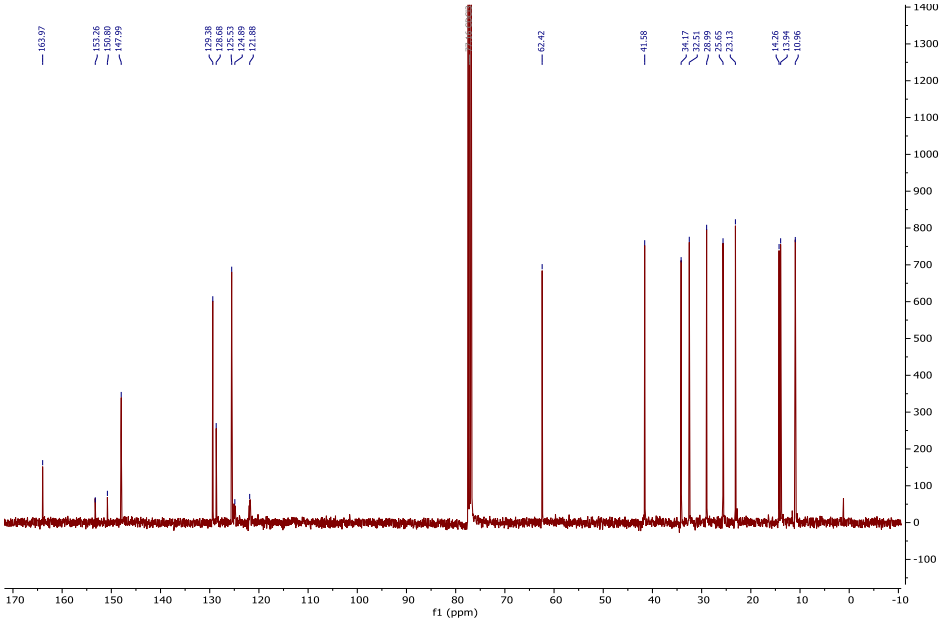


Figure A41: *^{13}C NMR of diethyl 2,5-difluoro-3,6-bis(5-(2-ethylhexyl)thiophen-2-yl)terephthalate in $CDCl_3$.*

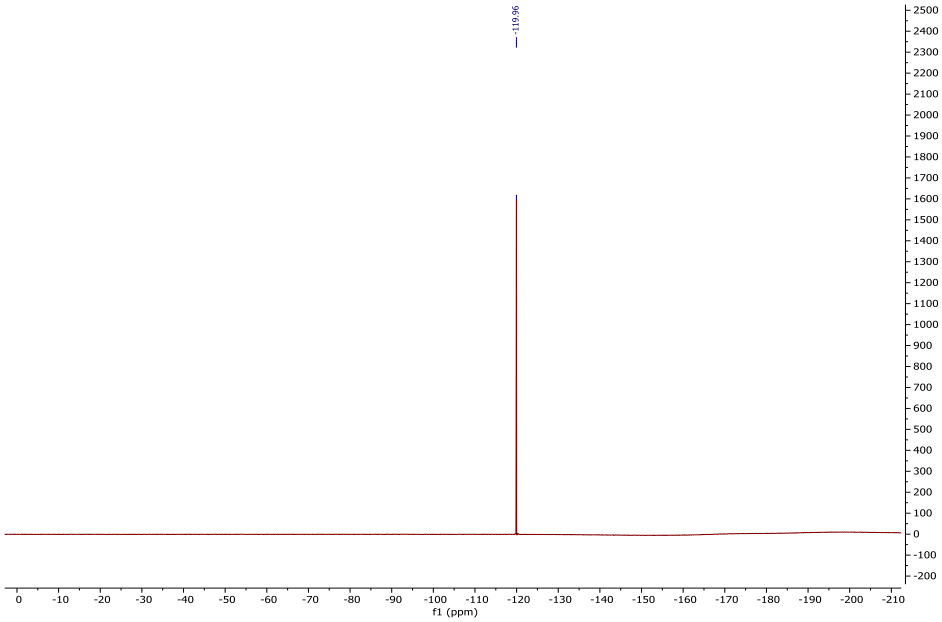


Figure A42: *^{19}F NMR of diethyl 2,5-difluoro-3,6-bis(5-(2-ethylhexyl)thiophen-2-yl)terephthalate in $CDCl_3$.*

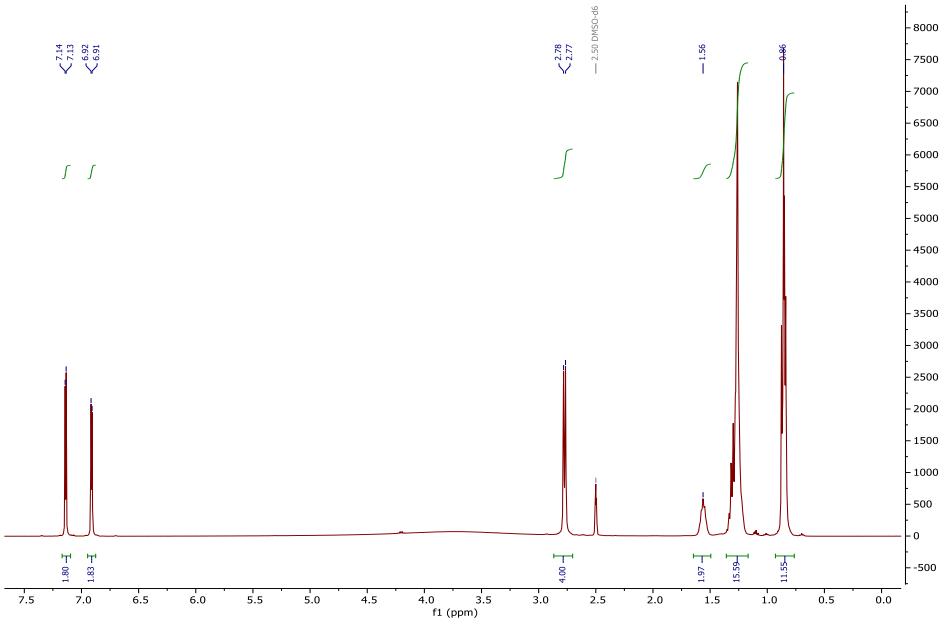


Figure A43: *^{1}H NMR of 2,5-bis(5-(2-ethylhexyl)thiophen-2-yl)-3,6-difluoroterephthalic acid in DMSO-d_6.*

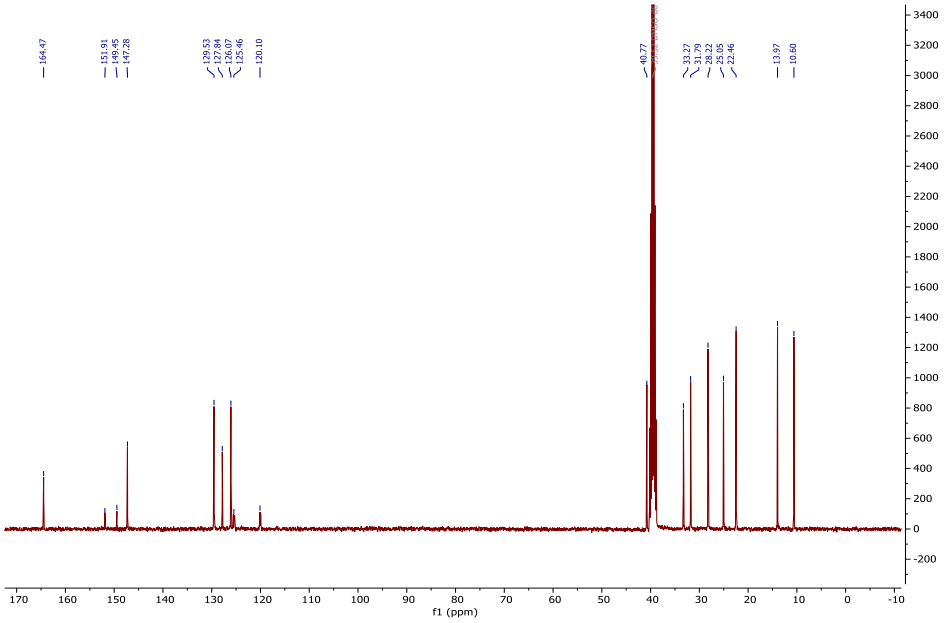


Figure A44: *^{13}C NMR of 2,5-bis(5-(2-ethylhexyl)thiophen-2-yl)-3,6-difluoroterephthalic acid in DMSO-d_6.*

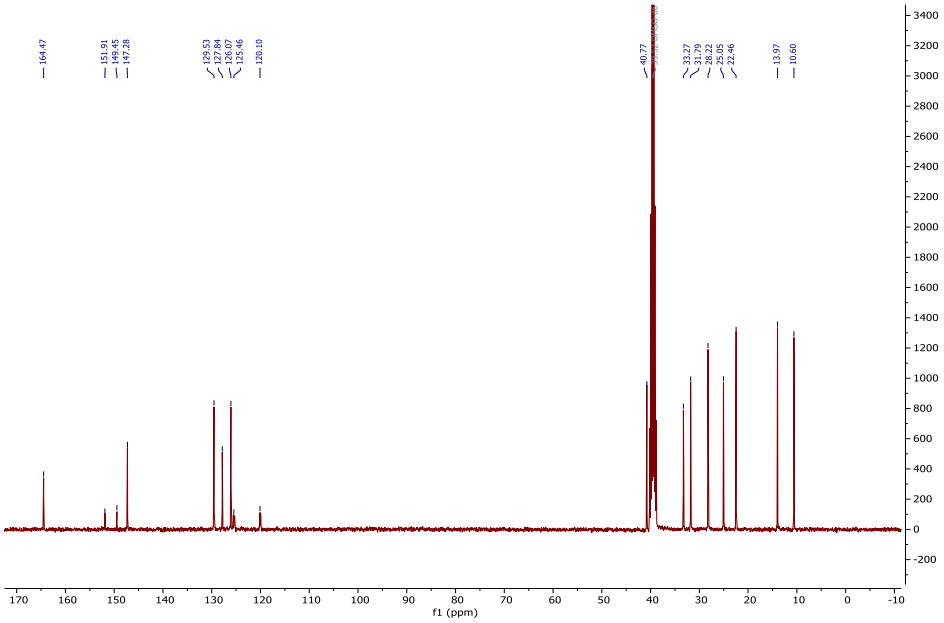


Figure A45: *^{19}F NMR of 2,5-bis(5-(2-ethylhexyl)thiophen-2-yl)-3,6-difluoroterephthalic acid in DMSO-d_6.*

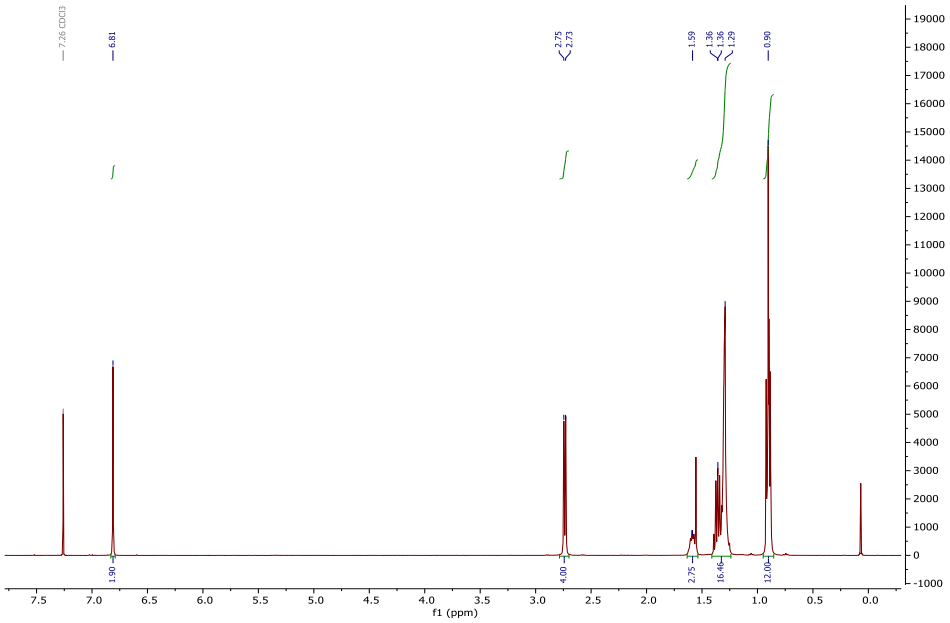


Figure A46: *^{1}H NMR of 2,7-bis(2-ethylhexyl)-5,10-difluoro-s-indaceno[1,2-b:5,6-b']dithiophene-4,9-dione (**2,7-bis(2-ethylhexyl)-diFIDT-di(O)**) in $CDCl_3$.*

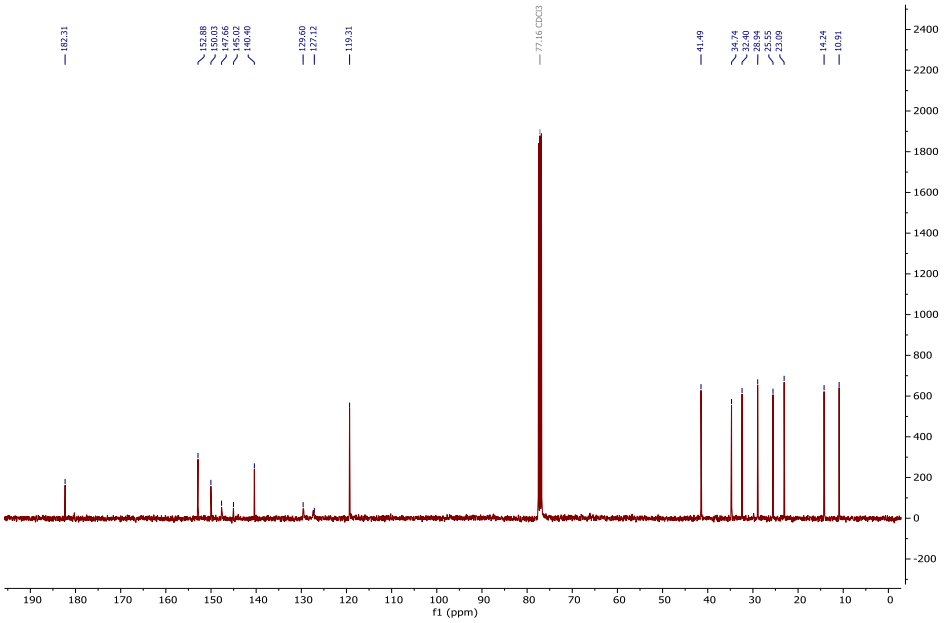


Figure A47: *^{13}C NMR of 2,7-bis(2-ethylhexyl)-5,10-difluoro-s-indaceno[1,2-b:5,6-b']dithiophene-4,9-dione (**2,7-bis(2-ethylhexyl)-diFIDT-di(O)**) in $CDCl_3$.*

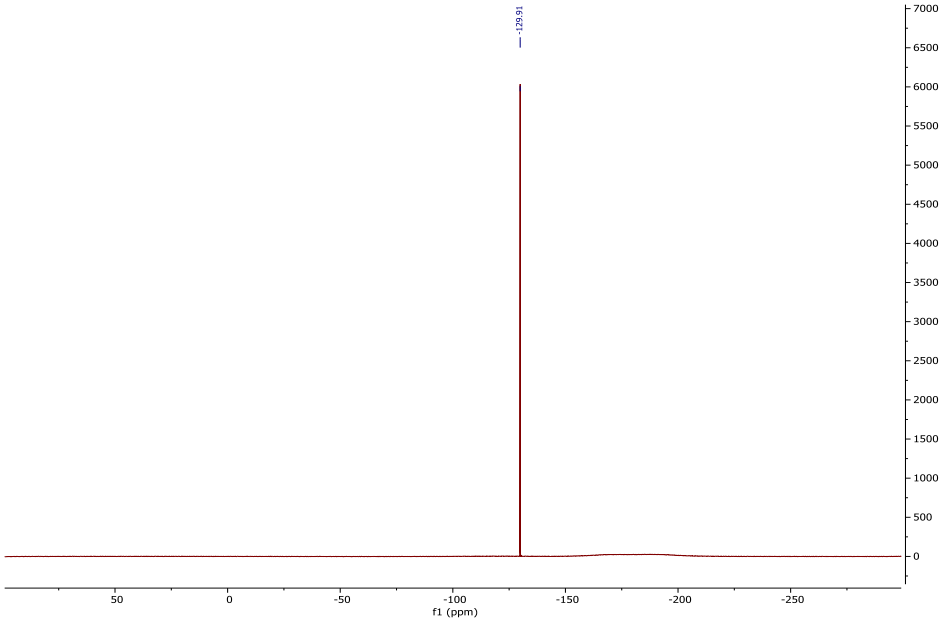


Figure A48: *^{19}F NMR of 2,7-bis(2-ethylhexyl)-5,10-difluoro-s-indaceno[1,2-b:5,6-b']dithiophene-4,9-dione (**2,7-bis(2-ethylhexyl)-diFIDT-di(O)**) in $CDCl_3$.*

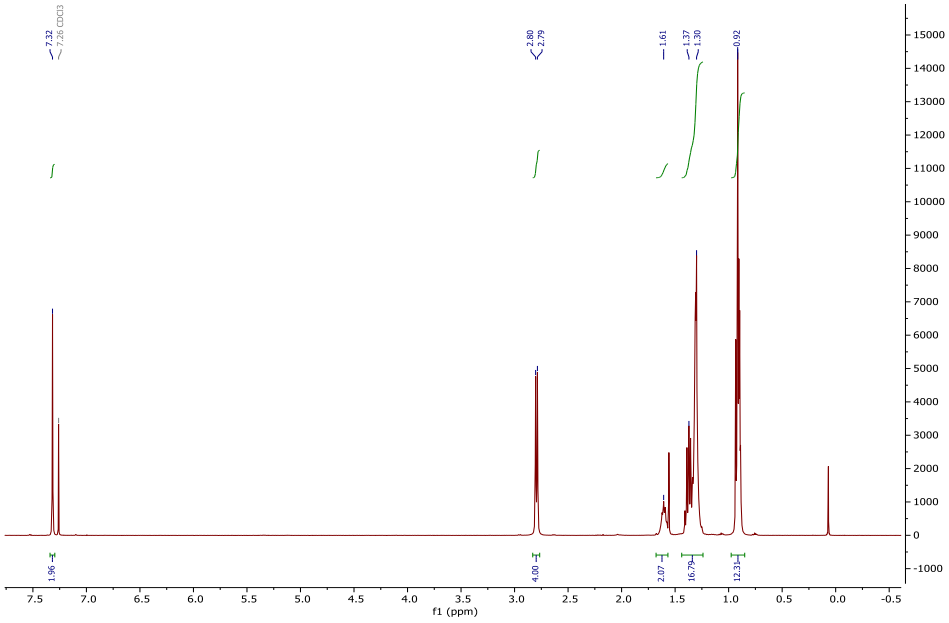


Figure A49: *^{1}H NMR of 2,2'-(5,10-difluoro-2,7-bis(2-ethylhexyl)-s-indaceno[1,2-b:5,6-b']dithiophene-4,9-diylidene)dimalononitrile (**2,7-bis(2-ethylhexyl)-diFIDT-di(C(CN)$_2$)**) in $CDCl_3$.*

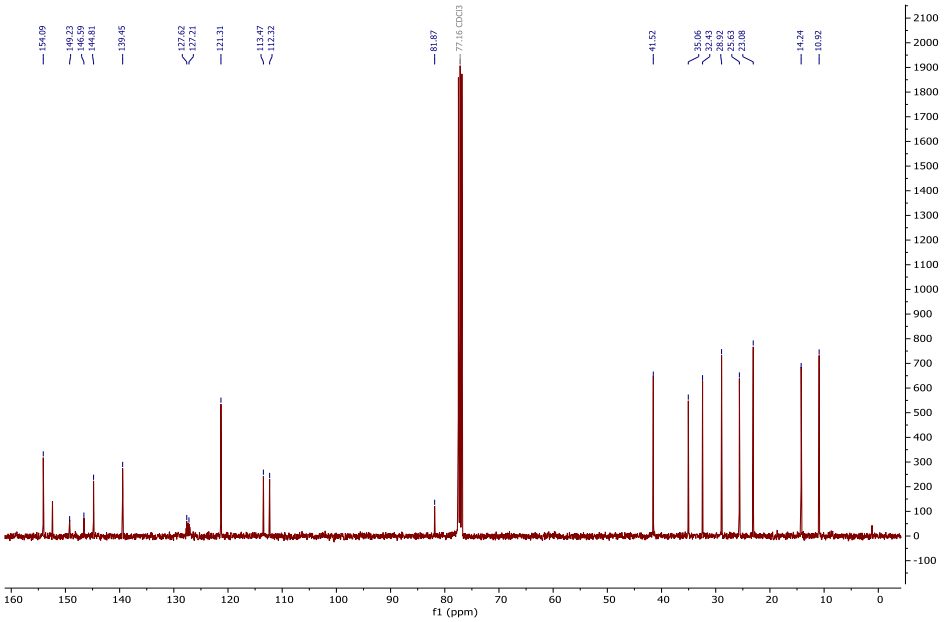


Figure A50: *^{13}C NMR of 2,2'-(5,10-difluoro-2,7-bis(2-ethylhexyl)-s-indaceno[1,2-b:5,6-b']dithiophene-4,9-diylidene)dimalononitrile (**2,7-bis(2-ethylhexyl)-diFIDT-di(C(CN)$_2$)**) in $CDCl_3$.*

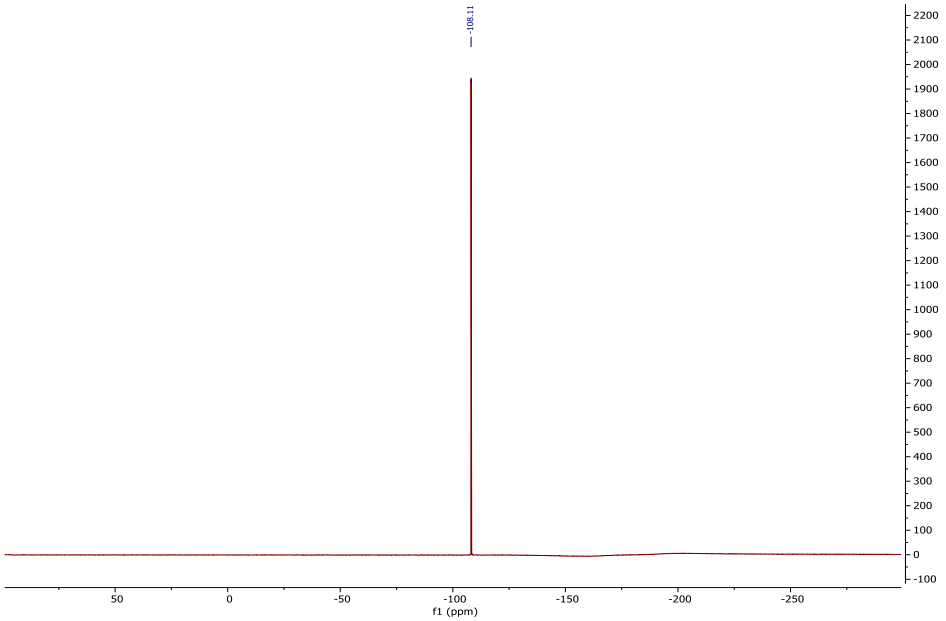


Figure A51: *^{19}F NMR of 2,2'-(5,10-difluoro-2,7-bis(2-ethylhexyl)-s-indaceno[1,2-b:5,6-b']dithiophene-4,9-diylidene)dimalononitrile (**2,7-bis(2-ethylhexyl)-diFIDT-di(C(CN)$_2$)**) in $CDCl_3$.*

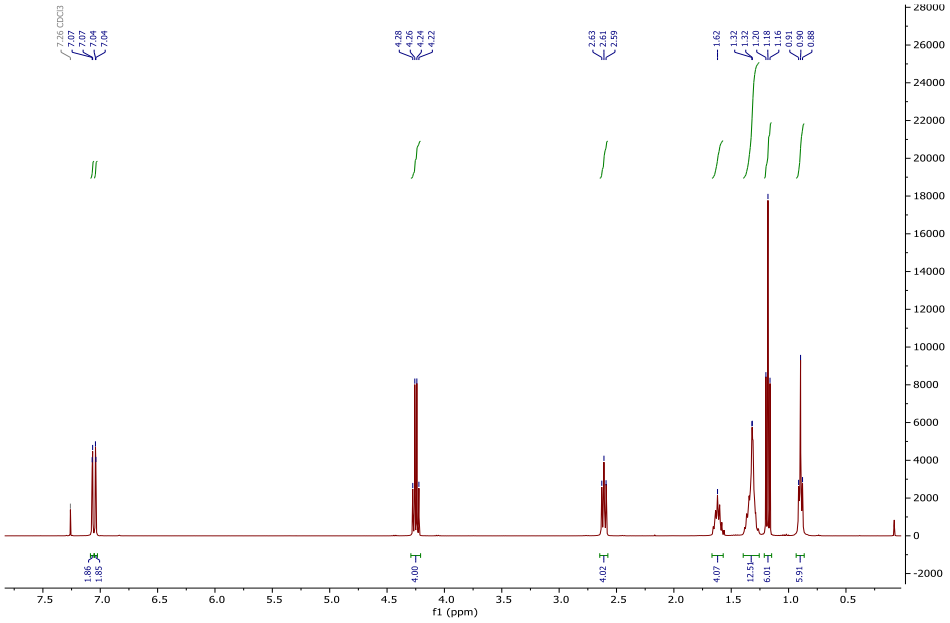


Figure A52: *^{1}H NMR of diethyl 2,5-difluoro-3,6-bis(4-hexylthiophen-2-yl)terephthalate in $CDCl_3$.*

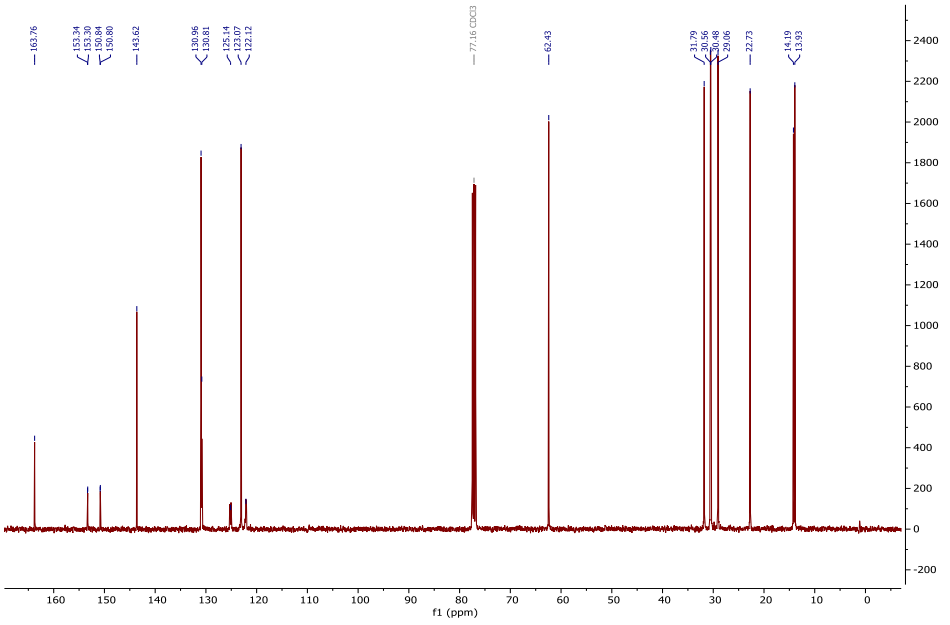


Figure A53: *^{13}C NMR of diethyl 2,5-difluoro-3,6-bis(4-hexylthiophen-2-yl)terephthalate in $CDCl_3$.*

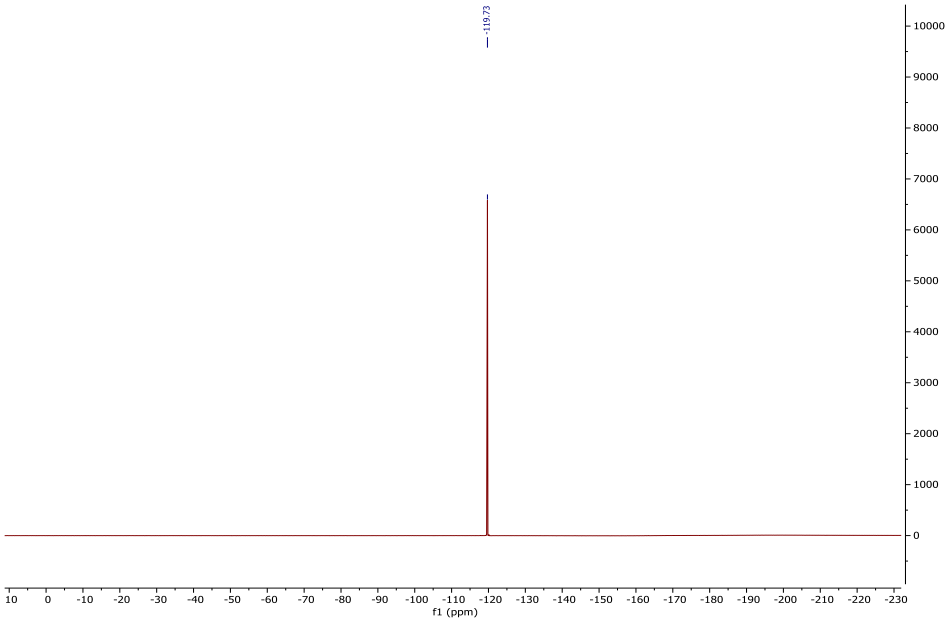


Figure A54: *^{19}F NMR of diethyl 2,5-difluoro-3,6-bis(4-hexylthiophen-2-yl)terephthalate in $CDCl_3$.*

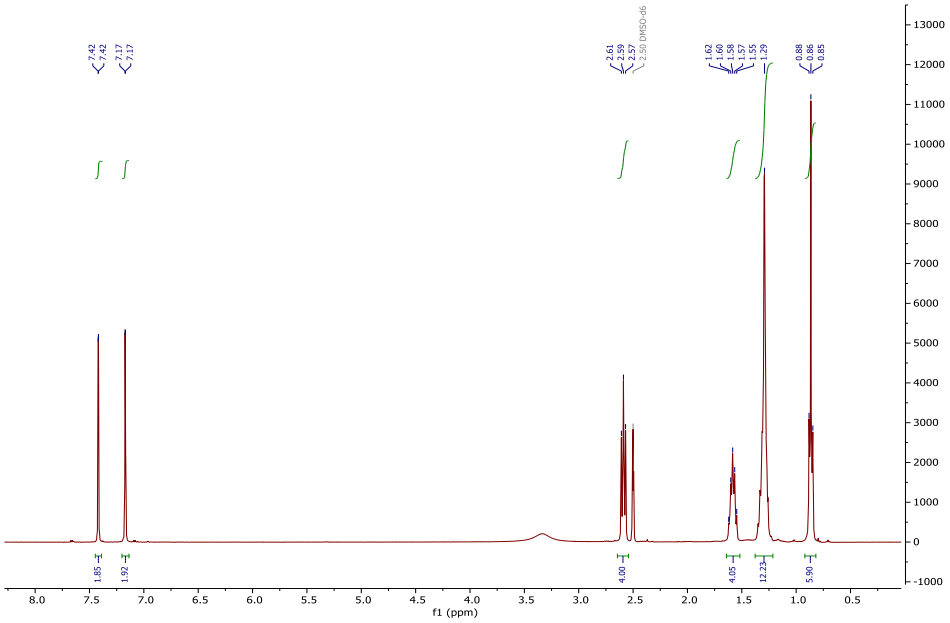


Figure A55: *^{1}H NMR of 2,5-bis(4-hexylthiophen-2-yl)-3,6-difluoroterephthalic acid in DMSO-d_6.*

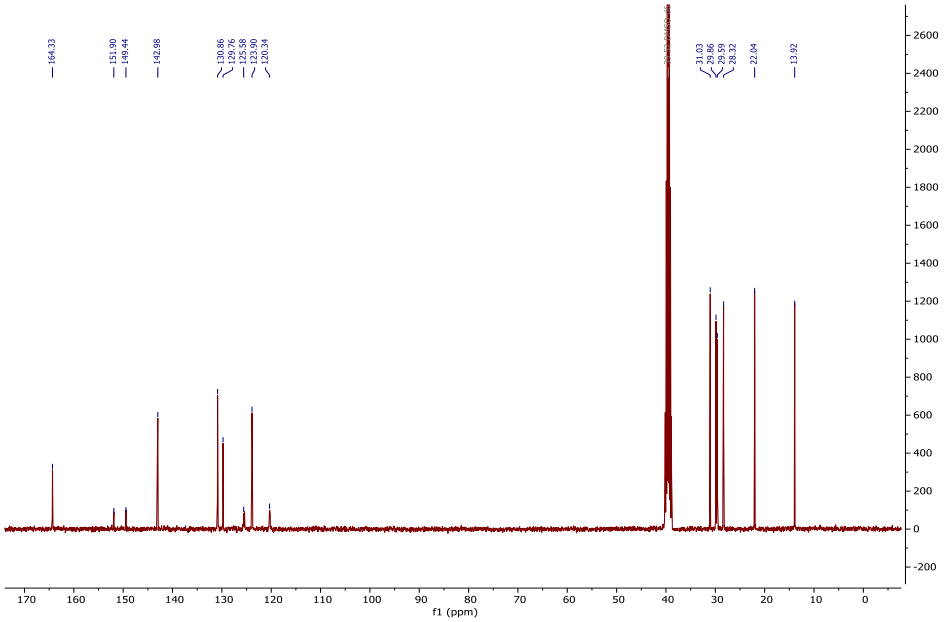


Figure A56: *^{13}C NMR of 2,5-bis(4-hexylthiophen-2-yl)-3,6-difluoroterephthalic acid in DMSO-d_6.*

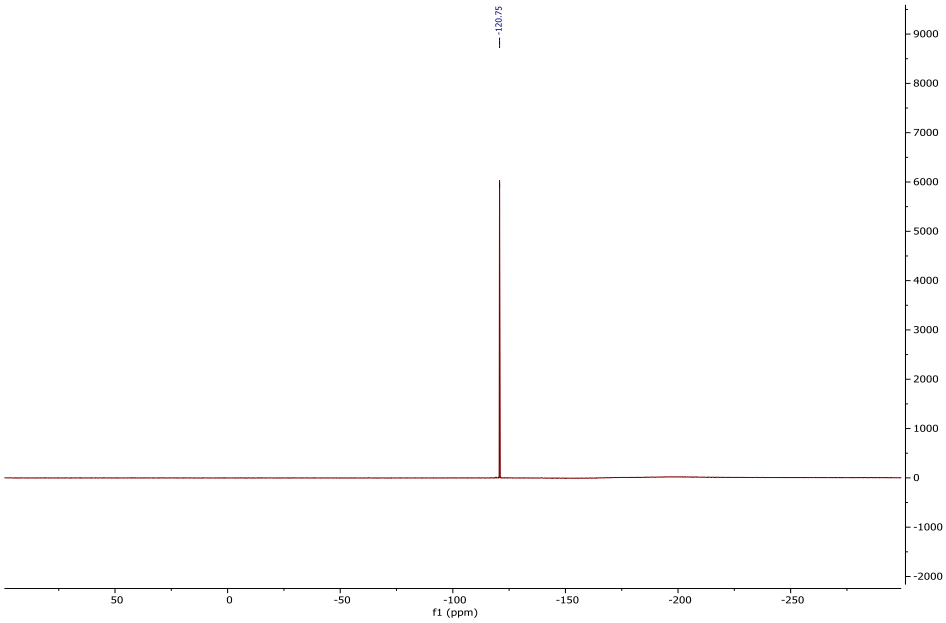


Figure A57: *^{19}F NMR of 2,5-bis(4-hexylthiophen-2-yl)-3,6-difluoroterephthalic acid in DMSO-d_6.*

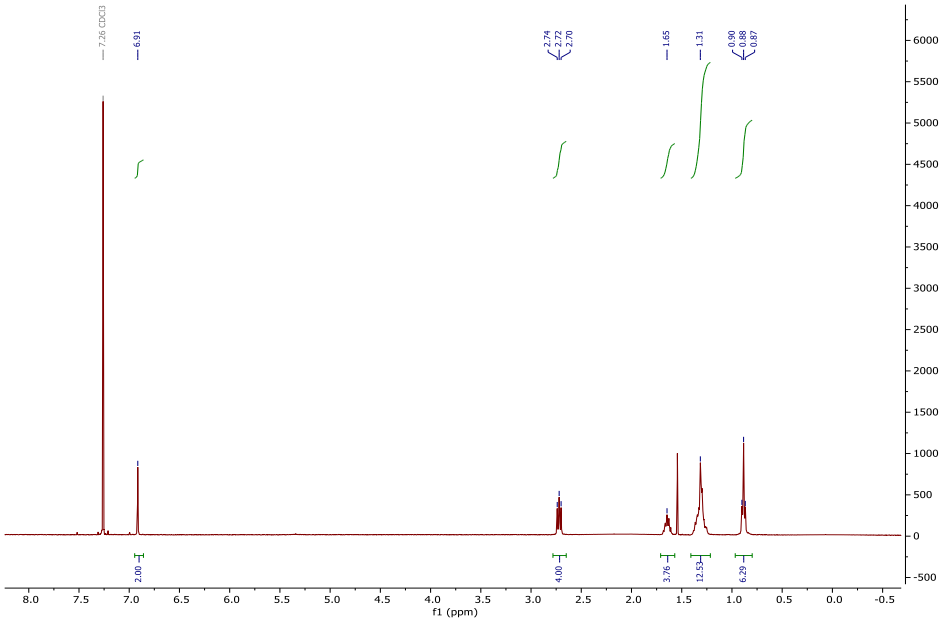


Figure A58: *^{1}H NMR of 3,8-dihexyl-5,10-difluoro-s-indaceno[1,2-b:5,6-b']dithiophene-4,9-dione (**3,8-dihexyl-diFIDT-di(O)**) in $CDCl_3$.*

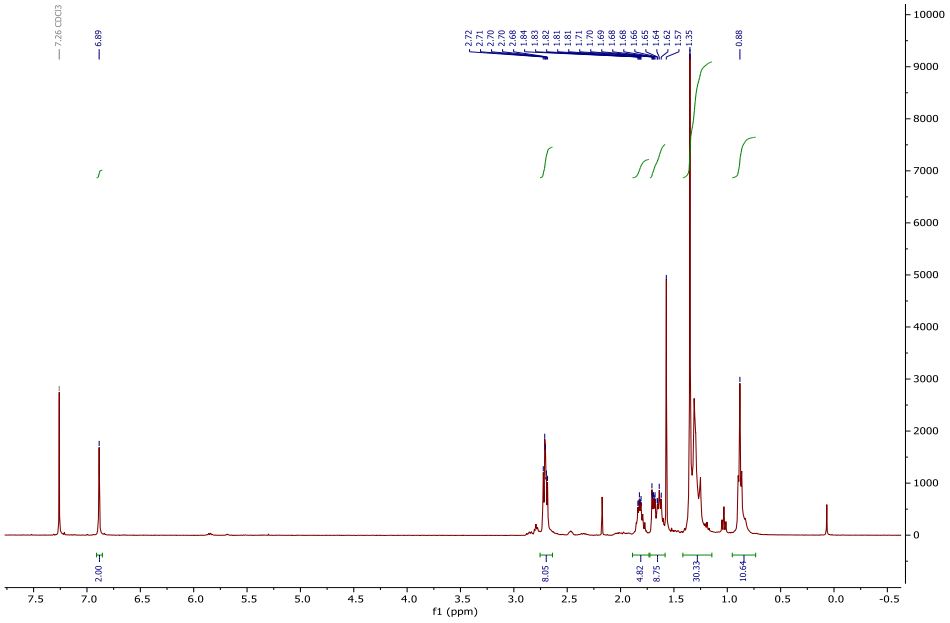


Figure A59: *^{1}H NMR of isolated side-product from Friedel-Crafts cyclisation in $CDCl_3$.*

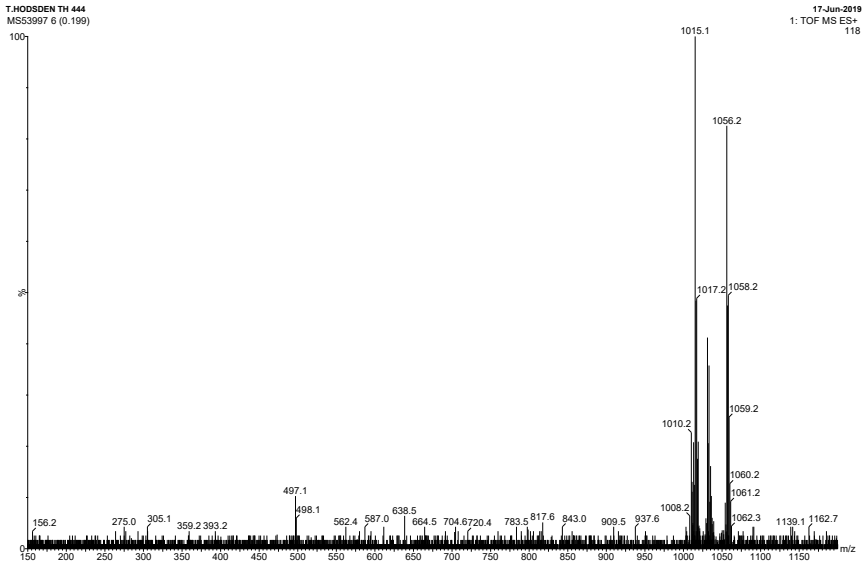


Figure A60: *TOF-ES MS of isolated side-product from Friedel-Crafts cyclisation.*

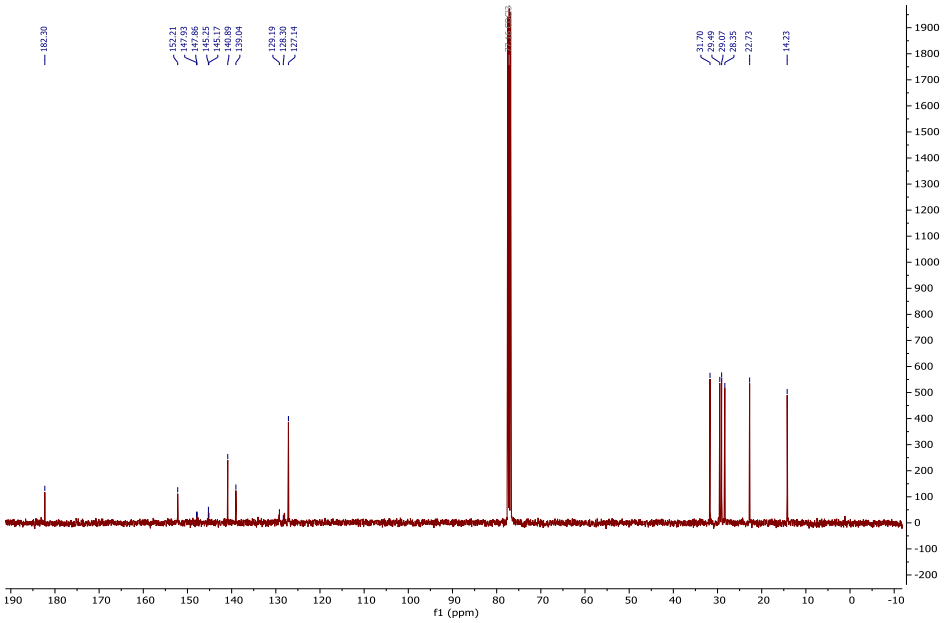


Figure A61: *^{13}C NMR of 3,8-dihexyl-5,10-difluoro-s-indaceno[1,2-b:5,6-b']dithiophene-4,9-dione (**3,8-dihexyl-diFIDT-di(O)**) in $CDCl_3$.*

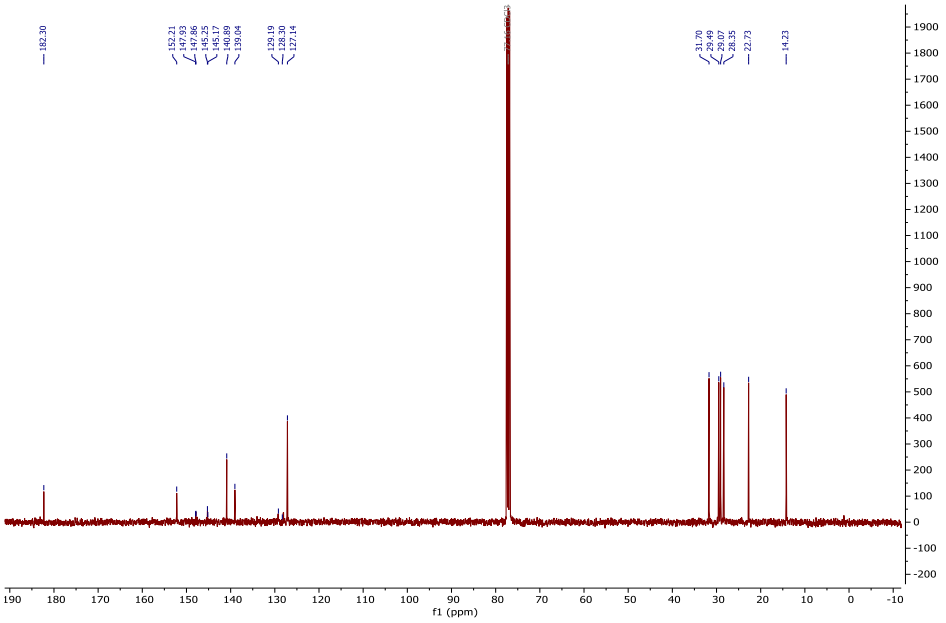


Figure A62: *^{19}F NMR of 3,8-dihexyl-5,10-difluoro-s-indaceno[1,2-b:5,6-b']dithiophene-4,9-dione (**3,8-dihexyl-diFIDT-di(O)**) in $CDCl_3$.*

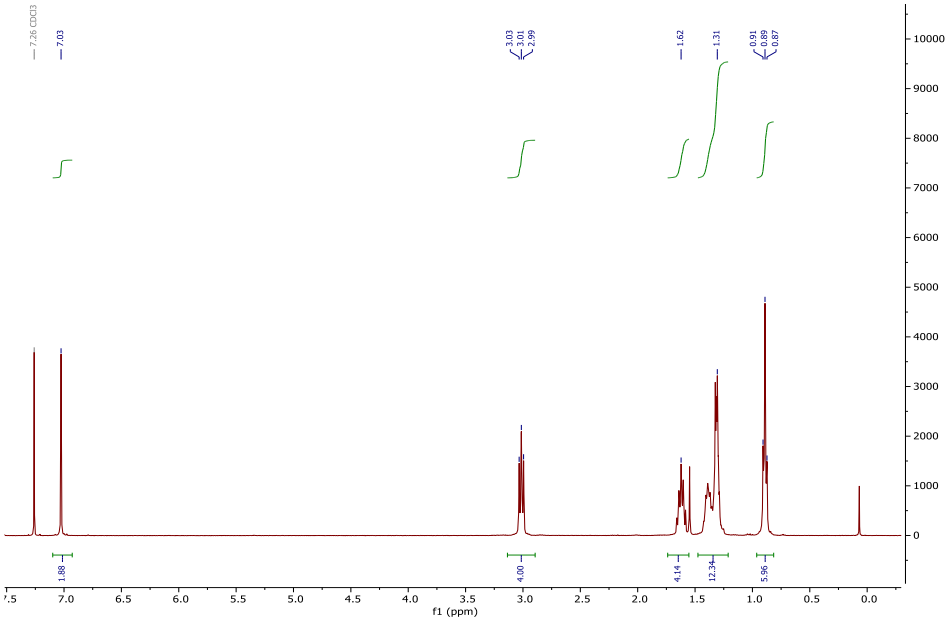


Figure A63: *^{1}H NMR of 2,2'-(5,10-difluoro-3,8-dihexyl-s-indaceno[1,2-b:5,6-b']dithiophene-4,9-diylidene)dimalononitrile (**3,8-dihexyl-diFIDT-di(C(CN)$_2$)**) in $CDCl_3$ at 50 °C.*

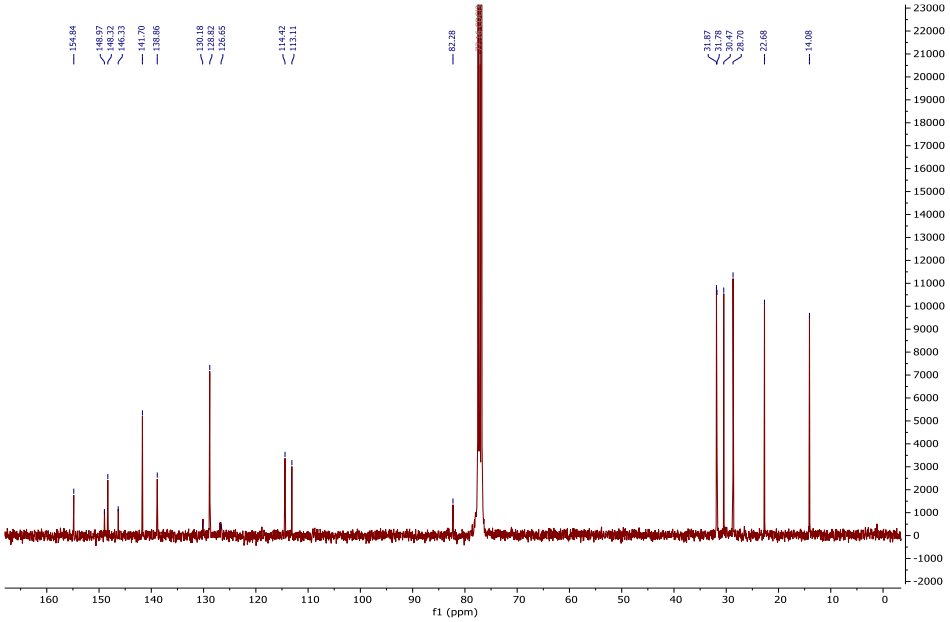


Figure A64: *^{13}C NMR of 2,2'-(5,10-difluoro-3,8-dihexyl-s-indaceno[1,2-b:5,6-b']dithiophene-4,9-diylidene)dimalononitrile (**3,8-dihexyl-diFIDT-di(C(CN)$_2$)**) in $CDCl_3$ at 50 °C.*

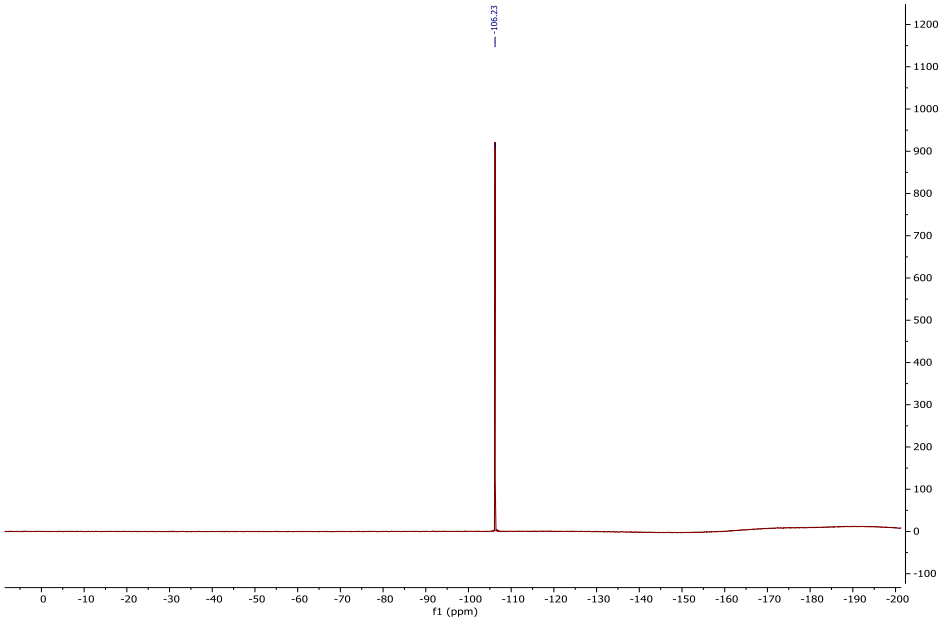
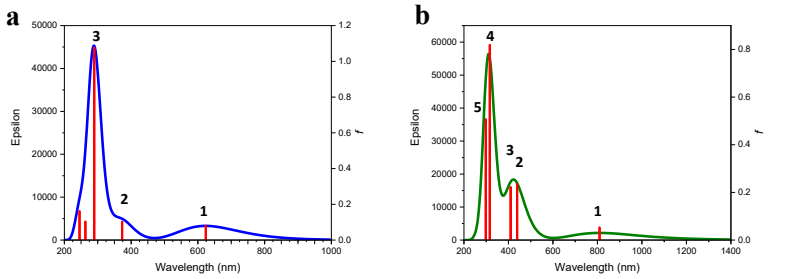


Figure A65: *^{19}F NMR of 2,2'-(5,10-difluoro-3,8-dihexyl-s-indaceno[1,2-b:5,6-b']dithiophene-4,9-diylidene)dimalononitrile (**3,8-dihexyl-diFIDT-di(C(CN)$_2$)**) in $CDCl_3$ at 50 °C.*



1. HOMO→LUMO, 623 nm, $f = 0.082$

2. HOMO-6→LUMO, 373 nm, $f = 0.103$
   HOMO-2→LUMO
   HOMO→LUMO+2

3. HOMO-6→LUMO, 290 nm, $f = 1.077$
   HOMO-2→LUMO
   HOMO→LUMO+2

1. HOMO→LUMO, 809 nm, $f = 0.053$

2. HOMO-4→LUMO, 437 nm, $f = 0.236$
   HOMO-1→LUMO

3. HOMO-4→LUMO, 409 nm, $f = 0.223$
   HOMO-1→LUMO
   HOMO→LUMO+2

4. HOMO-5→LUMO, 315 nm, $f = 0.820$
   HOMO-4→LUMO+1
   HOMO→LUMO+2

5. HOMO-5→LUMO, 299 nm, $f = 0.507$
   HOMO-3→LUMO+1
   HOMO-2→LUMO+1
   HOMO→LUMO+2

Figure A66: *Predicted UV-Vis spectra from TD-DFT energy calculations of a)* ***3,8-dialkyl-diFIDT-di(O)*** *and b)* ***3,8-dialkyl-diFIDT-di(C(CN)$_2$)*** *after geometry optimisation with DFT B3LYP/6-311+G(d,p), with selected excitations highlighted.*

The X-ray crystal structure of 2,7-bis(2-ethylhexyl)-diFIDT-di(O)

Crystal data for **2,7-bis(2-ethylhexyl)-diFIDT-di(O)**: $C_{32}H_{36}F_2O_2S_2$, $M = 554.73$, triclinic, P-1, $a = 5.8970(8)$, $b = 6.1544(7)$, $c = 19.764(3)$ Å, $\alpha = 82.318(10)$, $\beta = 86.207(12)$, $\gamma = 84.799(10)$ °, $V = 706.87(16)$ Å^3, $Z = 1$ [*C*i symmetry], $D_c = 1.303$ g cm^{-3}, μ(Cu-Kα) = 20439 mm–1, $T =$ 173 K, brown-green dichroic plate, Agilent Xcalibur PX Ultra A diffractometer; 3987 independent measured reflections (R_{int} = 0.0454), F^2 refinement,[^{X1,X2}] R_1(obs) = 0.0686, wR_2(all) = 0.2106, 1803 independent observed absorption-corrected reflections [$|F_o| > 4\sigma(|F_o|)$, completeness to θ_{full}(75.8 °)], 201 parameters.

The structure of **2,7-bis(2-ethylhexyl)-di(O)** was found to sit across a centre of symmetry at the middle of the central C_6F_2 ring.

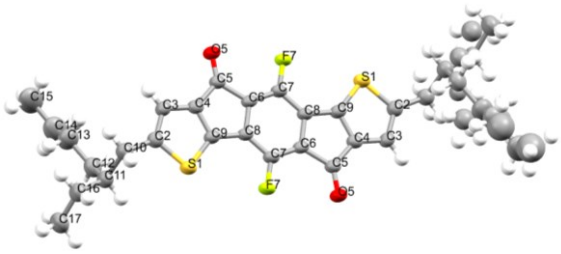


***Figure A67**: The crystal structure of **2,7-bis(2-ethylhexyl)-diFIDT-di(O)** (50 % probability ellipsoids). The molecule sits across a centre of symmetry at the middle of the central C_6F_2 ring.*

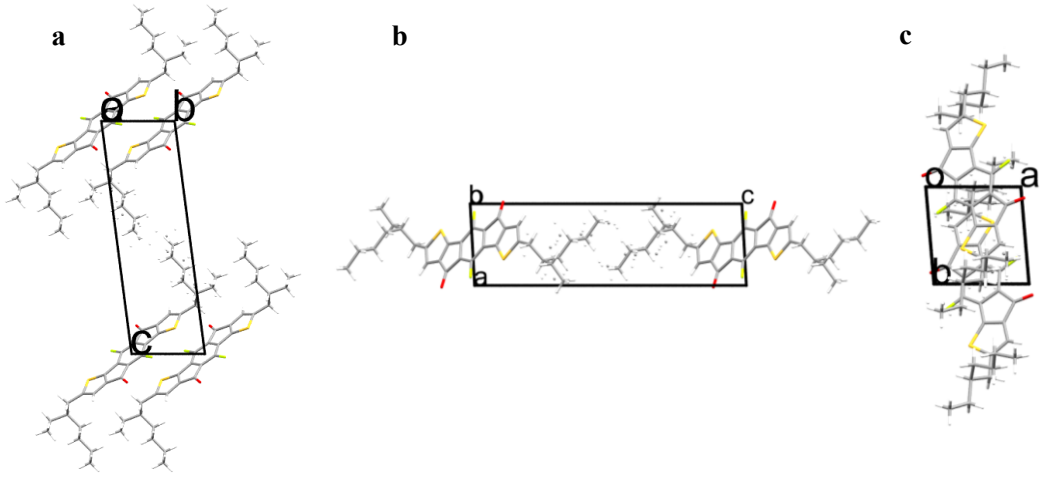


***Figure A68**: Unit cell of **2,7-bis(2-ethylhexyl)-diFIDT-di(O)** as viewed along the a-, b- and c-axes (left to right).*

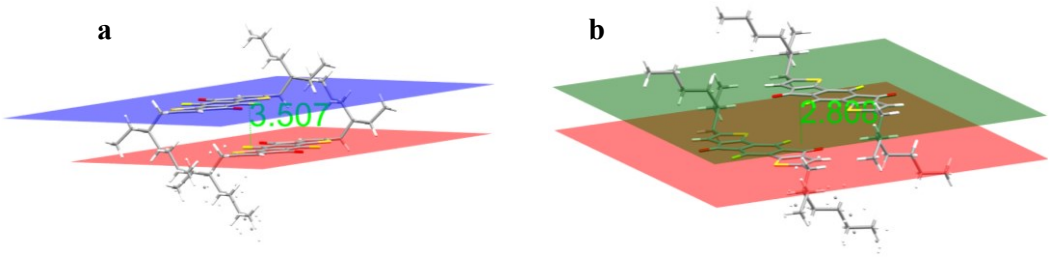


***Figure A69**: Interlayer spacing in pseudo-brickwork packing of **2,7-bis(2-ethylhexyl)-diFIDT-di(O)**. a) Main π-stack. b) 2° π-stack.*

The X-ray crystal structure of 3,8-dihexyl-diFIDT-di(O)

Crystal data for **3,8-dihexyl-diFIDT-di(O)**: $C_{28}H_{28}F_2O_2S_2$, M = 498.62, monoclinic, P2/c, a = 16.0899(6), b = 4.73078(16), c = 15.9771(5) Å, α = 90, β = 102.184(3), γ = 90 °, V = 1188.75(7) Å^3, Z = 2 [*C*i symmetry], D_c = 1.393 g cm^{-3}, μ(Cu-Kα) = 2.369 mm–1, T = 173 K, dark blue platy needles, Agilent Xcalibur PX Ultra A diffractometer; 2260 independent measured

reflections (R_{int} = 0.0288), F^2 refinement,[X1,X2] R_1(obs) = 0.0386, wR_2(all) = 0.1038, 1792 independent observed absorption-corrected reflections [$|F_o| > 4\sigma(|F_o|)$, completeness to θ_{full}(68.6 °)], 155 parameters.

The structure of **3,8-dihexyl-diFIDT-di(O)** was found to sit across a centre of symmetry at the middle of the central C_6F_2 ring.

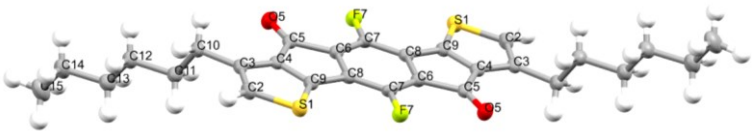


*Figure A70: The crystal structure of **3,8-dihexyl-diFIDT-di(O)** (50 % probability ellipsoids). The molecule sits across a centre of symmetry at the middle of the central C_6F_2 ring.*

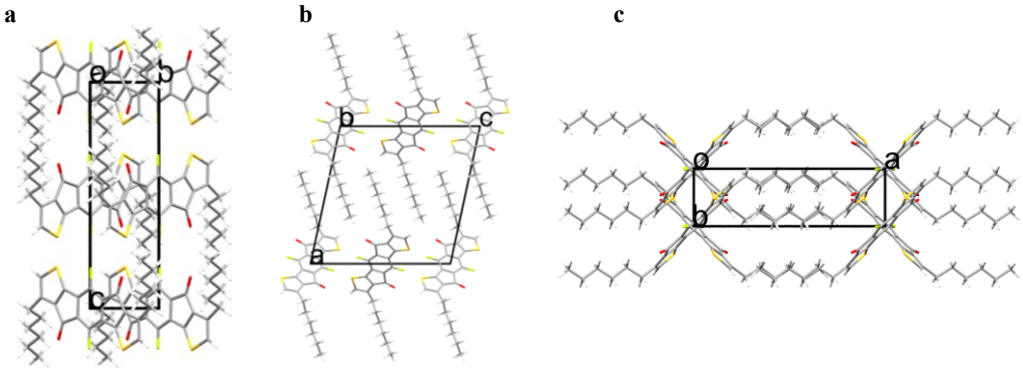


*Figure A71: Unit cell of **3,8-dihexyl-diFIDT-di(O)** as viewed along the a-, b- and c-axes (left to right).*

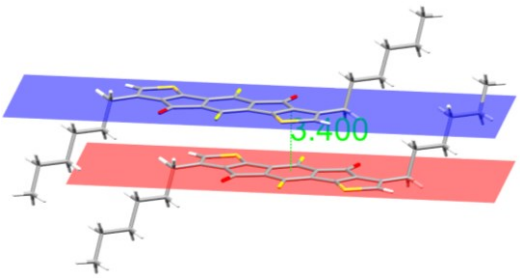


*Figure A72: Interlayer spacing of **3,8-dihexyl-diFIDT-di(O)**.*

The X-ray crystal structure of 3,8-dihexyl-diFIDT-di(C(CN)$_2$)

Crystal data for **3,8-dihexyl-diFIDT-di(C(CN)$_2$)**: $C_{34}H_{28}F_2N_4S_2$, M = 594.72, monoclinic, $P2_1/c$, a = 15.7229(16), b = 4.8221(2), c = 19.2518(8) Å, α = 90, β = 90.655(6), γ = 90 °, V = 1459.51(18) Å^3, Z = 2 [*C*i symmetry], D_c = 1.353 g cm^{-3}, μ(Cu-Kα) = 2.015 mm–1, T = 173 K, green thin platy needles, Agilent Xcalibur PX Ultra A diffractometer; 2765 independent measured reflections (R_{int} = 0.0707), F^2 refinement,[^{X1,X2}] R_1(obs) = 0.0524, wR_2(all) = 0.1285, 1735 independent observed absorption-corrected reflections [$|F_o| > 4\sigma(|F_o|)$, completeness to θ_{full}(74.9 °)], 207 parameters.

The structure of **3,8-dihexyl-diFIDT-di(C(CN)$_2$)** was found to sit across a centre of symmetry at the middle of the central C_6F_2 ring.

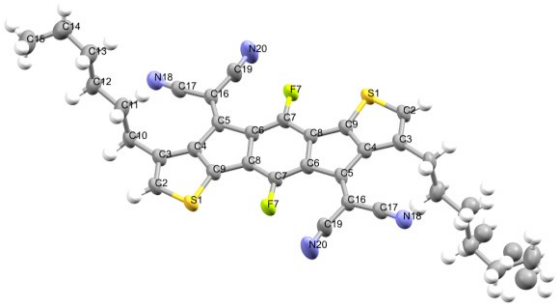


***Figure A73**: The crystal structure of **3,8-dihexyl-diFIDT-di(C(CN)$_2$)** (50 % probability ellipsoids). The molecule sits across a centre of symmetry at the middle of the central C_6F_2 ring.*

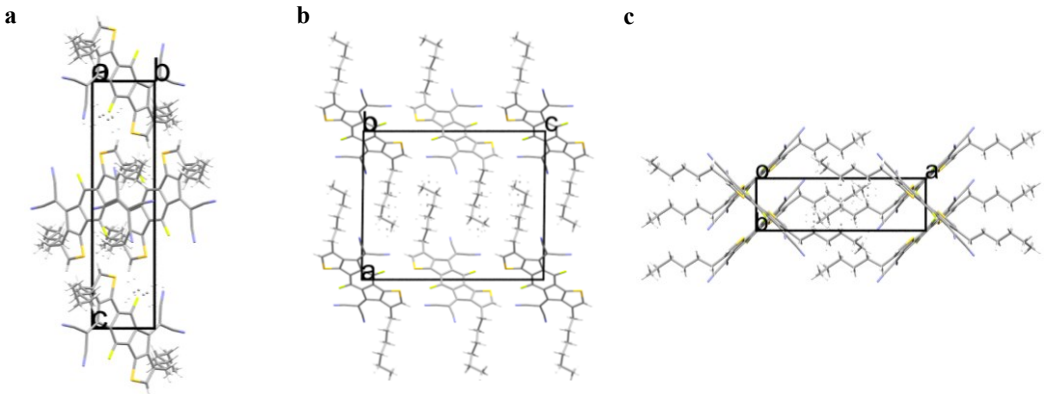


***Figure A74**: Unit cell of **3,8-dihexyl-diFIDT-di(C(CN)$_2$)** as viewed along the a-, b- and c-axes (left to right).*

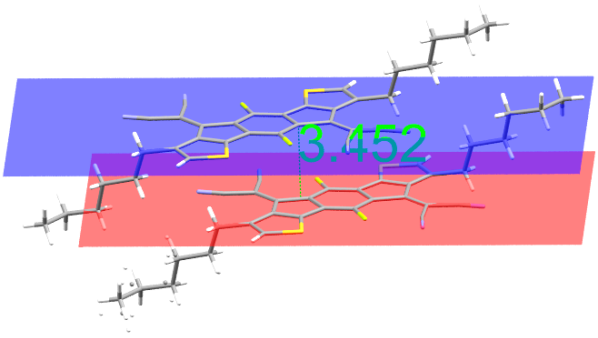


*Figure A75: Interlayer spacing of **3,8-dihexyl-diFIDT-di(C(CN)$_2$)**.*

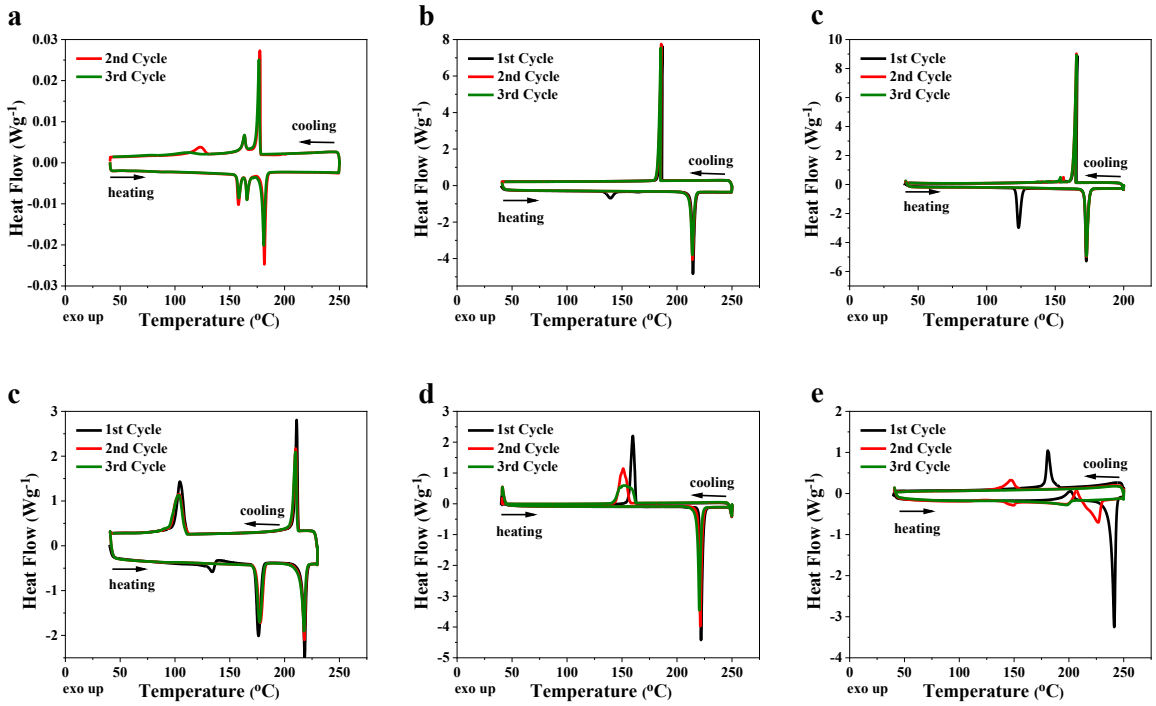


***Figure A76:** DSC plots (all cycles) for a) **2,7-didodecyl-diFIDT-di(O)**. b) **2,7-bis(2-ethylhexyl)-diFIDT-di(O)**. c) **3,8-dihexyl-diFIDT-di(O)**. d) **2,7-didodecyl-diFIDT-di(C(CN)$_2$)**. e) **2,7-bis(2-ethylhexyl)-diFIDT-di(C(CN)$_2$)**. f) **3,8-dihexyl-diFIDT-di(C(CN)$_2$)**.*

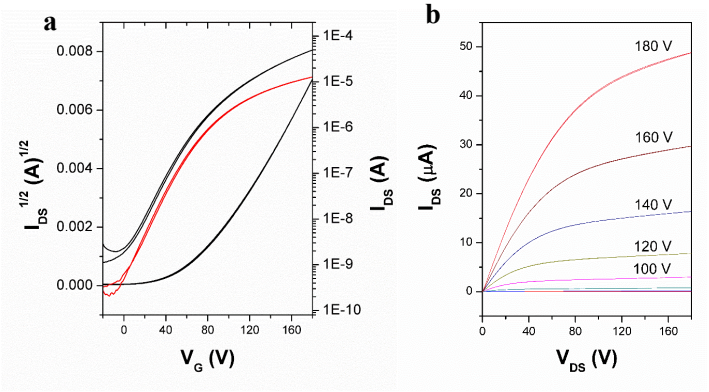


Figure A77: *Device data for best performing BC-TG spin-coated devices of* ***2,7-didodecyl-diFIDT-di(C(CN)2)****.*

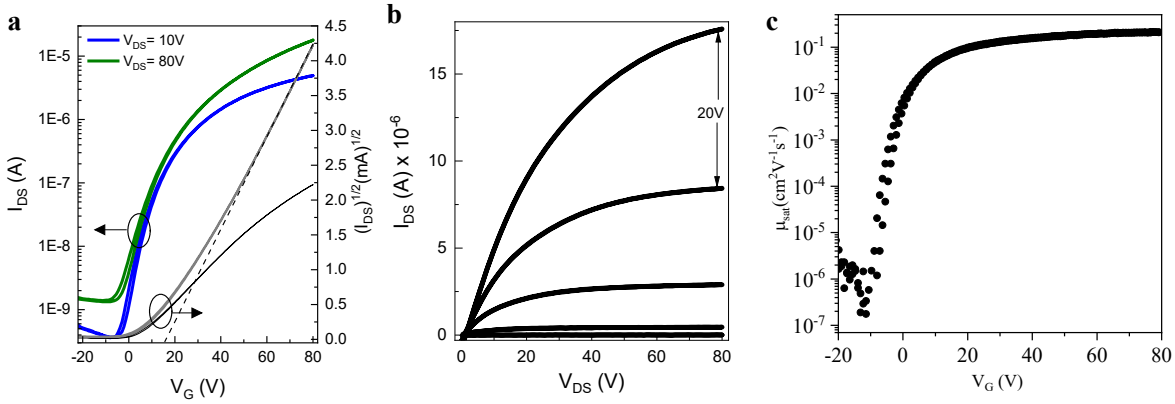


Figure A78: *Device data for best performing BC-TG blade-coated devices of* ***3,8-dihexyl-diFIDT-di(C(CN)2)****.*

10.3 Chapter 4

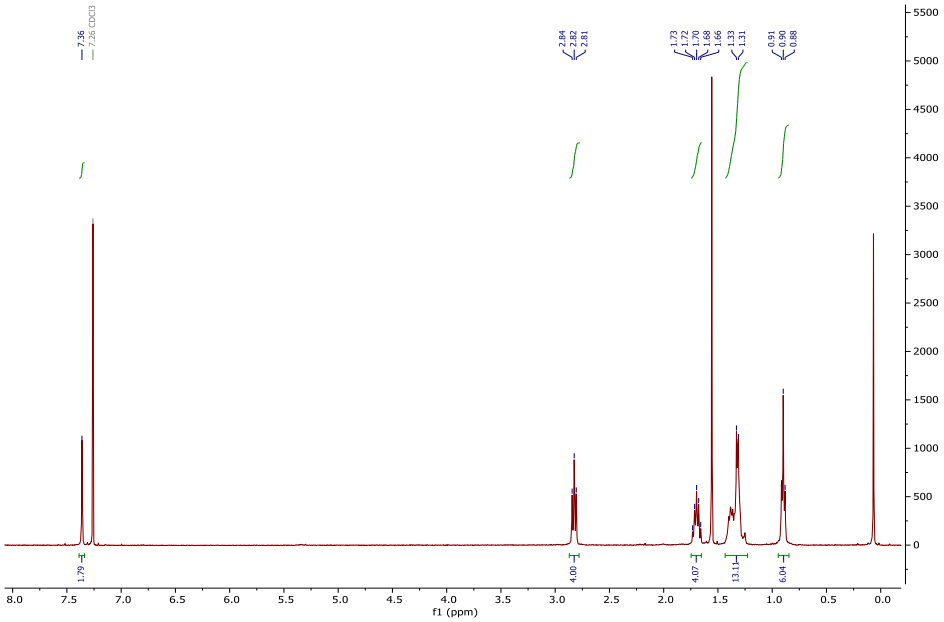


Figure A79: *^{1}H NMR of 2,2'-(5,10-difluoro-2,7-dihexyl-s-indaceno[1,2-b:5,6-b']dithiophene-4,9-diylidene)dicyanoimine* ***(2,7-dihexyl-diFIDT-di(N(CN)))*** *in $CDCl_3$.*

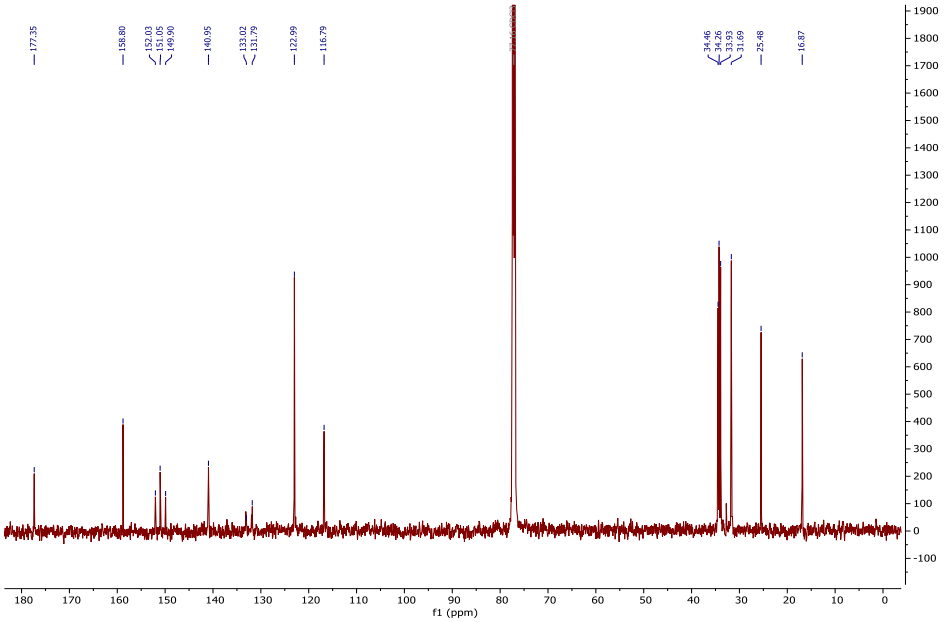


Figure A80: *^{13}C NMR of 2,2'-(5,10-difluoro-2,7-dihexyl-s-indaceno[1,2-b:5,6-b']dithiophene-4,9-diylidene)dicyanoimine* ***(2,7-dihexyl-diFIDT-di(N(CN)))*** *in TCE-d_2 at 120 °C.*

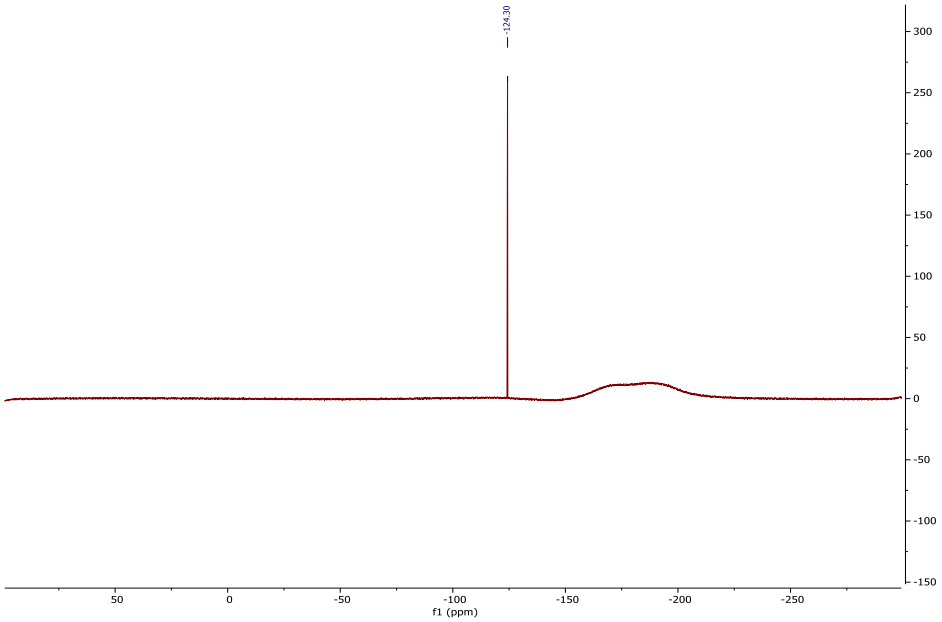


Figure A81: *^{19}F NMR of 2,2'-(5,10-difluoro-2,7-dihexyl-s-indaceno[1,2-b:5,6-b']dithiophene-4,9-diylidene)dicyanoimine (**2,7-dihexyl-diFIDT-di(N(CN))**) in $CDCl_3$.*

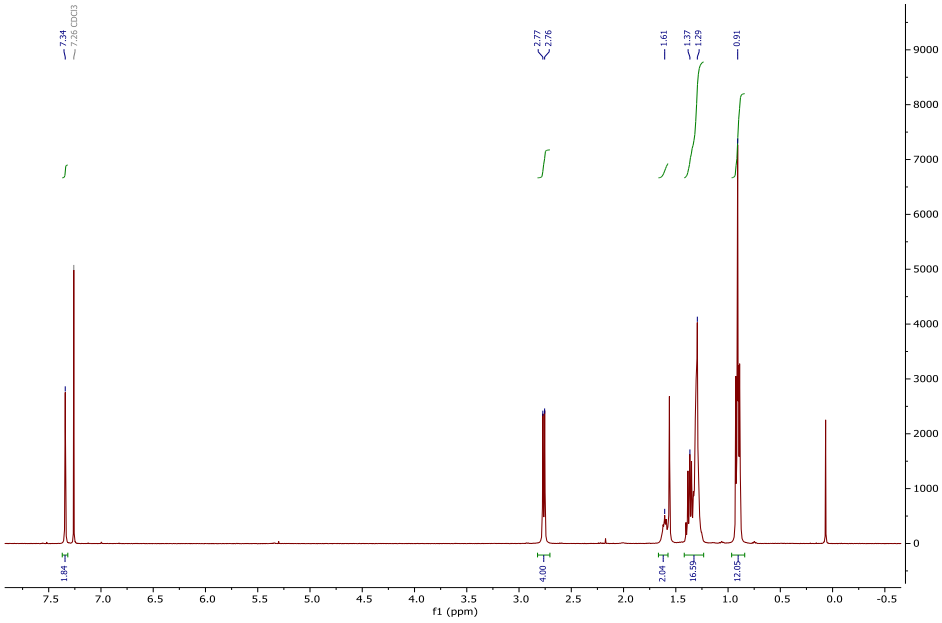


Figure A82: *^{1}H NMR of 2,2'-(2,7-bis(2-ethylhexyl)-5,10-difluoro-s-indaceno[1,2-b:5,6-b']dithiophene-4,9-diylidene)dicyanoimine (**2,7-bis(2-ethylhexyl)-diFIDT-di(N(CN))**) in $CDCl_3$.*

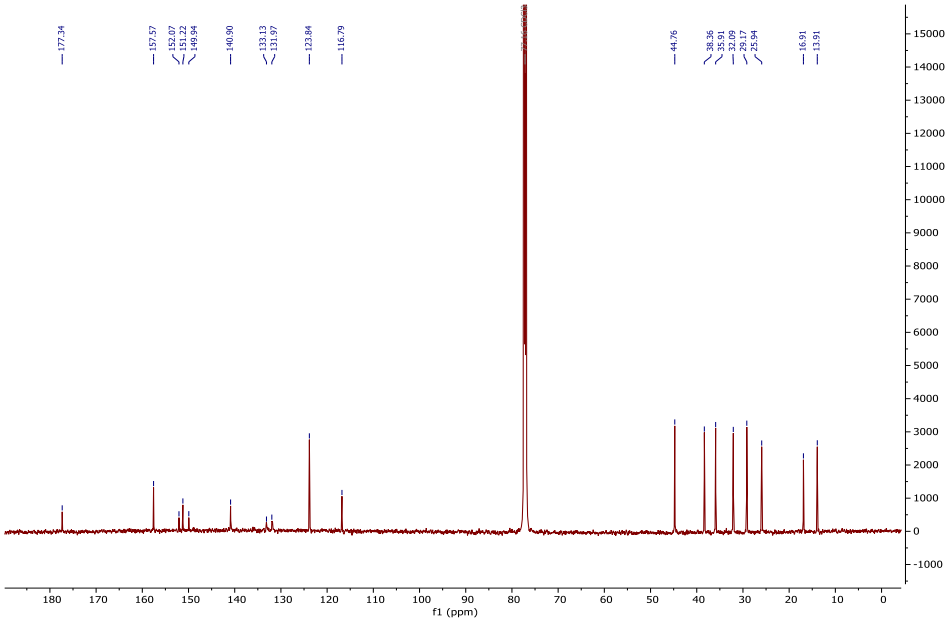


Figure A83: *^{13}C NMR of 2,2'-(2,7-bis(2-ethylhexyl)-5,10-difluoro-s-indaceno[1,2-b:5,6-b']dithiophene-4,9-diylidene)dicyanoimine (**2,7-bis(2-ethylhexyl)-diFIDT-di(N(CN))**) in TCE-d_2 at 120 °C.*

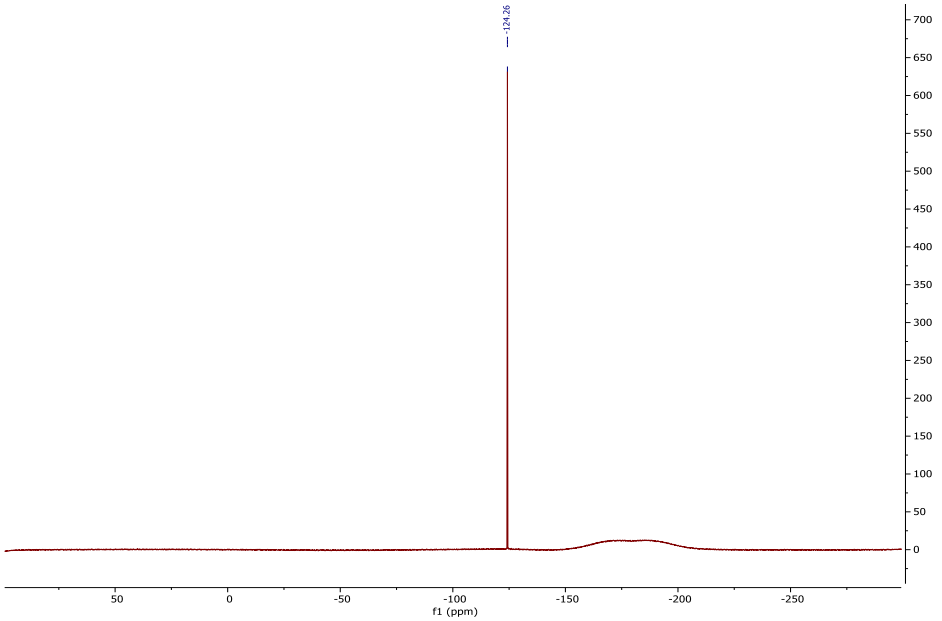


Figure A84: *^{19}F NMR of 2,2'-(2,7-bis(2-ethylhexyl)-5,10-difluoro-s-indaceno[1,2-b:5,6-b']dithiophene-4,9-diylidene)dicyanoimine (**2,7-bis(2-ethylhexyl)-diFIDT-di(N(CN))**) in $CDCl_3$.*

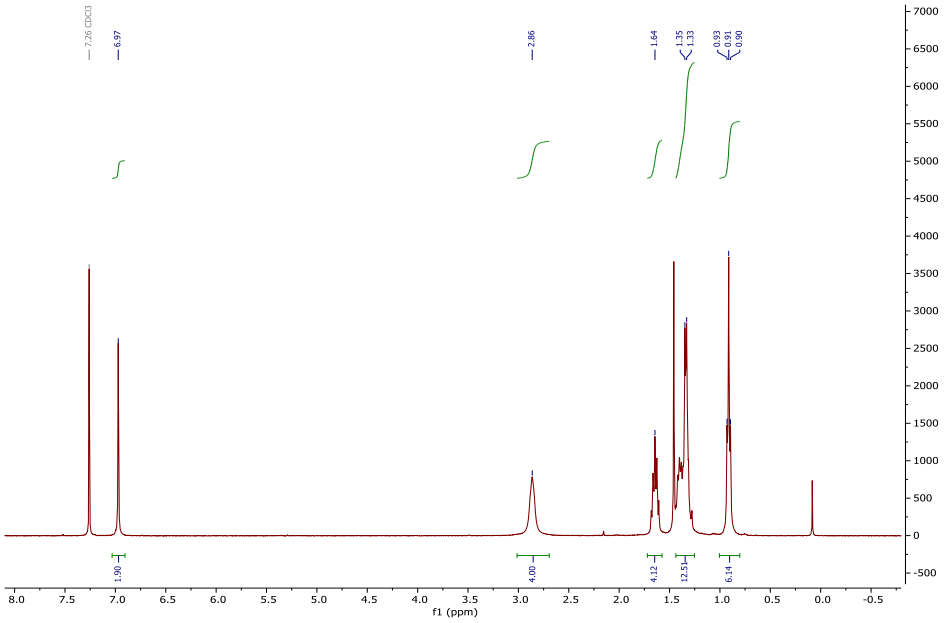


Figure A85: *^{1}H NMR of 2,2'-(5,10-difluoro-3,8-dihexyl-s-indaceno[1,2-b:5,6-b']dithiophene-4,9-diylidene)dicyanoimine (**3,8-dihexyl-diFIDT-di(N(CN))**) in $CDCl_3$ at 50 °C.*

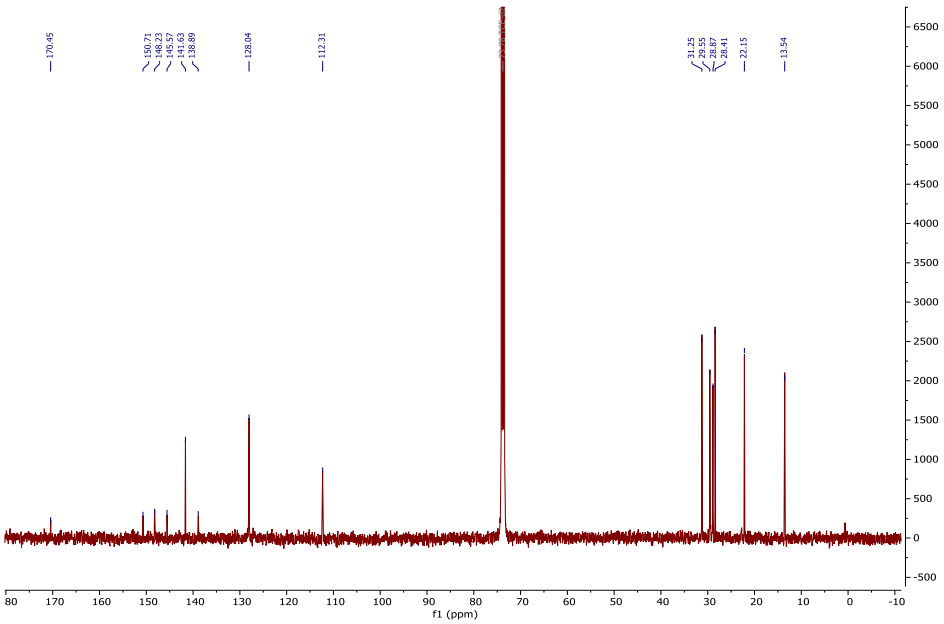


Figure A86: *^{13}C NMR of 2,2'-(5,10-difluoro-3,8-dihexyl-s-indaceno[1,2-b:5,6-b']dithiophene-4,9-diylidene)dicyanoimine (**3,8-dihexyl-diFIDT-di(N(CN))**) in TCE-d_2 at 120 °C.*

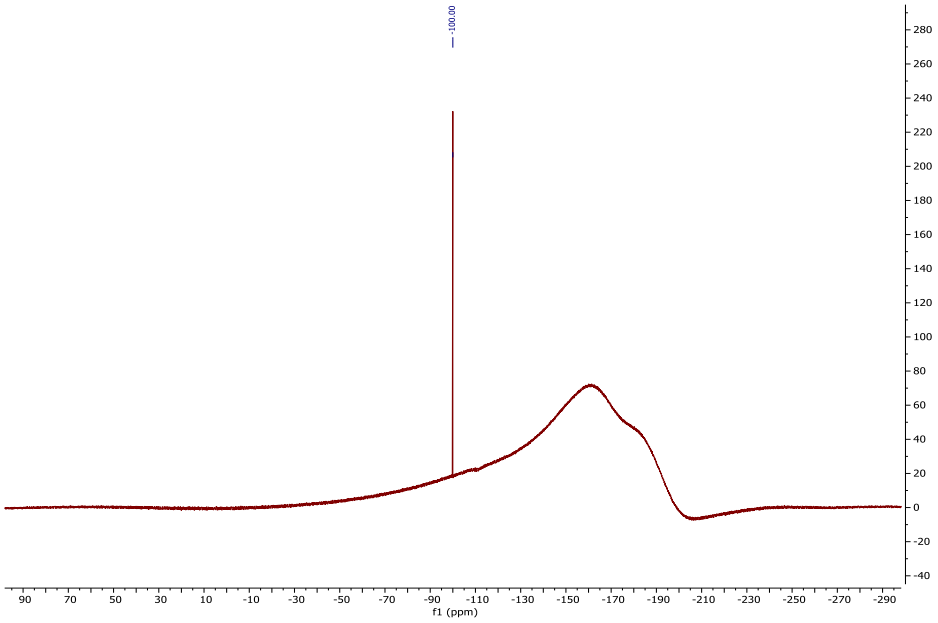
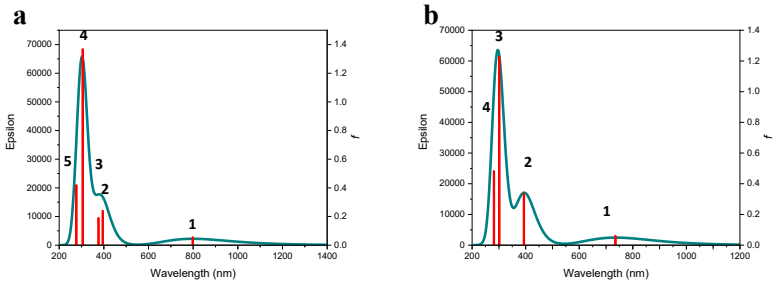


Figure A87: *^{19}F NMR of 2,2'-(5,10-difluoro-3,8-dihexyl-s-indaceno[1,2-b:5,6-b']dithiophene-4,9-diylidene)dicyanoimine (**3,8-dihexyl-diFIDT-di(N(CN))**) in $CDCl_3$ at 50 °C.*



1. HOMO→LUMO, 798 nm, f = 0.055
2. HOMO-4→LUMO, 395 nm, f = 0.240
   HOMO-2→LUMO
   HOMO→LUMO+2
3. HOMO-4→LUMO, 378 nm, f = 0.190
   HOMO-2→LUMO
   HOMO-1→LUMO+1
4. HOMO-7→LUMO, 306 nm, f = 1.369
   HOMO-4→LUMO
   HOMO-2→LUMO
   HOMO→LUMO+2
5. HOMO-7→LUMO, 277 nm, f = 0.420
   HOMO-3→LUMO+1
   HOMO-1→LUMO+1
   HOMO→LUMO+2

1. HOMO→LUMO, 736 nm, f = 0.061
2. HOMO-4→LUMO, 393 nm, f = 0.336
   HOMO-2→LUMO
   HOMO→LUMO+2
3. HOMO-7→LUMO, 301 nm, f = 1.227
   HOMO-4→LUMO
   HOMO-3→LUMO+1
   HOMO→LUMO+2
4. HOMO-7→LUMO, 282 nm, f = 0.483
   HOMO-3→LUMO+1
   HOMO→LUMO+2

Figure A88: *Predicted UV-Vis spectra from TD-DFT energy calculations of a) **2,7-dialkyl-diFIDT-di(N(CN))** and b) **3,8-dialkyl-diFIDT-di(N(CN))** after geometry optimisation with DFT B3LYP/6-311+G(d,p), with selected excitations highlighted.*

The X-ray crystal structure of 2,7-dihexyl-diFIDT-di(N(CN))

Crystal data for **2,7-dihexyl-diFIDT-di(N(CN))**: $C_{30}H_{28}F_2N_4S_2$, M = 546.68, monoclinic, $P2_1/n$, a = 4.70133(12), b = 16.7253(7), c = 16.7198(5) Å, α = 90, β = 97.105(2), γ = 90 °, V = 1304.60(7) Å^3, Z = 2 [*C*i symmetry], D_c = 1.392 g cm^{-3}, μ(Cu-Kα) = 2.199 mm–1, T = 173 K, black platy needles, Agilent Xcalibur PX Ultra A diffractometer; 4504 independent measured reflections (R_{int} = 0.0332), F^2 refinement,[X1,X2] R_1(obs) = 0.0538, wR_2(all) = 0.2202, 3845 independent observed absorption-corrected reflections [$|F_o| > 4\sigma(|F_o|)$, completeness to θ_{full}(38.6 °)], 174 parameters.

The structure of **2,7-dihexyl-diFIDT-di(N(CN))** was found to sit across a centre of symmetry at the middle of the central C_6F_2 ring.

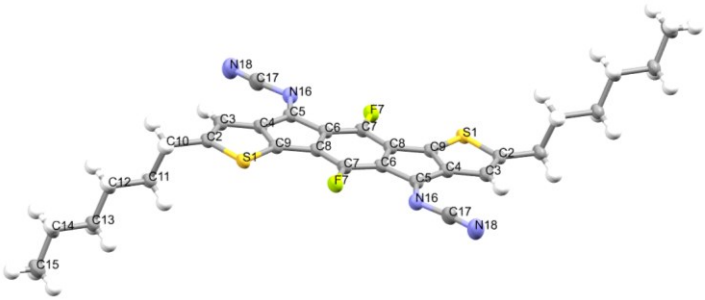


***Figure A89**: The crystal structure of **2,7-dihexyl-diFIDT-di(N(CN))** (50% probability ellipsoids). The molecule sits across a centre of symmetry at the middle of the central C_6F_2 ring.*

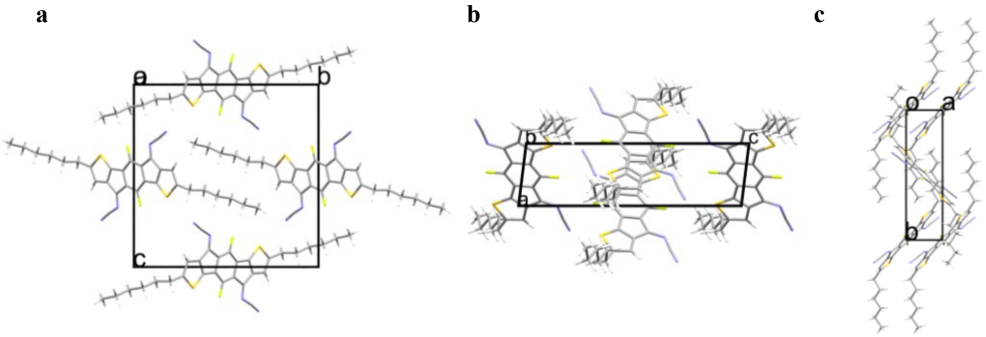


***Figure A90**: Unit cell of **2,7-dihexyl-diFIDT-di(N(CN))** as viewed along the a-, b- and c-axes (left to right).*

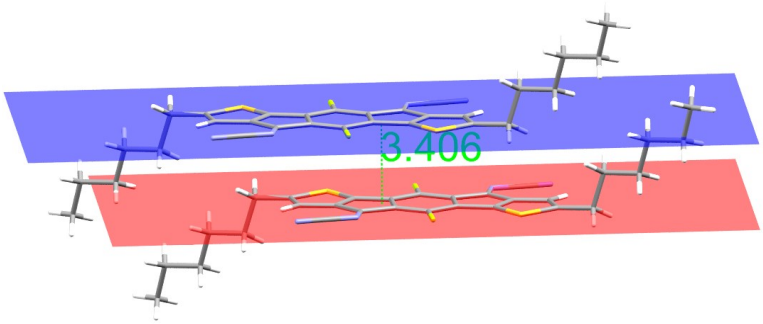
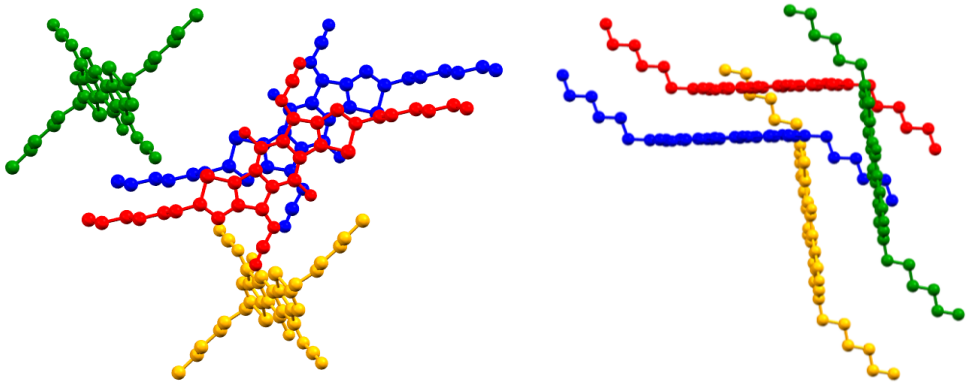
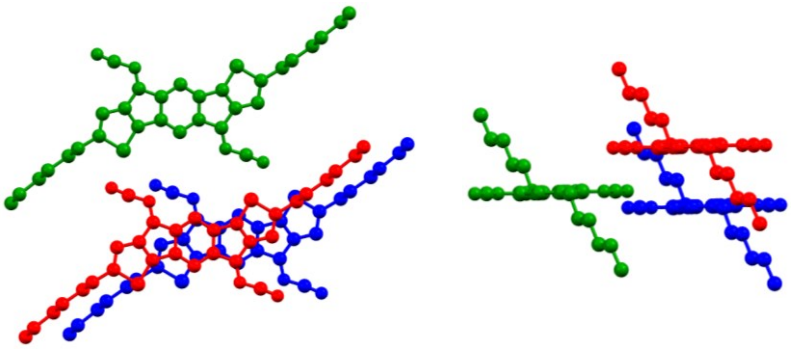


***Figure A91**: Interlayer spacing of **2,7-dihexyl-diFIDT-di(N(CN))**.*



2,7-dihexyl-diFIDT-di(N(CN)) Crystal	X	ES	EX	IND	DISP	TOT
Blue/Green	H	-3.79	4.59	-1.23	-4.71	-5.15
Blue/Green	F	-3.95	4.53	-1.20	-4.72	-5.34
Blue/Orange	H	-1.54	2.87	-0.55	-4.89	-4.11
Blue/Orange	F	-2.12	3.65	-0.60	-5.41	-4.47
Blue/Red	H	-10.59	33.22	-3.52	-49.03	-29.92
Blue/Red	F	-8.12	32.43	-3.78	-49.04	-28.50

Figure A92: *SAPT0 energies for selective dimers of* ***2,7-dihexyl-IDT-di(N(CN))*** *and* ***2,7-dihexyl-diFIDT-di(N(CN))*** *in the* ***2,7-dihexyl-diFIDT-di(N(CN))*** *crystal packing motif.*



2,7-dihexyl-IDT-di(N(CN)) Crystal	X	ES	EX	IND	DISP	TOT
Blue/Green	H	-5.43	6.96	-1.73	-7.93	-8.13
Blue/Green	F	-8.68	22.20	-2.84	-10.48	0.20
Red/Green	H	-6.08	8.89	-2.86	-8.45	-8.49
Red/Green	F	-5.97	6.96	-1.78	-8.18	-8.97
Blue/Red	H	-8.98	28.89	-3.18	-45.15	-28.43
Blue/Red	F	-6.72	28.36	-3.41	-45.18	-26.95

Figure A93: *SAPT0 energies for selective dimers of* ***2,7-dihexyl-IDT-di(N(CN))*** *and* ***2,7-dihexyl-diFIDT-di(N(CN))*** *in the* ***2,7-dihexyl-IDT-di(N(CN))*** *crystal packing motif.*

The X-ray crystal structure of 3,8-dihexyl-diFIDT-di(N(CN))

Crystal data for **3,8-dihexyl-diFIDT-di(N(CN))**: $C_{30}H_{28}F_2N_4S_2$, M = 546.68, triclinic, P-1, a = 4.6926(6), b = 8.4797(19), c = 17.028(3) Å, α = 78.265(17), β = 88.149(12), γ = 75.301(14) °, V = 641.6(2 Å^3, Z = 2 [Ci symmetry], D_c = 1.415 g cm^{-3}, μ(Cu-Kα) = 2.236 mm–1, T = 173 K, dark green needles, Agilent Xcalibur PX Ultra A diffractometer; 2401 independent measured reflections (R_{int} = 0.0628), F^2 refinement,[^{X1,X2}] R_1(obs) = 0.0652, wR_2(all) = 0.1839,

2401 independent observed absorption-corrected reflections [$|F_o| > 4\sigma(|F_o|)$, completeness to θ_{full}(72.15 °)], 173 parameters.

The structure of **3,8-dihexyl-diFIDT-di(N(CN))** was found to sit across a centre of symmetry at the middle of the central C_6F_2 ring.

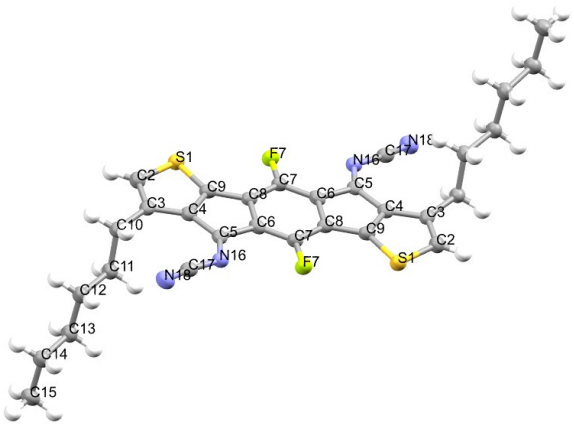


***Figure A94**: The crystal structure of **3,8-dihexyl-diFIDT-di(N(CN))** (50% probability ellipsoids). The molecule sits across a centre of symmetry at the middle of the central C_6F_2 ring.*

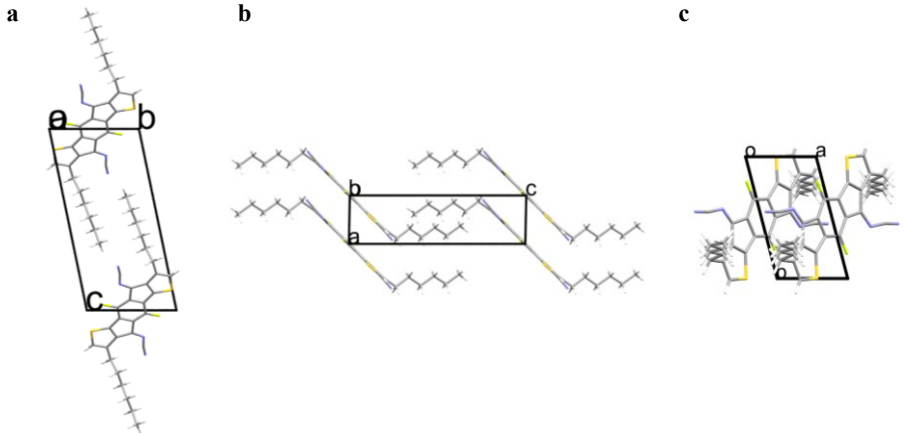


***Figure A95**: Unit cell of **3,8-dihexyl-diFIDT-di(N(CN))** as viewed along the a-, b- and c-axes (left to right).*

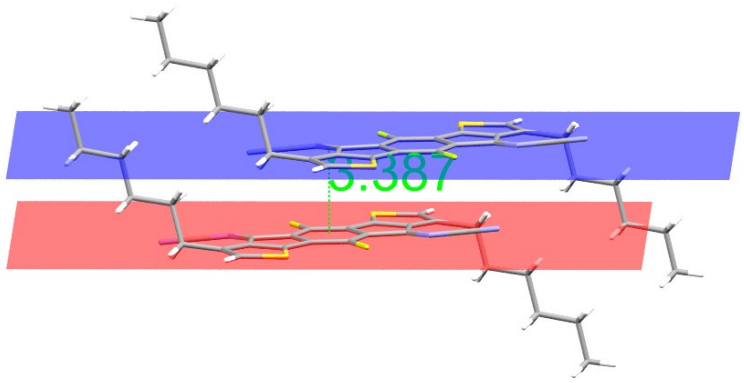


***Figure A96**: Interlayer spacing of **3,8-dihexyl-diFIDT-di(N(CN))**.*

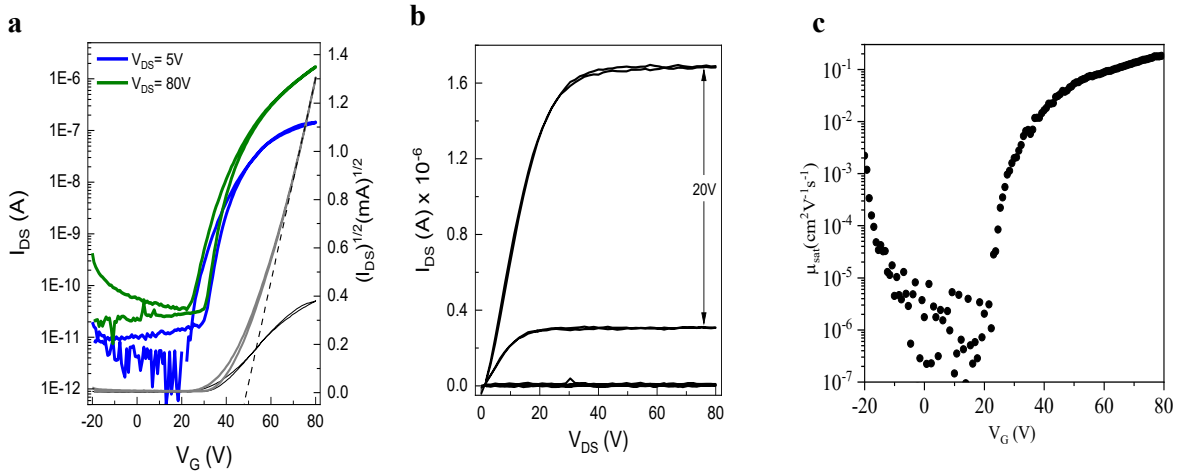


***Figure A97:** Device data for best performing BC-TG blade-coated devices of **2,7-dihexyl-diFIDT-di(N(CN))**.*

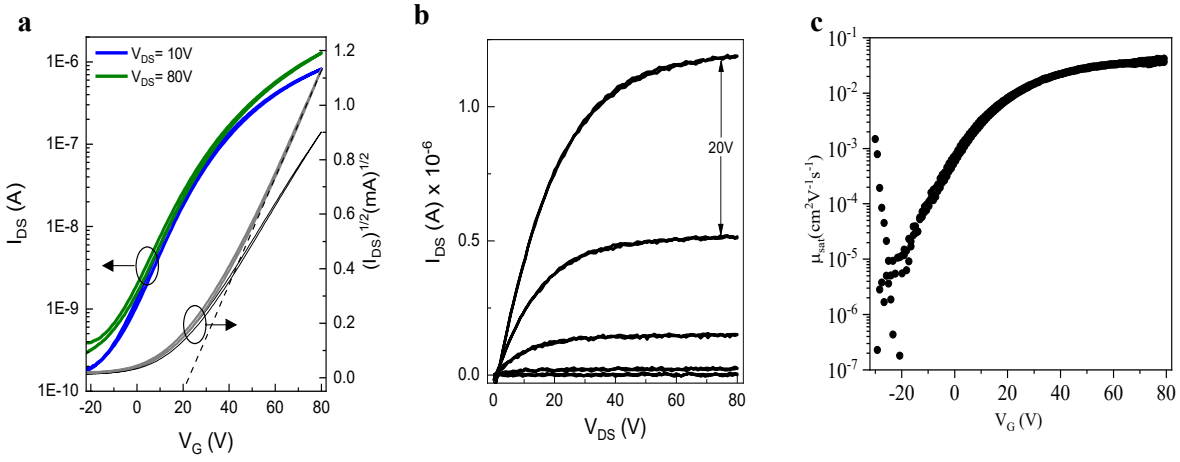


***Figure A98:** Device data for best performing BC-TG blade-coated devices of **3,8-dihexyl-diFIDT-di(N(CN))**.*

10.4 Chapter 5

10.4.1 End-functionalisation via Direct (Hetero)arylation

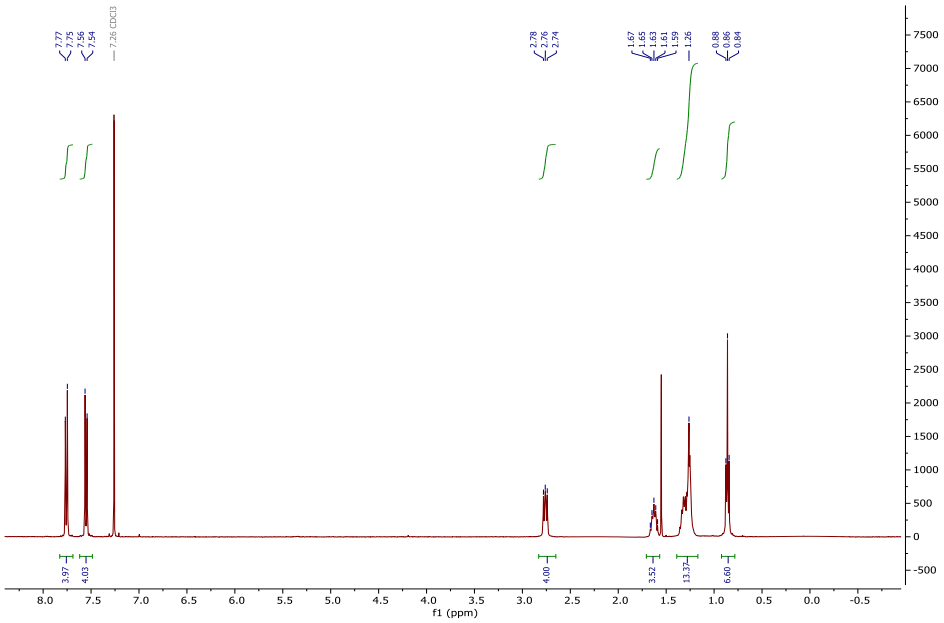


Figure A99: *^{1}H NMR of 4,4'-(5,10-difluoro-3,8-dihexyl-4,9-dioxo-4,9-dihydro-s-indaceno[1,2-b5,6-b']dithiophene-2,7-diyl)dibenzonitrile (**2,7-bis(4-benzonitrile)-3,8-dihexyl-diFIDT-di(O)**) in $CDCl_3$.*

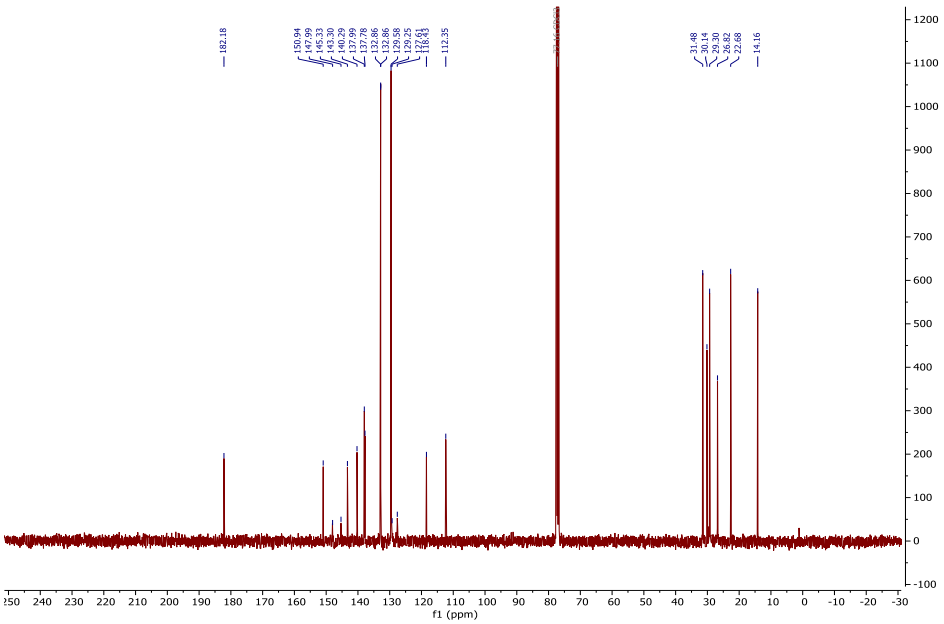


Figure A100: *^{13}C NMR of 4,4'-(5,10-difluoro-3,8-dihexyl-4,9-dioxo-4,9-dihydro-s-indaceno[1,2-b5,6-b']dithiophene-2,7-diyl)dibenzonitrile (**2,7-bis(4-benzonitrile)-3,8-dihexyl-diFIDT-di(O)**) in $CDCl_3$.*

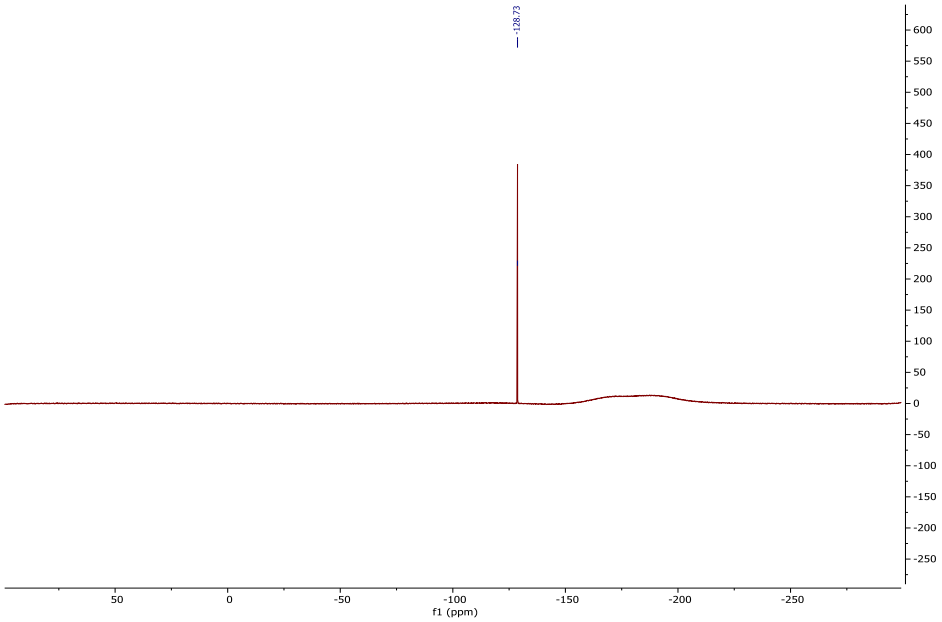
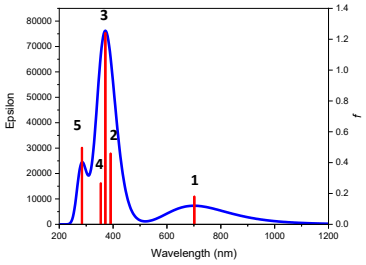


Figure A101: *^{19}F NMR of 4,4'-(5,10-difluoro-3,8-dihexyl-4,9-dioxo-4,9-dihydro-s-indaceno[1,2-b5,6-b']dithiophene-2,7-diyl)dibenzonitrile (**2,7-bis(4-benzonitrile)-3,8-dihexyl-diFIDT-di(O)**) in $CDCl_3$.*



1. HOMO→LUMO, 700 nm, f = 0.181
2. HOMO-4→LUMO, 389 nm, f = 0.460
   HOMO-2→LUMO
   HOMO→LUMO+2
3. HOMO-2→LUMO, 370 nm, f = 1.241
   HOMO→LUMO+2
4. HOMO-7→LUMO, 354 nm, f = 0.267
   HOMO-6→LUMO
   HOMO-4→LUMO
   HOMO→LUMO+2
   HOMO→LUMO+4
5. HOMO-1→LUMO+3, 284 nm, f = 0.497
   HOMO→LUMO+4

Figure A102: *Predicted UV-Vis spectrum from TD-DFT energy calculations of **2,7-bis(4-benzonitrile)-3,8-dialkyl-diFIDT-di(O)** after geometry optimisation with DFT B3LYP/6-311+G(d,p), with selected excitations highlighted.*

The X-ray crystal structure of 2,7-bis(4-benzonitrile)-3,8-dihexyl-diFIDT-di(O)

Crystal data for **2,7-bis(4-benzonitrile)-3,8-dihexyl-diFIDT-di(O)**: $C_{42}H_{34}F_2N_2O_2S_2$, (C_6H_5Cl), M = 813.38, triclinic, P-1, a = 9.2114(4), b = 13.4692(8), c = 17.5352(11) Å, α = 99.146(5), β = 99.776(4), γ = 98.626(4) °, V = 2081.4(2) Å^3, Z = 2 [Ci symmetry], D_c = 1.298 g cm^{-3}, μ(Cu-Kα) = 2.159 mm–1, T = 173 K, black platy needles, Agilent Xcalibur PX Ultra A diffractometer; 7837 independent measured reflections (R_{int} = 0.0364), F^2 refinement,[X1,X2]

R_1(obs) = 0.0440, wR_2(all) = 0.1163, 5421 independent observed absorption-corrected reflections [$|F_o| > 4\sigma(|F_o|)$, completeness to θ_{full}(59.8 °)], 469 parameters.

The structure of **2,7-bis(4-benzonitrile)-3,8-dihexyl-diFIDT-di(O)** was found to sit across a centre of symmetry at the middle of the central C_6F_2 ring.

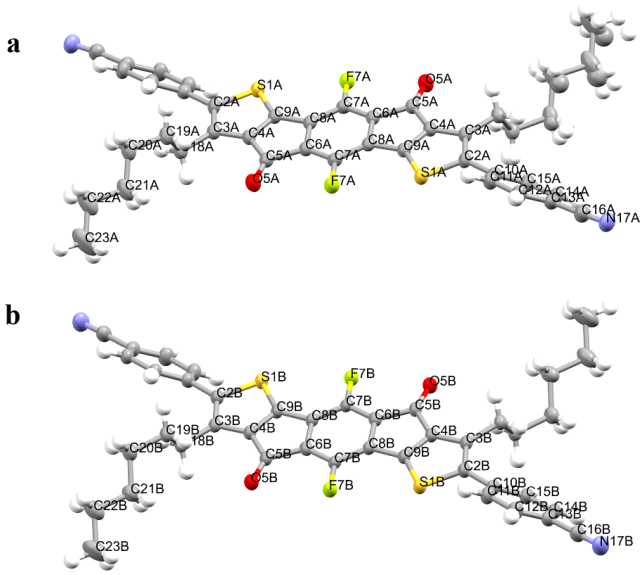


Figure A103: *The crystal structure of* ***2,7-bis(4-benzonitrile)-3,8-dihexyl-diFIDT-di(O)*** *(50% probability ellipsoids), showing a) molecule* ***A*** *and b) molecule* ***B****. The molecules sit across a centre of symmetry at the middle of the central* C_6F_2 *ring.*

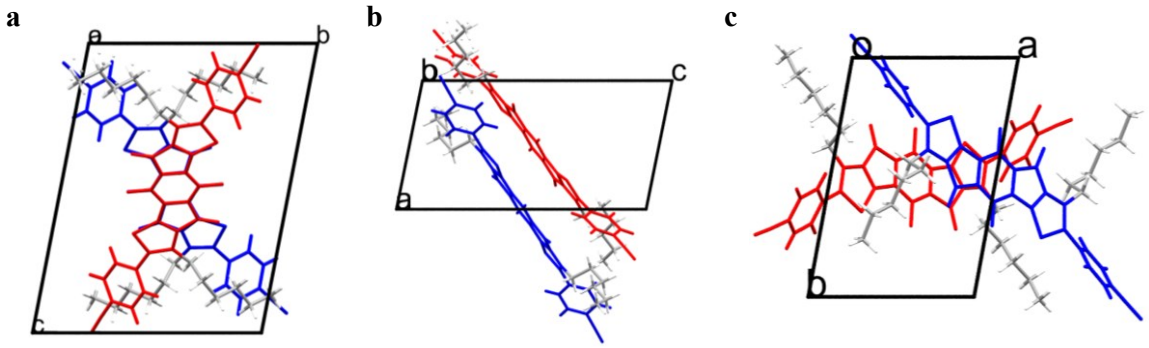


Figure A104*: Unit cell of* ***2,7-bis(4-benzonitrile)-3,8-dihexyl-diFIDT-di(O)*** *as viewed along the a-, b- and c-axes (left to right), highlighting molecule* ***A*** *(red) and molecule* ***B*** *(blue).*

10.4.2 Nucleophilic Aromatic Substitution (S_NAr) of the Fluorine Group

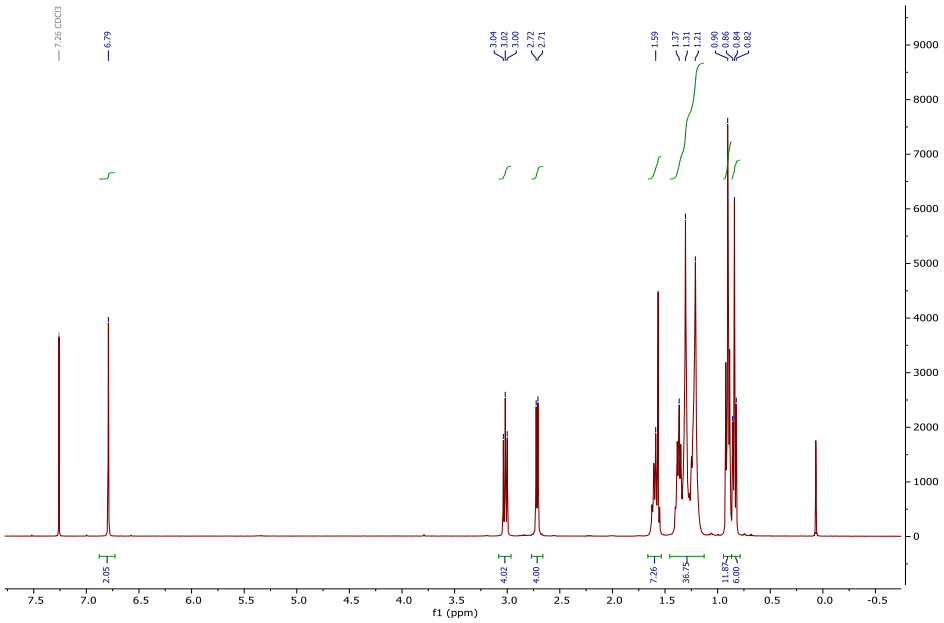


Figure A105: *^{1}H NMR of 2,7-bis(2-ethylhexyl)-5,10-bis(octylthio)-s-indaceno[1,2-b:5,6-b']dithiophene-4,9-dione (**2,7-bis(2-ethylhexyl)-diSRIDT-di(O)**) in $CDCl_3$.*

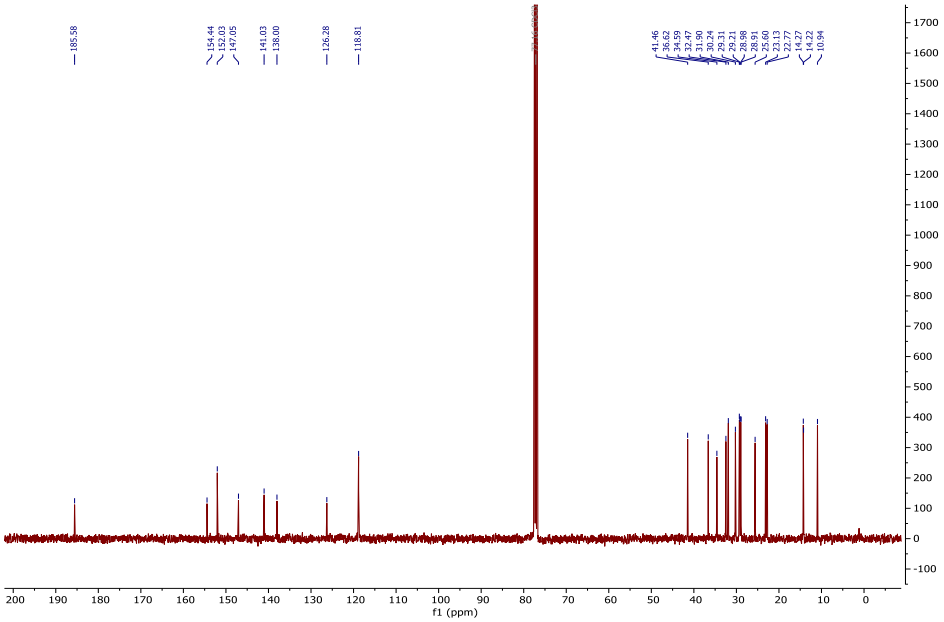


Figure A106: *^{13}C NMR of 2,7-bis(2-ethylhexyl)-5,10-bis(octylthio)-s-indaceno[1,2-b:5,6-b']dithiophene-4,9-dione (**2,7-bis(2-ethylhexyl)-diSRIDT-di(O)**) in $CDCl_3$.*

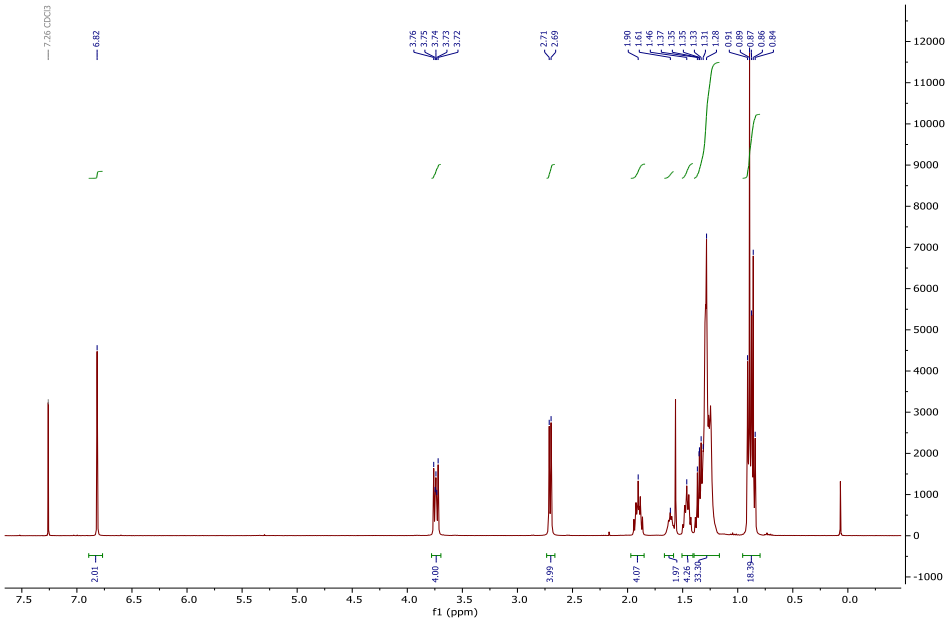


Figure A107: *^{1}H NMR of 2,7-bis(2-ethylhexyl)-5,10-bis(octylsulfonyl)-s-indaceno[1,2-b:5,6-b']dithiophene-4,9-dione (**2,7-bis(2-ethylhexyl)-diSO$_2$RIDT-di(O)**) in $CDCl_3$.*

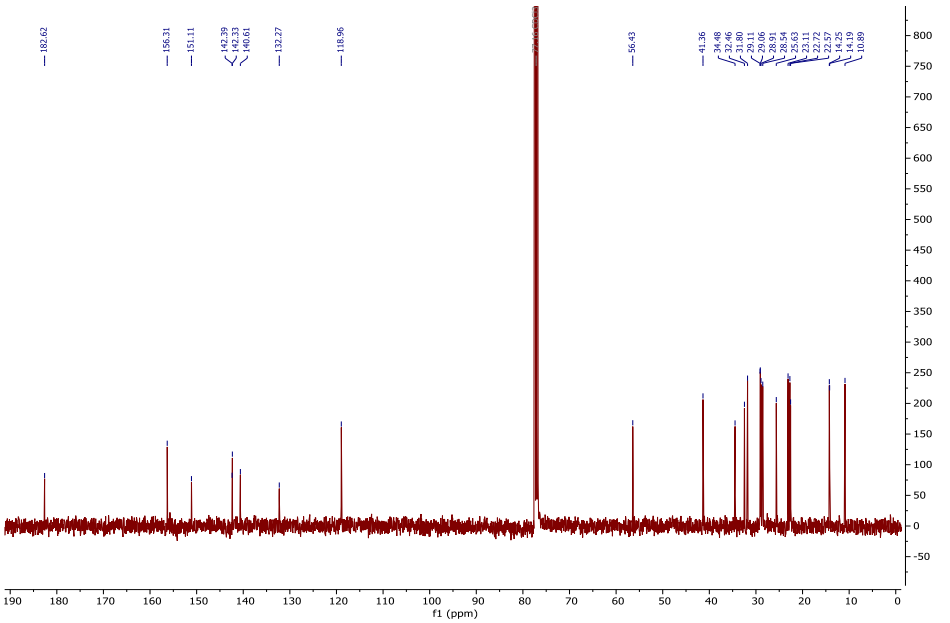


Figure A108: *^{13}C NMR of 2,7-bis(2-ethylhexyl)-5,10-bis(octylsulfonyl)-s-indaceno[1,2-b:5,6-b']dithiophene-4,9-dione (**2,7-bis(2-ethylhexyl)-diSO$_2$RIDT-di(O)**) in $CDCl_3$.*

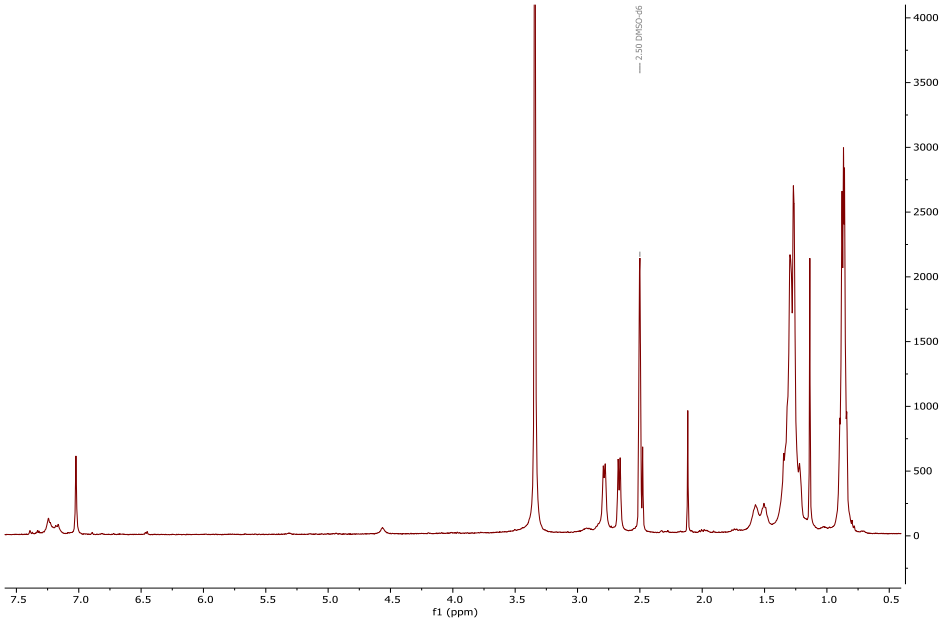


Figure A109: *^{1}H NMR of possible thiol-Michael addition of* ***2,7-bis(2-ethylhexyl)-diFIDT-di(C(CN)$_2$)*** *in DMSO-d$_6$.*

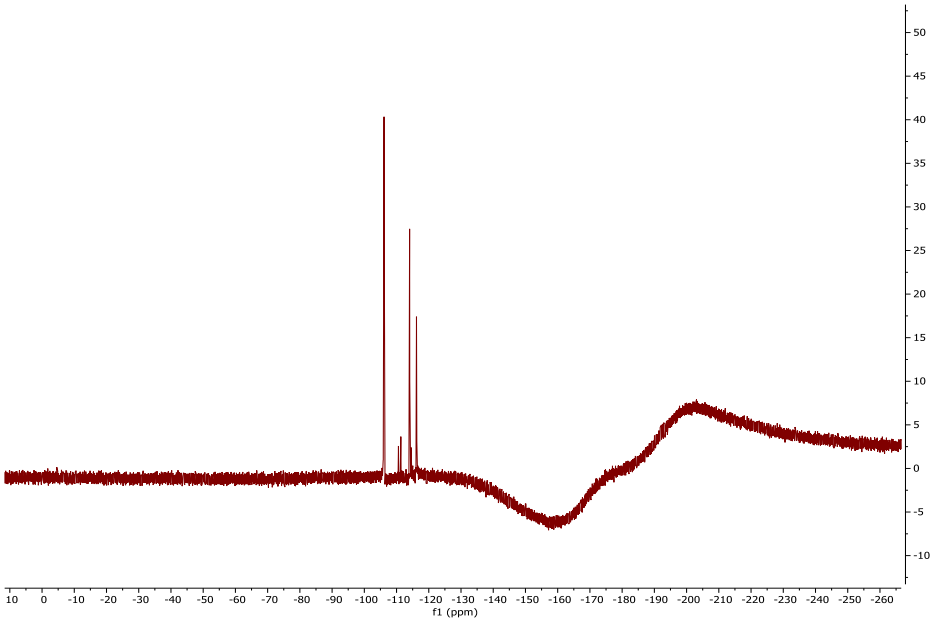
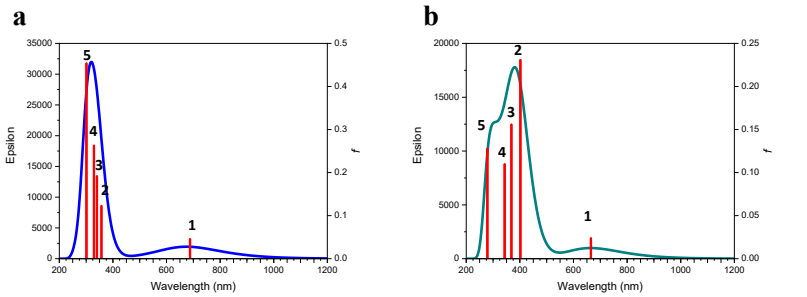


Figure A110: *^{19}F NMR of possible thiol-Michael addition of* ***2,7-bis(2-ethylhexyl)-diFIDT-di(C(CN)$_2$)*** *in DMSO-d$_6$.*



1. HOMO→LUMO, 786 nm, $f = 0.046$

2. HOMO-8→LUMO, 357 nm, $f = 0.123$
   HOMO-6→LUMO
   HOMO-3→LUMO
   HOMO→LUMO+2

3. HOMO-6→LUMO, 340 nm, $f = 0.192$
   HOMO-4→LUMO
   HOMO-2→LUMO+1
   HOMO-1→LUMO+2
   HOMO→LUMO+2

4. HOMO-8→LUMO, 328 nm, $f = 0.263$
   HOMO-6→LUMO
   HOMO-4→LUMO
   HOMO-3→LUMO+1
   HOMO-2→LUMO+1
   HOMO-1→LUMO+2
   HOMO→LUMO+2

5. HOMO-9→LUMO, 302 nm, $f = 0.454$
   HOMO-8→LUMO
   HOMO-1→LUMO+2
   HOMO→LUMO+2

1. HOMO→LUMO, 665 nm, $f = 0.024$

2. HOMO-6→LUMO, 401 nm, $f = 0.231$
   HOMO-3→LUMO
   HOMO-1→LUMO
   HOMO→LUMO+1
   HOMO→LUMO+2

3. HOMO-3→LUMO, 368 nm, $f = 0.156$
   HOMO-2→LUMO
   HOMO→LUMO+1

4. HOMO-5→LUMO, 343 nm, $f = 0.110$
   HOMO-4→LUMO

5. HOMO-10→LUMO, 280 nm, $f = 0.128$
   HOMO-5→LUMO+1
   HOMO-3→LUMO+2
   HOMO-2→LUMO+2

Figure A111: *Predicted UV-Vis spectra from TD-DFT energy calculations of a)* ***2,7-dialkyl-diSRIDT-di(O)*** *and b)* ***2,7-dialkyl-diSO$_2$IDT-di(O)*** *after geometry optimisation with DFT B3LYP/6-311+G(d,p), with selected excitations highlighted.*

10.5 Chapter 6

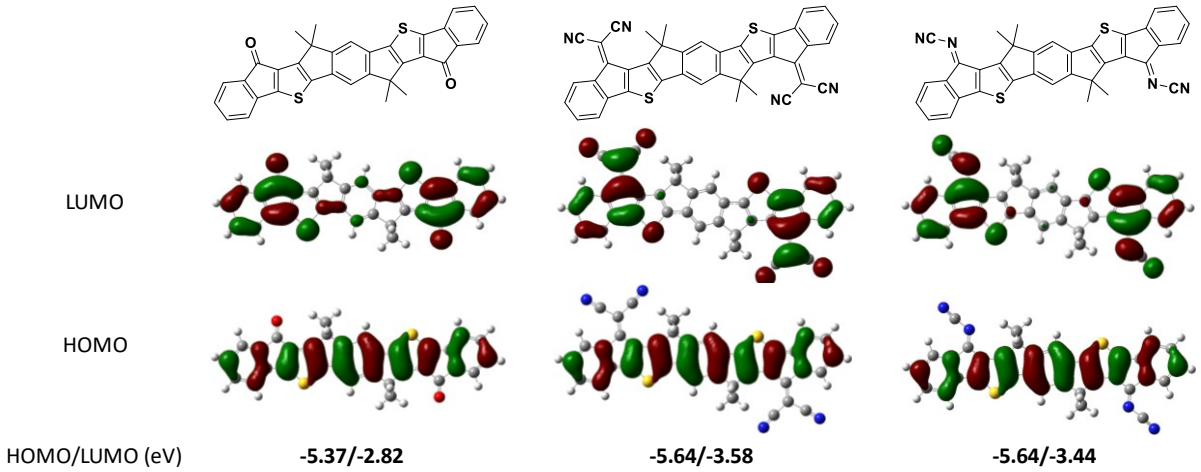


Figure A112: *HOMO and LUMO distributions predicted from DFT calculations.*

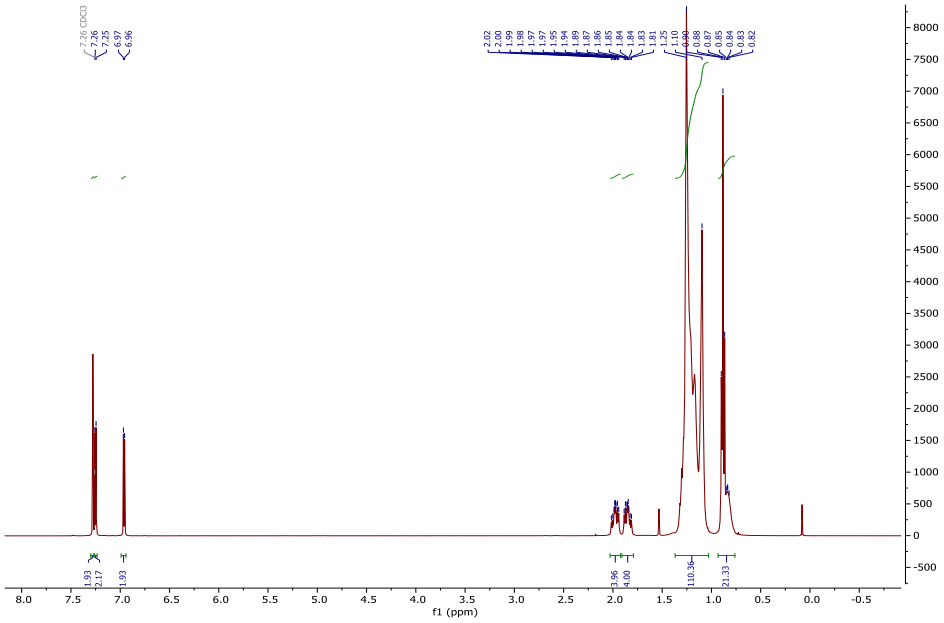


Figure A113: *^{1}H NMR of 4,9-dihydro-4,4,9,9-tetrahexadecyl-s-indaceno[1,2-b:5,6-b']-dithiophene in $CDCl_3$.*

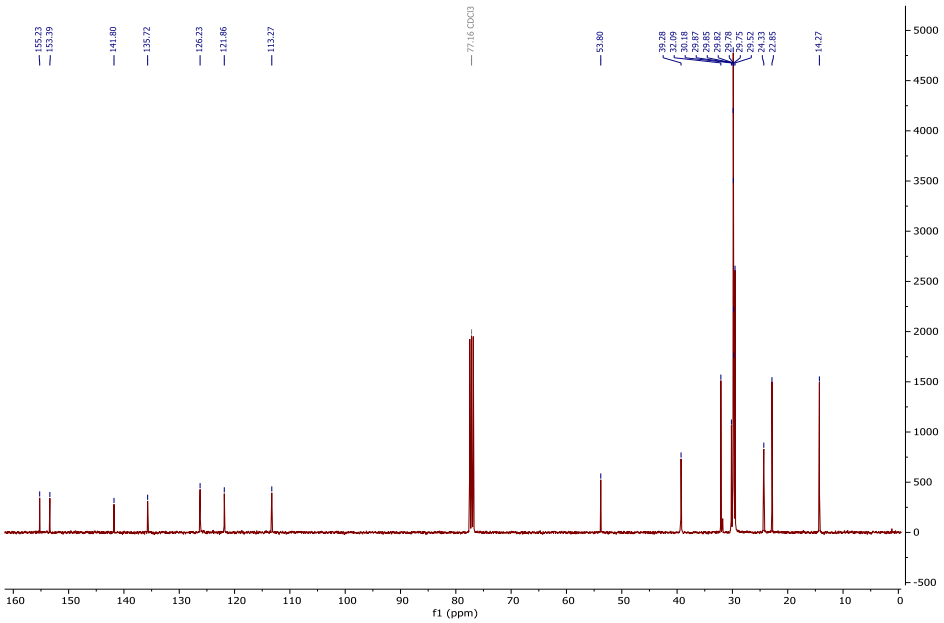


Figure A114: *^{13}C NMR of 4,9-dihydro-4,4,9,9-tetrahexadecyl-s-indaceno[1,2-b:5,6-b']-dithiophene in $CDCl_3$.*

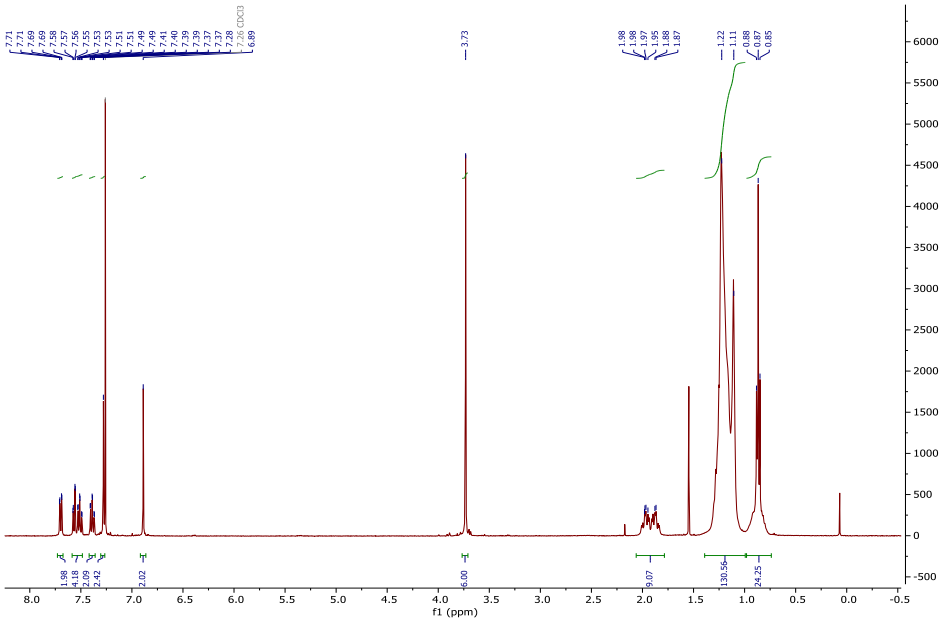


Figure A115: *^{1}H NMR of dimethyl 2,2'-(4,4,9,9-tetrahexadecyl-4,9-dihydro-s-indaceno[1,2-b:5,6-b']dithiophene-2,7-diyl)dibenzoate in $CDCl_3$.*

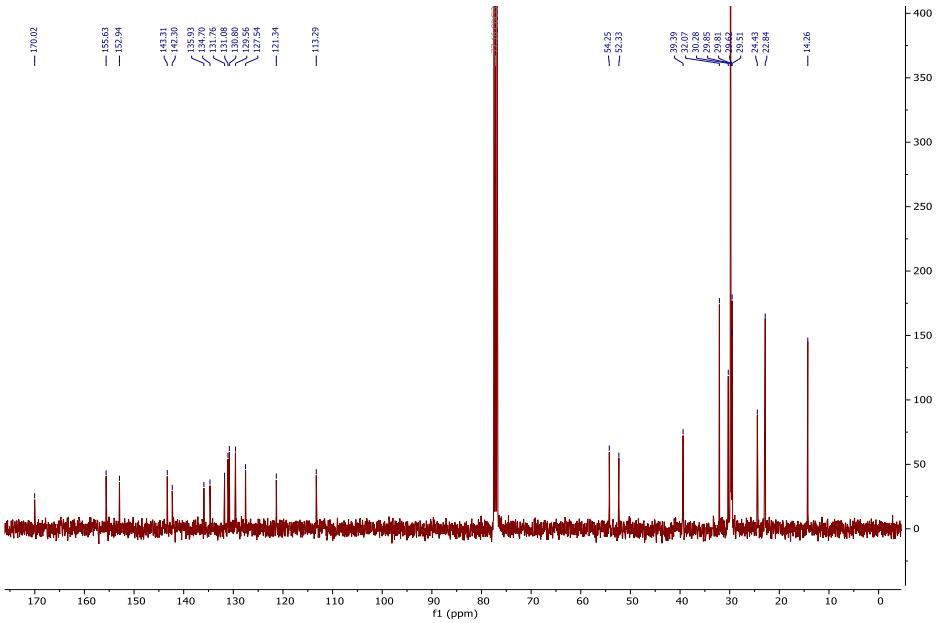


Figure A116: *^{13}C NMR of dimethyl 2,2'-(4,4,9,9-tetrahexadecyl-4,9-dihydro-s-indaceno[1,2-b:5,6-b']dithiophene-2,7-diyl)dibenzoate in $CDCl_3$.*

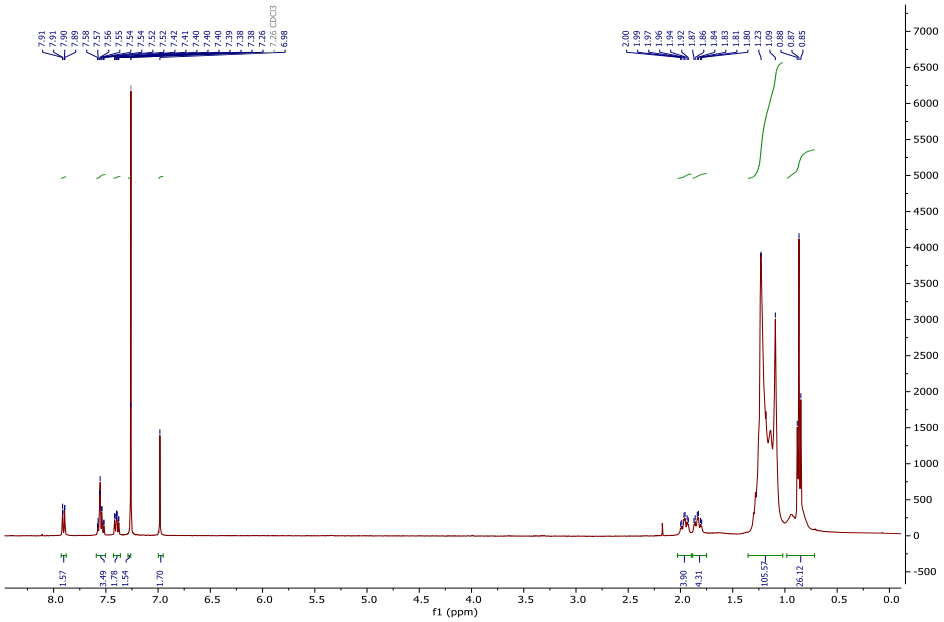


Figure A117: *^{1}H NMR of 2,2'-(4,4,9,9-tetrahexadecyl-4,9-dihydro-s-indaceno[1,2-b:5,6-b']dithiophene-2,7-diyl)dibenzoic acid in $CDCl_3$.*

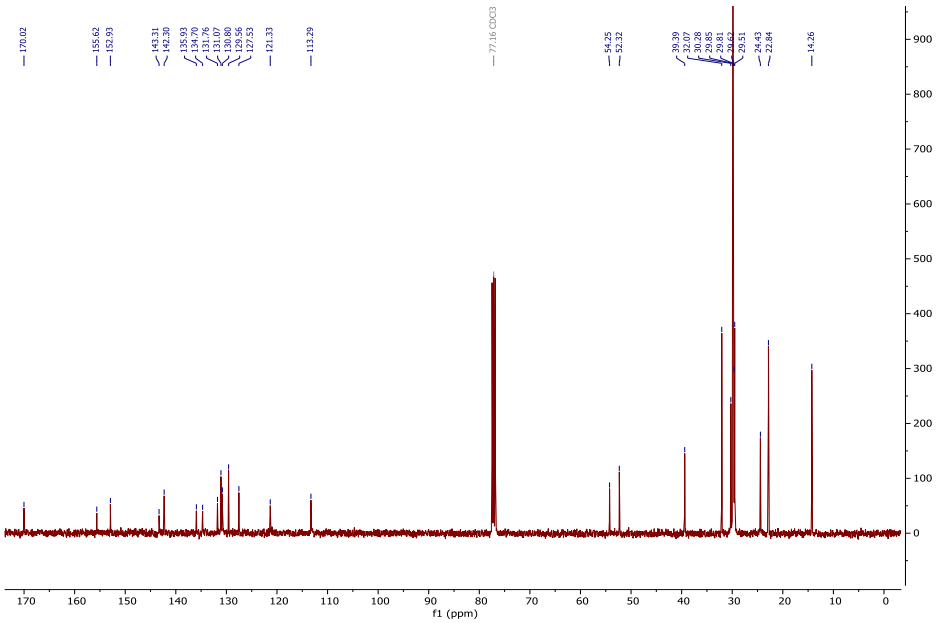


Figure A118: *^{13}C NMR of 2,2'-(4,4,9,9-tetrahexadecyl-4,9-dihydro-s-indaceno[1,2-b:5,6-b']dithiophene-2,7-diyl)dibenzoic acid in $CDCl_3$.*

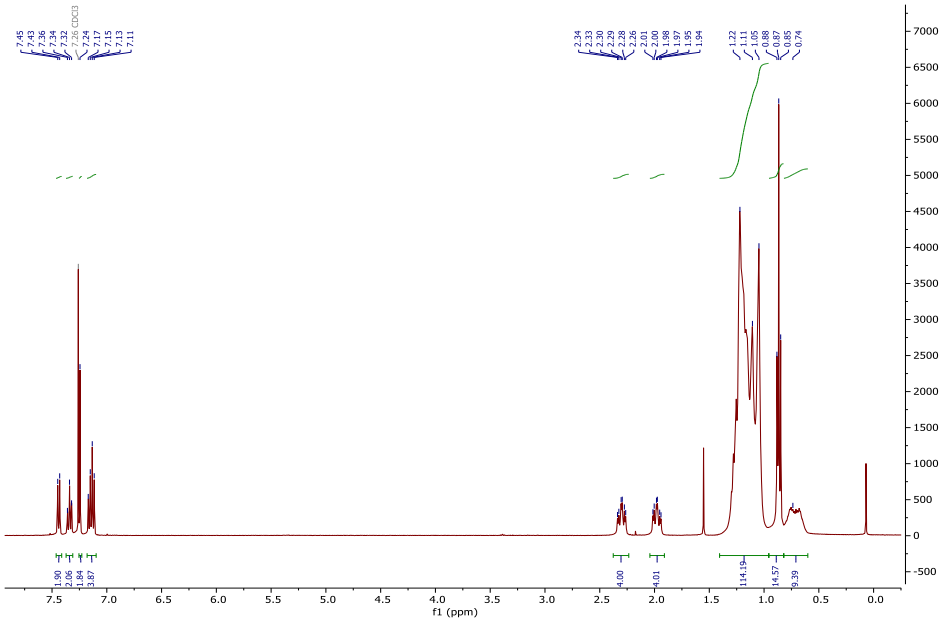


Figure A119: *^{1}H NMR of 2,2'-(4,4,9,9-tetrahexadecyl-4,9-dihydro-s-indaceno[1,2-b:5,6-b']dithiophene-2,7-diyl)difluorenone (**IDT-difluorenone**) in $CDCl_3$.*

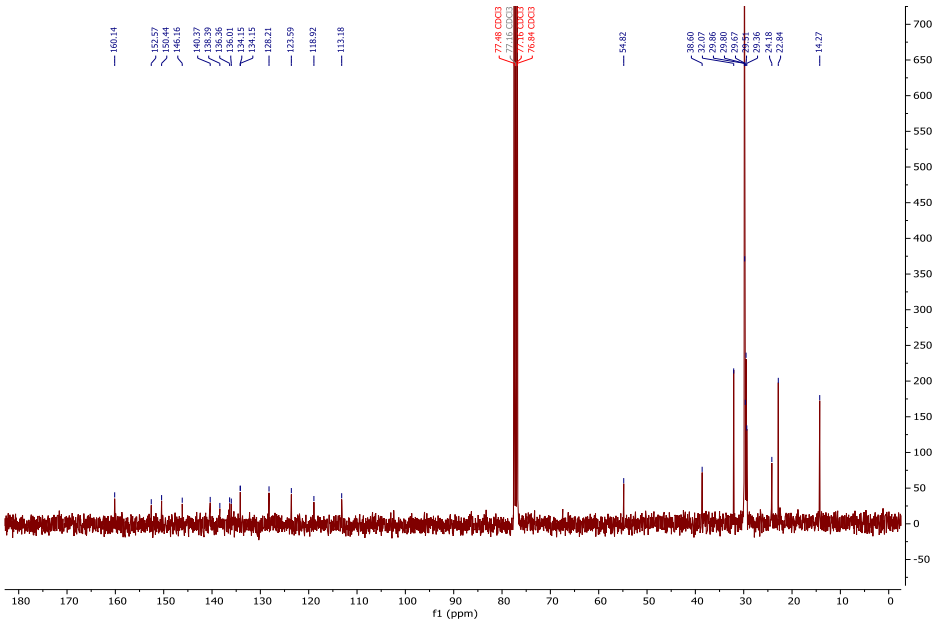


Figure A120: *^{13}C NMR of 2,2'-(4,4,9,9-tetrahexadecyl-4,9-dihydro-s-indaceno[1,2-b:5,6-b']dithiophene-2,7-diyl)difluorenone (**IDT-difluorenone**) in $CDCl_3$ at 50 °C.*

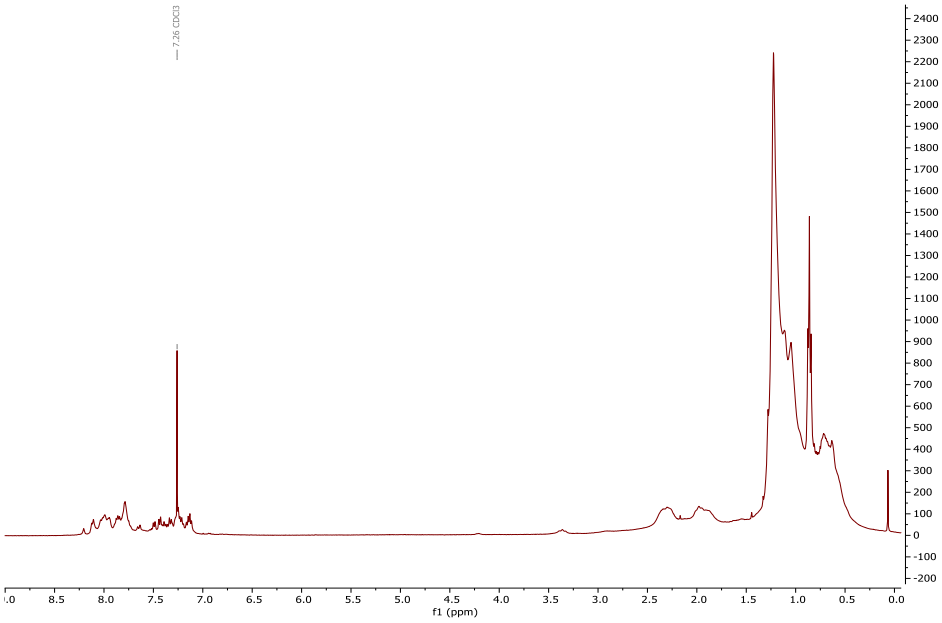


Figure A121: *^{1}H NMR of 2,2'-(4,4,9,9-tetrahexadecyl-4,9-dihydro-s-indaceno[1,2-b:5,6-b']dithiophene-2,7-diyl)difluorenone (**IDT-difluorenone**) after ~ 1 week exposed to air and light in $CDCl_3$.*

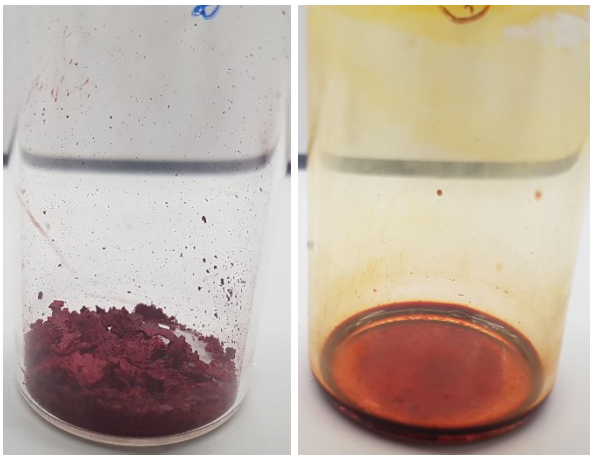


Figure A122: *Appearance of 2,2'-(4,4,9,9-tetrahexadecyl-4,9-dihydro-s-indaceno[1,2-b:5,6-b']dithiophene-2,7-diyl)difluorenone (**IDT-difluorenone**) before (left) and after ~ 1 week exposed to air and light (right).*

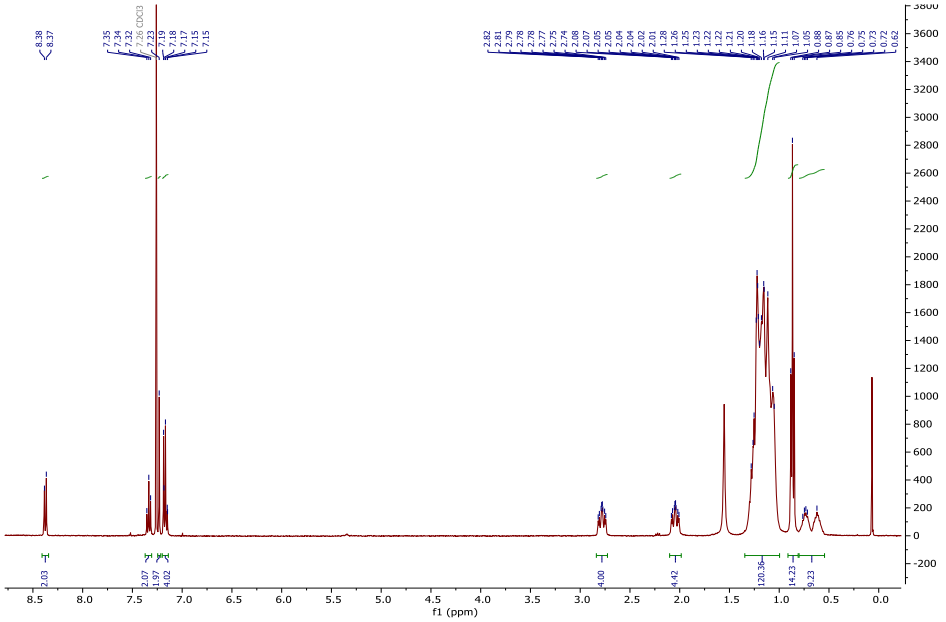


Figure A123: *^{1}H NMR of 2,2'-(4,4,9,9-tetrahexadecyl-4,9-dihydro-s-indaceno[1,2-b:5,6-b']dithiophene-2,7-diyl)difluorene-ylidene)dimalononitrile (**IDT-difluorenylidene-di(C(CN)$_2$)**) in $CDCl_3$.*

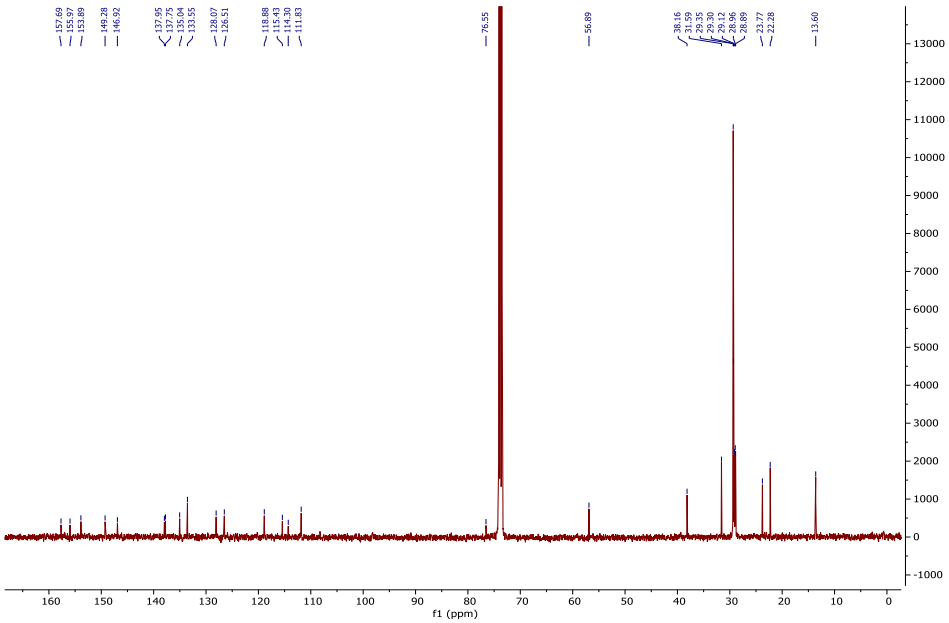


Figure A124: *^{13}C NMR of 2,2'-(4,4,9,9-tetrahexadecyl-4,9-dihydro-s-indaceno[1,2-b:5,6-b']dithiophene-2,7-diyl)difluorene-ylidene)dimalononitrile (**IDT-difluorenylidene-di(C(CN)$_2$)**) in $CDCl_3$.*

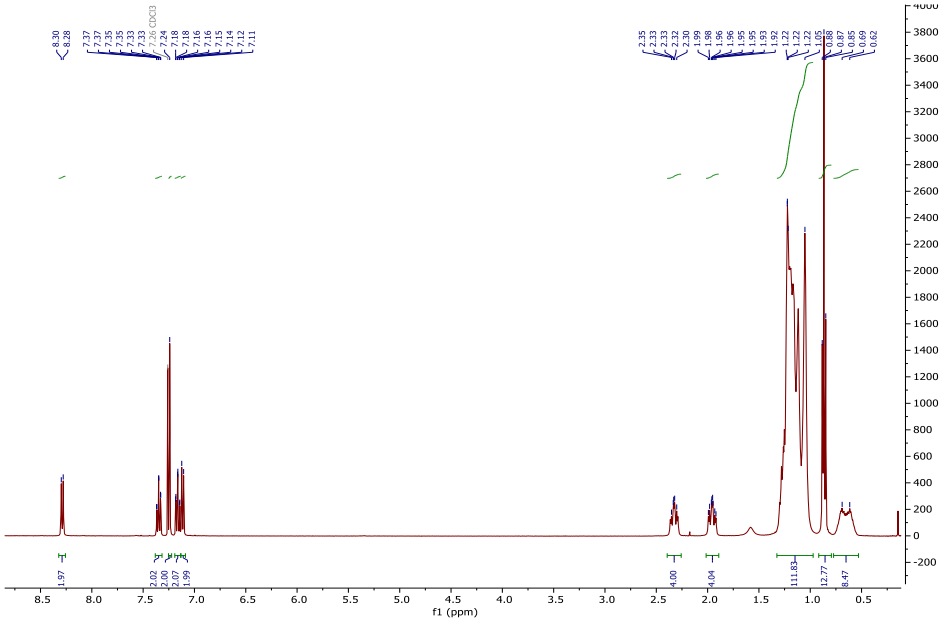


Figure A125: *^{1}H NMR of 2,2'-(4,4,9,9-tetrahexadecyl-4,9-dihydro-s-IDT-2,7-diyl)difluorene-ylidene)dicyanoimine (**IDT-difluorenylidene-di(N(CN))** in $CDCl_3$.*

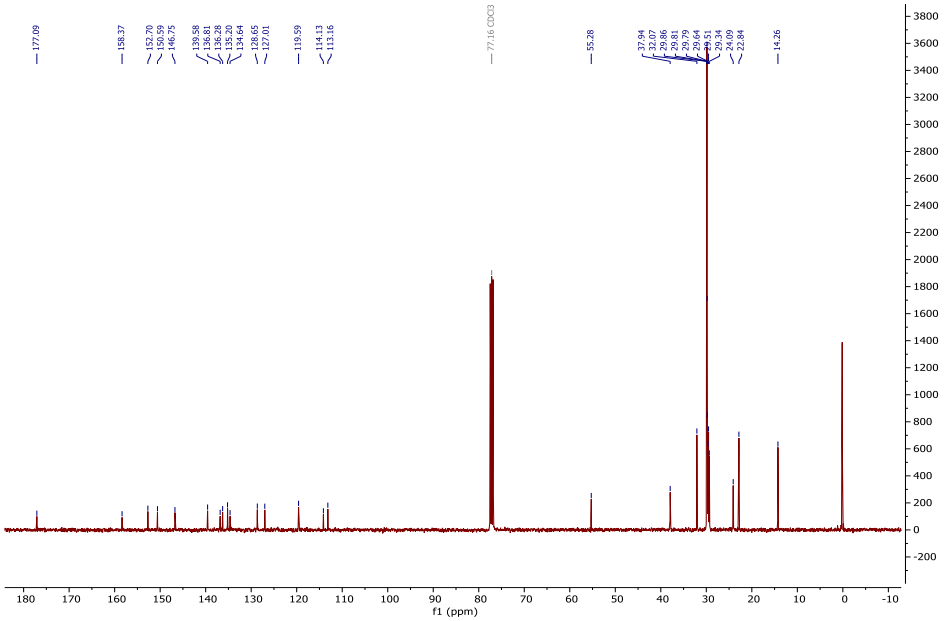
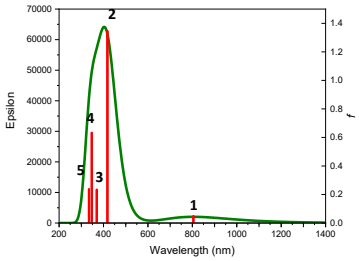


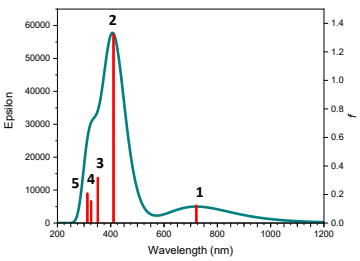
Figure A126: *^{13}C NMR of 2,2'-(4,4,9,9-tetrahexadecyl-4,9-dihydro-s-IDT-2,7-diyl)difluorene-ylidene)dicyanoimine (**IDT-difluorenylidene-di(N(CN))** in $CDCl_3$.*

a



1. HOMO-1→LUMO+1, 805 nm, $f = 0.05$
   HOMO→LUMO
2. HOMO→LUMO+2, 417 nm, $f = 1.348$
3. HOMO-6→LUMO+1, 368 nm, $f = 0.235$
   HOMO-5→LUMO
   HOMO-4→LUMO
   HOMO-3→LUMO+1
   HOMO-2→LUMO
4. HOMO-8→LUMO+1, 348 nm, $f = 0.634$
   HOMO-7→LUMO
   HOMO-6→LUMO+1
   HOMO-5→LUMO
   HOMO-4→LUMO
   HOMO-3→LUMO+1
   HOMO-2→LUMO
   HOMO→LUMO+2
5. HOMO-7→LUMO, 333 nm, $f = 0.239$
   HOMO-6→LUMO+1
   HOMO-5→LUMO
   HOMO-4→LUMO
   HOMO-3→LUMO+1
   HOMO-2→LUMO

b



1. HOMO-1→LUMO+1, 722 nm, $f = 0.123$
   HOMO→LUMO
2. HOMO→LUMO+2, 411 nm, $f = 1.326$
3. HOMO-6→LUMO+1, 352 nm, $f = 0.318$
   HOMO-5→LUMO
   HOMO-4→LUMO+1
   HOMO-3→LUMO
   HOMO-1→LUMO+1
4. HOMO-7→LUMO, 328 nm, $f = 0.155$
   HOMO-6→LUMO+1
   HOMO-5→LUMO
   HOMO-4→LUMO+1
   HOMO-3→LUMO
   HOMO→LUMO+5
5. HOMO-7→LUMO, 312 nm, $f = 0.209$
   HOMO-5→LUMO
   HOMO-4→LUMO+1
   HOMO-3→LUMO
   HOMO-2→LUMO+2
   HOMO→LUMO+4
   HOMO→LUMO+5

Figure A127: *Predicted UV-Vis spectra from TD-DFT energy calculations of a)* ***IDT-difluorenylidene-di(C(CN)$_2$)*** *and b)* ***IDT-difluorenylidene-di(N(CN))*** *after geometry optimisation with DFT B3LYP/6-311+G(d,p), with selected excitations highlighted.*

11. Permissions

Permission to reproduce text and figures for use in Chapter 1 and/or Chapter 2.

JOHN WILEY AND SONS LICENSE
TERMS AND CONDITIONS
Mar 12, 2020

This Agreement between Imperial College London -- Thomas Hodsden ("You") and John Wiley and Sons ("John Wiley and Sons") consists of your license details and the terms and conditions provided by John Wiley and Sons and Copyright Clearance Center.

License Number	4786380735440
License date	Mar 12, 2020
Licensed Content Publisher	John Wiley and Sons
Licensed Content Publication	Advanced Functional Materials
Licensed Content Title	Core Fluorination Enhances Solubility and Ambient Stability of an IDT-Based n-Type Semiconductor in Transistor Devices
Licensed Content Author	Thomas Hodsden, Karl J. Thorley, Julianna Panidi, et al
Licensed Content Date	Feb 26, 2020
Licensed Content Volume	0
Licensed Content Issue	0
Licensed Content Pages	12
Type of use	Dissertation/Thesis
Requestor type	Author of this Wiley article
Format	Electronic
Portion	Full article
Will you be translating?	No
Title of your thesis / dissertation	Synthesis and Characterisation of Novel Molecular Indacenodithiophene Semiconductors for Transistor Applications

Expected completion date	May 2020
Expected size (number of pages)	250
Requestor Location	Imperial College London White City Campus Wood Lane London, W12 0BZ United Kingdom Attn: Imperial College London
Publisher Tax ID	EU826007151
Total	0.00 GBP
Terms and Conditions	

TERMS AND CONDITIONS

This copyrighted material is owned by or exclusively licensed to John Wiley & Sons, Inc. or one of its group companies (each a"Wiley Company") or handled on behalf of a society with which a Wiley Company has exclusive publishing rights in relation to a particular work (collectively "WILEY"). By clicking "accept" in connection with completing this licensing transaction, you agree that the following terms and conditions apply to this transaction (along with the billing and payment terms and conditions established by the Copyright Clearance Center Inc., ("CCC's Billing and Payment terms and conditions"), at the time that you opened your RightsLink account (these are available at any time at http://myaccount.copyright.com).

Terms and Conditions

- The materials you have requested permission to reproduce or reuse (the "Wiley Materials") are protected by copyright.

- You are hereby granted a personal, non-exclusive, non-sub licensable (on a stand-alone basis), non-transferable, worldwide, limited license to reproduce the Wiley Materials for the purpose specified in the licensing process. This license, **and any CONTENT (PDF or image file) purchased as part of your order,** is for a one-time use only and limited to any maximum distribution number specified in the license. The first instance of republication or reuse granted by this license must be completed within two years of the date of the grant of this license (although copies prepared before the end date may be distributed thereafter). The Wiley Materials shall not be used in any other manner or for any other purpose, beyond what is granted in the license. Permission is granted subject to an appropriate acknowledgement given to the author, title of the material/book/journal and the publisher. You shall also duplicate the copyright notice that appears in the Wiley publication in your use of the Wiley Material. Permission is also granted on the understanding that nowhere in the text is a previously published source

acknowledged for all or part of this Wiley Material. Any third party content is expressly excluded from this permission.

- With respect to the Wiley Materials, all rights are reserved. Except as expressly granted by the terms of the license, no part of the Wiley Materials may be copied, modified, adapted (except for minor reformatting required by the new Publication), translated, reproduced, transferred or distributed, in any form or by any means, and no derivative works may be made based on the Wiley Materials without the prior permission of the respective copyright owner.**For STM Signatory Publishers clearing permission under the terms of the STM Permissions Guidelines only, the terms of the license are extended to include subsequent editions and for editions in other languages, provided such editions are for the work as a whole in situ and does not involve the separate exploitation of the permitted figures or extracts,** You may not alter, remove or suppress in any manner any copyright, trademark or other notices displayed by the Wiley Materials. You may not license, rent, sell, loan, lease, pledge, offer as security, transfer or assign the Wiley Materials on a stand-alone basis, or any of the rights granted to you hereunder to any other person.

- The Wiley Materials and all of the intellectual property rights therein shall at all times remain the exclusive property of John Wiley & Sons Inc, the Wiley Companies, or their respective licensors, and your interest therein is only that of having possession of and the right to reproduce the Wiley Materials pursuant to Section 2 herein during the continuance of this Agreement. You agree that you own no right, title or interest in or to the Wiley Materials or any of the intellectual property rights therein. You shall have no rights hereunder other than the license as provided for above in Section 2. No right, license or interest to any trademark, trade name, service mark or other branding ("Marks") of WILEY or its licensors is granted hereunder, and you agree that you shall not assert any such right, license or interest with respect thereto

- NEITHER WILEY NOR ITS LICENSORS MAKES ANY WARRANTY OR REPRESENTATION OF ANY KIND TO YOU OR ANY THIRD PARTY, EXPRESS, IMPLIED OR STATUTORY, WITH RESPECT TO THE MATERIALS OR THE ACCURACY OF ANY INFORMATION CONTAINED IN THE MATERIALS, INCLUDING, WITHOUT LIMITATION, ANY IMPLIED WARRANTY OF MERCHANTABILITY, ACCURACY, SATISFACTORY QUALITY, FITNESS FOR A PARTICULAR PURPOSE, USABILITY, INTEGRATION OR NON-INFRINGEMENT AND ALL SUCH WARRANTIES ARE HEREBY EXCLUDED BY WILEY AND ITS LICENSORS AND WAIVED BY YOU.

- WILEY shall have the right to terminate this Agreement immediately upon breach of this Agreement by you.

- You shall indemnify, defend and hold harmless WILEY, its Licensors and their respective directors, officers, agents and employees, from and against any actual or threatened claims, demands, causes of action or proceedings arising from any breach of this Agreement by you.

- IN NO EVENT SHALL WILEY OR ITS LICENSORS BE LIABLE TO YOU OR ANY OTHER PARTY OR ANY OTHER PERSON OR ENTITY FOR ANY SPECIAL, CONSEQUENTIAL, INCIDENTAL, INDIRECT, EXEMPLARY OR PUNITIVE DAMAGES, HOWEVER CAUSED, ARISING OUT OF OR IN CONNECTION WITH THE DOWNLOADING, PROVISIONING, VIEWING OR USE OF THE MATERIALS REGARDLESS OF THE FORM OF ACTION, WHETHER FOR BREACH OF CONTRACT, BREACH OF WARRANTY, TORT, NEGLIGENCE, INFRINGEMENT OR OTHERWISE (INCLUDING, WITHOUT LIMITATION, DAMAGES BASED ON LOSS OF PROFITS, DATA, FILES, USE, BUSINESS OPPORTUNITY OR CLAIMS OF THIRD PARTIES), AND WHETHER OR NOT THE PARTY HAS BEEN ADVISED OF THE POSSIBILITY OF SUCH DAMAGES. THIS LIMITATION SHALL APPLY NOTWITHSTANDING ANY FAILURE OF ESSENTIAL PURPOSE OF ANY LIMITED REMEDY PROVIDED HEREIN.

- Should any provision of this Agreement be held by a court of competent jurisdiction to be illegal, invalid, or unenforceable, that provision shall be deemed amended to achieve as nearly as possible the same economic effect as the original provision, and the legality, validity and enforceability of the remaining provisions of this Agreement shall not be affected or impaired thereby.

- The failure of either party to enforce any term or condition of this Agreement shall not constitute a waiver of either party's right to enforce each and every term and condition of this Agreement. No breach under this agreement shall be deemed waived or excused by either party unless such waiver or consent is in writing signed by the party granting such waiver or consent. The waiver by or consent of a party to a breach of any provision of this Agreement shall not operate or be construed as a waiver of or consent to any other or subsequent breach by such other party.

- This Agreement may not be assigned (including by operation of law or otherwise) by you without WILEY's prior written consent.

- Any fee required for this permission shall be non-refundable after thirty (30) days from receipt by the CCC.

- These terms and conditions together with CCC's Billing and Payment terms and conditions (which are incorporated herein) form the entire agreement between you and WILEY concerning this licensing transaction and (in the absence of fraud) supersedes all prior agreements and representations of the parties, oral or written. This Agreement may not be amended except in writing signed by both parties. This Agreement shall be binding upon and inure to the benefit of the parties' successors, legal representatives, and authorized assigns.

- In the event of any conflict between your obligations established by these terms and conditions and those established by CCC's Billing and Payment terms and conditions, these terms and conditions shall prevail.

- WILEY expressly reserves all rights not specifically granted in the combination of (i) the license details provided by you and accepted in the course of this licensing

transaction, (ii) these terms and conditions and (iii) CCC's Billing and Payment terms and conditions.

- This Agreement will be void if the Type of Use, Format, Circulation, or Requestor Type was misrepresented during the licensing process.

- This Agreement shall be governed by and construed in accordance with the laws of the State of New York, USA, without regards to such state's conflict of law rules. Any legal action, suit or proceeding arising out of or relating to these Terms and Conditions or the breach thereof shall be instituted in a court of competent jurisdiction in New York County in the State of New York in the United States of America and each party hereby consents and submits to the personal jurisdiction of such court, waives any objection to venue in such court and consents to service of process by registered or certified mail, return receipt requested, at the last known address of such party.

WILEY OPEN ACCESS TERMS AND CONDITIONS

Wiley Publishes Open Access Articles in fully Open Access Journals and in Subscription journals offering Online Open. Although most of the fully Open Access journals publish open access articles under the terms of the Creative Commons Attribution (CC BY) License only, the subscription journals and a few of the Open Access Journals offer a choice of Creative Commons Licenses. The license type is clearly identified on the article.

The Creative Commons Attribution License

The Creative Commons Attribution License (CC-BY) allows users to copy, distribute and transmit an article, adapt the article and make commercial use of the article. The CC-BY license permits commercial and non-

Creative Commons Attribution Non-Commercial License

The Creative Commons Attribution Non-Commercial (CC-BY-NC)License permits use, distribution and reproduction in any medium, provided the original work is properly cited and is not used for commercial purposes.(see below)

Creative Commons Attribution-Non-Commercial-NoDerivs License

The Creative Commons Attribution Non-Commercial-NoDerivs License (CC-BY-NC-ND) permits use, distribution and reproduction in any medium, provided the original work is properly cited, is not used for commercial purposes and no modifications or adaptations are made. (see below)

Use by commercial "for-profit" organizations

Use of Wiley Open Access articles for commercial, promotional, or marketing purposes requires further explicit permission from Wiley and will be subject to a fee.

Further details can be found on Wiley Online
Library http://olabout.wiley.com/WileyCDA/Section/id-410895.html

Other Terms and Conditions:

v1.10 Last updated September 2015

Questions? customercare@copyright.com or +1-855-239-3415 (toll free in the US) or +1-978-646-2777.
